A Photophysical Study of Excited State Dynamics in Donor-Acceptor Copolymer Photovoltaic Blends

Max Planck Graduate Center
mit der Johannes Gutenberg-Universität

Fabian Etzold

Dissertation

zur Erlangung des Grades eines „Doktor rerum naturalium (Dr. rer. nat.)“
der Fachbereiche: 08 - Physik, Mathematik und Informatik
09 - Chemie, Pharmazie und Geowissenschaften,
10 – Biologie, Universitätsmedizin
der Johannes Gutenberg-Universität Mainz

I hereby declare that I wrote the dissertation submitted without any unauthorized external assistance and used only sources acknowledged in the work. All textual passages which are appropriated verbatim or paraphrased from published and unpublished texts as well as all information obtained from oral sources are duly indicated and listed in accordance with bibliographical rules. In carrying out this research, I complied with the rules of standard scientific practice as formulated in the statutes of Johannes Gutenberg-University Mainz to insure standard scientific practice. I will write in the first person plural instead of singular (we instead of I) to make the text more readable.

Fabian Etzold

Summary

This thesis deals with the investigation of charge generation and recombination processes in three different polymer:fullerene photovoltaic blends by means of ultrafast time-resolved optical spectroscopy. The first donor polymer, namely poly[N-11"-henicosanyl-2,7-carbazole-alt-5,5-(4',7'-di-2-thienyl-2',1',3'-benzothiadiazole)] (PCDTBT), is a mid-bandgap polymer, the other two materials are the low-bandgap donor polymers poly[2,6-(4,4-bis-(2-ethylhexyl)-4H-cyclopenta[2,1-b;3,4-b']-dithiophene)-alt-4,7-(2,1,3-benzothiadiazole) (PCPDTBT) and poly[(4,4'-bis(2-ethylhexyl)dithieno[3,2-b:2',3'-d]silole)-2,6-diyl-alt-(2,1,3-benzothiadiazole)-4,7-diyl] (PSBTBT). Despite their broader absorption, the low-bandgap polymers do not show enhanced photovoltaic efficiencies compared to the mid-bandgap system.

Transient absorption spectroscopy revealed that energetic disorder plays an important role in the photophysics of PCDTBT and that in a blend with PCBM geminate losses are small. The photophysics of the low-bandgap system PCPDTBT were strongly altered by adding a high boiling point cosolvent to the polymer:fullerene blend due to a partial demixing of the materials. We observed an increase in device performance together with a reduction of geminate recombination upon addition of the cosolvent. By applying model-free multi-variate curve resolution to the spectroscopic data, we found that fast non-geminate recombination due to polymer triplet state formation is a limiting loss channel in the low-bandgap material system PCPDTBT, whereas in PSBTBT triplet formation has a smaller impact on device performance, and thus higher efficiencies are obtained.

Zusammenfassung

Diese Arbeit befasst sich mit der Untersuchung von Ladungserzeugungs- und Rekombinationsprozessen in drei Polymer-Fulleren-Systemen, die in organischen Solarzellen verwendet werden. Dazu wurde ultraschnelle, zeitaufgelöste Spektroskopie verwendet. Beim ersten Donor-Polymer handelt es sich um Poly[*N*-11"-henicosanyl-2,7-carbazol-alt-5,5-(4',7'-di-2-thienyl-2',1',3'-benzothiadiazol)] (PCDTBT), welches eine mittelgroße Bandlücke aufweist. Die anderen beiden Donormaterialien, Poly[2,6-(4,4-bis-(2-ethylhexyl)-4H-cyclopenta[2,1-b;3,4-b']-dithiophen)-alt-4,7-(2,1,3-benzothiadiazol) (PCPDTBT) und Poly[(4,4'-bis(2-ethylhexyl)dithieno[3,2-b:2',3'-d]silol)-2,6-diyl-alt-(2,1,3-benzothiadiazol)-4,7-diyl] (PSBTBT), sind Polymere mit einer kleinen Bandlücke. Trotz breiterer Absorption erreichen die rot absorbierenden Polymere keine oder eine nur geringfügig verbesserte Effizienz in einer organischen Solarzelle.

Transiente Absorptionsspektroskopie zeigte, dass die photophysikalischen Prozesse in PCDTBT stark von der energetischen Unordnung des Systems beeinflusst werden und nur wenig geminale Verluste in einer Mischung mit PCBM vorliegen. Die photophysikalischen Prozesse in PCPDTBT zeigten eine starke Abhängigkeit von verwendeten Lösungsmittelzusätzen. So konnte durch Zugabe von ODT eine Effizienzsteigerung beobachtet werden, die mit einer Reduktion der geminalen Rekombination einherging. Mittels eines *soft-modeling* Ansatzes konnten wir weiterhin beobachten, dass schnelle, nicht-geminale Rekombination, bedingt durch Polymer-Triplettgeneration, die Effizienz des rot absorbierenden PCPDTBT Polymers in Solarzellen beeinträchtigt, wohingegen das PSBTBT Polymer weniger stark davon betroffen ist und bessere Effizienzen zeigt.

The acknowledgements are not contained in this version.

Contents

List of Figures

Chapter 1

Introduction

Every second 3.86×10^{26} J energy is released at the core of the sun, of which 1366 Wm^{-2} reach the earth's atmosphere.[1] Absorption losses in the atmosphere further reduce the irradiance of the sun yielding approximately 1000 Wm^{-2} at the surface of the earth. For Germany, a yearly average of the global radiation of 1096 $kWhm^{-2}$ was measured in 2012,[2] together with a gross electricity consumption of 605.6 TWh.[3] Assuming that the global radiation could be converted with 100 % efficiency, less than 0.2 % of the total area of Germany would have to be covered with solar panels to generate the yearly gross electricity consumption. Obviously, the assumed efficiency is far from being realistic and completely ignores the difficult questions of energy storage, but nonetheless the example stresses the immense potential of solar energy. Conventional photovoltaics are based on silicon because of module efficiencies in excess of 20 % and a stability of more than 25 years. However, the production of silicon-based solar cells is energy consuming and expensive, motivating the development of organic photovoltaics (OPV) which are unrivaled in terms of processing cost, processing speed and processing simplicity.[4] The variety of different polymers offers a large versatility regarding color and transparency of the solar cells and together with the mechanical flexibility of the systems, several new applications are being targeted. Recently, a backpack with an integrated OPV panel, used to charge e.g. a cell phone, was developed, or applications in architecture like the integration of solar panels in large area facades are possible due to their light weight. With the semi-transparency of organic solar cells one could further think of sun light passing through a window and at the same time generating electricity.

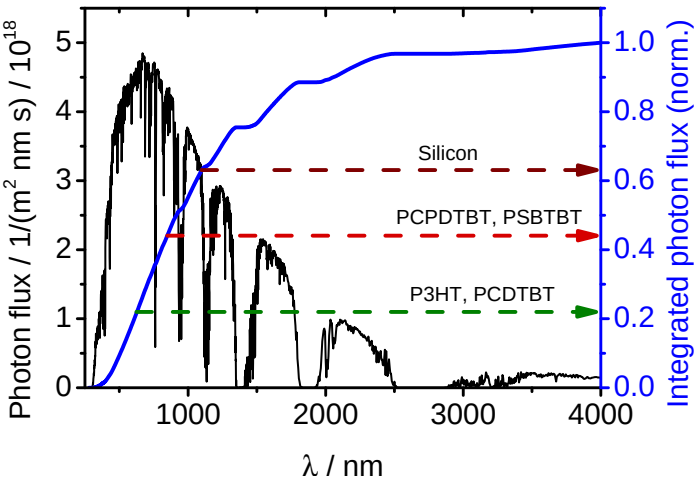

Figure 1.1: Photon flux calculated from the AM1.5G solar spectrum together with the normalized integrated photon flux and the approximate onset of absorption of several materials used in photovoltaics. The AM1.5G data is taken from [7].

The state of the art single junction solution processed organic solar cell shows a device efficiency exceeding 9 %,[5] and efficiencies exceeding 10 % have been reported for tandem devices.[6] However, in order to compete with conventional silicon solar cells the efficiency of organic solar cells and their lifetime have to be increased further. The long time benchmark system of first generation of OPV materials is a blend consisting of the donor polymer poly(3-hexylthiophene) (P3HT) and the fullerene acceptor [6,6]-phenyl-C61-butyric acid methyl ester (PCBM), which is limited to approximately 5 % efficiency. This is in part caused by the poor overlap of absorption with the solar spectrum, as P3HT:PCBM exhibits an onset of absorption around 630 nm. The charge generation usually is a one photon process so that the absorption of the solar cell should match the photon flux rather than the irradiance of the sun, with the latter being slightly blue-shifted.

Figure 1.1 shows the photon flux calculated from the AM1.5G solar spectrum together with the normalized integrated photon flux, indicating that only about 22 % of the emitted solar photons can be harvested for photocurrent generation in a mid-bandgap polymer fullerene device like P3HT:PCBM. Silicon has an onset of absorption around 1100 nm increasing the available photon flux to 63 % of the

total photon flux, almost a factor of 3 larger than that of P3HT:PCBM. This stimulated the development of low-bandgap polymers for application in organic solar cells. Two prototypic candidates, namely poly[2,6-(4,4-bis-(2-ethylhexyl)-4H-cyclopenta[2,1-b;3,4-b']-dithiophene)-alt-4,7-(2,1,3-benzothiadiazole), in short PCPDTBT, and poly[(4,4'-bis(2-ethylhexyl)dithieno[3,2-b:2',3'-d]silole)-2,6-diyl-alt-(2,1,3-benzothiadiazole)-4,7-diyl] (PSBTBT), exhibit an onset of absorption around 850 nm, thereby increasing the fraction of accessible photon flux to approximately 44 %. However, device efficiencies are reported to be only around 5 %, clearly missing the expected increase compared to the mid-bandgap polymer P3HT. Therefore, more insight into the photophysics of charge generation and recombination are necessary to develop novel, better performing materials.

In this thesis the photophysics of the mid-bandgap polymer poly[N-11"-henicosanyl-2,7-carbazole-alt-5,5-(4',7'-di-2-thienyl-2',1',3'-benzothiadiazole)] (PCDTBT) and the above mentioned PCPDTBT and PSBTBT are investigated to gain insight into the loss mechanisms of organic solar cells.

This thesis consists of five chapters, of which the present one shortly introduces organic photovoltaics and motivates the aim of this work. The second chapter (Theoretical Background) contains the theoretical framework of the photophysics of organic solar cells and ultrafast spectroscopy. First, a short introduction to the photophysics of conjugated polymers is given, followed by a general description of organic photovoltaics and a short review of the materials used in organic solar cells. After that the mechanisms of charge photogeneration in organic materials are presented and current results from literature are discussed. The loss processes in organic solar cells are explained, followed by a short introduction to ultrafast phenomena and nonlinear optics as a basis for femtosecond time-resolved spectroscopy.

The third chapter (Experimental Methods and Materials) contains information about the characterization of organic solar cells and describes the setups used for time-resolved spectroscopy. The focus is placed on transient absorption spectroscopy, and a short overview of the techniques employed to analyze transient absorption data is given.

In chapter four (Results and Discussion) the results of all experimental work done for this thesis are presented and discussed. Some of the projects were partially

published in peer reviewed journals, and therefore the results are partially a collection of published articles.[1] The first case study deals with the mid-bandgap polymer PCDTBT and the charge generation and recombination mechanisms in its blend with a fullerene electron acceptor. Furthermore, the effect of large energetic disorder observed in this material blend is discussed. In the second case study the effect of a high boiling point cosolvent on the photophysics and the morphology of the low-bandgap polymer PCPDTBT in a photovoltaic blend is presented. The third case study investigates the low-bandgap donor PSBTBT, which is very similar to PCPDTBT except for the substitution of the bridge-head atom. The model-free analysis of the spectroscopic data revealed that polymer triplet states are generated in the polymer fullerene blend, representing an additional loss channel limiting device performance. The PCPDTBT material system is revisited and the results for the two donor polymers are compared, revealing that the triplet generation is faster in PCPDTBT and limits its performance in a solar cell.

Chapter five (Conclusion and Outlook) contains a short summary of the results, and conclusions concerning charge generation and loss mechanisms are presented. Finally, a short outlook is given, in which ways to improve the materials for organic photovoltaics are discussed and improvements of the experimental techniques are suggested.

[1] In accordance with the MPGC examination regulations §11.1

Chapter 2

Theoretical Background

2.1 Electronic Configuration of Carbon in Organic Semiconductors

The carbon atom has six electrons with the configuration $1s^2 2s^2 2p^2$ of which four electrons are placed in the outer shell. These four electrons participate in bonding interactions, and by linear combination of s- and p-orbitals so called hybrid orbitals are formed which are necessary to explain the different bonding types of carbon.

In organic semiconductors mostly sp^2-hybridization can be found in which three in-plane sp^2-hybrid orbitals and one p_z-orbital oriented perpendicular to the plane are formed. When carbon atoms are brought together, two overlapping sp^2-orbitals interact to form a strong σ-bond which yields the backbone of a polymer chain. Due to the in-phase interference of the electronic wave functions in a σ-bond, the participating electrons are localized between the carbon atoms and therefore do not contribute to electrical conductivity. The p_z-orbitals also interact with each other to form π-bonds, which are weaker than σ-bonds. Each carbon atom contributes one p_z-electron to the π-bond which has the same symmetry as the p_z-orbital. This leads to a delocalization of π-electrons along the chain, which is called π-conjugation. For a long linear array of carbon atoms, the delocalized π-orbitals would lead to a half-filled conduction band, similar to that of a metal. However, it was shown that it is energetically favorable to have

a redistribution of the bond lengths in such a system, causing the opening of a bandgap and explaining the semiconductor properties of the carbon chain.[8] Due to the phase of the electronic wavefunction, the overlap of two orbitals can lead to the above mentioned constructive interference, but also destructive interference is possible from which the anti-bonding orbitals are created. In conjugated polymer chains the energetically highest lying and filled orbital is usually a bonding π-orbital and is called highest occupied molecular orbital (HOMO). Accordingly, the highest unoccupied molecular orbital (LUMO) is defined as the energetically lowest orbital that does not contain electrons, for example an anti-bonding $\pi^{\star}$-orbital. The difference in energy between these two states is often referred to as the optical band-gap. In real world systems the lengths of the conjugated system is limited by structural distortions and system defects so that a polymer usually contains a distribution of conjugation lengths.

2.2 Excitons in Organic Solids

2.2.1 Exciton Models

Electronic excitation of an organic molecule leads to the promotion of an electron from the HOMO level of the system to the LUMO to form an electron-hole pair. The characteristics of the exciton strongly depend on the material properties, especially on the dielectric constant in the solid state. Wannier excitons are the limiting case of excitonic states in which the electron-hole pairs are strongly delocalized over several lattice sites. The binding energy is on the order of kT ($\approx 25\,\mathrm{meV}$) resulting in efficient exciton splitting at room temperature and a distance between the excited electron and the hole which is one order of magnitude larger than the lattice structure.[9] Wannier excitons are predominately found in inorganic semiconductors (like Si or Ge) due to their high dielectric constants ($\epsilon_{Si} \approx 11$).

The other limiting case is represented by Frenkel excitons in which the excited electron-hole pair is localized on a single molecule within the lattice with a binding energy of approximately $0.5\,\mathrm{eV}$. This is caused by the lower dielectric constant, which is only about 3 in conjugated polymers, making Frenkel excitons the predominant neutral exciton in this material class. Frenkel excitons are mobile along

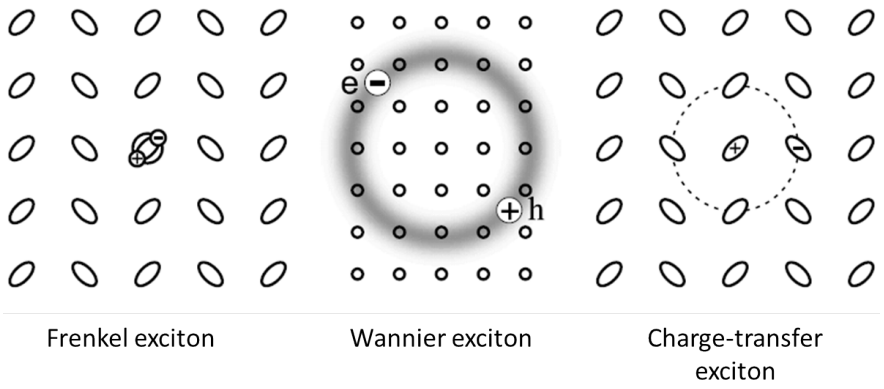

Figure 2.1: Illustration of different exciton types. (a) Frenkel exciton localized on one molecule. (b) Quasi-unbound Wannier exciton. (c) CT exciton delocalized over 1-2 neighboring molecules. Reprinted from figure 6.13, page 150 in [9]. Copyright Wiley-VCH Verlag GmbH & Co. KGaA, Weinheim. Reproduced with permission.

the polymer chain and can move as an entity by a statistical hopping process, described by energy transfer between different hopping sites in the solid state. This process is often called exciton diffusion.

The third excitonic species is the charge-transfer (CT) exciton. In the case of a CT exciton the electron or hole is transferred to a neighboring molecule so that the distance between the pair is one or two times greater than the molecular structure and the exciton is polar. The energy of the CT exciton is given by

$$E_{CT} = I_D - E_A - P_{eh} - E_{B,eh} \tag{2.1}$$

in which I_D is the ionization potential of the donor, E_A the electron affinity of the acceptor, P_{eh} the polarization energy of the lattice, and $E_{B,eh}$ the binding energy of the electron-hole pair.[9] Charge-transfer excitons can often be found in blends of organic materials in which one material has donor character (e.g. P3HT) and the other material acceptor character (e.g. PCBM). In these systems a charge-transfer exciton with a hole on the donor and an electron on the acceptor has often been observed.[10–12] The excitons are schematically illustrated in figure 2.1.

2.2.2 Light-matter interactions

The interaction of light with molecules leads to electronic, vibrational, and rotational excitations of the molecule. The former involves the promotion of an electron to an energetically higher lying state, whereas the latter describes the excitation of relative movement between the nuclei of the molecule. In an ideal gas of atoms in a radiation field of photons electronic transitions in a 2-level system occur only via absorption or emission of photons, and radiationless transitions are neglected. In these systems three basic processes occur and are described by the Einstein coefficients:

- Induced absorption B_{12}
- Induced emission B_{21}
- Spontaneous emission A_{21}

Einstein showed that the coefficients for the induced processes are equal whereas for spontaneous emission $A_{21} \propto \nu^3 B_{21}$.

In general, the probability for a transition between an initial and a final state is proportional to the square of the expectation value of the involved operator. For most optical transitions the radiation field couples to the dipole operator $\boldsymbol{M} = \sum_i e\boldsymbol{r_i}$ so that for the expectation value of the transition dipole moment between states i and f

$$\langle \boldsymbol{M}_{fi} \rangle = \langle \Psi_f | \, \boldsymbol{M} \, | \Psi_i \rangle \, . \tag{2.2}$$

The resulting transition probability is then related to the transition dipole moment by $P_{fi} \propto |\langle \boldsymbol{M}_{fi} \rangle|^2$. Transitions in which $\langle \boldsymbol{M}_{fi} \rangle \neq 0$ are called dipole allowed transitions, whereas if $\langle \boldsymbol{M}_{fi} \rangle = 0$, transitions are termed dipole forbidden. To solve the Schrödinger equation for a molecule, the Born-Oppenheimer approximation can be applied which states that the molecular wavefunction can be separated into an electronic and a nuclear part. This is justified as the large mass difference between electrons and the nuclei causes the electrons to move much faster than the nuclei, thereby being able to instantaneously follow the core movement. From the perspective of an electron the nuclei are immobile

meaning that the kinetic term of the nuclei in the Hamiltonian can be neglected for the electrons, and therefore only a parametric dependence of the nuclei position for the electron energy remains, resulting from the attractive interaction between nucleus and electron and the repulsive nucleus-nucleus interaction. The molecular wavefunction then reads

$$\Psi = \psi_{electron}\xi_{nuclei}S_{spin}, \tag{2.3}$$

where $\psi_{electron}$ is the electronic wavefunction and ξ_{nuclei} the nuclei part. The third factor S_{spin} in (2.3) includes the spin function. As the dipole moment operator only interacts with the electronic wavefunction, the transition probability changes into

$$P_{fi} \propto |\langle\psi_f| \boldsymbol{M} |\psi_i\rangle|^2 |\langle\xi_f|\xi_i\rangle|^2 |\langle S_f|S_i\rangle|^2 . \tag{2.4}$$

This is the result of the Born-Oppenheimer approximation, and simple symmetry considerations of the involved operators and wavefunctions lead to selection rules for the transitions as every factor of (2.4) has to be non-zero to yield a significant transition probability:

1. Symmetry: The dipole moment operator has odd symmetry $\boldsymbol{M(-r)} = -\boldsymbol{M(r)}$. This restricts the possible dipole allowed transitions to those between initial and final states which have different symmetry as otherwise the expectation value of the dipole moment operator becomes zero.

2. Spatial overlap: The larger the spatial overlap between the involved initial and final wavefunctions is, the bigger the transition probability. Transitions between $\sigma \rightarrow \sigma^\star$ or $\pi \rightarrow \pi^\star$ are therefore more likely than $n \rightarrow \pi^\star$ transitions.

3. Franck-Condon factor: The factor $\langle\xi_f|\xi_i\rangle$ is called Franck-Condon factor and describes the spatial overlap of nuclei or vibrational wavefunctions at the final and initial electronic states. In figure 2.2 the configuration-coordinate diagram for a diatomic molecule is shown, which contains the potential energy surface plotted against the internuclear distance for the initial and final state. As an electronic transition changes the configuration of the molecule (e.g. an electron is promoted from a binding orbital to an

anti-binding orbital), the energy surfaces are shifted along the x-axis indicating that the internuclear distance in the initial and final state is different. Additionally, the wavy lines represent the vibrational nuclei wavefunctions for each state. The Franck-Condon principle then states that for a vibronic transition, which is an electronic transition with a simultaneous change of the vibrational state, the transition probability to a different vibrational state is large when the spatial overlap of the vibrational wavefunctions in the final and initial state is significant. Since electronic transitions in a molecule are much faster than the vibrational motion of the nuclei, the nuclei positions stay constant during an electronic transition, causing the transitions in figure 2.2 to always occur vertically.

4. Spin Selection Rule: The factor $|\langle S_f|S_i\rangle|^2$ is only non-zero if the intial and final spin state are the same. A direct consequence is that transitions between pure singlet and triplet states are forbidden, however in molecules containing heavy atoms strong spin-orbit coupling of electrons can lead to mixed states in which intersystem-crossing and phosphorescence is possible.

Typical absorption end emission spectra of molecules can be understood by application of Kasha's rules.[14] These rules are empirical findings which explain the molecular spectrum at room temperature, and they state that the absorption of light from the zero vibrational level of the ground state S_0 has the highest probability due to the occupation probability of the vibrational levels following a Boltzmann distribution. Furthermore, Kasha assumed that internal conversion in an excited state, which is the relaxation through the vibrational levels, is faster than the lifetime of the electronic transition, causing the emission of light to mostly originate from the lowest vibrational level of the excited state.

2.3 Organic photovoltaics

Organic solar cells belong to the class of excitonic solar cells,[15, 16] as the primary excitation in these cells are strongly bound Frenkel excitons. In contrast to their inorganic counterparts, the low dielectric constant and strong electron-lattice interactions in organic materials cause localization of the excitons,[17] and therefore the direct electron-hole dissociation as known from pn-junction so-

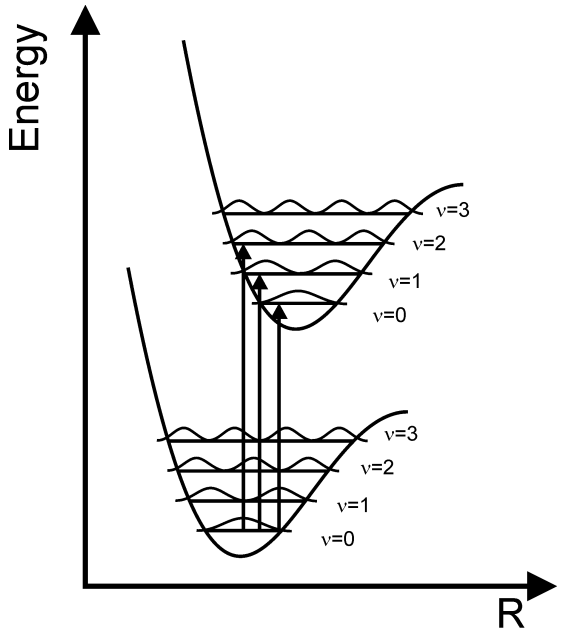

Figure 2.2: Vibronic transitions between the ground (S_0) and excited (S_1) state of a diatomic molecule. The thick lines are the energy potential surfaces for ground and excited states, the thin lines indicate the vibrational sublevels. Reproduced from [13].

lar cells is not possible. First reports on organic solar cells are based on single organic layers sandwiched between two metal contacts in which charge separation is driven by the work function difference of the electrodes. First publications go back as far as 1958 in which Kearns et al. observed photocurrent generation in laminated organic systems,[18] followed, for example, by Weinberger et al. and Glenis et al. who used conjugated polymers.[19, 20] However, the poor efficiencies of 0.01%-0.3% required the development of novel device architectures.

2.3.1 Device architecture of OPVs

The separation of bound electron-hole pairs is the key to efficient photocurrent generation. In order to overcome the high binding energy of excitons in organic materials and to increase the efficiency of single layer devices, a bilayer structure, or planar heterojunction, of two materials with different electron affinity and ionization potential was employed, in which charge separation is supported by the interfacial energy offset between the layers. One layer acts as an electron donor and the other as an electron acceptor. Figure 2.3 compares the different

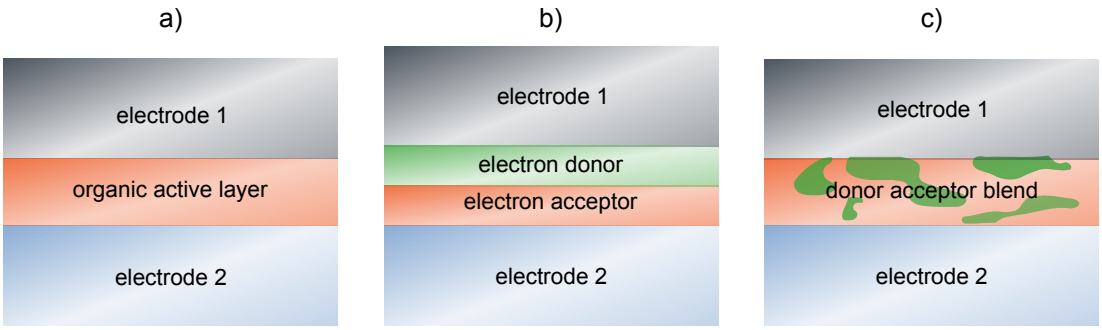

Figure 2.3: a) Single layer solar cell. b) Bilayer solar cell. c) Bulk heterojunction solar cell.

device architectures. Tang reported a CuPC/perylene derivative bilayer cell with a power conversion efficiency of approx. 1%,[21] and in 1992 Sariciftci et al. published the first use of C_{60} molecules as an electron acceptor,[22] which is still used in today's most efficient OPVs. The large drawback of bilayer solar cells is the limited spatial region from which excitons can be quenched. Due to the short exciton diffusion length in organic materials ($\approx 10\,\mathrm{nm}$), most of the excitons generated in the bulk decay radiatively or non-radiatively before they can reach the donor-acceptor interface. The solution to this problem is the so called bulk heterojunction (BHJ) in which donor and acceptor component are intimately mixed forming ideally an interdigitating network for electron and hole extraction. Thereby, the total interfacial area is increased and the average diffusion length for excitons to be quenched is largely reduced. Exciton quenching efficiencies close to unity are typical. Heeger et al. first presented a BHJ device consisting of MEH-PPV:C_{60} in 1995 with a power conversion efficiency of 2.9%.[23] Also polymer/polymer blends were investigated and Halls et al. presented a CN-PPV:MEH-PPV solar cell in the same year,[24] but power conversion efficiencies were lower.

Over the last years the number of publications in the field of organic photovoltaics has drastically increased, and with that new efficiency records were reported regularly. Figure 2.4 gives an overview of all photovoltaic technology, in which organic photovoltaics still plays a minor role, however, the rapid development over the past few years indicates a promising trend.

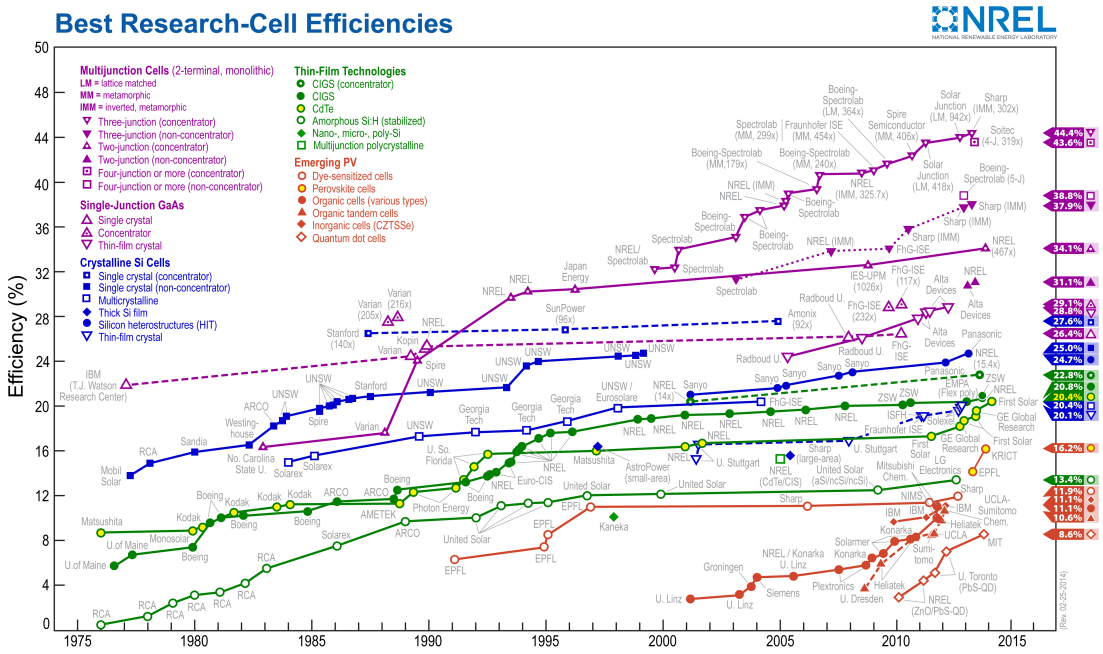

Figure 2.4: Recent developments in photovoltaics. Organic solar cells are displayed as emerging photovoltaics in filled red circles. Reproduced from [7]. The chart "Best Research-Cell Efficiencies" is reprinted with permission by the National Renewable Energy Laboratory, ***http://www.nrel.gov/ncpv/images/efficiency_chart.jpg****, Accessed March 11,2014.*

2.3.2 Materials for organic solar cells

In the beginning of OPV research mostly polyphenylene vinylene derivatives were used as donor polymers,[22, 23] which are still model systems for studies of fundamental processes in organic semiconductors.[25, 26] However, with maximum power conversion efficiencies limited to about 3 % different material classes became more attractive.[27] One of these new systems is polythiophenes, especially poly(3-hexylthiophene) (P3HT), which in combination with the fullerene electron acceptor [6,6]-phenyl-C61-butyric acid methyl ester (PCBM) represented the work horse of organic photovoltaics for several years. P3HT has been extensively studied to optimize efficiencies (see table in [28]) and with power conversion efficiencies exceeding 5 % [29] it was the long time record holder of polymer solar cells. Another promising material class are the poly(2,7)carbazoles synthesized by Leclerc et al.[30, 31] Power conversion efficiencies of up to 6 % with internal quantum efficiencies approaching unity have been reported.[32]

The disadvantage of the above mentioned donor materials is their low photocurrent compared to other solar cell types.[28] This is mainly caused by the relatively large optical bandgap (for P3HT $\approx$ 1.9-2.0 eV [33]) which limits the part of the solar spectrum suitable for photon harvesting compared to, for example, silicon which has a bandgap of 1.1 eV. This let to the development of low-bandgap polymers, of which poly[2,6-(4,4-bis-(2-ethylhexyl)-4H-cyclopenta[2,1-b;3,4-b']-dithiophene)-alt-4,7-(2,1,3-benzothiadiazole)], PCPDTBT, is a prototypical representative.[34] The substitution of the carbon bridgehead atom with a silicon atom resulted in an even more favorable solid state morphology, leading to efficiencies around 5 %.[35, 36] To further improve the efficiency, the moderate open circuit voltage of only 0.58 V needed to be increased, which was successfully achieved with PTB-type polymers by Yu et al.[37] Although efficiencies exceeding 9% have been published, [5] PTB7 suffers from strong degradation and is consequently not a suitable candidate for large scale production of commercial cells.

The general idea of the design of low-bandgap polymers is the alternation of electron donor and electron acceptor units in a copolymer. The high HOMO energy level of the electron rich donor and the low LUMO energy level of the electron deficient acceptor effectively lower the band gap of the D-A unit by orbital mixing.[1] Figure 2.5 illustrates this effect. The alternation of the D-A units causes an intra-chain charge transfer that in turn causes a reduction of the band gap. A further reduction of the bandgap can be achieved by increasing the planarity of the polymer backbone, so that the π-electron delocalization is maximized. This is, however, often in competition to solubility, as the addition of sidechains increases the solubility but causes steric hindrance. The hindrance can decrease the planarity and reduce the band gap.[38] Furthermore, the HOMO energy level of the donor has to be kept sufficiently low to guarantee a high open circuit voltage, according to the empirical relation [39]

$$V_{OC} = \frac{1}{e}(|E_{\mathrm{HOMO}}^{\mathrm{DONOR}}| - |E_{\mathrm{LUMO}}^{\mathrm{PCBM}}|) - 0.3\,\mathrm{eV}. \tag{2.5}$$

In the field of acceptors for OPVs fullerenes are the material of choice. So far, mostly derivatives of C_{60} and C_{70}, the latter showing an increased absorption in the visible spectral region compared to C_{60}, have been reported to yield efficient BHJ solar cells [28], either vacuum-processed with small molecule donors, or

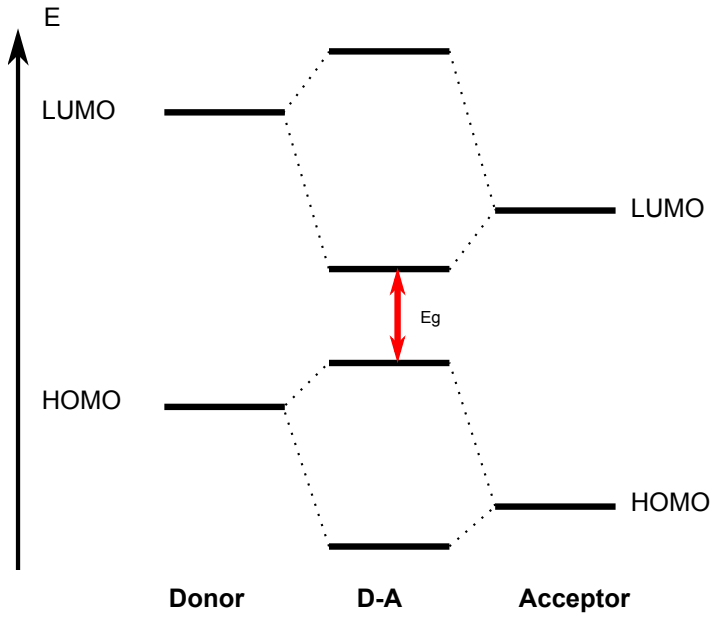

Figure 2.5: Orbital mixing causes a reduction of the bandgap in a D-A copolymer. Adapted from [1].

solution processed with polymer donors. As the HOMO and LUMO level of the fullerenes are not ideal and because the absorption in the visible is rather weak, several different acceptors have recently been studied. For example, Narayan et al. reported non-planar perylene diimides (PDIs) as acceptors which gave 2.7 % power conversion efficiency with a polymer donor,[40] indicating that these materials may compete with fullerenes. For the acceptor, the general idea is to have strong absorption complementary to the donor absorption with a LUMO-LUMO offset large enough to ensure efficient charge transfer, but as small as possible to minimize thermalization losses.[28]

BHJ solar cells can be fabricated either from solution using solution processable polymers or small molecules in combination with solution processable fullerene derivatives, for example PCBM, or vacuum deposition techniques can be employed. Recently, Sun et al. and Wang et al. presented single junction solution processed small molecule BHJ solar cells with efficiencies up to 8.2 %,[41, 42] whereas for vacuum fabricated cells Heliatek presented tandem cells with an efficiency of 12.0 %.[43]

The typical setup of a BHJ solar cell can be seen in figure 2.6. Almost all organic solar cells use ITO coated substrates as transparent electrodes, followed by a layer of PEDOT:PSS. PEDOT:PSS is a hole conductor that smooths out surface roughness of the ITO and enables good hole extraction from the active layer. On top of the PEDOT:PSS layer the BHJ active layer is spincast, followed by an evaporated metal electrode. The choice of the correct electrode material strongly depends on the energy level alignment in the active layer, which in return means that the choice of donor and acceptor materials is strongly restricted by the available back electrodes or their work functions. The usual materials are aluminum, silver, gold, or calcium.

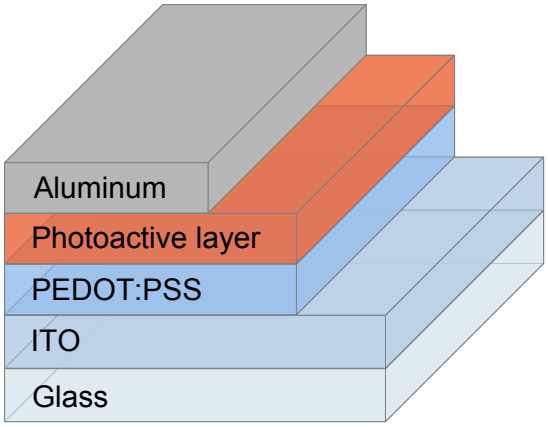

Figure 2.6: Typical setup of an organic solar cell. The device consists of a semi-transparent ITO covered glass substrate, followed by a layer of PEDOT:PSS. Above that the active layer is prepared, and a back electrode is evaporated.

In a simplified metal-insulator-metal (MIM) model the operation of a solar cell is illustrated in figure 2.7. The two electrodes are represented by their Fermi levels, and the energy levels of the organic semiconductor are shown as valence and conduction band, corresponding to the HOMO and LUMO.[44] If no voltage is applied to the contacts, i.e. at short-circuit conditions (see section 3.2) as displayed in figure 2.7a, the electrodes are on the same potential and the bands are tilted. Under illumination the photogenerated carriers can drift to the electrodes (electrons downhill, holes uphill), and photocurrent is generated. An additional electric field in reverse direction (2.7b), which supports the built-in field, further tilts the bands, and in the dark only a very small injection current flows. Upon illumination, the carriers drift in the strong field and produce a photocurrent.

In this configuration the device works as a photodetector.[44] If the direction of the external field is opposite in sign compared to the built-in field, a flat band condition can be reached, in which the external field exactly compensates the built-in potential (2.7c). This configuration is called open-circuit voltage condition, and the generated charge carriers are not extracted anymore. Hence, the net current is zero. Increasing the external field in forward direction leads to a large injection current (2.7d), and the device acts as a diode.

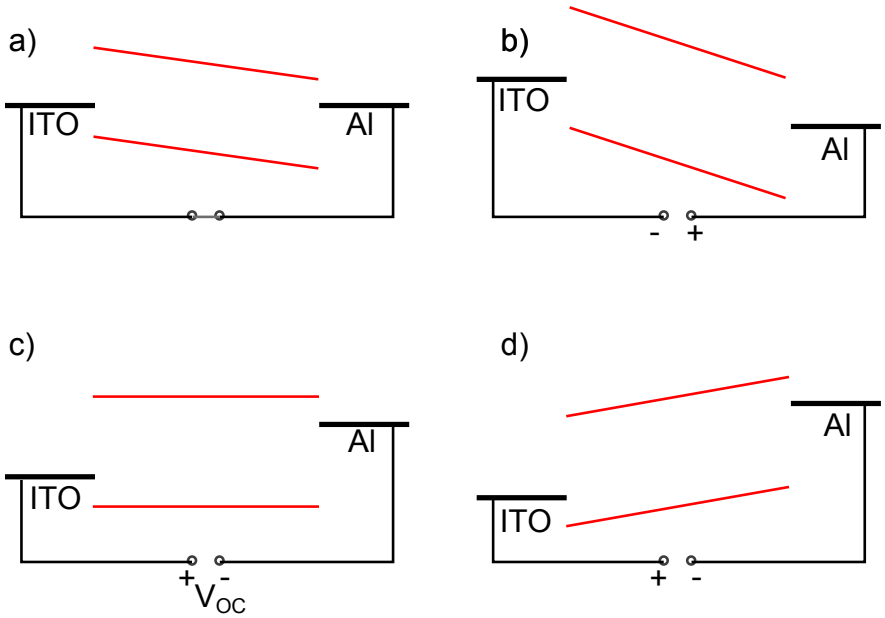

Figure 2.7: Simplified band model of an organic solar cell. a) At short-circuit conditions both contacts are leveled, leading to tilting of the bands. b) Application of an electric field in backward direction further tilts the bands, and the photogenerated carriers drift in the strong field. c) An external forward bias compensates the built-in field at open-circuit conditions, at which the bands are flat. d) A large foward bias causes an increase in injection current.

2.4 Charge photogeneration

This section summarizes the key processes of the photogeneration of charges. An in depth description can be found elsewhere [45–47]. Figure 2.8 graphically summarizes the different steps. The first step in charge generation in organic solar cells is the absorption of a photon, either in the donor or acceptor domain. The photon creates a tightly bound Frenkel exciton (see section 2.2.1) which needs

to diffuse to a donor/acceptor interface to contribute to charge generation as the exciton binding energy is far larger than $k_BT = 0.025\,\text{eV}$ at room temperature, and therefore prompt exciton dissociation is unlikely. At the interface between the donor and acceptor an electron transfer reaction can take place (assuming initial excitation of the donor) in which a charge-transfer exciton is formed. If an intimately mixed BHJ domain is excited, the Frenkel exciton quenching can occur on an ultrafast timescale ($< 100\,\text{fs}$), whereas in larger phase separated blends excitons diffuse for several ps, before they are quenched [11, 45, 48, 49]. The latter process is also termed diffusion-limited exciton quenching as the exciton diffusion now dictates the time scale for the process. After charge separation the free carriers move via hopping transport to the electrodes, where they are extracted in kinetic competition with recombination processes further discussed in section 2.5.

This picture of charge generation was recently challenged by Banerji et al., who pointed out a discrepancy.[47] As mentioned before, charge generation can occur on a time scale faster than 100 fs which corresponds to a diffusion length of roughly 0.1-0.2 nm [50, 51], whereas domain sizes of usually 10 nm are observed in BJH solar cells. Furthermore, Förster energy transfer, responsible for exciton hopping, occurs on a time scale faster than 1 ps,[47] meaning that this process is too slow to explain ultrafast charge generation. Durrant et al. proposed that in BHJ solar cells several different morphologies are present so that exciton quenching occurs in intimately mixed domains, whereas larger and purer domains are then responsible for efficient dissociation and transport.[52] However, Banerji et al. suggested a mechanism in which initial delocalization of the excited state plays an import role.[53–55] They argue that due to the larger spatial extent of an hot, delocalized exciton, an interfacial quenching site can be reached on the ultrafast time scale assisted by coherent electronic energy transfer.[56, 57] Recent theoretical work on this subject was presented by Caruso et al., supporting the idea of long-range exciton dissociation in organic solar cells via electron tunneling.[58]

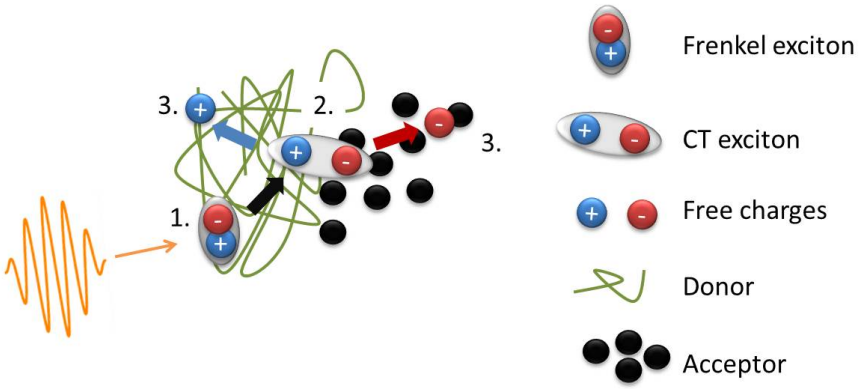

Figure 2.8: Illustration of the charge generation processes in organic solar cells. Excitation of the blend creates a polymer exciton (1.) which then diffuses to an interface, where it is effectively quenched, and a charge-transfer exciton is formed (2.). The CT exciton dissociates and the free charge carriers are extracted (3.).

2.4.1 Charge transfer

The electron transfer process was first described by Marcus in a semiclassical nonadiabatic approach [59], followed by a full quantum mechanical analysis by Jortner [60]. Following Clarke's excellent review on charge photogeneration,[45] we will briefly summarize the semiclassical approach as it is more intuitive and helpful to understand the general concept. Marcus pictured the electron transfer as a transition between an excited donor/acceptor site $D^{\star}/A$ to a charge-transferred site D^{+}/A^{-}. In this simplified quasi one particle picture, the reactant ($D^{\star}/A$) and product (D^{+}/A^{-}) potential energy surfaces are depicted as two intersecting harmonic oscillators depending on the generalized reaction coordinate. The approach is semiclassical as the electronic coupling between the states is treated quantum mechanically, whereas the nuclear motion is described classically. Figure 2.9 illustrates the concept. In order to isoenergetically transfer an electron from the excited donor to the acceptor, the reactant site has to move on the potential energy surface to the intersection by changing its nuclear configuration. Only at this point a vertical transition is possible, which is necessary as electronic transitions occur much faster than nuclear motion (see Franck-Condon-principle 2.2). The energy difference between the minimum of the reactant's po-

tential energy surface and the intersection $G^{\dagger}$ is an activation barrier which can be expressed as

$$\Delta G^{\dagger} = \frac{(\lambda + \Delta G^{\circ})^2}{4\lambda}, \tag{2.6}$$

where ΔG° is the Gibbs free energy, given by the energy difference between the minima of the reactant's and product's potential energy parabolas, and λ is the reorganization energy. The reorganization energy consists of the vibrational contribution required for the reactant to reach the desired nuclear configuration and the energy connected to polarization changes in the surrounding medium to stabilize the product state. The kinetics of charge transfer and the corresponding

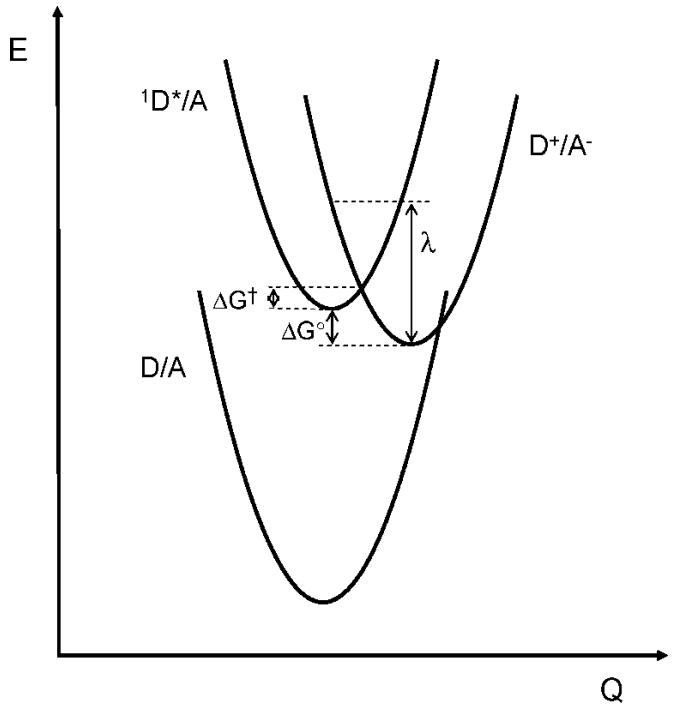

Figure 2.9: Illustration of the electron transfer process. The three parabolas represent the potential energy landscape of the ground state donor/acceptor pair (D/A), the excited ($D^{\star}/A$) and the charge-transferred (D^{+}/A^{-}) system. $\Delta G^{\dagger}$ is the energy activation barrier for the charge transfer, and ΔG° is the difference between the minima of the involved potential energy surfaces (Gibbs free energy). λ is the reorganization energy. Figure adapted with permission from [45]. Copyright (2010) American Chemical Society.

rate constant k_{ET} are obtained from Fermi's Golden rule, so that

$$k_{ET} = \frac{2\pi}{\hbar\sqrt{4\pi\lambda kT}} V^2 \exp\left(-\frac{(\lambda + \Delta G^\circ)^2}{4\lambda kT}\right). \tag{2.7}$$

V is the transition matrix element containing information about electronic coupling between the states. Equation 2.7 is only valid for weak coupling. A closer look at equation (2.7) indicates that the transfer rate increases with increasing $-\Delta G^\circ$ to a point where it equals the reorganization energy. From this point on, at which the reaction takes place without activation, a further increase in $-\Delta G^\circ$ leads to a decrease of the transfer rate. This region is called the Marcus inverted region and its observation is an evidence for the applicability and validity of the Marcus theory.

2.4.2 Charge-transfer state dissociation

The charge transfer discussed in the last section leads to the formation of a charge-transfer exciton, also called geminate pair, which needs to be dissociated for free charge carrier generation. The CT exciton still has a significant binding energy of ≈ 0.1 - $0.5\,\mathrm{eV}$ [45]. The precise mechanisms governing the separation process are still controversially discussed, and this section gives an overview of the different aspects affecting charge-transfer state dissociation. Onsager first presented a theoretical description of the separation of a Coulombically bound charge pair in a weak electrolyte [61] and was able to predict the escape probability as a function of the applied electric field and temperature. Braun refined this theory by including a finite lifetime of the CT excitons [62], and later Tachiya and Wojcik modified the theory to be applicable to materials with high electron mobility and for conjugated polymers [63, 64]. In figure 2.10 the Onsager-Braun model of charge separation is illustrated. After absorption of a photon and charge transfer at the interface, the hot charge-transfer state thermalizes. From there on the process of charge separation and geminate recombination (see section 2.5) are in kinetic competition, which means that direct charge recombination is not possible because there is always a possibility for redissociation. Onsager defined a distance r_C, the Coulomb capture radius, which is the distance of an electron-hole pair at which the Coulomb attraction equals $k_B T$. Photoexcitation creates a hot electron which then thermalizes at a distance a. If a is larger than r_C the charges are fully dissociated. However, if the electron-hole distance a is smaller than

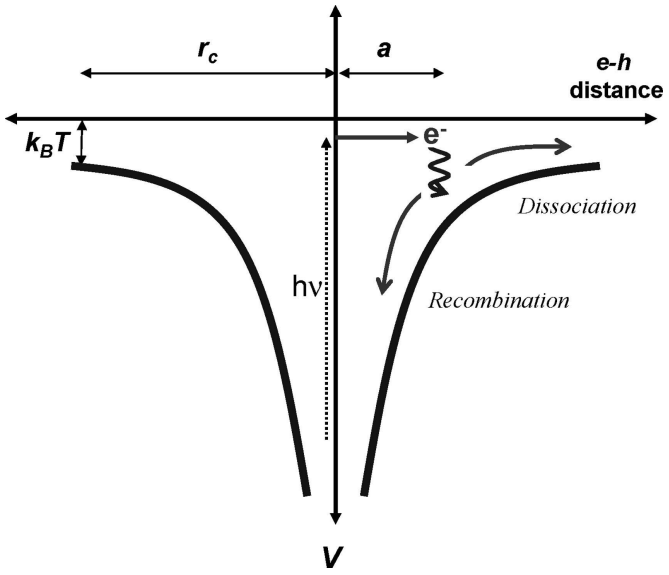

Figure 2.10: Potential energy diagram displaying the features of Onsager-Braun theory. r_C is the Coulomb capture radius, and a represents the thermalization length. Reprinted with permission from [45]. Copyright (2010) American Chemical Society.

the capture radius, the geminate pair either recombines or escape occurs with a finite probability $P(E)$ which depends on the applied electric field. With Braun's extension of the theory to a finite CT lifetime, the dissociation probability equals the product of the dissociation rate constant $k_d(E)$ and the CT state lifetime $\tau(E)$

$$P(E) = \frac{k_d(E)}{k_g + k_d(E)} = k_d(E)\tau(E). \tag{2.8}$$

The rate constant k_g describes the geminate recombination. The dissociation constant was then calculated as

$$k_d = \nu \exp\left(\frac{-\Delta E}{k_B T}\right)\left(1 + b + \frac{b^2}{3} + \frac{b^3}{18} + \cdots\right), \tag{2.9}$$

where ν is the separation attempt frequency

$$\nu = \frac{3\langle\mu\rangle e}{4\pi\langle\epsilon\rangle\epsilon_0 a^3}, \tag{2.10}$$

in which $\langle\mu\rangle$ and $\langle\epsilon\rangle$ are the spatial averaged sum of electron and hole mobility and the spatial average of the dielectric constant, respectively.[65] ΔE is the

Coulomb attraction of the charge pair at the thermalization distance, and b is the effective field parameter given by

$$b = \frac{e^3 E}{8\pi\langle\epsilon\rangle\epsilon_0 k_b^2 T^2}. \tag{2.11}$$

In literature several cases for the application of Onsager-Braun theory in organic photovoltaic blends can be found.[66–68] In the following, we will briefly review some of the work. Furthermore the influence of excess energy, electric field, temperature, and morphology on the dissociation process is discussed.

2.4.2.1 Excess energy

The influence of excess energy on the CT state dissociation is not completely resolved. To avoid confusion, two types of excess energy have to be distinguished. On the one hand there is the excess vibrational and electronic energy of the CT exciton, and on the other hand there is the excess energy of the singlet exciton which is generated before charge transfer. Experimental evidence supporting enhanced dissociation with increasing excess energy can be found as well as studies concluding that excess energy is not important for efficient charge generation. Referring to the Onsager-Braun model, the thermalization length of the relaxed CT exciton is a critical parameter for charge separation. Due to the offset between the LUMOs of donor and acceptor usually used in organic photovoltaics, the electron has excess thermal energy after charge transfer to the acceptor. Within the Onsager-Braun model this excess energy causes a larger electron-hole distance prior to thermalization, which facilitates the dissociation process. The intermediate states are often called 'hot' CT states. Lee et al. performed Fourier-transform photocurrent spectroscopy and photothermal deflection spectroscopy to accurately measure the external quantum efficiency (EQE) and absorption of organic photovoltaic blends (MDMO-PPV:PCBM and P3HT:PCBM).[12] They connected the appearance of a new absorption band in the blend, which is absent in the pristine materials, to CT state absorption, and by obtaining the internal quantum efficiency (IQE) from the EQE and the blend's absorption, they showed a constant IQE from above to below optical gap excitation. As the IQE was also found to be independent of the excitation wavelength throughout the CT band, they argue that thermally relaxed CT states are the precursor of free

charge carriers and excess energy is not needed. Van der Hofstadt et al. reported similar findings for P3HT:PCBM. [69] They employed charge extraction by linear increasing voltage (CELIV) measurements and compared the averaged extracted charge carrier density and the fraction of extractable charges for above- and sub-bandgap excitation for different time delays between excitation and extraction. For as-cast as well as for annealed samples the results look almost identical, independent of the excitation wavelength, showing that for P3HT:PCBM excess singlet energy is not needed to efficiently generate free charge carriers.

These findings are in contradiction to field dependent time-resolved photoluminescence (PL) measurements by Morteani et al. on polymer:polymer blends, who observed a CT emission that was reduced upon application of an electric field, but without changing its lifetime.[70] The PL of the pristine materials did not show any field dependent quenching, indicating that the emissive CT state must have a dark precursor state. They interpreted this precursor state to be a hot charge-transfer state with a larger binding distance that can either dissociate into free carriers or relax into the emissive CT state, which they named exciplex. In 2008, Okhita et al. further investigated the issue by blending a series of polymers with varying LUMO energies with PCBM and observing the charge yield by transient absorption spectroscopy.[71] They correlated the free energy of charge separation, $\Delta G_{CS} = E_S - (IP_D - EA_A)$, in which E_S is the polymer singlet exciton energy, IP_D the ionization potential of the donor, and EA_A the electron affinity of the acceptor, to the magnitude of the transient signal at 1 μs and observed an increase in signal with increasing ΔG_{CS}. The photophyiscal model describing these processes contains a hot CT state, which they called excited bound radical pair, created by the excess energy, that can directly create free charge carriers. Several follow-up studies on polythiophene:PCBM blends confirmed this observation, for example, Clarke et al. performed transient absorption spectroscopy on PCBM blends with a series of polythiophenes and polyselenophenes. The polymers had similar ionization potentials but different LUMOs, so that the free energy of charge separation varied between the blends. They took the transient absorption signal at 1 μs as a measure for the free charge carrier generation, which showed an increase with increasing ΔG_{CS}.[72] These studies were extended to P3HT blends with PDI in which the correlation was also observed.[73] However, in all these studies they point out that excess energy is not the only factor determining

charge generation, as a change in nanomorphology cannot be completely ruled out between the different polymers. A generalization of their findings to other systems is even more difficult as Clarke et al. observed for the low-bandgap polymer PCPDTBT a two-fold increase in charge yield compared to P3HT although ΔG_{CS} is approximately 0.4 eV smaller.[74] They explain this observation with the donor-acceptor character of PCPDTBT which should facilitate charge separation. However, the recombination before 1 μs is likely to differ for the different material systems, raising the question of how reliable the remaining signal after 1 μs is as a measure of charge yield.

An elegant approach to unravel the role of excess energy in the charge generation process was recently presented by Bakulin et al.[75] In a pump-push photocurrent experiment they excited an organic solar cell with a pump laser pulse to generate charge carriers and CT states and monitored the changes in extracted photocurrent upon application of an additional IR push pulse with variable time delay. The push pulse selectively excites the CT_0 to CT_n transition as indicated in figure 2.11a), causing a repopulation of hot CT_n states from 'cooled' CT_0 states. As can be seen in figure 2.11b) a change in photocurrent is observed for MDMO-PPV:$PC_{70}BM$ up to approx. 600 ps. They attributed this time to the CT state lifetime. In a second all-optical pump-push-probe transient absorption experiment the temporal evolution of the hot CT state was determined to be < 1 ps. From their experiments and additional atomistic many-body modeling they concluded that excitation of relaxed CT states leads to a short-lived state with increased intrachain hole delocalization facilitating long-range charge separation. The unchanged extraction kinetics employing above- and sub-bandgap excitation pulses (see 2.11b)) furthermore showed that the excess energy of the donor singlet exciton is not necessary for this system to generate free charges.

In a later publication Dimitrov et al. extended these studies to a blend system without energetic driving force, i.e. $\Delta G_{CS} \approx 0$ eV, which exhibits poor charge generation efficiency (BTT-DPP:$PC_{60}BM$) to further investigate the effect of excess singlet exciton energy on free charge generation.[76] As a reference system DPP-TT-T:$PC_{60}BM$ ($\Delta G_{CS} \approx 0.15$ eV) was used, showing efficient charge generation. They observed that increasing the photon energy by ≈ 0.2 eV above the optical gap led to a doubling of the dissociation efficiency correlated with a

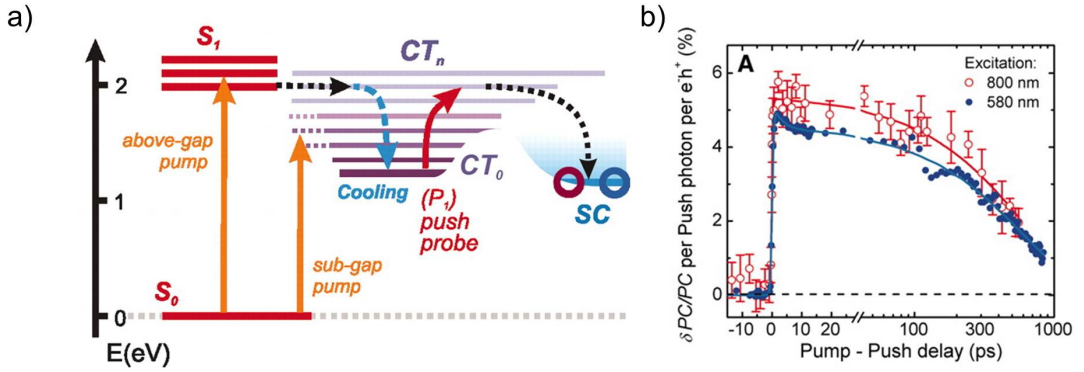

Figure 2.11: a) Illustration of the involved energy levels in the pump-push photocurrent experiment. b) Pump-push photocurrent transients for MDMO-PPV:$PC_{70}BM$ for above and sub-bandgap excitation. From [75]. Reprinted with permission from AAAS.

reduction of the bound CT state yield in the inefficient blend system. Additional temperature dependent measurements showed that the charge generation in both systems is temperature independent indicating that the bound CT state strongly traps the carriers, as thermal activation was not possible.

Shortly after the publications by Bakulin et al. and Dimitrov et al. two more publications addressed the same problem and presented experimental evidence for the importance of hot charge-transfer states for charge generation. Jailaubekov et al. performed transient second-harmonic generation spectroscopy to investigate the transient field at the interface created by the charge carriers, followed by time-resolved two-photon photoemission (TR-2PPE) measurements which allow the assignment of the photoexcitation from which the electron is emitted.[77] For a copper phthalocyanine heterojunction they found an interfacial field rise time of 80 fs independent of the excitation photon energy within the bulk absorption, indicating that excess singlet exciton energy does not enhance the charge transfer process. An immediate rise of the transient field is observed for sub-bandgap excitation, which is consistent with the direct excitation of the CT exciton. The TR-2PPE measurements revealed that hot CT states 0.3 eV higher in energy than the relaxed CT states are generated which thermalize within ≈ 1 ps. Additional charge separation simulations led to the conclusion that the hot CT states have a higher initial electron-hole separation distance and therefore are more likely to dissociate into free carriers. The 1 ps cooling time therefore sets the limit

of charge generation as during this time period dissociation and relaxation are in direct kinetic competition. Once cooled down to the CT_0-state, the binding energy is too high for delayed charge separation.

The second publication was presented by Grancini et al. who investigated charge generation processes in PCPDTBT:PCBM with transform-limited sub-15 fs time resolution transient absorption spectroscopy.[78] They observed that polymer excitons dissociate within 50 fs after excitation to form either CT states or free charge carriers. With increasing excitation photon energy hot CT states are populated which accelerate the formation of separated charge carriers due to stronger delocalization. The cooling to relaxed CT states is also determined to be a loss channel, again setting a time limit for efficient charge pair dissociation. Figure 2.12 gives an overview over their findings.

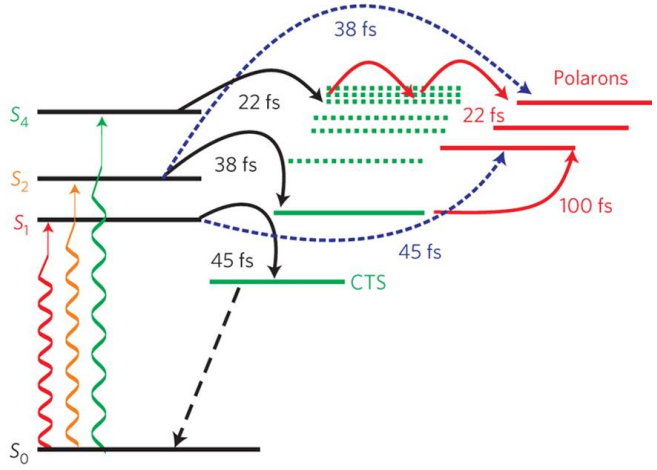

Figure 2.12: Influence of excess singlet energy on charge generation. The wavy arrows represent different excitation energies, green lines indicate CT state population, red arrows the transition from hot CT states to free charge carriers, and the dashed blue arrows show singlet quenching into free charge carriers. Reprinted by permission from Macmillan Publishers Ltd: Nature Materials [78], copyright (2013).

2.4.2.2 Electric field

According to Onsager-Braun theory the dissociation probability of CT states can be enhanced by applying an external electric field. The electric field causes a lowering of the Coulomb potential and thereby facilitates the escape of the electron.

Veldman et al. investigated the field dependence of charge-transfer state dissociation by single photon counting fluorescence studies in a fluorene copolymer (PF10TBT) fullerene blend.[79] They observed a reduction of the charge-transfer state decay time with increasing electric field and related that to enhanced CT state dissociation caused by the external field. An experimentally observed recombination time of 4 ns was extracted from their measurements. However, it has to be mentioned that significant changes in the decay time could only be observed at high negative voltages (-20 V) corresponding to internal fields on the order of $10^7\,\mathrm{Vm}^{-1}$ for a 220 nm thick device. As this clearly exceeds the usual photovoltaic operating conditions, the emerging question is, if this is a system specific phenomenon or if other organic photovoltaic systems show field-dependent charge generation at lower fields present under OPV operation conditions.

Marsh et al. performed field-dependent TA measurements on P3HT:PCBM and observed a prolonged signal lifetime at negative voltages (-2 to -5 V) compared to open-circuit conditions.[80] They interpreted this reduced recombination as the field-assisted separation of CT states (which must be relaxed as ns time resolution was employed). This assignment is, however, not completely doubtless, as their measurements were carried out at $12\,\mu\mathrm{Jcm}^{-2}$, definitely exceeding AM1.5G conditions, which means that non-geminate recombination has to play a non-negligible role. The prolonged signal lifetime at negative voltage could also be explained by a reduction of non-geminate recombination caused by the electric field.

Extensive work on this topic has also been done on the low-bandgap polymer PCPDTBT and its blends with PCBM. Compared to P3HT:PCBM the fill-factor is low in these devices indicating field-dependent processes. Lenes et al. modeled the JV characteristics of a PCPDTBT:PCBM solar cell by considering free carrier generation via field-assisted CT state separation and were able to explain the low fill-factor in these devices with a lifetime reduction of the CT states compared to other polymer:fullerene systems.[68] A CT state lifetime of 58 ns was extracted for PCPDTBT:PCBM whereas for MDMO-PPV:PCBM and P3HT:PCBM similar modeling studies revealed lifetimes of several μs.[66, 67].

The modeled CT lifetimes appear to be rather long as Jarzab et al. extracted CT state lifetimes from time-resolved photoluminescence experiments for PCPDTBT-

PCBM in the order of 480 ps.[81] They also investigated the effect of external bias on the CT emission and observed a reduction of the intensity, but an independent lifetime between 0.6 to -2 V which is shown in figure 2.13. This is in contrast to the above mentioned results from Veldman et al. and indicates a dark precursor state to the emissive CT state, whose dissociation can be enhanced with an external electric field. Furthermore, this study also confirms that the relaxed CT state cannot be separated with applied field strengths corresponding to normal solar cell operating conditions. A slight drawback of these time-resolved PL studies is the blend composition which was chosen to be 1:1. For efficient solar cells higher ratios are reported, which makes it difficult to assess the importance of these findings for efficient devices as higher PCBM ratios often enhance carrier generation and facilitate CT state splitting.

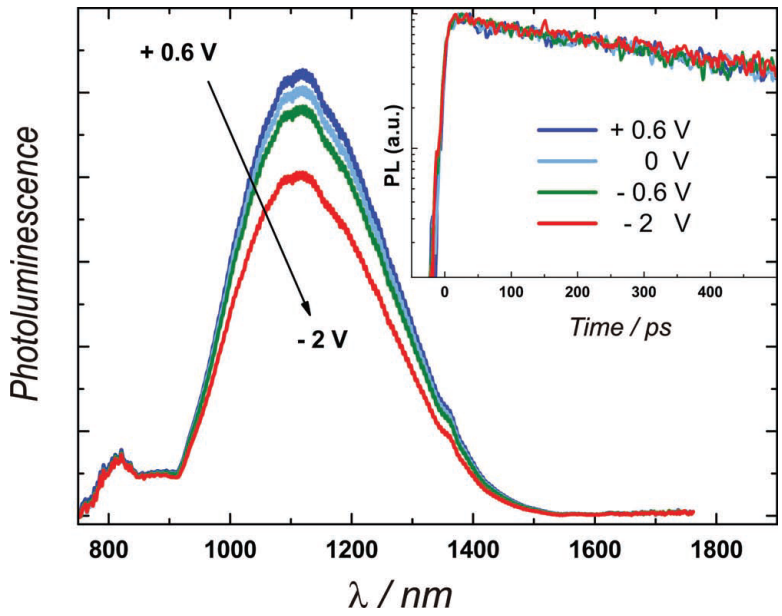

Figure 2.13: PL spectra of PCPDTBT:PCBM (1:1) as a function of the applied electric field. The inset shows the PL decay traces at 1075 nm for different fields. Reproduced with permission from [81]. Copyright (2011) Wiley-VCH Verlag GmbH & Co. KGaA, Weinheim.

The same material system was investigated by Jamieson et al. with field-dependent transient absorption measurements.[82] They did not observe any changes of the transient signal decay for applied voltages between +1 V and -4 V pointing to field-independent charge generation in PCPDTBT:PCBM. The transient signal

was observed from 20 ns onwards, and the signal height at this delay time was chosen as a measure of the charge yield. This assignment is problematic as short time recombination effects are neglected although they are definitely present at the excitation densities (8 μJcm^{-2}) used.[11, 49, 83]. Albrecht et al. therefore conducted time-delayed collection field (TDCF) and photo-CELIV measurements on PCPDTBT:PCBM with pulse fluences between 0.2 and 0.5 μJcm^{-2} corresponding to initial photogenerated carrier densities comparable to AM1.5G illumination at 1 sun.[84] In their TDCF experiments the amount of extracted charges is measured depending on the delay time between excitation and extraction pulse. Additionally, a pre-bias between -2 V and 0.6 V is applied during excitation, granting direct access to the field-dependence of charge generation. As shown in figure 2.14, PCPDTBT:PCBM clearly exhibits a field-dependence measured after 10 ns in agreement with results from Jarzab et al.[81] Interestingly, the same experiments yielded field-independent generation dynamics for P3HT:PCBM,[85] in contrast to the results from Marsh et al.[80]. However, it has to be mentioned that the time resolution of the TDCF experiments on P3HT:PCBM was significantly worse than in those performed on PCPDTBT:PCBM (500 ns compared to 10 ns).

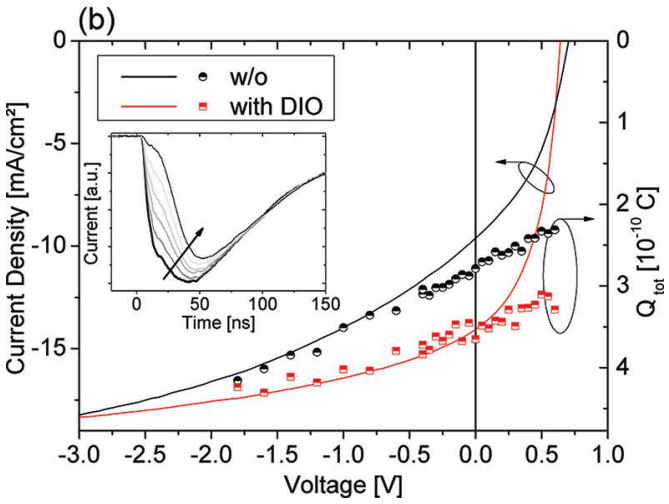

Figure 2.14: JV-curves together with the collected current after 10ns as a function of pre-bias. Reprinted with permission from [84]. Copyright (2012) American Chemical Society.

The above experimental findings reveal that the experimental access to the effect of external bias on charge generation is extremely difficult due to the short time scale on which these processes happen and due to overlapping non-geminate recombination. It seems that the effect of external bias on charge generation is a very system specific characteristic.

2.4.2.3 Temperature

According to Onsager-Braun theory, the dissociation probability depends exponentially on temperature, and therefore higher temperatures should increase CT splitting. Mauer et al. performed temperature dependent transient absorption measurements on P3HT:PCBM and observed an independent yield of separated charges when measuring at room temperature or liquid nitrogen temperature (80 K).[86] These results are in good agreement with the previously mentioned measurements by Dimitrov et al.[76], who also observed temperature independent charge generation. Both studies indicate that the thermal activation at room temperature (≈ 25 meV) is negligible compared to the trapping potential of relaxed charge-transfer states. For the low-bandgap polymer PCPDTBT similar results were observed by Jarzab et al.[81] This suggests that the temperature independence of charge generation in organic photovoltaic systems is a general phenomenon.

2.4.2.4 Morphology

The nanomorphology present in the OPV system strongly influences the efficiency of charge generation and also regulates the loss mechanisms. In general, the photovoltaic performance depends on the absorption efficiency, exciton quenching efficiency, CT state separation efficiency, and charge carrier extraction efficiency. Assuming good absorption properties, the last three parameters remain, all depending on the morphology. Starting with exciton quenching, it is on the one hand desirable to have as much interface as possible, best realized in a finely intermixed donor-acceptor blend with small domains. This guarantees that every created exciton can find an interface during its lifetime, where it is successively quenched. On the other hand, small domains increase the probability to generate isolated islands, which enhance geminate recombination and suppress efficient CT state dissociation, instead of a percolated bi-phasic network. Furthermore,

Clarke et al. argued that entropy plays an important role in the separation of charge carriers and is directly connected to morphology.[45] Assuming that only the electron of the charge pair moves away, an increase in the separation distance between the hole and the electron would lead to an increase in entropy caused by the larger number of available acceptor molecules for the electron, stabilizing the charge separated state from collapsing back into a CT state. Nayak et al. put forward a similar idea regarding entropy.[65]

In the literature a lot of experimental evidence for the influence of morphology on charge generation can be found. In the above mentioned study of the field dependence of charge generation in PF10TBT by Veldman et al.[79], they also investigated the impact of fullerene concentration on PL quenching and CT state emission. In agreement with the general ideas of the last paragraph, they observed improved exciton quenching with an increased PCBM fraction together with a red-shifting of the CT state emission that furthermore decreased in intensity and lifetime with increasing fullerene concentration. They concluded that by adding more PCBM to the blend, larger and more crystalline domains are formed which facilitate charge separation. By modeling the data with the Onsager-Braun theory, they obtained high average mobilities and large electron-hole separation distances for high PCBM fractions, whereas smaller mobilities and separation distances were found for low PCBM fractions.

Further examples were presented for P3HT:PCBM for which Chirvase et al. reported better percolation with increasing PCBM content.[87] For the same material system our own group presented a photophyiscal study in which they showed a reduction of geminate recombination upon annealing of regio-regular P3HT:PCBM blends.[11] Together with the reduction of geminate recombination, the charge generation mechanism was observed to change from exclusively ultrafast charge generation to partially diffusion-limited charge generation, which manifested itself in the observation of stimulated emission. This means that the excitons have to travel further before reaching a quenching site, which points to an increase in domain size after thermal annealing and matches the reduced geminate recombination associated with larger domains.

Jamieson et al. investigated in detail the effect of PCBM content on charge generation in combination with different donor polymers and proposed a model

of the charge generation process.[52] According to their findings, PCBM has the key property to be able on the one hand to intimately mix with donor polymers, but on the other hand also to be able to form large, pure crystalline domains. In cyclic voltammetry measurements they could show an increase in electron affinity of the PCBM upon crystallization, turning the pure PCBM domains into electron sinks, thus driving charge separation. The model they propose is displayed in figure 2.15 and illustrates that charge pairs might be generated in the more intermixed blend regions before being separated at the boundaries to larger and purer domains. They further conclude that the success of the donor

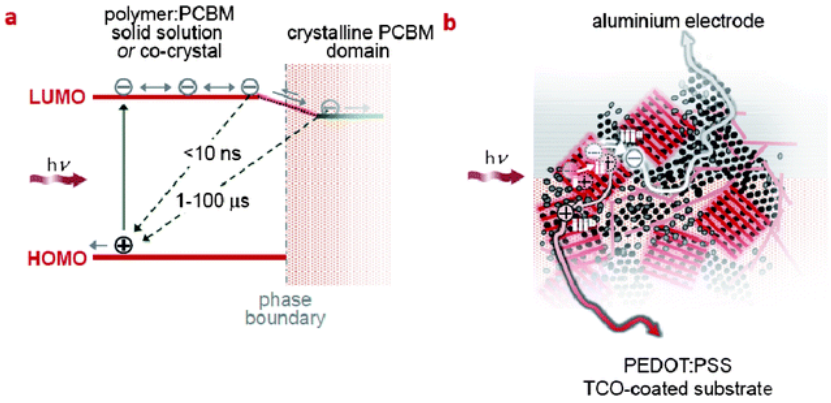

Figure 2.15: a) The LUMO level of PCBM shifts to lower values upon crystallization and facilitates charge separation. b) Charge pairs are created in well intermixed domains and separate at the boundaries of purer and larger domains from which they are extracted. Reproduced from [52] with permission of The Royal Society of Chemistry.

P3HT is especially based on the fact that P3HT itself is able to form crystalline structures upon annealing and is therefore not so much dependent on the acceptor crystallinity as other donors. In fact, Reid et al. investigated charge generation in neat P3HT films depending on molecular weight and showed that in high molecular weight samples amorphous as well as crystalline domains are formed which might generate a type II heterojunction driving charge separation even in the pristine materials.[88] All the above findings indicate the large impact of morphology on charge generation and furthermore demonstrate that treating neat materials as single-phase materials may lead to incorrect conclusions.

2.5 Loss processes in organic solar cells

As seen above, the efficiency of solar cells can be written as

$$\eta = \eta_{\text{absorption}}\eta_{\text{quenching}}\eta_{\text{separation}}\eta_{\text{extraction}}, \tag{2.12}$$

where $\eta_{absorption}$ describes how much incident photons are absorbed, $\eta_{quenching}$ is the quenching efficiency, $\eta_{separation}$ the efficiency with which the interfacial CT states separate, and $\eta_{extraction}$ represents the charge carrier extraction efficiency. Each of these processes competes with loss channels. The absorption efficiency is basically determined by the optical density, but a small fraction of photons is also scattered and absorbed in parasitic regions. However, this effect is minor compared to the other loss channels. The second loss channel lies in the incomplete quenching of excitons. As mentioned above a certain phase segregation is necessary for efficient charge generation which leads to larger domain sizes. This means that the initial exciton delocalization has to be larger for quenching or that the exciton has to undergo more hopping steps before a quenching site is reached. Some of the excitons can recombine before reaching an interface and thus are lost for photocurrent generation. In a working solar cell these first two loss channels usually have minor impact and the reduced efficiency can be explained by geminate and non-geminate recombination further detailed in the next sections.

2.5.1 Geminate recombination

Geminate recombination describes the recombination process of an electron and a hole that originate from the same exciton and can at no point be considered to be spatially separated far enough to be treated as free charge carriers. Geminate recombination therefore describes the recombination of charge-transfer states, which were found to be immobile at the interface.[10] The interaction between different CT states is therefore negligible, and the decay behavior of the CT states only depends on their lifetime and not on their concentration. This can be modeled as

$$\frac{d}{dt}N_{CT} = -k_{gem}N_{CT}, \tag{2.13}$$

resulting in a monoexponential, concentration independent decay with a rate constant k_{gem}. This characteristic decay behavior can help to identify the involved

species in a transient absorption experiment (see chapter 4) and is, as was already mentioned when the Onsager-Braun theory was described, in kinetic competition with charge separation.

2.5.2 Non-geminate recombination of free charge carriers

After the successful separation of the interfacial charge pairs, the free charge carriers need to be extracted to contribute to the photocurrent. However, on their way to extraction these carriers can meet oppositely charged charge carriers and undergo recombination. This process is called non-geminate recombination as the carriers are likely not to originate from the same bound charge pair. The theory governing this recombination process is based on the Langevin recombination model, which was developed for the recombination of ions in gases.[89] In order to undergo a recombination process, the charge carriers first have to encounter each other in a distance smaller than the Coulomb capture radius, which means that the recombination probability is directly governed by the probability for an encounter. The Langevin recombination rate is therefore proportional to the product of electron (n_e) and hole densities (n_h), so that

$$R = \gamma n_e n_h. \tag{2.14}$$

The higher the mobility of the carriers, the higher is the probability for them to meet. The factor γ can therefore be expressed as

$$\gamma = \frac{e(\mu_e + \mu_h)}{\epsilon_0 \epsilon_r}, \tag{2.15}$$

in which e is the elementary charge and ϵ_0 is the vacuum permittivity. In several experimental approaches including TAS, photo-CELIV, and intensity-dependent photocurrent measurements, the non-geminate recombination rate was determined but always a rate one to four orders of magnitude smaller than the predicted Langevin rate was observed.[11, 46, 90–93] Several reasons for this behavior were presented. For example Deibel et al. showed that because of different injection barriers for electrons and holes in an OPV device the charge carrier density varies throughout the thickness of the device, so that the recombination rate based on the averaged charge carrier density is higher than the one calculated from the local densities. As in charge extraction experiments averaged carrier

densities are measured, the local densities are overestimated. For experiments perfomed on samples without electrodes, which is all-optical experiments like TAS, different reasons were put forward. First of all, Langevin theory was developed for three dimensional isotropic systems, which is definitely not the case in an organic semiconductor, as recombination can only occur at an interface. This reduces the experimentally observed recombination rate. Furthermore, shifts of the energy levels due to disorder might further alter the recombination rate.

Another deviation observed in experiments is the different recombination order, i.e. a higher exponent for the charge carrier density dependence than 2.[94] Again, this can be caused by a reduced dimensionality in recombination,[94] but also a charge carrier density dependence of mobility can change the recombination order. The modified Langevin recombination rate can then be described by

$$R = \xi \frac{e\mu_e + \mu_h}{\epsilon_0 \epsilon_r} n^{\lambda+1}, \tag{2.16}$$

in which ξ is the Langevin reduction factor and $\lambda + 1$ the generalized reaction order. Compared to geminate recombination, the non-geminate recombination distinctively depends on the charge carrier concentration, which helps to experimentally distinguish it from geminate recombination as a loss channel.

2.6 Ultrafast phenomena

The basis for ultrafast time-resolved spectroscopy experiments is the ability to generate high sampling bandwidth. This bandwidth is ultimately determined by the pulse duration of the light employed in the spectroscopic setup. As previously mentioned, photophyiscal processes in organic semiconductors start to occur on a femtosecond timescale stressing the demand for ultrafast light pulses. The only way to advance to these timescales is the use of modelocked lasers, and the next sections give a short overview of the generation of ultrashort pulses and the associated nonlinear processes.

2.6.1 Short laser pulses

An optical laser pulse can be described as a linear wave with a time dependent amplitude. The electric field describing an optical pulse with central frequency ω_0 is given by

$$\boldsymbol{E}(\boldsymbol{r},t) = A(t)\exp\left(i(\boldsymbol{kr}+\omega_0 t+\varphi)\right). \tag{2.17}$$

For simplification, let's consider the electric field at a fixed position $\boldsymbol{r}=0$ with the electric field in the y-direction and propagation along the x-axis so that

$$E(t) = \Re(A(t)\exp\left(i\omega_0 t\right)). \tag{2.18}$$

$\Re$ is the real-valued part of the function. Assuming a Gaussian time-dependence of the amplitude of the laser pulse with

$$A(t) = E_0\exp\left(-\sigma t^2\right), \tag{2.19}$$

the time-dependent electric field is given by

$$E(t) = \Re(E_0\exp\left(-\sigma t^2+i\omega_0 t\right)). \tag{2.20}$$

Figure 2.16 shows the electric field of a typical pulse together with the slowly varying envelope which determines the pulse duration. The pulse has a central wavelength of 800 nm and full width at half maximum (FWHM) of 50 fs. As a direct consequence of the Heisenberg uncertainty principle, every optical pulse with a duration Δt has a spectral bandwidth $\Delta\omega$ connected by the time-energy uncertainty:

$$\Delta E\Delta t \geq \hbar/2 \tag{2.21}$$

This means that ultrashort laser pulses usually have large bandwidths, which has direct consequences for their propagation in matter. When an optical pulse travels through a dielectric medium, the dielectric function directly acts on the phase of the pulse. The dielectric function is a complex function whose real part represents the refractive index and the imaginary part is proportional to the extinction. In general the refractive index is dispersive, meaning that its values vary for different wavelengths. In the frequency domain the pulse therefore changes its phase during the propagation over a distance r so that

$$\hat{E}(\omega) = E(\omega)\exp\left(i\varphi\right) = E(\omega)\exp\left(i\hat{k}r\right) = E(\omega)\exp\left(\frac{i\omega\hat{n}(\omega)r}{c}\right), \tag{2.22}$$

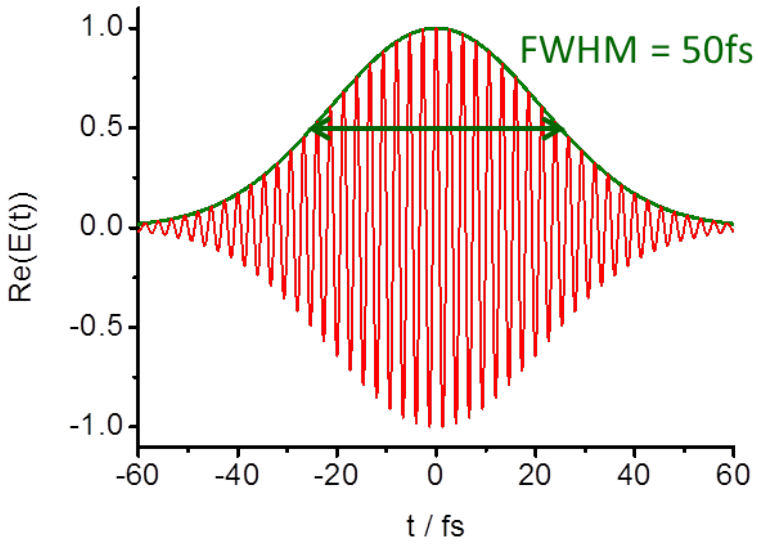

Figure 2.16: The electric field of an optical pulse with a FWHM of 50 fs at 800 nm central wavelength (red line). The green line indicates the time-dependent Gaussian envelope.

in which the optical phase φ is altered by the complex-valued propagation constant $\hat{k}$ that depends on the frequency and the complex-valued refractive index $\hat{n}$. Neglecting absorption effects, only the real-valued refractive index n remains. To simplify the effect of the dielectric on the phase of the wave packet, it is convenient to expand the optical phase into a Taylor series in the vincinity of the central frequency $\omega = \omega_0$ so that

$$\varphi(\omega) = \omega\frac{n(\omega)}{c}r = (\omega-\omega_0)\left.\frac{d\varphi}{d\omega}\right|_{\omega_0} + \frac{1}{2!}(\omega-\omega_0)^2\left.\frac{d^2\varphi}{d\omega^2}\right|_{\omega_0} + \frac{1}{3!}(\omega-\omega_0)^3\left.\frac{d^3\varphi}{d\omega^3}\right|_{\omega_0} + \ldots \tag{2.23}$$

From the different Taylor coefficients, a group index n_g can then be defined

$$\varphi_1 = \frac{d\varphi}{d\omega} = \frac{r}{c}\left(n(\omega) + \omega\frac{dn(\omega)}{d\omega}\right) = r\frac{n_g}{c} \tag{2.24}$$

$$n_g = n + \omega\frac{dn}{d\omega}, \tag{2.25}$$

which describes the propagation of the pulse as a whole. Compared to the phase velocity, given by $v_\varphi = \frac{\omega}{k} = \frac{c}{n}$, which describes the propagation of the individual optical cycles, the group velocity $v_g = \frac{d\omega}{dk} = \frac{c}{n_g}$ expresses the propagation of the

envelope of the wavepacket. Since the group velocity is itself often frequency dependent and an optical pulse is never monochromatic, the different frequency components of the pulse travel with different velocities. This phenomenon is called group velocity dispersion (GVD) and is described by the second term of the Taylor series. The higher terms in the expansion will be abbreviated with higher-order dispersion (HOD). The above derivation leads to the definition of propagation coefficients:

$$k_1 = \frac{n_g}{c} \qquad \rightarrow \text{Inverse group velocity} \tag{2.26}$$

$$k_2 = \frac{1}{c}\frac{dn_g}{d\omega} \qquad \rightarrow \text{Group velocity dispersion} \tag{2.27}$$

$$k_m = \frac{1}{c}\frac{d^m n_g}{d\omega^m} \qquad \rightarrow \text{Higher-order dispersion} \tag{2.28}$$

In the presence of GVD an optical pulse is reshaped during propagation. The effect of GVD on a Gaussian pulse is shown in figure 2.17. Due to the quadratic phase the pulse is linearly stretched so that in a normal dispersion regime (GVD > 0) the red frequency components travel faster than the blue ones. This is called optical chirp. Especially in ultrafast time-resolved experiments chirp is an important parameter which needs to be considered carefully, as every dispersive optical element can cause pulse reshaping leading to a decreased temporal resolution. However, it is also possible to experimentally compensate for pulse broadening up to a certain order of dispersion by introducing different optical path lengths for the different colors. This can be achieved with a prism or a grating compressor whose working principle is indicated in figure 2.18. The angular dispersion in the prism generates a different optical path for the high frequencies compared to the lower frequencies resulting in a recompressed pulse.

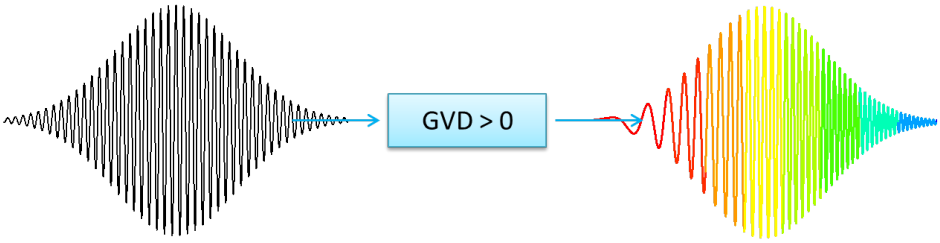

Figure 2.17: Propagation of a short laser pulse through a dispersive medium. The GVD causes a frequency dependence of the group velocity, which leads to a delay of the blue components in a normal dispersion material.

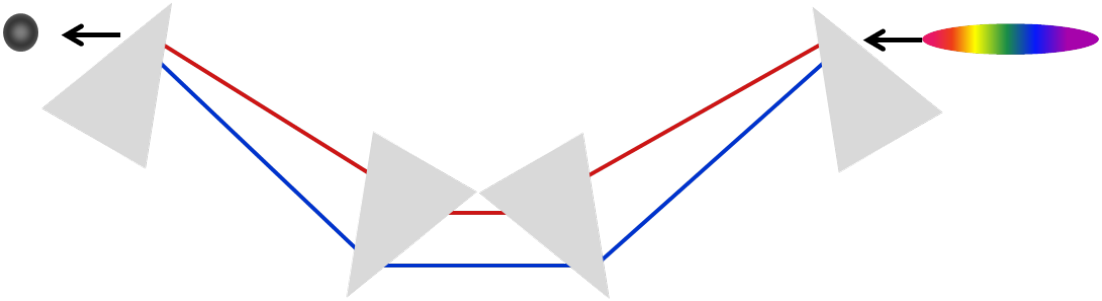

Figure 2.18: Pulse compression in a four prism setup. The chirp of the incoming pulse from the right is compensated by different optical paths for the faster traveling frequency components than for the slower ones.

2.6.2 Modelocking

The time-energy uncertainty relation (vide infra) suggests that for short pulse durations laser pulses with large spectral bandwidth are obligatory. In the following, we will briefly establish how that can be achieved. A typical laser setup consists of a cavity in which an active medium is placed that is pumped by a continuous wave (cw) light source. Inside the cavity only light with a certain wavelength is supported, which fulfills the condition $\lambda_m = \frac{2nL}{m}$, where n is the refractive index, L is the cavity length, and m an integer value. This condition leads to a frequency comb of longitudinal cavity modes with a spacing of Δf determined by the cavity round-trip time. Every wavelength of the active medium gain profile complying with a longitudinal cavity mode can be supported. Initially the different modes do not have a fixed phase relation, so that the out-coupled light exhibits a noise

like output over time (see figure 2.19 left side) with an intensity of mI_m, where I_m is the intensity of one m-th mode. If a fixed phase relationship between the individual modes can be established, constructive interference between the modes occurs, so that a pulsed signal is generated. This signal still has the same average output intensity, but the coupling of the modes leads to temporal concentration of the light energy with a peak intensity of $m^2 I_m$. The right side in figure 2.19 shows the corresponding modelocked signal for 5, 10, 20, and 50 modes. It is clearly visible that by increasing the spectral bandwidth, which is the number of longitudinal cavity modes, the pulses become smaller in temporal width. Several

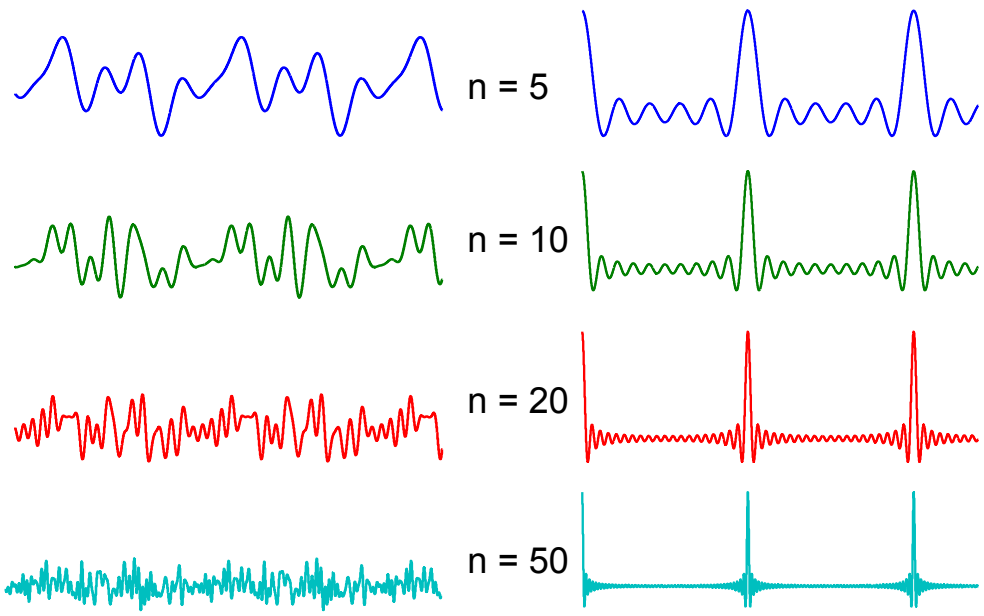

Figure 2.19: Representation of the electric field of 5 (blue), 10 (green), 20 (red), and 50 (cyan) uncoupled (left side) and modelocked (right side) waves. The uncoupled waves have a chaotic phase relation, whereas for the modelocked waves a similar phase for each mode is simulated.

experimental schemes for modelocking have been suggested, from which Kerr lens modelocking (KLM) will be discussed in the following. Kerr lens modelocking relies on a nonlinear interaction of light with a Kerr medium, in which the refractive index changes with the intensity of light (see 2.6.3). The Kerr medium acts as a switch, which blocks low intensity light associated with unlocked laser modes and only transmits light of high intensity. As the intensity dramatically increases with the number of locked modes, pulsed operation is favored. Figure 2.20 il-

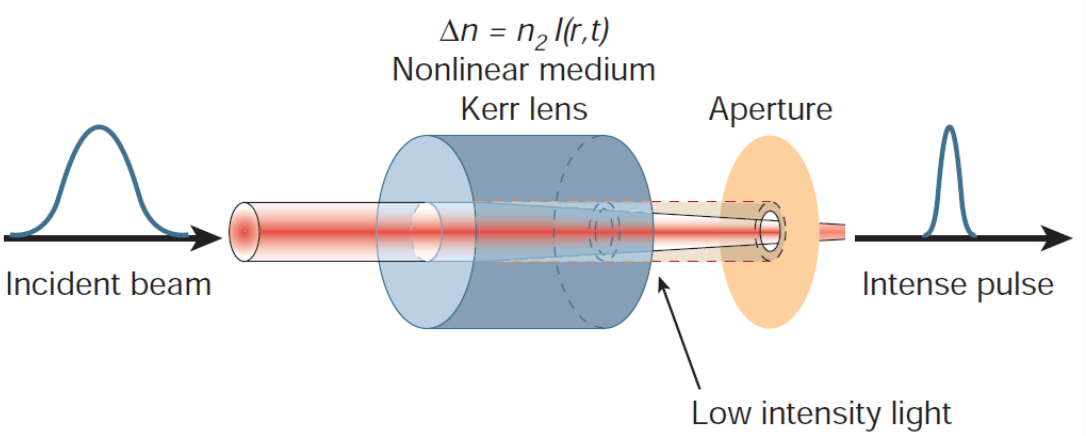

Figure 2.20: Illustration of the Kerr lens modelocking process. Only high intensity pulses carry the necessary intensity to generate strong self-focussing for transmission through the aperture. Reprinted by permission from Macmillan Publishers Ltd: Nature [95], copyright (2003).

lustrates the Kerr lens modelocking. By placing a Kerr medium in the cavity in combination with an aperture, only focused light is able to pass the aperture, whereas unfocused light is blocked. Assuming a Gaussian intensity profile, the intensity is highest in the center of the beam decreasing to the sides. This leads to the formation of a Kerr lens causing self-focusing of the input beam. Only if the intensity is high enough the self-focusing is strong enough, and the beam is not blocked by the aperture. This process is called passive modelocking.

2.6.3 Nonlinear optics

A typical regenerative amplifier delivers laser pulses usually around a central wavelength of 800 nm if Ti:Sa is involved as an active medium. In spectroscopic applications the materials may exhibit different absorption properties so that frequency conversion of the 800 nm becomes necessary. This is possible by exploiting the high peak intensities of the femtosecond pulses to drive nonlinear conversion. Maxwell's equations which describe how electric and magnetic fields are generated and how they influence each other can be combined to form the forced wave equation

$$\nabla^2 E - \frac{1}{c_0^2}\frac{\partial^2 E}{\partial t^2} = \mu_0 \frac{\partial^2 P}{\partial t^2}, \tag{2.29}$$

with the electric field E, the polarization density P, $c = \frac{c_0}{n}$, and $c_0 = \frac{1}{(\epsilon_0\mu_0)^{0.5}}$. The electric field and the polarization density are both vectors, but the wave equation is valid for arbitrary homogeneous, isotropic dielectric media allowing a component-by-component examination of the vectors, which leads to equation (2.29).[96] When an intense laser pulse enters a medium, the electric field of the light creates a polarization. In a linear dielectric medium the polarization density and the electric field are linearly related by

$$P = \epsilon_0 \chi E. \tag{2.30}$$

χ is the dielectric susceptibility of the medium given by $\chi = (\epsilon - 1)$. In a nonlinear medium the linear relation between electric field and polarization is not longer valid. In this case a Taylor series expansion of the polarization density leads to

$$P(t) = \epsilon_0(\chi^{(1)}E(t) + \chi^{(2)}E(t)^2 + \chi^{(3)}E(t)^3 + ...) \tag{2.31}$$

$$= P^{(1)} + P^{(NL)} \tag{2.32}$$

$$P^{(1)} = \epsilon_0 \chi E \tag{2.33}$$

$$P^{(NL)} = \epsilon_0 \sum_{n \geq 2} \chi^{(n)} E(t)^n, \tag{2.34}$$

where $P^{(NL)}$ is the nonlinear polarization. With these equations the wave equation (2.29) can be rewritten so that

$$\nabla^2 E - \frac{1}{c^2}\frac{\partial^2 E}{\partial t^2} = \mu_0 \frac{\partial^2 P^{(NL)}}{\partial t^2}. \tag{2.35}$$

The right side of equation (2.35) is regarded as the source term of radiation, and this equation is the basis of the theory of nonlinear optics. For optical frequencies $\chi^{(1)}$ is approximately 1, $\chi^{(2)} \approx 10^{-12}\,\mathrm{m/V}$, and $\chi^{(3)} \approx 10^{-24}\,\mathrm{m^2/V^2}$.

2.6.3.1 Optical parametric processes

Optical frequency conversion is a parametric process, which means that no energy, momentum, or angular momentum is transferred to the dielectric medium during the light-matter interaction. It is a $\chi^{(2)}$-interaction which will be illustrated in a small example. Let us assume that we have an electric field comprising two harmonic components at optical frequencies ω_1 and ω_2 so that

$E(t) = E_1 \cos(\omega_1 t) + E_2 \cos(\omega_2 t)$. In a nonlinear medium the 2nd-order polarization then gives rise to five different frequency components because $P^{(2)}$ can be written as

$$\begin{aligned} P^{(2)} = \frac{1}{2}\epsilon_0 \chi^{(2)} [E_1^2 [\cos(2\omega_1 t) + \cos((\omega_1 - \omega_1)t)] \\ + E_2^2 [\cos(2\omega_2 t) + \cos((\omega_2 - \omega_2)t)] \\ + 2E_1 E_2 \cos((\omega_1 + \omega_2)t) + 2E_1 E_2 \cos((\omega_1 - \omega_2)t)], \end{aligned} \tag{2.36}$$

which can be summarized as

$$P^{(2)}(\omega) = P(2\omega_1) + P(2\omega_2) + P(0\omega) + P(\omega_1 + \omega_2) + P(\omega_1 - \omega_2). \tag{2.37}$$

The red and green components $P(2\omega_1)$ and $P(2\omega_2)$ describe second-harmonic generation (SHG), the term $P(\omega_1 + \omega_2)$ is sum-frequency generation (SFG), $P(\omega_1 - \omega_2)$ is difference-frequency generation (DFG), and $P(0\omega)$ is called optical rectification (OR). The different parametric interactions are explained in figure 2.21.

Besides optical frequency generation, optical parametric amplification (OPA) plays an important role in our laser setup and will therefore be briefly explained. Instead of mixing two frequencies to get an up-converted frequency, in an OPA a weak signal frequency ω_1 and a strong pump wave ω_2 interact, so that energy from the pump is transferred to the signal wave during which the auxiliary wave ω_3 (called idler) is created. By choosing a whitelight continuum (see 2.6.3.2), which is usually weak in intensity, an OPA offers a large wavelength tuning range. In general not all of the mentioned frequency components can be generated at the same time as energy and momentum conservation must be fulfilled. So far only the time-domain picture of mixing was considered, but the argument of the complex wavefunction also includes a position dependence given by $\boldsymbol{k} \cdot \boldsymbol{r}$. If two waves at frequencies ω_1 and ω_2 are mixed, the second order susceptibility gives rise to a polarization at frequency $\omega_3 = \omega_1 + \omega_2$. This new frequency component has the wavevector $\boldsymbol{k}_3 = \boldsymbol{k}_1 + \boldsymbol{k}_2$ and as $k = \omega n(\omega)$, we obtain the phase-matching condition

$$\omega_1 n(\omega_1) + \omega_2 n(\omega_2) = \omega_3 n(\omega_3). \tag{2.38}$$

Usually, it is not possible to fulfill these conditions as most materials exhibit dispersion. Therefore, birefringent media are often used as they show polarization

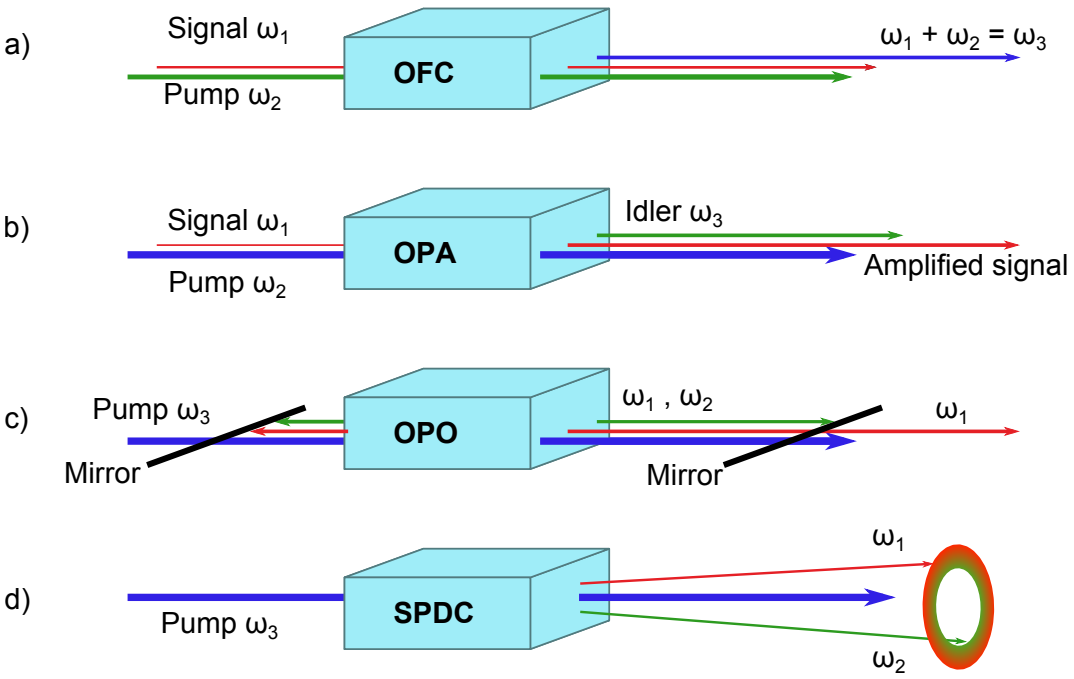

Figure 2.21: Overview of optical parametric processes. a) In optical frequency conversion two waves are mixed with the help of a third wave which is generated during this process. b) Optical parametric amplification: A weak signal at ω_1 is amplified by the pump beam. In this process an idler beam is generated. c) Optical parametric oscillator: Two mirrors provide feedback so that upon excitation with the pump beam an oscillator is created for the signal or idler wave. d) In spontaneous parametric downconversion a pump beam is spontaneously split into two waves fulfilling the phase-matching condition. Adapted from [96].

dependent refractive indices. For example, an uniaxial crystal can be used in which the refractive index also depends on the angle of the incoming wave in relation to the optical axis. If the polarization of the signal and idler waves are the same, the process is called **Type 1** phase-matching, whereas if signal and idler have orthogonal polarization it is termed **Type 2**.

2.6.3.2 Supercontinuum generation

Supercontinuum (SC) laser light or white light is extremely broadband coherent laser light generated in bulk media, liquids, gases, or various types of waveguides via nonlinear optical processes. Due to the large spectral range covered by a SC source, SC generation is a very valuable tool in spectroscopy. SC light is

also used in our transient absorption experiments (see section 3.3), and therefore this section tries to point out some of the nonlinear processes involved in the generation. The involved processes are highly complex and strongly depend on the media used for SC generation. Additionally, input wavelength, intensity, beam shape, and pulse length strongly influence the generation process. An extensive discussion on SC generation in bulk material can be found in [97–99], and SC generation in photonic crystal fibers is well reviewed by Dudley et al. in [100]. The first observations of SC generation date back to 1970 when Alfano and Shapiro reported the generation of white laser light in bulk BK7 glass.[101] They assigned this effect to self-phase modulation and small-scale filaments, but a complete consistent explanation based on full three-dimensional simulations of light propagation was not given until 2000 by Gaeta et al.[102] In the following we try to follow his argumentation and an introduction to the main processes is given.

When high intensity laser light enters an optical Kerr medium, the refractive index becomes intensity dependent due to the third order nonlinear polarization ($\chi^{(3)}$), so that $n(I) = n + n_2 I$. The Kerr effect introduces a phase change $\Delta\phi = -n_2 I k_0 z$ in which z is the propagation axis for the wave with a wavenumber k_0. In an optical pulse the intensity is time-dependent, and therefore the nonlinear phase change also becomes time-dependent given by

$$\Delta\phi(t) = -n_2 I(t) k_0 z. \tag{2.39}$$

This leads to a change of the instantaneous frequency described by

$$\Delta\omega = -n_2 \frac{dI}{dt} k_0 z. \tag{2.40}$$

For a pulse with Gaussian intensity distribution the effect is illustrated in figure 2.22. The trailing half of the pulse exhibits a negative slope in intensity change as $\frac{dI}{dt} < 0$, and if n_2 is positive this part of the pulse experiences a positive frequency change. Accordingly, the leading half will be reduced in frequency causing an effective chirp of the pulse and spectral broadening to the blue and red. This is called self-phase modulation (SPM), and as this effect is strongly intensity dependent, the self-focusing characteristic in a Kerr medium further supports the broadening due to the associated increase in pulse intensity. Theoretically, the self-focusing would lead to a beam collapsing on itself, but in reality several

higher nonlinear phenomena prevent this behaviour. For example, at high enough intensities multi-photon absorption sets in and causes an ionization of the surrounding atoms. The created plasma then leads to defocusing counteracting the self-focusing and keeping the pulse peak power below, but in the vicinity of the catastrophic beam collapse threshold.[97, 100] The above mentioned SPM is only valid for small bandwidth pulses, which fulfill the slowly varying envelope approximation (SVEA). If, however, the pulse is very broadband and of short pulse duration, the approximation is no longer valid. For the self-focusing of femtosecond pulses the slowly varying envelope approximation breaks down,[103] and this gives rise to asymmetric pulse-splitting, space-time focusing and self-steepening, leading to the formation of an optical shock wave, which is important for the correct description of SC generation.[102] This is the case for pulses in which the spectral width is comparable to the optical frequency. Comparing this to the pulses used in our experiment ($\approx 80\,\mathrm{fs}$), the SVEA seems to be justified, but due to the self-focusing, a spatio-temporal collapse occurs, and the SVEA is no longer valid.[99] A full mathematical description of these processes can be

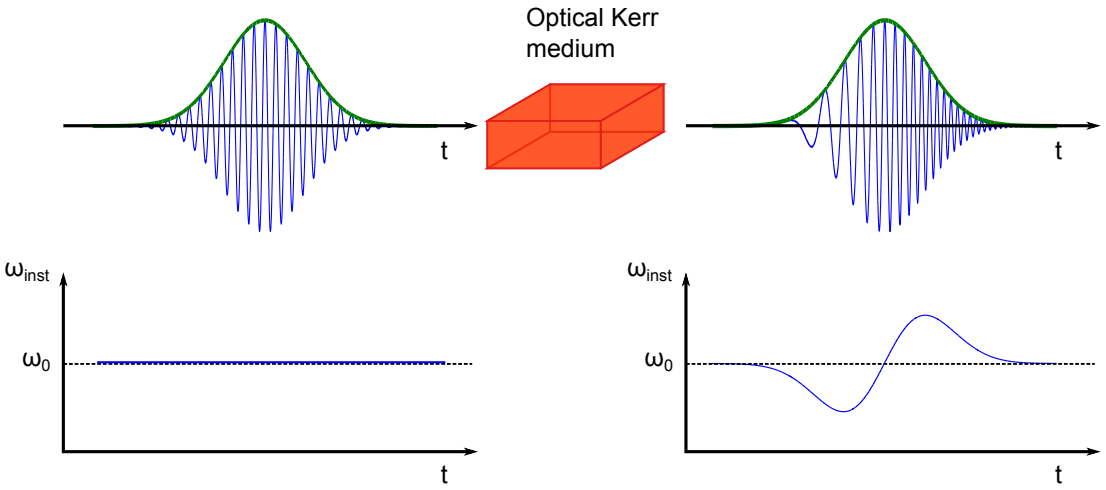

Figure 2.22: Self-phase modulation of a laser pulse. The Kerr medium causes a frequency change which is time-dependent due to the time-dependent intensity of the pulse envelope. This leads to a time-dependent change of the instantaneous frequency causing the generation of new frequency components. Adapted from [96]

found in [102], and only a phenomenological summary will be given here. Within the SVEA a high intensity laser pulse that is focused into a Kerr medium will split into two symmetric pulses in time caused by the mixture of GVD together

with SPM.[98, 103] As mentioned above, the SVEA is not valid in this regime anymore, and Rotheburg et al. proposed an alternative description of the envelope and named the associated physics describing the group velocity space-time focusing.[103] The self-steepening effect causes a reduction of the group velocity and therefore an increasing (steepening) slope of the trailing part of the pulse. Space-time focusing and self-steepening push the peak intensity of the split pulse to the rear until only a weak pedestal in the leading part remains. Figure 2.23 illustrates the propagation and the steepening. The steepening of the pulse then leads to the formation of a shock front that is associated with a phase jump, which causes then massive broadening of the spectrum, which is in turn responsible for SC generation.

For experimental application several characteristics of the seeding laser pulse are important. The results relevant for our experiments will be briefly summarized. Bradler et al. provided an excellent overview in which they investigated SC generation in different single crystals depending on focusing conditions, crystal thickness, pump pulse energy, and pump wavelength.[104] For SC reaching to the UV spectral region only CaF_2 was found to be suitable, but it needs to be constantly moved to prevent damage. For continua extending from the visible to the NIR, sapphire, yttrium aluminium garnet (YAG), or YVO_4 are more suitable. For all materials, they observed the onset of SC generation to approximately coincide with the characteristic power for self-focusing

$$P_{SF} \approx \frac{0.15\lambda_0}{n_0 n_2}, \tag{2.41}$$

again pointing out that this is the initial process leading to SC generation. By increasing the pulse energy, an enhanced NIR contribution was observed up to a point where single filament generation breaks up and colorful patterns probably obtained from multi-filament interference are observed. Furthermore, they found that for a long focal length of the lens focusing the seed into the crystal, enhanced NIR spectral components are generated. The pump wavelength also determines whether the generation of white light is possible or not. In literature it was reported that for SC generation the ratio between the bandgap of the crystal and the pump photon energy has to be larger than three as otherwise multiphoton absorption processes restrict self-focusing.[105] Shifting the pump wavelength to the NIR region, however, was shown to leave the visible part of the white light

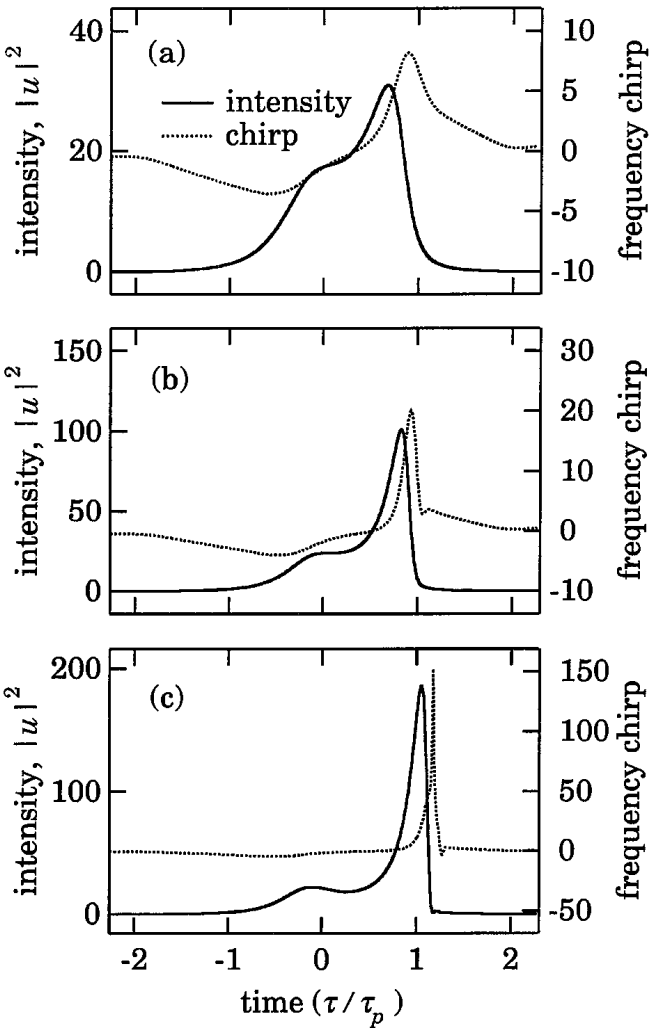

Figure 2.23: Temporal profile and frequency chirp of a laser pulse propagating in a nonlinear Kerr medium. In a) the profiles are shown at the onset of pulse splitting. b) and c) show further propagated pulses in which self-steepening and space-time focusing have pushed the intensity to the trailing part of the pulse leading to the formation of a shock front. Reprinted figure with permission from [102]. Copyright (2000) by the American Physical Society, http://journals.aps.org/prl/abstract/10.1103/PhysRevLett.84.3582.

almost unchanged whereas the NIR spectral region was further broadened.[104] In summary, for the generation of a broadband SC reaching from the visible up to the NIR spectral region, an NIR pump wavelength in combination with a long focal length lens should be used with sufficient power to start the SC generation, but lower than the onset of multi-filament generation.

Chapter 3

Experimental Methods and Materials

3.1 Solar cell preparation

The device architecture used for all solar cells prepared in this work is similar to that in figure 2.6, consisting of an ITO-covered quartz substrate, which is covered by a layer of PEDOT:PSS. Above that, the active layer is positioned, followed by the back electrode. The quartz substrates have a size of 24×24 mm and are completely covered with ITO. The fabrication follows the preceeding steps:

- ITO patterning: The ITO layer is removed in a wet etching process at the right and left side, so that a 12 mm broad ITO stripe remains in the middle (see figure 3.1).
- PEDOT:PSS: After ultrasonic cleaning in several solvents, a PEDOT:PSS layer of approximately 40 nm is spin-cast from aqueous solution on top of the ITO stripe. The sample is then transferred into the glovebox system where it is annealed at 150 °C for 10 minutes to get rid of residual water in the film.
- Active layer: After thermal annealing of the device, the photoactive layer is spin cast on top of the PEDOT:PSS layer from a solution of polymer and fullerne. Further details for the individual material systems investigated in this thesis can be found in table 3.1.

- Evaporation: The back electrode is evaporated on top of the photoactive layer without exposing the sample to air. The evaporation mask creates six equal pixels on each substrate which each have an active area of $0.14\,\mathrm{cm}^2$. The choice of the electrode depends on the active layer material.

- Contacting: To contact the solar cell, above and below the pixels the active layer and the PEDOT:PSS are removed by wiping, so that the ITO can be directly contacted. The counter contact is the evaporated back electrode which is protected during measurements by a thin layer of silver paste.

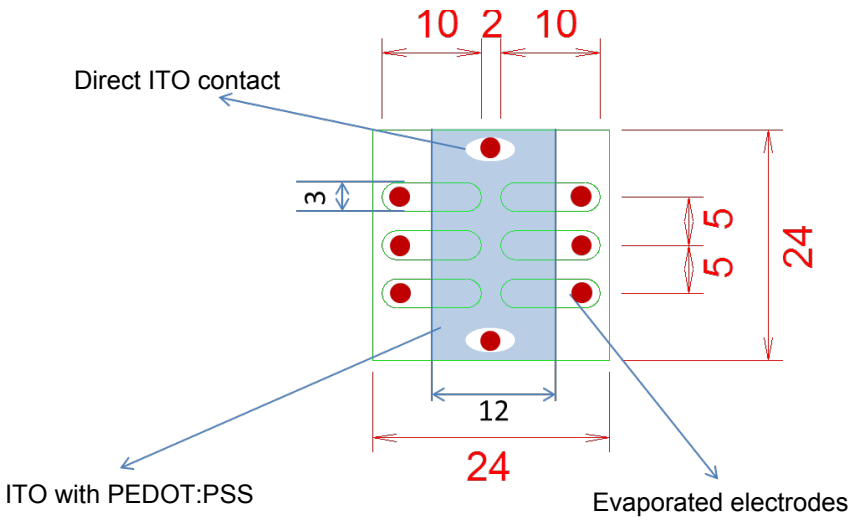

Figure 3.1: Layout of the solar cell. The blue area represents the ITO stripe which was removed at the sides. The overlap of the green electrodes with the blue ITO stripe defines the pixel size of 0.14 cm^2.

3.2 Solar cell characterization

In order to quantify the performance of solar cells, several experimental methods can be employed. In the following a short overview of the characterization of solar cells will be given.

3.2.1 J-V characteristics

The most important parameter for the characterization of a solar cell is the power conversion efficiency η, which is defined as the ratio of the electrical power generated by the solar cell at the maximum power point P_{MPP} and the incident light power with which the device is illuminated P_{in}. The maximum power point of a solar cell is determined by measuring the JV-curve of the device under illumination, for which the voltage is sweeped in a certain range and the corresponding current at each point is measured. A typical JV-curve is shown in figure 3.2, which is characterized by four prominent parameters:

- V_{OC}: The intersection of the JV-curve with the x-axis at zero current is called open-circuit voltage. At this voltage no net current is flowing in the external circuit.
- J_{SC}: The intersection of the JV-curve with the y-axis at zero voltage is called short-circuit current.
- FF: The fill-factor (FF) is an ideality factor which is defined as the ratio of the product of the current and the voltage at MPP and the product of J_{SC} and V_{OC}. It is dimensionless and varies between zero and one, describing how rectangular the JV-curve is.
- Dark current: The dark current characterizes the JV-curve of solar cell without illumination. At reverse bias the dark current is zero, but with decreasing internal field at some point charges are injected into the devices and create a current in forward direction. The dark current is part responsible for the reduction of the fill-factor.

The parameters are connected in the following way:

$$\eta = \frac{P_{MPP}}{P_{in}} = FF\frac{V_{OC}J_{SC}}{P_{in}} \tag{3.1}$$

$$FF = \frac{P_{MPP}}{V_{OC}J_{SC}} \tag{3.2}$$

In our experimental setup the source of illumination is a solar simulator (K.H. Steuernagel Lichtechnik) which imitates AM 1.5G conditions. AM 1.5G represents the solar spectrum after the light has traveled 1.5 times through the

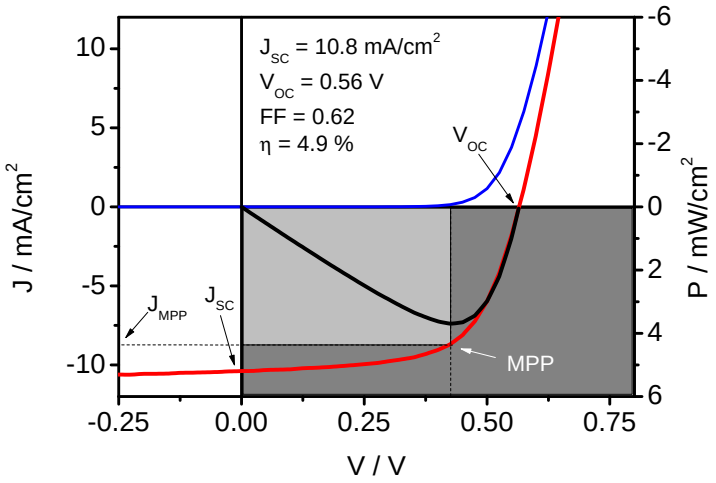

Figure 3.2: JV-curve of PSBTBT:$PC_{70}BM$ with the figures of merit to characterize a solar cell. The blue line is the dark current, the red line is the measured current under AM1.5G like conditions, and the black line represents the electrical power generated in the cell. The fraction of the gray shaded areas is the fill-factor.

atmosphere compared to the distance light would have traveled if it traveled perpendicularly through the atmosphere, thereby accounting for the average angle of incidence of 48° of solar light, which is the yearly average in the USA including also diffusive light. The JV measurement is performed by a Keithely 236 SMU.

3.2.2 External quantum efficiency measurements

Another important method for the characterization of a solar cell is the external quantum efficiency (EQE) measurement in which the fraction of extracted charges per incident photon is calculated. This number can be corrected for scattering and parasitic absorption to obtain the internal quantum efficiency (IQE) which represents the ratio of extracted charge carriers per absorbed photon. By scanning the excitation wavelength, a whole EQE spectrum can be recorded from which information about the photon energy dependence of charge carrier generation can be deduced. If the solar cell contains a blended active layer with separated absorption profiles, conclusions about the charge carrier generation efficiency of the individual components can be drawn. A typical EQE spectrum is shown in figure 3.3. The experimental setup consists of a tungsten halogen lamp and a TRIAX 180 monochromator used as a tunable excitation source. The num-

ber of incident photons for each wavelength is obtained from a calibrated silicon photodiode and the current is measured with a Keithley 236 SMU.

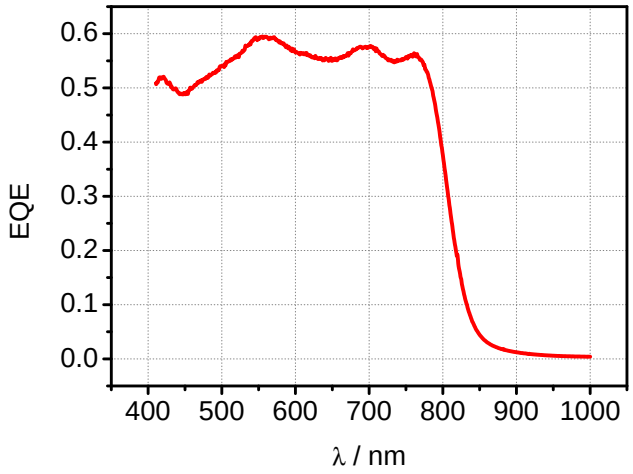

Figure 3.3: External quantum efficiency of a PSBTBT:$PC_{70}BM$ device.

3.3 Transient absorption spectroscopy

Transient absorption spectroscopy (TAS) enables the observation of excited state dynamics by recording their changes in absorption following photo-excitation. In a typical experiment the transmission of a weak probe laser pulse through the sample is recorded after excitation of the sample by an intense pump laser pulse and compared to the transmission without a pump pulse. The transient evolution of absorption in such a pump-probe experiment can then be obtained by changing the delay time between the probe and the pump pulse. The time resolution is consequently determined by the length of the pump and probe pulses. Due to the availability of femtosecond laser technology, a time-resolution of 150 fs is possible without further experimental effort, which can be enhanced to sub-20 fs by pulse recompression.[78] Furthermore, the possibility to use optical parametric processes with femtosecond pulses (see 2.6.3.1) gives access to spectral regions for excitation as well as probing from the UV/VIS to the NIR. However, with monochromatic probing the generation of transient absorption spectra is time-consuming, since the probe wavelength needs to be scanned over the desired spec-

tral range for each time delay. An elegant alternative is the use of a broadband supercontinuum source as a probe pulse. Depending on the choice of material for the SC generation, wavelengths from the UV up to the NIR region are accessible with high pulse to pulse stability, necessary to obtain a decent signal-to-noise ratio. Broadband probing is especially helpful to identify spectral shifts which undetected could lead to erroneous excited state kinetics. TAS experiments should be carried out in the linear absorption regime, and when coherent effects, visible only with very short pulses, and non-linear effects are disregarded, the transient signal can be written as

$$\frac{\Delta T}{T}(\lambda, t) = -\sum_{i,f} \sigma_{if}(\lambda) \Delta N_i(t) d. \tag{3.3}$$

The indices i and f represent the initial and final state of the probed transition, $\sigma_{if}(\lambda)$ is the corresponding crossection, ΔN_i is the population density change of state i due to the perturbation by the pump, and d is the sample thickness. The convention is that the crossection is negative for upward transitions and positive for downward transitions. The typical signals observed in TAS are depicted in figure 3.4 and explained in the following:

- Ground State Bleach (GSB): A positive change in transmission indicates that the sample absorbs less light in this wavelength region upon application of the pump. This feature coincides with the ground state absorption of the material as during excitation by the pump the population of the ground state is decreased by transitions to excited states. Consequently, less probe light can be absorbed in the ground state leading to positive a $\frac{\Delta T}{T}$. The GSB monitors all excited states.

- Stimulated Emission (SE): In a fluorescent material excitation leads to the population of emissive states. The interaction of the probe pulse with the excited system can then result in the stimulated emission of photons, which show up as a positive $\frac{\Delta T}{T}$ in the fluorescence region of the material.

- Photoinduced Absorption (PIA): Excitation of the sample generates excited states that also have absorption. The probe pulse probes transitions from the excited state to higher lying excited states, which usually leads to a broad negative $\frac{\Delta T}{T}$ due to the overlap of several excited state transitions.

The decay characteristics of the PIA can be used to identify different excited species.

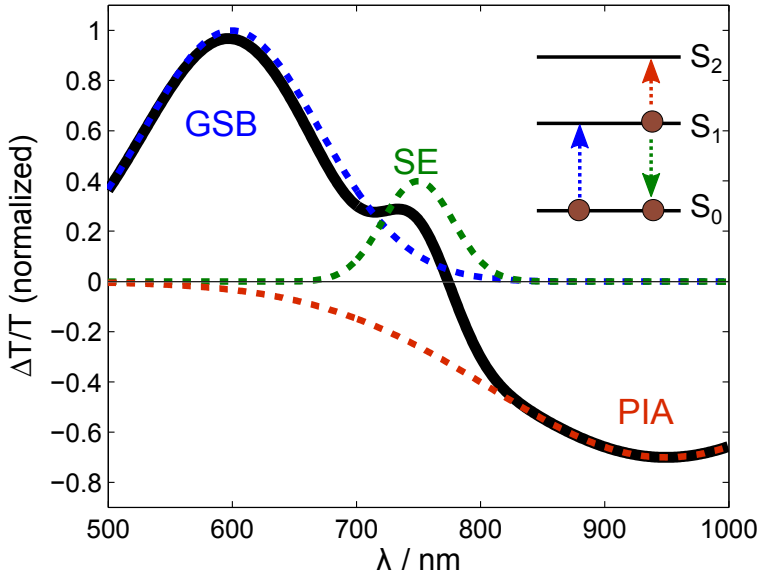

Figure 3.4: Typical signals observed in a TAS experiment. The thick black line is the resulting spectrum consisting of a GSB (blue), SE (green), and a PIA (red). The inset shows the corresponding transitions.

3.3.1 Experimental setup

Our experimental setup covers a time-range up to 4ns with a time resolution of $\approx$ 150 fs (short time setup), and in a second experiment the time-range between 1 ns up to 1 ms (long time setup) with 500 ps time resolution can be observed. Both experiments can be conducted with a supercontinuum probe in a spectral range between 450-1100 nm and 1100-2600 nm. The center of our setup is a 1 kHz Ti:Sapphire-based regenerative amplifier one-box system (Coherent Libra HE) with an integrated oscillator and pump laser delivering 80 fs pulses at 800 nm with an energy of 3.5 mJ. The oscillator (Coherent Vitesse) is a mode-locked Ti:Sapphire laser pumped by a green cw diode-pumped laser (Coherent Verdi V2). The output of our laser system is split and injected into two optical parametric amplifiers (OPerA Solo) of which one is used to generated pump pulses in the UV/VIS to the NIR for the femtosecond to nanosecond pump-probe experiments. The second OPA creates the seed wavelength for the SC generation

which is used as a probe in both setups. The pump pulse for the long time setup is provided by an Nd:YVO_4 MOPA laser (AOT MOPA 100) which produces pump pulses at 1064 nm that can be doubled to 532 nm. For UV excitation the third harmonic can also be generated.

Figure 3.5 schematically displays the design of our setups which are identical for both time ranges except for the way the delay between pump and probe pulses is obtained. In the short time experiment the delay is varied by a linear motorized delay stage with a maximum optical path difference corresponding to 4 ns. Special care has to be taken to guarantee perfect overlap for all delay times, which requires fine adjustment of the in-coupling into the stage. Furthermore, collimation of the pump beam plays an important role as divergence or focusing lead to varying excitation densities for each delay time. Hence, spot size measurements with a beam profiler are inevitable. In the long time range (ns-μs) a mechanical time delay is obviously not possible. Therefore, an actively triggered Q-switched laser is used as a pump source, and the delay is electronically varied by a delay generator (SRS DG535). In both setups pump and probe beam are overlapped under an angle to enable the separation of the pump pulse behind the sample. Due to the degradation of organic films in air, a small vacuum chamber is used to create a dynamic high vaccum. For field dependent measurements on solar cell devices, the setup can be changed to reflection mode, where the back electrode of the device is used as a mirror to reflect the probe beam. Additionally, liquid nitrogen can be used to cool down the chamber, so that temperature dependent measurements can be conducted. Another critical issue is to find the correct spatial overlap between pump and probe pulse. The general idea in pump-probe spectroscopy is to use a large pump beam which is overlapped with a focused probe, to simulate spatial homogeneity of the excitation density for the size of the probe. For measurements conducted with visible probe continua, perfect overlap can be guaranteed with a beam profiler that displays pump and probe beam at the same time. The overlap can then be optimized by maximizing the transient signal. For measurements in the NIR the procedure was altered as visible components are almost completely absent in the NIR continua. Therefore, a substrate with a small pinhole was placed in the vacuum chamber next to the sample, and the chamber was adjusted with an xyz-stage to maximize the transmission of the probe beam through the pinhole. The pinhole size is chosen so that the focused

probe beam passes the aperture without being clipped. After optimizing the transmission, the pump pulse is adjusted on the aperture with a spot size larger than the aperture, and the sample chamber is moved in the plane perpendicular to the probe beam to place the sample in the optical path. Again transient signal optimization can be used to tune the overlap. In TAS, the transmission of the

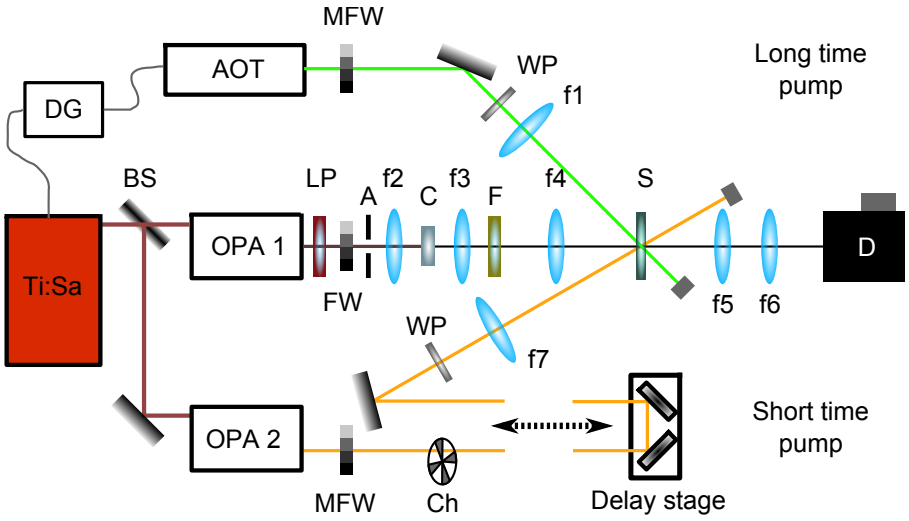

Figure 3.5: Schematic representation of the TAS setup. The whole experiment is powered by the output of the Ti:Sa regenerative amplifier, which pumps OPA1 and OPA2. The long delay pump (AOT) is triggered by a delay generator (DG) which is synchronized to the libra. f1 to f7 are lenses, MFW is a motorized filter wheel, FW is a manual filter wheel, WP is a lambda half wave plate, LP is long pass filter, A an iris aperture, C is the crystal for white light generation, F is a filter to remove the residual seed wavelength, BS is a beam splitter, and Ch is the chopper wheel. The transmitted probe is detected in D.

probe pulse through the sample (pump off) is compared to the transmission of the probe pulse upon application of the pump pulse (pump on). Experimentally this is achieved by chopping the pump pulse so that a reduced repetition rate of 500 Hz is generated in relation to the 1 kHz repetition rate of the probe pulse. This means that every second probe pulse carries transmission information with pump on or pump off, respectively. In the long time setup the pump laser can be triggered at 500 Hz so that additional chopping is not necessary. For data recording linear dispersion grating spectrometers with silicon array detectors (256 or 512 pixels) or an extended InGaAs array detector (512 pixels) are used. The grating spectrometers (Princeton Instruments Acton SP2150) are equipped with

two sets of gratings, for the visible range blazed at 500 nm with a groove density of 150 g/mm for broadband detection or with 600 g/mm for high resolution spectra, and in the NIR with gratings blazed at 1.2 μm and groove densities of 300 g/mm and 150 g/mm. Special care has to be taken when working with SC probes that extend over more than an optical octave as higher diffraction orders can alter the signal. This can be dealt with with suitable long and short pass filters. Calibration of the spectrometers is achieved by inserting narrow-band line filters into the optical path, whose maximum transmission is then associated to a pixel number, and a linear wavelengths calibration is performed. To avoid anisotropy effects the polarization of the pump pulse is rotated by a $\lambda/2$-plate in relation to the probe pulse so that magic angle conditions are achieved.

To calculate the resulting change of transmission normalized to the transmission of the probe without pump, 1000 shots are averaged for pump on and for pump off, and after that the difference is calculated so that

$$\frac{\Delta T}{T} = \frac{T_{\text{on averaged}} - T_{\text{off averaged}}}{T_{\text{off averaged}}}. \tag{3.4}$$

3.3.2 Parameters for SC generation

In our setup, supercontinuum generation in undoped laser crystals is used to create broadband probe pulses. Depending on the desired spectral range, different materials and seed wavelengths are employed to generate stable continua. For measurements spanning from 450 nm - 1100 nm, a c-cut sapphire crystal is used with a thickness of 3 mm, and a 1300 nm seed pulse generated by the OPA is focused on the front facet. In literature, usually 800 nm seeds are used to generate whitelight in the visible, however the residual 800 nm cannot be entirely separated from the SC without causing a spectral gap and therefore renders this spectral region useless. By pushing the seed wavelength above the detection limit of the silicon array, a continuous TA spectrum can be recorded. The 1300 nm seed is focused with a 50 mm lens, and an additional iris aperture in front of the lens offers control of the beam shape. The seed pulse contains approximately 1-2 μJ and is carefully adjusted with a continuous neutral density filter, so that single filament whitelight is generated. For stability reasons an additional long pass filter is inserted into the optical path in front of the focusing lens to block parasitic wavelengths, and the iris and ND filter are adjusted to optimize stability and

spectral range. The transition between single and multi filament SC generation can easily be observed by inserting a piece of white paper into the optical path after the SC generation and increasing the pulse energy.

The creation of stable whitelight in the spectral region between 1000 nm - 2000 nm was part of the work carried out in this thesis. For the NIR TAS measurements described in [49] a sapphire crystal was used with a seed wavelength of 2100 nm. This resulted in a broad spectral output, but the SC was very sensitive to small fluctuations in the seed pulse energy. By replacing the sapphire crystal by an yttrium orthovanadate (YVO_4) crystal seeded at 2100 nm, a very stable SC was generated, comparable to the stability of the visible whitelight described above. The focusing lens was also replaced by a 75 mm focal length lens to increase the amount of NIR whitelight.[104] However, the combination of YVO_4 with 2100 nm produces almost no visible output, and therefore, a sapphire crystal is used for alignment. Once the system is aligned, the sapphire was replaced with the YVO_4 crystal, and the signal was optimized for spectral range and stability. With careful adjustments a stability around 1 % rms can be achieved. It has to be noted that it is experimentally easier to detect only a part of the generated SC spectrum, for example between 1050 nm and 1600 nm, by using a diffraction grating with a higher groove density because the dynamic range of the detector is too small to compensate the spectral intensity differences of the SC. The reasons for the spectral inhomogeneous intensity are hidden in the generation process itself, but also in the diffraction efficiency of the grating and the response of the InGaAs detector array. In figure 3.6 the shape of the different SC are shown as detected by our setup. It can be seen that for both crystals the signal increases to the red, whereas in the blue region only a weaker signal is detected. However, the exchange of sapphire with the YVO_4 crystal strongly increases the generated whitelight in the spectral region between 1100-1450 nm.

3.3.3 Sample data and data processing

A typical transient absorption experiment produces a data surface similar to that shown in figure 3.7. The VIS and NIR measurements are merged into one surface for demonstration purposes. Taking a slice along the photon energy axis produces a transient absorption spectrum at a fixed time delay, in which the different

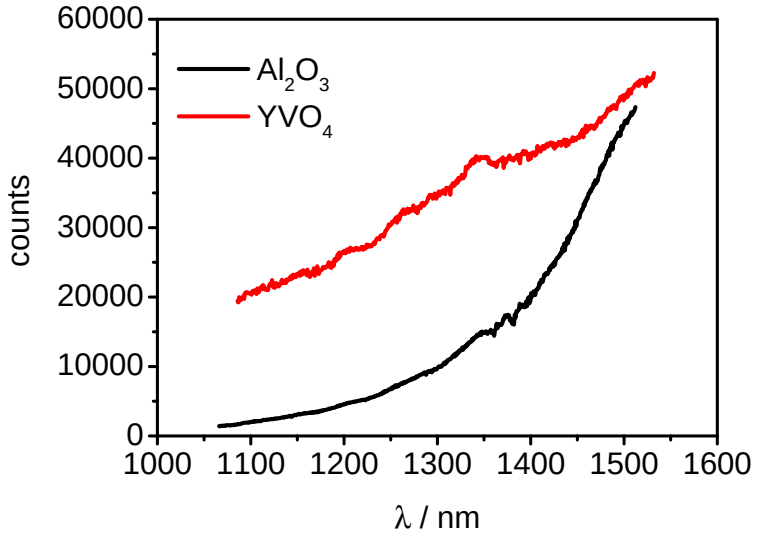

Figure 3.6: Comparison of the whitelight spectra generated with sapphire (black line) and YVO_4 (red line). Both spectra show a signal increase to the red, but for YVO_4 the detected signal is not as steep as for sapphire. Note that these spectra are a convolution of the actual whitelight spectrum with the diffraction efficiency of the grating and the detector response.

contributions of GSB and PIA can be identified. The kinetics corresponding to a certain spectral feature can then be extracted as shown in the lower right panel. Before the data can be analyzed, a chirp correction of the short time data has to be performed as chirp causes a time delay between different probe wavelengths of ≈ 1 ps in the visible. To correct for this, the chirp region is manually redrawn and then fitted to a polynomial in a 2D plot and subtracted (see figure 3.8). Due to the design of the experiment it is possible that a part of the pump light is scattered in the direction of the probe beam and becomes visible in the TA signal as an artifact visible throughout the entire time range and even before zero time, when the probe passes the sample before the pump. This can be corrected by a background correction, where the signal before zero time is averaged and subtracted. However, special care has to be taken when identifying artifacts as also photoexcited species longer lived than the inverse repetition rate (1 ms) can cause such signals.

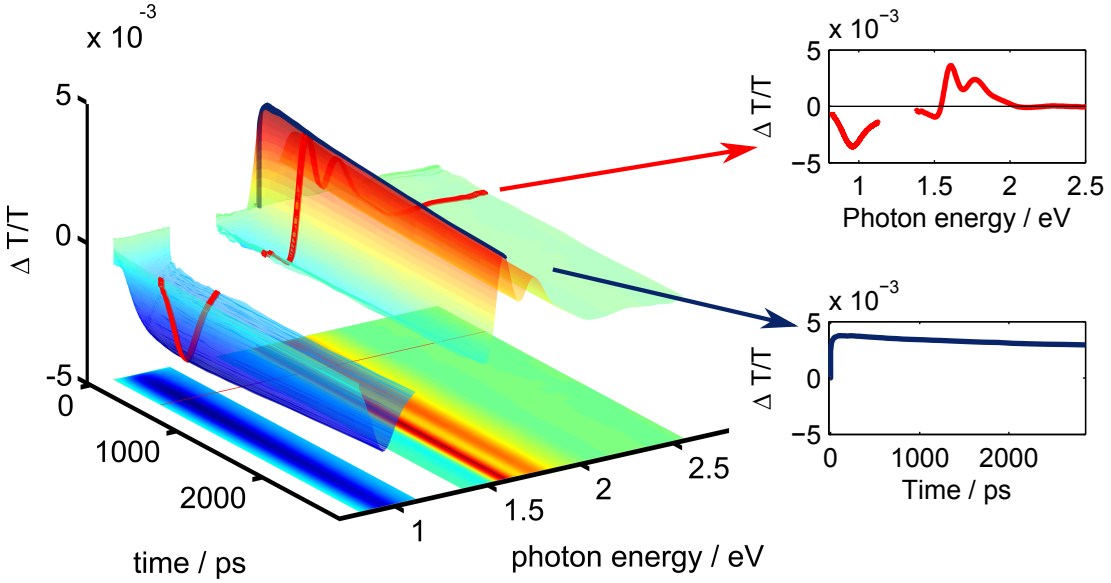

Figure 3.7: Transient absorption data surface with corresponding spectra (red line) and kinetics (blue line).

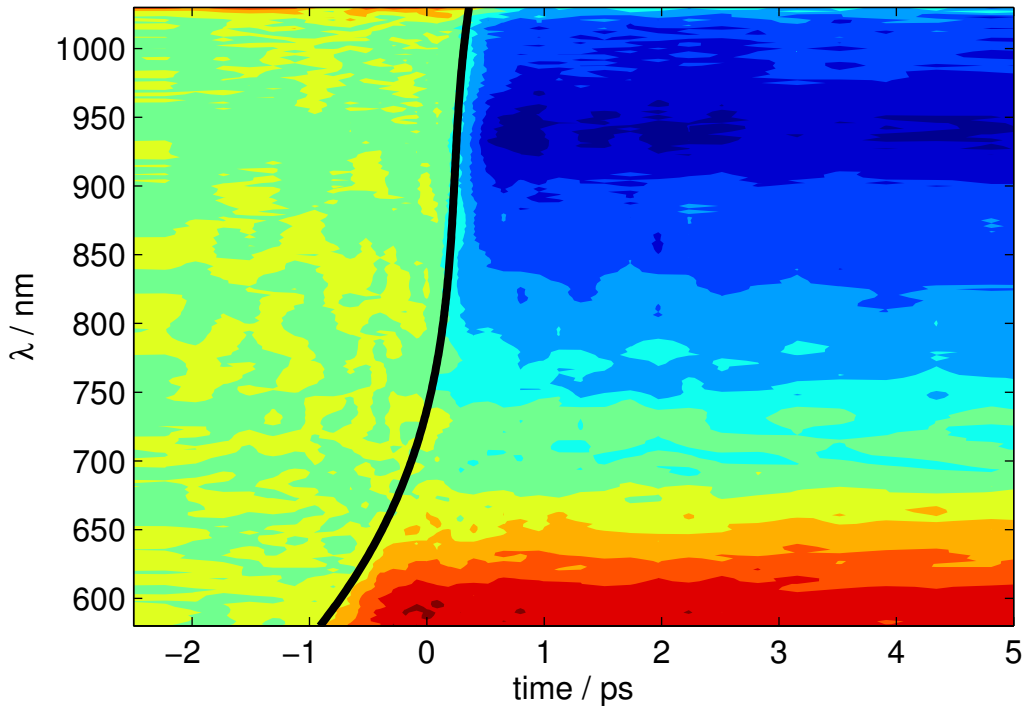

Figure 3.8: Contour plot of short time TA data with a solid black line indicating the chirp. The black line is subtracted from the TA data to correct the chirp.

3.3.4 Multivariate curve resolution and global fitting

Pure kinetics of a certain species can only by extracted if there is no overlap between different excited state spectra. In the case of strongly overlapping features several more sophisticated methods can be employed, excellently summarized in [106]. Only a short overview will be given in this context. If the shape of the excited-state spectra does not change over time, the measured data surface can be represented by a bilinear decomposition so that $D = CS + E$ in which the matrix C carries the concentration profiles and S the corresponding crossections (spectra). E is the error matrix that ideally only contains experimental noise. One method to determine C and S is the global analysis in which a simulated data matrix is created by hard modeling the expected photophysical processes with certain amplitudes and time constants, which are then optimized by minimizing the difference between the experimentally measured data set and simulated data set.[107] The drawback of this method is that the fraction of each species involved in the process has to be known and identified to create a meaningful model.

An alternative approach is the multivariate curve resolution (MCR), which is extensively reviewed in [108–111]. MCR is a so-called soft modeling approach in which only constraints are used that do not require knowledge of each individual species, but are based on basic physical and mathematical assumptions. Possible assumptions are for example non-negativity of spectra and concentrations. The idea behind the method is to use an initial guess of the concentration profiles from which in the next step the corresponding spectra are calculated with the least squares method. The calculated spectra are then again altered with additional constraints and used to recalculate new concentration profiles. This process continues until a tolerance limit is reached and the best fit is found. The initial guess for the concentrations is obtained by evolving factor analysis (EFA) based on singular value decomposition (SVD), which additionally indicates how many species are needed to correctly describe the data set at different times. For further details about the method and application to simple examples the reader is referred to [106].

3.4 Quasi-steady-state photoinduced absorption spectroscopy

The working principle of quasi-steady-state photoinduced absorption spectroscopy (cw-PIA) is very similar to TAS as the same photo-physical properties of the samples are probed. The difference is that, unlike in TAS, in which a fs laser is used for pump and probe, no ultrafast light source is needed. Our setup consists of a 100 W tungsten-halogen lamp that in combination with a monochromator (LOTOriel Omni-λ 300) is used as a probe. As a pump source the output of different cw lasers (633 nm and 808 nm) or high power LEDs (355 and 527 nm) is chopped or directly electronically modulated. The samples are placed in a nitrogen-cooled optical cryostat (Oxford Instruments Optistat CF) at 80 K in helium atmosphere or at room temperature in a dynamic vacuum. The transmitted probe light is dispersed by a second identical monochromator and then detected by a photodiode detector. For measurements in the wavelength range from 500 to 1100 nm, an amplified silicon photodetector (Thorlabs PDA 100A) is employed, which can be substituted by an amplified germanium detector (Thorlabs PDA 50B) for the wavelength range from 900 to 1800 nm. An InSb detector covers the region between 1750 to 4000 nm, which is limited by the spectral range of the light source. The pump light is chopped at 317 Hz to induce changes in the transmission ΔT, which are measured by using a lock-in amplifier (EG&G Princeton Applied Research model 5210). To calculate ΔT/T, the transmission is recorded prior to the cw-PIA measurement and corrected for photoluminescence. Compared to TAS, the cw-PIA technique allows prescreening of the material to identify interesting spectral regions for TAS experiments. However, the signal in cw-PIA is always a life-time averaged ensemble of the individual signatures of excited states which leads to the loss of short-lived features in this technique.

3.5 Time-resolved photoluminescence measurements

For the detection of time-resolved photoluminescence a Hamamatsu Streak Camera system is used, which allows for spectral and temporal analysis of emitted photons. In a typical experiment the sample is excited by a short laser pulse,

and the emission is spectrally resolved in a spectrograph. The spectrograph is connected to a photocathode which converts the incident photons into electrons. The electrons then interact with a time dependent electric field perpendicular to the propagation direction and perpendicular to the spectrograph dispersion. The electric field is triggered by the excitation laser pulse so that depending on the time the emitted photons arrive at the photocathode, the corresponding electrons experience different accelerations in the electric field. This technique allows to temporally resolve the emission. The generated electrons are incident on a phosphorescent screen which is monitored by 2D CCD camera as illustrated in figure 3.9. The measurements conducted for this work were carried out after excitation with pulses from a 80 MHz Ti:Sa laser system delivering pulses of approximately 100 fs length, which were then frequency doubled in a BBO crystal to obtain an excitation wavelength of 400 nm, suitable for most organic materials.

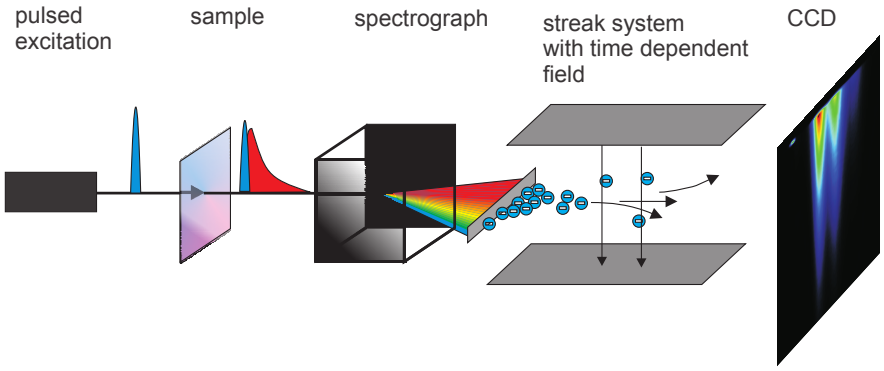

Figure 3.9: Working principle of a streak camera system. The emission of the sample is spectrally dispersed in a spectrograph and the photons are successively converted to electrons in a photocathode. An electric field synchronized to the laser trigger then sorts the electrons in time by a varying electric field, so that on a phosphorescent screen a 2D plot can be observed with the spectral information on one axis and the temporal evolution on the other. Taken from [13].

3.6 Materials

In this thesis three different donor polymers were investigated, namely PCDTBT, PCPDTBT, and PSBTBT. This section gives a short overview of the material properties and processing conditions. Figure 3.10 shows the chemical structures of the investigated polymers. PCDTBT, poly[N-11"-henicosanyl-2,7-carbazole-alt-

5,5-(4',7'-di-2-thienyl-2',1',3'-benzothiadiazole)], was first synthesized by Leclerc et al.,[30, 31] and belongs to the class of the poly(2,7)carbazoles. In this thesis a PCDTBT with modified, longer side chains was investigated, synthesized by Lee et al.[112] The modified side chains were added to increase the solubility of the material.

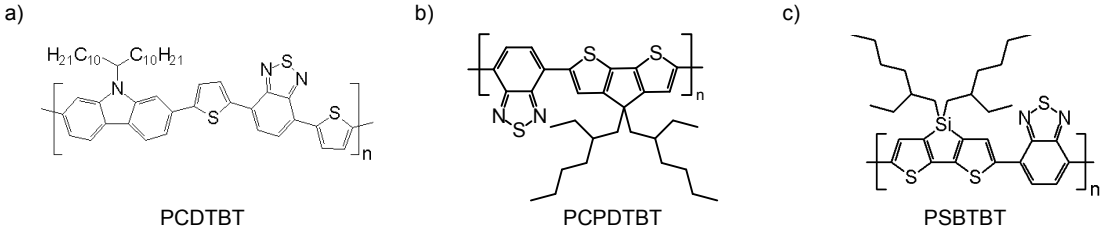

Figure 3.10: Donor polymers investigated in this work.

The second material system is the low-bandgap donor polymer poly[2,6-(4,4-bis-(2-ethylhexyl)-4H-cyclopenta[2,1-b;3,4-b']-dithiophene)-alt-4,7-(2,1,3-benzothiadiazole) (PCPDTBT), which was first synthesized by Muehlbacher et al.[34] The material used in this work was synthesized and further purified by Cho et al. [49, 113] to yield a molecular weight of $M_N = 16000\,\mathrm{g/mol}$. For later experiments additional PCPDTBT was purchased from 1-Material with a molecular weight of $M_N = 18000\,\mathrm{g/mol}$. Both material batches delivered similar photovoltaic performance.

The third donor polymer is based on silole-containing polythiophenes and 2,1,3-benzothiadiazole and is called poly[(4,4'-bis(2-ethylhexyl)dithieno[3,2-b:2',3'-d]-silole)-2,6-diyl-alt-(2,1,3-benzothiadiazole)-4,7-diyl] (PSBTBT), synthesized by Hou et al.[114] PSBTBT is very similar to PCPDTBT except for the substituted bridgehead atom as shown in figures 3.10b) and 3.10c). The spectroscopic investigations presented in this work were done on PSBTBT obtained from Konarka with a molecular weight of $M_N = 16000\,\mathrm{g/mol}$ and $M_W = 60000\,\mathrm{g/mol}$. For comparison of the solar cell performance another batch was obtained from Solarmer with $M_N = 6000\,\mathrm{g/mol}$.

The donor polymers were blended with the fullerene acceptors $PC_{60}BM$ or $PC_{70}BM$ purchased from Sigma Aldrich and table 3.1 gives an overview of the processing conditions used for the material systems.

	PCDTBT	PCPDTBT	PSBTBT
c(Donor) / mg/ml	5	10	14
DA-ratio	1:2	1:2	1:1.5
Solvent	CF	CB	DCB
Annealing	-	-	-
Additives	-	ODT, 2.4 vol%	-
Thickness / nm	105	100	100
Electrodes	100nm Al	10nm Ca 100nm Al	10nm Ca 100nm Al

Table 3.1: Processing conditions of the investigated material systems

Chapter 4

Results and Discussion

4.1 Ultrafast Exciton Dissociation Followed by Nongeminate Charge Recombination in PCDTBT:PCBM Photovoltaic Blends

JACS
JOURNAL OF THE AMERICAN CHEMICAL SOCIETY
ARTICLE
pubs.acs.org/JACS

Ultrafast Exciton Dissociation Followed by Nongeminate Charge Recombination in PCDTBT:PCBM Photovoltaic Blends

Fabian Etzold,[†] Ian A. Howard,[*,†] Ralf Mauer,[†] Michael Meister,[†] Tae-Dong Kim,[‡] Kwang-Sup Lee,[*,‡] Nam Seob Baek,[§] and Frédéric Laquai[*,†]

[†]Max Planck Research Group for Organic Optoelectronics, Max Planck Institute for Polymer Research, Ackermannweg 10, Mainz D-55128, Germany

[‡]Department of Advanced Materials, Hannam University, Daejeon 305-811, Republic of Korea

[§]IT Convergence Technology Research Laboratory, Electronics and Telecommunications Research Institute, Daejeon 305-700, Republic of Korea

Supporting Information

ABSTRACT: The precise mechanism and dynamics of charge generation and recombination in bulk heterojunction polymer:fullerene blend films typically used in organic photovoltaic devices have been intensively studied by many research groups, but nonetheless remain debated. In particular the role of interfacial charge-transfer (CT) states in the generation of free charge carriers, an important step for the understanding of device function, is still under active discussion. In this article we present direct optical probes of the exciton dynamics in pristine films of a prototypic polycarbazole-based photovoltaic donor polymer, namely poly[*N*-11′′-henicosanyl-2,7-carbazole-alt-5,5-(4′,7′-di-2-thienyl-2′,1′,3′-benzothiadiazole)] (PCDTBT), as well as the charge generation and recombination dynamics in as-cast and annealed photovoltaic blend films using methanofullerene ($PC_{61}BM$) as electron acceptor. In contrast to earlier studies we use broadband (500−1100 nm) transient absorption spectroscopy including the previously unobserved but very important time range between 2 ns and 1 ms, which allows us not only to observe the entire charge carrier recombination dynamics but also to quantify the existing decay channels. We determine that ultrafast exciton dissociation occurs in blends and leads to two separate pools of products, namely Coulombically bound charge-transfer (CT) states and unbound (free) charge carriers. The recombination dynamics are analyzed within the framework of a previously reported model for poly(3-hexylthiophene):PCBM (Howard, I. A. et al. J. Am. Chem. Soc. 2010, 132, 14866) based on concomitant geminate recombination of CT states and nongeminate recombination of free charge carriers. The results reveal that only ∼11% of the initial photoexcitations generate interfacial CT states that recombine exclusively by fast nanosecond geminate recombination and thus do not contribute to the photocurrent, whereas ∼89% of excitons create free charge carriers on an ultrafast time scale that then contribute to the extracted photocurrent. Despite the high yield of free charges the power conversion efficiency of devices remains moderate at about 3.0%. This is largely a consequence of the low fill factor of devices. We relate the low fill factor to significant energetic disorder present in the pristine polymer and in the polymer:fullerene blends. In the former we observed a significant spectral relaxation of exciton emission (fluorescence) and in the latter of the polaron-induced ground-state bleaching, implying that the density of states (DOS) for both excitons and charge carriers is significantly broadened by energetic disorder in pristine PCDTBT and in its blend with PCBM. This disorder leads to charge trapping in solar cells, which in turn causes higher carrier concentrations and more significant nongeminate recombination. The nongeminate recombination has a significant impact on the *IV* curves of devices, namely its competition with charge carrier extraction causes a stronger bias dependence of the photocurrent of devices, in turn leading to the poor device fill factor. In addition our results demonstrate the importance of ultrafast free carrier generation and suppression of interfacial CT-state formation and question the applicability of the often used Braun−Onsager model to describe the bias dependence of the photocurrent in polymer:fullerene organic photovoltaic devices.

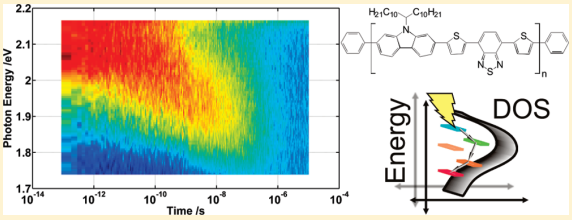

1. INTRODUCTION

Photovoltaic devices are considered to be one of the most important alternatives to fossil fuels for clean and renewable energy production and to satisfy the world's ever growing energy demand by exploiting a quasi-inexhaustible energy source, the sun. During the last two decades organic semiconductors have emerged as a new class of photovoltaic materials that promise low-cost and large-area production of organic photovoltaic (OPV) devices using energy-efficient solution-cast techniques

Received: February 28, 2011
Published: May 10, 2011

Journal of the American Chemical Society ARTICLE

and add unprecedented features such as mechanical flexibility and very low weight, which is of utmost importance for the growing market of mobile electronic devices.[1] In fact organic solar cells based on intimately mixed electron-rich donor polymers and electron-deficient fullerene-based acceptors, commonly referred to as 'bulk heterojunction (BHJ)', have recently demonstrated certified power conversion efficiencies (PCE) exceeding 7−8%.[2,3] However, the photophysical processes that govern charge generation, transport, and extraction as well as the efficiency-limiting loss channels remain not well understood.[4] This is partially a consequence of the very complicated interplay between the chemical structure of the individual components, the solid-state morphology of the blend, and the blend photophysics that finally altogether determine the device efficiency.[5−7]

It is now widely accepted that in archetypical polymer:fullerene bulk heterojunctions photon absorption leads to the generation of Coulombically bound Frenkel-type excitons, which are the primary photoexcitations in conjugated polymers and small organic molecules.[8−10] After diffusion to an interface, the exciton is ionized in an ultrafast (<100 fs) process leading to the generation of Coulombically bound charge-transfer (CT) states (also termed bound radical pairs), and free charge carriers (polarons). The ratio of CT states to free charge carriers formed by exciton quenching depends on both the material system and morphology. For efficient photovoltaic operation the ultrafast formation of free carriers is preferred, and although the mechanism for this ultrafast formation of free carriers is unclear, it has been shown to dominate in efficient P3HT:PCBM blends.[11,12] The effect of interfacial charge transfer states, should they be formed, on photovoltaic efficiency is still debated.[13−16] Theoretically the CT states could either recombine to the ground state, a process termed geminate recombination, or dissociate into free charge carriers that can be extracted from the blend as photocurrent. The field and temperature dependence of CT-state dissociation (theoretically explored by Onsager, Braun, and Tachiya)[17−20] have been often invoked to explain the bias dependence of photocurrent. However, recent results in the P3HT:PCBM system suggest the field dependence of the competition between extraction and nongeminate recombination of free carriers determines the field dependence of the photocurrent,[21,22] calling into question the relevance of field-dependent CT-state splitting in efficient photovoltaic devices. We do note, however, that Lee et al. demonstrated P3HT:PCBM devices exhibit similar internal quantum efficiencies for band gap excitation of Frenkel-type excitons and below band gap direct excitation of CT states,[23] which could imply that what is measured in transient absorption as ultrafast free charge generation could actually very briefly pass through a (hot) charge-transfer state within the ∼100 fs instrument response time of the system. What is clear, is that the ratio between what we will continue to term ultrafast generated free charge carriers (with the aforementioned proviso born in mind) and CT states that have been found to geminately recombine on the time scale of approximately a nanosecond in a variety of systems, is an important factor in efficient photovoltaic operation and one that differentiates whether improvement should be sought in improving the separation of charge carriers from the interface by energetic or nanomorphological changes or in their extraction by improvement in mobility or mesoscopic device structure.

In the present work we report direct optical probes of exciton and charge carrier dynamics in a donor−acceptor copolymer, namely poly[*N*-11′′-henicosanyl-2,7-carbazole-*alt*-5,5-(4′,7′-di-2-thienyl-2′,1′,3′-benzothiadiazole)] (PCDTBT). Copolymers based on alternating donor−acceptor moieties have recently attracted considerable attention since they in principle can offer better photon harvesting in the lower-energy part of the solar spectrum and/or an increased open-circuit voltage of the devices by fine-tuning of the energy levels of the polymer. PCDTBT attracted our attention because internal quantum efficiencies approaching unity in blends with PCBM have been demonstrated by the Heeger group in conjunction with power conversion efficiencies up to 6.1% upon insertion of optical spacers and in inverted solar cell structures.[24,25] Earlier work by Leclerc and co-workers on PCDTBT:PCBM photovoltaic devices has demonstrated reproducible efficiencies of more than 3% in simple as-cast device structures, with efficiencies exceeding 5% upon optimizing the light management of the device.[26,27] Interestingly it was also observed that annealing did not have a positive effect on the device efficiency unlike that typically observed for the prototypic photovoltaic system P3HT:PCBM.[28] Recently, Street and co-workers have performed transient photoconductivity measurements on PCDTBT:PCBM devices and concluded that geminate recombination, as can be expected due to the high IQEs, is not at all a significant loss channel in this system.[29] Tong et al. have investigated the exciton dynamics in pristine PCDTBT polymer films and charge generation in blends with $PC_{70}BM$ by means of optical probes,[30] however, only up to 2 ns, which hampers a clear comparison between geminate and nongeminate recombination and thereby also a direct comparison between CT state and ultrafast free carrier formation. Their analysis is also limited by the fact that the excited-state dynamics were fitted with a sum of exponential functions rather than kinetic equations based on a photophysical model. Hence, the lifetimes reported have no direct physical meaning and only information about the approximate time scale of the processes after the precise excitation fluences used can be gained, making a general comparison problematic. Furthermore, a quantification of the different decay channels occurring on largely varying time scales is also impossible. In a subsequent work the Heeger group studied also the exciton dynamics in pristine PCDTBT polymer films by ultrafast fluorescence upconversion to disentangle the very early excited-state dynamics which occur below 100 fs.[31] It was suggested that charge carriers are directly generated as primary photoexcitations and collapse into Coulombically bound excitons within the first 100 fs, which is in stark disagreement with the common notion that the primary photoexcitations in conjugated polymers are Frenkel-type excitons. In the present work we report on exciton dynamics in pristine polymer films and charge generation and recombination dynamics covering a dynamic range of 10 orders, i.e., from 100 fs to 1 ms. By studying the entire relevant time scale, we can directly compare geminate (occurring on roughly a few nanoseconds time scale) and nongeminate recombination (occurring, depending on the fluence, on roughly 1 ns to 1 μs time scales at typical transient absorption pump fluences) processes by studying the charge recombination as a function of initial charge density (i.e., as a function of different excitation fluences). In contrast to previous work, we use our recently introduced analytical model to describe the data and thereby extract the absolute fractions of geminate and nongeminate recombination as well as the relevant rate constants, recombination coefficients, and order of the recombination process. Our results demonstrate that geminate recombination plays a minor role in PCDTBT:PCBM blends and free charge carriers are created without passing through CT states as intermediates, a fact which has recently been demonstrated in P3HT:PCBM

Journal of the American Chemical Society ARTICLE

Scheme 1. Synthesis of the Solution-Processable Poly(2,7-carbazole) Derivative PCDTBT

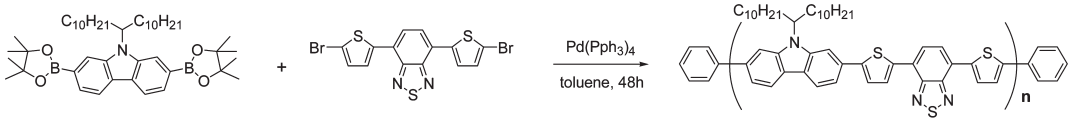

M1 M2 PCDTBT

blends, but whose universal validity for high-efficiency polymer: fullerene blends is a matter of ongoing debate.[4,13] However, we not only quantify the photophysical processes in PCDTBT:PCBM blends by studying the entire relevant time scale but also observe various spectral signatures of significant energetic disorder in the PCDTBT blend not seen in P3HT:PCBM blends by using a broadband probe, which allows us to clearly distinguish between spectral shifts and recombination processes. Having excluded that geminate recombination plays an important role as a loss channel, our experimental results let us conclude that the high disorder leads to higher carrier densities which in turn shift the competition between charge extraction and nongeminate recombination in favor of nongeminate recombination. The increased importance of nongeminate recombination in these devices leads to this recombination playing an increased role in devices under standard operation conditions and explains the reduced fill factor, which is a consequence of the increased bias dependence of the photocurrent. Hence, the investigated devices exhibit only moderate efficiencies not exceeding those obtained from P3HT:PCBM reference cells, despite their higher open-circuit voltage and similar short-circuit current.

2. MATERIAL SYNTHESIS

For the present work a slightly different PCDTBT derivative than has previously been used by most groups was prepared. The material has slightly longer alkyl chains, which provides better solubility in commonly used organic solvents such as toluene and chloroform. The starting materials 2,7-bis(4′,4′,5′,5′-tetramethyl-1′,3′,2′-dioxaborolan-2′-yl)-*N*-11′′-henicosanylcarbazole and 4,7-bis(5-bromo-2-thienyl)-2,1,3,-benzothiadiazole used for polymerization were prepared according to a high-yield synthesis previously described in the literature.[26,32] The dioxoborolan-functionalized carbazole unit (M1) was reacted with the dibromo-functionalized benzothiadiazole (M2) unit under typical Suzuki cross-coupling conditions catalyzed by $Pd(PPh_3)_4$ in toluene to give PCDTBT as shown in Scheme 1. The resulting polymer was subsequently purified by Soxhlet extraction with hexane, acetone, and methanol. The benzothiadiazole-based poly(2,7-carbazole) was highly soluble in common organic solvents and showed good thermal stability.

3. EXPERIMENTAL SECTION

Tetrakis(triphenylphosphine)palladium(0) ($Pd(PPh_3)_4$) and tetraethylammonium hydroxide (Et_4NOH, 20% solution) were obtained from Aldrich Chemical Co. and used without further purification. Tetrahydrofuran (THF) was distilled over sodium benzophenone ketyl under nitrogen prior to use. ^1H NMR and ^{13}C NMR spectra were recorded with a Varian Oxford 300 MHz NMR spectrometer; chemical shifts are given in ppm with tetramethylsilane used as the internal standard. Mass spectra were taken with a JEOL JMS-AX505WA mass spectrometer.

Synthesis of 2,7-Bis(4′,4′,5′,5′-tetramethyl-1′,3′,2′-dioxaborolan-2′-yl)-*N*-11′′-henicosanylcarbazole. *N*-11′-Henicosanyl-2,7-dibromocarbazole (1.62 g, 2.61 mmol) was dissolved in 30 mL of anhydrous THF in a well-dried round flask under nitrogen atmosphere; 3.6 mL (5.73 mmol) of *n*-butyllithium (1.6 M in hexanes) was added dropwise at −78 °C with stirring for 1 h. After formation of white precipitation, 2-isopropoxy-4,4,5,5-tetrametyl-1,3,2-dioxaborolane (1.3 mL, 6.52 mmol) was added dropwise, and the mixture was allowed to warm to room temperature and stirred for another 6 h. After the reaction, the crude mixture was poured into the water and extracted with dichloromethane. The organic layer was washed with brine (30 mL) and dried over anhydrous magnesium sulfate. The residue was purified by column chromatography to give M1 (1.5 g, 81%) as white powder. ^1H NMR (300 MHz, $CDCl_3$, ppm): δ 8.59 (br, 1H); 8.40 (br, 1H); 8.19 (d, 1H); 8.15 (t, 2H); 8.09 (d, 1H); 4.50(m, 1H); 2.32 (m, 2H); 1.61 (m, 2H); 1.21 (br, 4H); 1.19−1.15 (br, 28H); 1.03 (br, 24H); 0.88 (t, 6H); EI-Mass: Calculated for $C_{45}H_{73}B_2NO_4$: 713.57, Found: 713.56

Synthesis of 4,7-Bis(5-bromo-2-thienyl)-2,1,3,-benzothiadiazole. ^1H NMR (300 MHz, $CDCl_3$, ppm): δ 7.84 (d, 2H), 7.82 (s, 2H), 7.19 (d, 2H); ^{13}C NMR (75 MHz, $CDCl_3$, ppm): δ 152.3, 140.7, 130.9, 127.8, 125.5, 125.0; EI-Mass: Calculated for $C_{14}H_6Br_2N_2S_3$: 455.81, Found: 455.82

Synthesis of Poly[*N*-11′′-henicosanyl-2,7-carbazole-alt-5,5-(4′,7′-di-2-thienyl-2′,1′,3′-benzothiadiazole)] (PCDTBT). A mixture of M1 (0.37 g, 0.524 mmol) and M2 (0.24 g, 0.524 mmol) in 8 mL of anhydrous toluene was degassed two times with N_2. Then, tetrakis(triphenylphosphine)palladium (0.03 g, 0.026 mmol) and 3 mL of 20% Bu_4NOH were added and stirred for 30 min. The mixture was stirred vigorously at reflux for 2 days. After the reaction, the crude product was poured into methanol. The resulting polymer was collected by filtration, and the filtrate was purified by Soxhlet extraction with hexane, acetone, and then methanol. (Yield 76%)

Photovoltaic Devices. For solar-cell preparation ITO-coated glass substrates (Präzisions Glas & Optik GmbH, Germany) were patterned by wet etching and successively cleaned in an ultrasonic bath with different solvents. Between the cleaning steps the samples were dried with nitrogen gas. Prior to spin-coating of the organic films, the substrates were plasma etched for 15 min in argon plasma. After spin-coating of a 20-nm layer of poly(3,4-ethylene-dioxythiopene):poly(styrenesulfonate) (PEDOT:PSS) (Clevios P VP Al 4083, H.C. Stark), the samples were transferred into a nitrogen-filled glovebox and baked for 1 h at 120 °C. For the active layer, PCDTBT and PCBM (Sigma Aldrich) were dissolved separately in chloroform for about 5 h and then mixed in a ratio of 1:2 by weight with a PCDTBT concentration of 5 mg mL^{-1}. The PCBM solution was filtered through a PTFE filter (0.45 μm), then mixed with the PCDTBT solution and spin-cast at 700−2500 rpm for 60 s, producing active-layer thicknesses between 80 and 130 nm. A 100-nm layer of aluminum was subsequently evaporated as a top electrode. For the spectroscopy the active layer was spin-cast onto quartz substrates under conditions similar to those for the solar cells, except that the concentration of PCDTBT in the pristine films was higher with c(PCDTBT) = 10 mg ml^{-1}. For measurements on annealed devices and films, these were heated in the glovebox for 20 min at 120 °C. Solar-cell device characterization was performed inside a nitrogen-filled glovebox employing a solar simulator (K.H.

Journal of the American Chemical Society ARTICLE

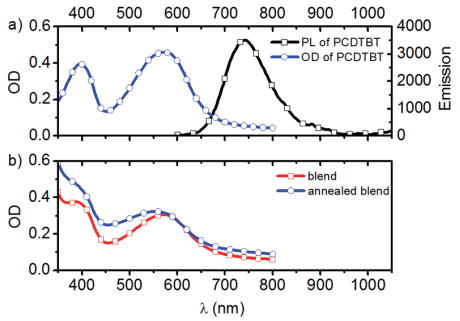

Figure 1. (a) Absorption and emission spectrum of a pristine PCDTBT film ($d \approx 100$ nm). (b) Absorption spectrum of a 1:2 by weight PCDTBT:PCBM blend before and after annealing.

Steuernagel Lichttechnik GmbH, Germany) with a 575 W metal halide lamp combined with a filter system to create a spectrum according to AM1.5G conditions, however, with an intensity of 90 mW cm^{-2}. The current−voltage curves were measured with a Keithley 236 Source-Measure Unit. For external quantum efficiency (EQE) measurements monochromatic light was created with a tungsten−halogen lamp and a TRIAX 180 monochromator between 300 and 800 nm. The light intensity was measured with a calibrated silicon diode leading to a maximum intensity of 0.7 W m^{-2} at 600 nm. EQE measurements were performed in the glovebox at short circuit conditions with a Keithley 236 Source-Measure Unit.

Steady-State Spectroscopy. The absorption measurements were conducted with a Perkin-Elmer Lambda 25 spectrophotometer. Photoluminescence spectra were recorded with a TIDAS 3D fluorescence spectrometer. To determine the layer thickness of the films a Tencor P10 surface profilometer was used.

Quasi-steady-state Spectroscopy. Quasi-steady-state photoinduced absorption spectroscopy (PIA) was performed with a pump−probe setup consisting of a 100 W tungsten-halogen lamp with a LOT-Oriel Omni-λ 300 monochromator as the probe and a Newport LED (LED-527-HP) working at 524 nm with 100 mW cm^{-2} used as a pump. The samples were placed in a nitrogen-cooled optical cryostat (Oxford Instruments Optistat CF) at 80 K in helium atmosphere. The transmitted light was dispersed by a second identical monochromator and then detected by a photodetector. For measurements in the wavelength range from 500 to 1100 nm, an amplified silicon photodetector (Thorlabs PDA 100A) was employed, which was replaced by an amplified germanium detector (Thorlabs PDA 50B) for the wavelength range from 900 to 1800 nm. The pump light was chopped at 317 Hz to induce changes in the transmission ΔT, which were measured by using a lock-in amplifier (EG&G Princeton Applied Research model 5210). To calculate $\Delta T/T$, the transmission was recorded prior to the PIA measurement and corrected for photoluminescence.

Time-Resolved Fluorescence. Time-resolved photoluminescence (TR-PL) spectra were measured with a C4742 Hamamatsu streak camera system. Samples were excited with the frequency doubled output from a mode-locked Ti:Sa oscillator (Coherent Mira 900 Duo) with a pulse width of 100 fs at 400 nm.

Transient Absorption Spectroscopy. Transient absorption (TA) measurements were performed with a home-built pump−probe setup. To measure in the time range of 1−4 ns with a resolution of ~100 fs, the output of a commercial titanium:sapphire amplifier (Coherent LIBRA HE, 3.5 mJ, 1 kHz, 100 fs) was split with one portion used to generate a 532 nm excitation pulse using a home-built two-stage narrowband non-collinear optical parametric amplifier (NOPA) and another used to generate a 1300 nm seed pulse (output of an optical

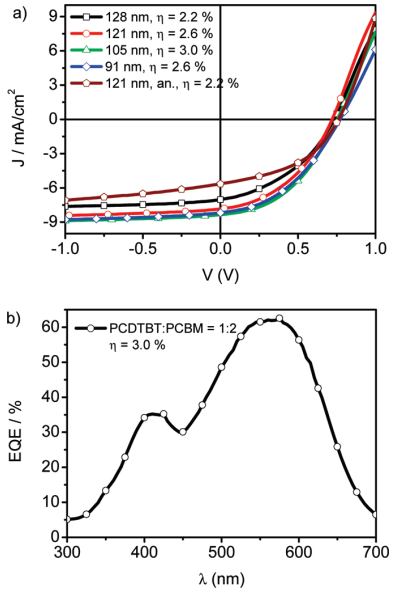

Figure 2. (a) The current−voltage ($J-V$) characteristics of BHJ solar cells made from 1:2 by weight PCDTBT:PCBM blends for different active layer thickness. η is the power conversion efficiency under solar illumination of 90 mW cm^{-2}. The efficiency is found to decrease upon annealing. (b) External quantum efficiency of the solar cell with a 105-nm active layer thickness measured at short-circuit conditions.

parametric amplifier (Coherent OPerA Solo)) for white-light generation in the visible and NIR in a c-cut 3 mm thick sapphire window. The variable delay of up to 4 ns between pump and probe was introduced by a broadband retroreflector mounted on a mechanical delay stage. Only reflective elements were used to guide the probe beam to the sample to minimize chirp. The excitation pulse was chopped at 500 Hz, while the white light pulses were dispersed onto a linear photodiode array which was read out at 1 kHz. Adjacent diode readings corresponding to the transmission of the sample after an excitation pulse and without an excitation pulse were used to calculate $\Delta T/T$. For measuring in the time range of 1 ns to 1 ms with a resolution of 600 ps, the excitation pulse was provided by an actively Q-switched Nd:YVO_4 laser (AOT Ltd. MOPA) at 532 nm. The delay between pump and probe in this case was controlled by an electronic delay generator (Stanford Research Systems DG535). TA measurements were performed at room temperature under dynamic vacuum at pressures <10^{-5} mbar.

4. EXPERIMENTAL RESULTS

4.1. Photovoltaic Performance. Figure 1a shows the steady-state absorption spectra of a pristine PCDTBT film and an as-cast and annealed 1:2 by weight PCDTBT:PCBM blend. We note that the PCDTBT derivative used in our study has a longer alkyl chain attached to the nitrogen of the carbazole comonomer (11″-henicosanyl instead of 9′-heptadecanyl) than the polymer used in previous studies, which provides better solubility of the polymer in organic solvents commonly used for thin film preparation. However, in agreement with previous reports we observe two distinct absorption bands from the polymer backbone peaking at 397 and 572 nm. The lower-energy absorption band has previously been assigned to the $\pi-\pi^*$-transition of the first excited singlet state (S_1) of the conjugated backbone, while

Journal of the American Chemical Society ARTICLE

Table 1. Photovoltaic Parameters of PCDTBT:PCBM (1:2) Solar Cells with Varying Active Layer Thickness under Solar Illumination of 90 mW cm^{-2}

device	active layer [nm]	V_{oc} [V]	J_{sc} [mA cm^{-2}]	FF	PCE [%]
1	128	0.73	−7.02	0.40	2.2
2	121	0.72	−7.84	0.42	2.6
3	105	0.75	−8.35	0.43	3.0
4	91	0.77	−8.17	0.41	2.6
5	121 annealed	0.76	−5.65	0.44	2.2

the higher-energy absorption band has been attributed to the $\pi-\pi^*$-transition into the second excited singlet state (S_2).[31] Excitation into both the lower-energy band of the absorption spectrum at 532 nm and the higher-energy band at 400 nm leads to a broad and unstructured emission between 620 and 940 nm, peaking at 742 nm in the steady-state spectrum. In blends with PCBM the energetically lower absorption peak of PCDTBT is still visible, whereas the band at 400 nm is superimposed by the fullerene absorption. We observe that annealing has only a limited impact on the absorption of the blend, unlike that observed for regioregular P3HT:PCBM blends.

Figure 2a shows the $J-V$ characteristics of PCDTBT:PCBM (1:2) solar cells under solar illumination of 90 mW cm^{-2}. The best power conversion efficiency (PCE) of ~3% was obtained for an active layer thickness of 105 nm. Typical photovoltaic parameters obtained from PCDTBT:PCBM(1:2) solar cells are shown in Table 1.

The best device showed a moderate fill factor (FF) of 0.43 (lower than the 0.6 typically observed for P3HT:PCBM)[22] with an open circuit voltage (V_{OC}) of 0.75 V and a short circuit current density (J_{SC}) of 8.35 mA cm^{-2}. A decrease of the device efficiency upon prolonged annealing can be observed in line with previous reports.[28] The short circuit current of the solar cells was found to depend linearly on the illumination intensity (see Supporting Information), indicating that at short circuit conditions the total fraction of recombination reducing the photocurrent (i.e., the sum of geminate and nongeminate recombination) is constant in the entire intensity range measured. As we consider further, the effects of nongeminate recombination may, however, increase as the internal field is reduced and the open-circuit voltage is approached. The external quantum efficiency for the best devices is shown in Figure 2b. The EQE exhibits two peaks coinciding with the absorption maxima of the blend. The EQE approaches 63% at the energetically lower peak, i.e. at the absorption maximum of the polymer. At around 400 nm the EQE is lower and around 35%, despite the higher absorption of the blend at this wavelength for reasons still not entirely understood. However, this seems to indicate that, as observed previously in the P3HT:PCBM system, quenching of excitons created on PCBM is less complete than quenching of excitons created on the polymer.[33]

4.2. Exciton Dynamics in Pristine PCDTBT Films. Figure 3 shows a contour plot of the time-resolved (0−2 ns) photoluminescence (PL) of a pristine PCDTBT polymer film at room temperature measured by a Streak Camera after excitation with the frequency doubled output of a titanium:sapphire femtosecond oscillator (400 nm, ~100 fs). The PL progressively redshifts, indicating relaxation of excitons in the density of states. The relaxation is significant, corresponding to a shift in energy of about 70 meV that is completed on the time scale of approximately 1 ns (see Supporting Information). Simulations have

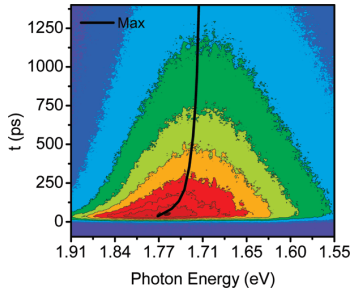

Figure 3. Temporal evolution (ps−ns) of the photoluminescence of pristine PCDTBT films as observed by the Streak Camera technique after excitation with a femtosecond laser pulse. The solid line shows the evolution of the peak position of a Gaussian line shape fit to the spectrum at each time delay.

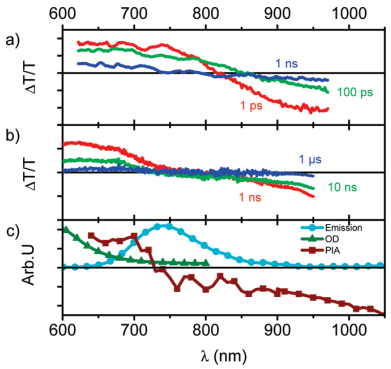

Figure 4. Transient absorption spectra for pristine PCDTBT films between 1 ps and 4.5 ns (panel a) and 1 ns to 4.5 μs (panel b). The short-time pump fluence was 7.1 μJ cm^{-2}, and the long-time pump fluence was 37 μJ cm^{-2}. (Panel c) Steady-state absorption and photoluminescence spectra and the quasi-steady-state PIA spectrum of pristine PCDTBT.

demonstrated that disorder on such a scale significantly influences device performance.[34] We will see later that this large broadening due to significant energetic disorder also plays a role in the kinetics of charge carriers formed in blends.

Figure 4 shows the short-time (fs−ns) and long-time (ns−μs) transient absorption spectra of the same pristine polymer film as well as the steady-state absorption, PL and PIA spectrum for comparison. Let us first discuss the short-time TA spectra shown in the upper panel of Figure 4. The early time spectra consist of a positive TA signal extending to shorter wavelengths, a time-dependent zero-crossing, and a broad negative TA signal extending to longer wavelengths than detected. The positive TA feature can be attributed to a superposition of the ground-state bleaching (GSB) and stimulated emission (SE) of the polymer, since in this spectral region the absorption and fluorescence of the polymer are typically observed. The latter can be attributed to photo-induced absorption mostly from singlet excitons. The SE redshifts with time in the same fashion observed in the time-resolved fluorescence measurement. The decay of the SE signal is pump intensity-dependent, indicating that higher-order processes occur at the higher-excitation fluences. However, at the two lowest-pump fluences the SE dynamics converge (see Figure 5) and can

Journal of the American Chemical Society ARTICLE

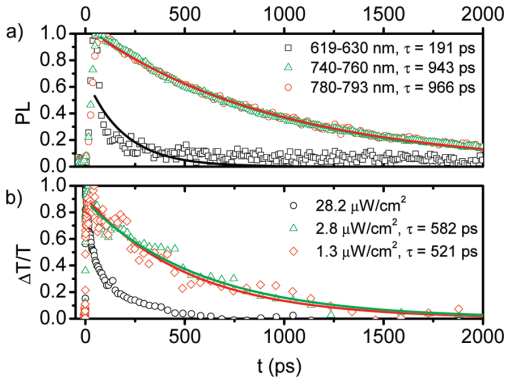

Figure 5. (a) Decay of the PL in pristine PCDTBT films obtained from Streak Camera measurements. The solid lines correspond to single exponential fits. The decay kinetics are affected by significant spectral relaxation. The decay in the lower-energy tail (i.e. longer-wavelength region of the fluorescence) is quasi-single exponential with a lifetime of ~966 ps, whereas that at shorter wavelength is a stretched exponential caused by fast energy transfer away from the high-energy states. The black line corresponds to a single-exponential decay but fails to fit the data. (b) Decay of the SE in pristine PCDTBT film averaged between 740 and 760 nm obtained from transient absorption measurements. The kinetics are fluence dependent. At the two lowest fluences measured, a single exponential fit to the data yields a SE lifetime between 500 and 600 ps.

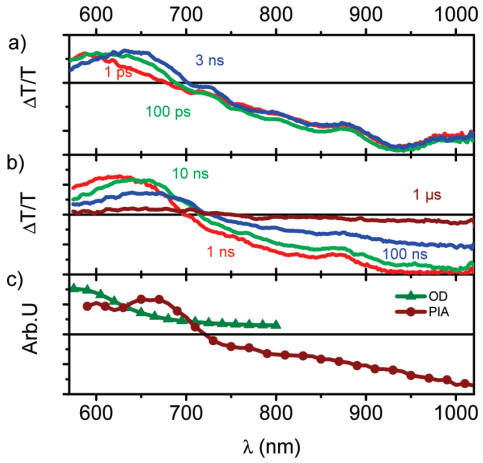

Figure 6. Transient absorption spectra of PCDTBT:PCBM(1:2) between 1 ps and 3 ns (panel a) and 1 ns and 4.5 μs (panel b) pumped at 23.7 μJ cm^{-2} and 25.7 μJ cm^{-2}, respectively. Panel c shows the ground-state absorption and PIA spectra of the blend.

be reasonably described by a single exponential with an inverse rate of ~600 ps. Comparing this value to the rates inferred from the time-resolved PL experiments, see Figure 5, demonstrates that very low excitation densities are needed in pristine PCDTBT to completely avoid bimolecular effects. This could be caused by the disorder effectively funneling excitons toward lower-energy sites increasing the local population at these low-energy areas and thereby promoting exciton−exciton interactions.

An isosbestic point (which indicates the presence of only a single excited species) is not observed in the short-delay spectra shown in the upper panel of Figure 4. Instead, the zero-crossing is time dependent and blue-shifts at longer delay times, indicating a second population is present, which is much longer-lived than the initial photoexcitations. The long-delay TA spectra shown in the middle panel of Figure 4 support this observation. Here we observe a clear isosbestic point between GSB and PA and no more SE pointing to the presence of a nonemissive species. Furthermore, the long-delay TA spectra are virtually identical to the quasi-steady-state PIA spectra shown in the bottom panel of Figure 4, which is expected, since the latter exclusively monitors long-lived excited states such as triplet states and charge carriers. We note at this point that the origin of the long-lived signal cannot be uniquely identified from the spectra, since it may be caused by triplet states or charge carriers generated in the pristine polymer. However, the decay dynamics of triplets and charge carriers are typically largely different, with triplets returning to the ground state in a monomolecular process[35,36] featuring a defined excited-state lifetime expected to be hundreds of nanoseconds to several microseconds and charge carriers typically following bimolecular or power-law recombination dynamics.[37] In fact, for the signal present in the long-delay TA spectra we observe a single-exponential decay (see Supporting Information) with a lifetime on the order of 2−3 μs and therefore assign this signal to triplet states. It is noteworthy to mention the similarity of the pristine PCDTBT photophysics to the processes recently reported for pristine films of regiorandom poly(3-hexylthiophene), where intersystem crossing from the singlet to the triplet state was observed by us and others.[11,38] To sum up, we note that pristine PCDTBT exhibits typical features of an energetically disordered conjugated polymer with a broad density of states, allowing for pronounced spectral relaxation of excited states. A fraction of the primary photoexcitations undergoes intersystem crossing to the triplet state. However, the absolute value of triplet state formation remains unknown, since the cross sections of the individual excited states have not been determined.

4.3. Photophysics of PCDTBT:PCBM Blends. *4.3.1. Charge Generation and Relaxation.* In Figure 6 we present results of transient absorption experiments on as-cast PCDTBT:PCBM (1:2) blends. Panel a shows the time range from 1 ps to 3 ns, and panel b longer delay times ranging from 1 ns up to 5 μs. In both time frames three distinct features can be observed, a positive signal from 550 to 700 nm, a time-dependent zero-crossing, and a broad negative signal between 700 and 1100 nm (upper limit of our silicon detector). Comparing panels a and b (Figure 6) with the steady-state measurements shown in panel c reveals that the positive change in transmission at smaller wavelengths is caused by the bleaching of the ground state, as it is coincident with the absorption spectrum in this wavelength range shown in panel c (Figure 6). The blue curve in panel c is obtained from PIA spectroscopy and indicates the existence of long-lived excited states. This signal is attributed to charge carriers because in the blend singlet excitons are quenched by electron transfer from the polymer to the PCBM with a rate much faster than that of triplet formation, so that very few triplets can be expected, if formed at all. The extended near-infrared wavelength range of the PIA also suggests that the PA of charge carriers expands further into the infrared at least up to 1800 nm which is the detection limit of our germanium detector (see Supporting Information). The absence of a positive signal between 700 and 850 nm in the short-delay TA measurements indicates that the SE, which could be observed

Journal of the American Chemical Society ARTICLE

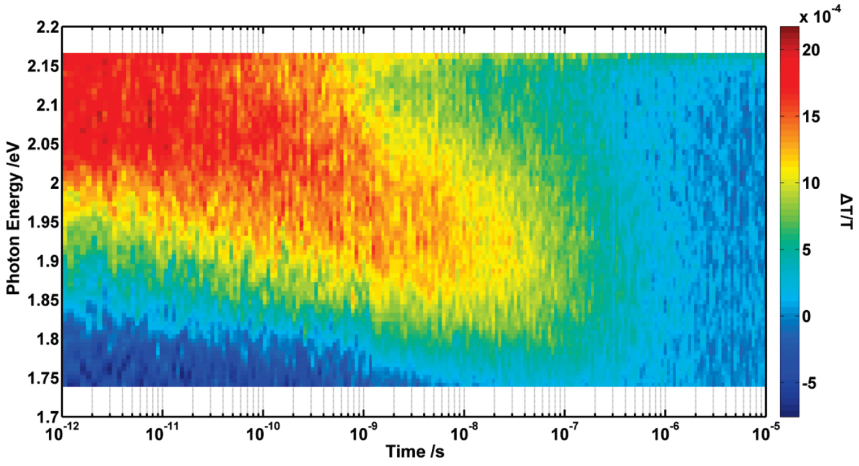

Figure 7. Spectral relaxation of the ground-state bleaching in PCDTBT:PCBM blend films after photoexcitation. Note that the bleaching is caused by charge carriers that relax in the blend film. The image is a straight combination of the short-delay (ps−ns) and the long delay (ns−ms) transient absorption data without any additional scaling parameter.

in the pristine polymer film, is strongly quenched due to (ultra)fast electron transfer from PCDTBT to PCBM, as expected for intimately mixed photovoltaic blends. We also note that the initial signal intensity scales linearly with the pump fluence (see Supporting Information) which shows that nonlinear processes caused by the high excitation fluence are virtually absent in the blend in contrast to the pristine polymer films, where an intensity dependence of the decay dynamics has been observed. This is a consequence of the ultrafast charge transfer process, which effectively suppresses exciton−exciton annihilation or exciton−charge annihilation, which can be observed, if excitons are not instantaneously quenched, as recently shown by us for annealed P3HT:PCBM blends.[11] In the region of the PA the signal intensity is almost constant over the entire time range of 3 ns for the pump fluence shown. At smaller wavelengths, where the bleaching is dominant, the signal similarly shows almost no decay, but interestingly does exhibit a spectral relaxation of about 80 meV during the first 3 ns. This relaxation of the ground-state bleaching, indicating that the hole polarons on the polymer shift to lower and lower energy sites, continues up to ∼150 ns as can be deduced from the long delay measurements, shown in panel b (Figure 6)). The zero-crossing finally coincides with the spectral position obtained from the quasi-steady-state PIA, shown in panel c (Figure 6)). The long-lived signal can be ascribed to charge carriers generated in the blend that recombine with a density dependent rate that at the fluences typical for transient absorption leads to decays varying from nanoseconds to microseconds, depending on the excitation intensity. The long time scale significant relaxation of these hole polarons is rather unusual for polymer:PCBM blends and has not yet been reported. One reason may be that the relevant time range from 1 ns to several hundred nanoseconds is rarely observed in transient absorption experiments to present. We further emphasize that only a broadband spectral detection of the transient absorption signals in the relevant time scale allows observing the relaxation process, which could easily be misinterpreted as a decay process if single-wavelength detection schemes were employed. Figure 7 displays the entire relaxation in a matrix image of the transient absorption data. The peak of the ground-state bleaching relaxes from approximately 2.1 eV at short time to 1.9 eV after ∼150 ns. This relaxation of ∼200 meV is surprisingly large and clearly indicates that energetic disorder significantly affects the charge carriers on the PCDTBT chains. In fact, the observed shift is even larger than observed for the excitons in pristine PCDTBT, suggesting that, if disorder has a similar broadening effect on the DOS for excitons and holes, disorder may be enhanced in the blend film most probably caused by the large fraction of PCBM molecules present in the blend. The observed spectral relaxation also indicates that the free charge carriers created immediately after photoexcitation are initially hot and tend to relax to states of lower energy within the DOS. This can be understood in terms of diffusion away from a rather disordered interfacial region, which intrinsically is of higher energy, into the bulk of the polymer, which provides better order and thus states of lower energy.

4.3.2. Charge Carrier Recombination Dynamics. In the following we analyze more closely the decay dynamics of the TA signals of PCDTBT:PCBM and find that an analytical model developed to describe charge recombination in prototypic P3HT:PCBM blends[11] also accurately describes the behavior of the current system. From this analytical model we evaluate (i) the branching ratio of geminate versus nongeminate recombination (which is equal to the branching ratio between CT and ultrafast free charge generation), (ii) the geminate recombination rate constant, (iii) the nongeminate recombination coefficient, and (iv) the order of nongeminate recombination.

Since the GSB is obscured by spectral relaxation as described above, the dynamics are strongly wavelength dependent. Therefore, in order to purely track the kinetics of the charge population we consider instead the red part of the PA signal averaged from 865 to 1000 nm which is undisturbed by spectral relaxation. The short-time decay dynamics of the PA are intensity dependent; however, at the lowest-excitation intensities used in our TA experiments the dynamics obtained after excitation at 532 nm converge and level off at ∼90% of the initial signal intensity after about 3 ns (see Supporting Information). A monoexponential fit to the early time 10% decay of this reveals a decay rate of $k = 4.5 \times 10^8\ s^{-1}$, corresponding to a lifetime of ∼2.2 ns, which we attribute to intensity-independent geminate recombination of

Journal of the American Chemical Society ARTICLE

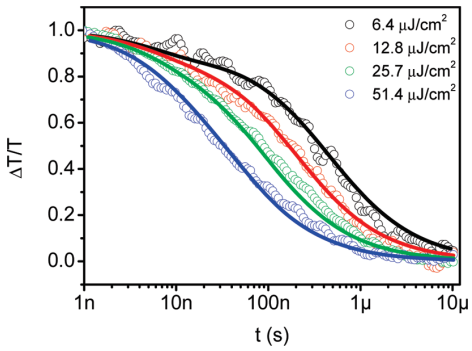

Figure 8. Normalized decay dynamics (ns−ms setup) of the charge-induced absorption between 865 and 1000 nm for different pump fluences. Note the faster decay at higher fluences due to accelerated nongeminate recombination of free charge carriers. The solid lines represent fits to our analytical model of charge recombination.

interfacial CT states. Interestingly, the decay rate and thus the CT-state lifetime is very similar to that observed previously in regiorandom P3HT:PCBM blends, as-cast (unannealed) regioregular P3HT:PCBM blends,[11,12] and also some polymer:polymer blends,[39] indicating that nanosecond CT-state recombination is not unusual, and may even be rather general in photovoltaic blends. The short time decay dynamics are also unaffected by annealing of the samples, indicating that the photophysical processes do not significantly change when the blends are annealed in line with the insignificant impact of annealing on the device efficiency (see Supporting Information).

In Figure 8 we present the decay traces of the PA signal obtained from long-delay TA measurements at pump energies between 6.4 μJ cm^{-2} and 51.4 μJ cm^{-2}. The decay profiles are intensity-dependent, indicating nongeminate recombination occurs in the blend on a time scale of several nanoseconds to tenths of microseconds. The solid lines shown in Figure 8 present fits according to a recently suggested model for charge recombination, which we briefly introduce in the following. The key aspect of the model is that dissociation of the initially formed strongly bound Frenkel-type singlet excitons leads to two population pools, one being interfacial charge-transfer (CT) states and the other one free charge carriers. The ultrafast exciton dissociation, i.e. the formation of CT states and free charge carriers, is not resolved in our experiment due to the limited instrument response time (~100 fs), and thus only the decay of each species is considered. The rate equations describing the population dynamics in the system are shown in eqs 1, 2, and 3.

$$\frac{dCT}{dt} = -k_{CT\rightarrow GS}CT \quad (1)$$

$$\frac{d(SSC)}{dt} = -\gamma SSC^{\lambda+1} \quad (2)$$

$$\frac{dGS}{dt} = k_{CT\rightarrow GS}CT + \gamma SSC^{\lambda+1} \quad (3)$$

The bound charge carriers (CT states) decay monomolecularly to the ground state (GS) with a decay rate $k_{CT\rightarrow GS}$. The spatially separated (free) charge carriers (SSC) decay with the recombination rate γ and the recombination order of λ. Therefore, the ground state is populated via two decay channels, either from interfacial CT states or from nongeminate recombination of free charge carriers. The solution of the system of differential equations is presented in eqs 4, 5, and 6

$$CT(t) = N_0(1-f)\exp(-k_{CT\rightarrow GS}t) \quad (4)$$

$$SSC(t) = (\lambda\gamma t + (fN_0)^{-\lambda})^{-1/\lambda} \quad (5)$$

$$GS(t) = N_0(1-f)(1-[\exp(-k_{CT\rightarrow GS}t)]) + N_0 f - (\lambda\gamma t + (fN_0)^{-\lambda})^{-1/\lambda} \quad (6)$$

where N_0 is the initial excited state density and f the fraction of nongeminate recombination.

The solution of the rate equations is used to globally fit the recombination dynamics at all the excitation intensities measured. As described above we used the spectral region of the charge-induced absorption to measure the total population of charge carriers and assumed that the cross sections of a charge in a CT state and a free charge are the same. The initial excited-state densities are calculated from the excitation pump fluence used to excite the blends, the blend film thickness, and its optical density at the excitation wavelength. The initial excited-state densities are the only fixed parameters of the fitting procedure. All other parameters are shared among the whole set of intensity-dependent dynamics. We found that the data can be well described by our model as can be seen in Figure 8. We also checked whether a fit based exclusively on nongeminate recombination (i.e., $f = 1$) could adequately reproduce the data, which would point to the absence of fast geminate recombination processes. However, the fit failed to reproduce the data and let to significantly larger deviations from the experimental data. The fitting parameters obtained from a global fit of the entire data set are summarized in Table 2. The model allows several details of the generation and recombination processes to be extracted. Most importantly, we can determine the branching ratio of geminate versus nongeminate recombination which also tells us the branching ratio between ultrafast free charge carrier and CT-state formation. In PCDTBT:PCBM blends we find ~89% nongeminate recombination (ultrafast free carrier formation) and ~11% geminate recombination (CT state formation), implying that only a small fraction of charge carriers are lost to geminate recombination of CT states and the majority can in principle be extracted as photocurrent. From the model we also obtain the order of the recombination process, which is found to be 2.16 and thus close to 2.0, indicating nongeminate recombination in PCDTBT:PCBM follows to a great extent typical three-dimensional Langevin-type recombination as can be expected for an intimately mixed polymer:fullerene blend. The fact that the order is slightly higher than 2 is typically explained by the density dependence of the carrier mobility further increasing the dependence of the rate of recombination on carrier density. In comparison to the single-exponential fits to the 10% decay in the short delay data we obtain a rate constant of 1.8×10^8 s^{-1}, i.e. an inverse rate of 5.6 ns, for the geminate recombination from the global fit to the long delay data. This further supports our previous finding on P3HT:PCBM that interfacial geminate recombination in photovoltaic systems is indeed on the order of a few nanoseconds, which thus appears to be of a more general validity for polymer:fullerene systems.

Journal of the American Chemical Society ARTICLE

Table 2. Parameters along with Standard Deviation Extracted from the Global Fit to the Long Delay TA Measurements

parameter	PCDTBT:PCBM	rr-P3HT:PCBM (as-cast)[a]	rr-P3HT:PCBM (annealed)[a]
$1-f$ (geminate recombination)	0.11 ± 0.01	0.32 ± 0.01	0.15 ± 0.01
f (nongeminate recombination)	0.89 ± 0.01	0.68 ± 0.01	0.85 ± 0.01
k 1/s (geminate recombination rate)	$(1.8 \pm 0.2) \times 10^8$	$(4.9 \pm 0.2) \times 10^8$	$(2.5 \pm 0.2) \times 10^8$
$\lambda + 1$ (order of nongeminate decay)	2.16 ± 0.01	2.18 ± 0.01	2.45 ± 0.01
γ $(cm^3)^{\lambda}$ s^{-1} (nongeminate decay constant)	$(5 \pm 1) \times 10^{-15}$	$(2.3 \pm 0.5) \times 10^{-15}$	$(1.9 \pm 0.3) \times 10^{-20}$
γ_{eff} cm^3 s^{-1} (effective $\lambda = 2$ bimolecular decay constant at a charge density of 5×10^{15} cm^{-3} for direct comparison with literature values)	1.7×10^{-12}	1.5×10^{-12}	1.3×10^{-12}

[a] Taken from ref 11.

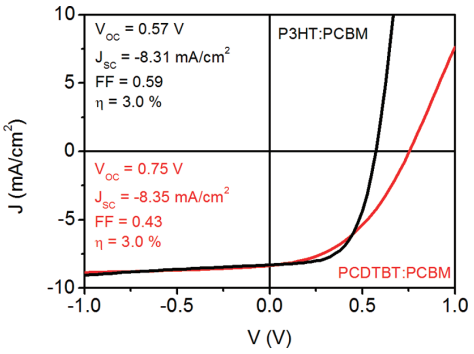

Figure 9. Comparison of the current−voltage characteristics and photovoltaic parameters of optimized regioregular P3HT:PCBM and PCDTBT:PCBM bulk heterojunction organic solar cells. The short-circuit currents are similar, while the increased V_{OC} of the latter material system is offset by a reduced fill factor resulting in very similar device efficiencies.

5. DISCUSSION

Figure 9 compares the current voltage characteristics of a PCDTBT:PCBM solar cell to that of a regioregular P3HT:PCBM solar cell, whose fabrication is described elsewhere.[22] Both cells were measured under equal illumination conditions and had similar optical densities. The short-circuit currents of the cells are almost identical, while the higher open-circuit voltage of the PCDTBT cell is offset by a poor fill factor leading to overall similar power conversion efficiencies. The fill factor of a solar cell is determined by its dark current, photocurrent, and their dependence on voltage. For typical dark currents (see Supporting Information) a large fill factor (>0.6) indicates little voltage dependence of the photocurrent while a small fill factor (<0.4) indicates significant voltage dependence of the photocurrent. The voltage dependence of the photocurrent can in principle have its origin in a field-dependent charge generation efficiency (field dependent splitting of CT states) and/or a field-dependent collection efficiency (field dependent competition between charge extraction and nongeminate recombination). In fact, the origin of the voltage dependence of the photocurrent is one of the most controversially discussed issues in the OPV community, as its understanding is of utmost importance, since it is directly related to the mechanism of charge carrier generation. Thus, any information about the early time charge generation and recombination processes of relevant donor:acceptor systems is very valuable and until now rarely reported in the literature, since the intermediate time range between 1 ns and 1 μs is experimentally difficult to observe. In the previous section we found that in the absence of field (i.e., under open-circuit conditions) only 11% of the quenched excitons form CT states. This is far too small a fraction of the entire population for a bias dependence of the CT state separation to account for the large change in photocurrent with voltage (to obtain this low fill factor the change of current with bias is much greater than 11% of the short circuit current). We therefore assert that the role of bias-dependent CT state separation cannot significantly contribute to the bias dependence of the photocurrent, which is supported by the recent work of Durrant and co-workers which shows that the field-dependence of the charge-generation efficiency in a prototypic low-bandgap polymer:fullerene photovoltaic device is negligible.[40] Furthermore, by going to low temperatures to lower the carrier mobility in P3HT:PCBM devices, we have previously shown that the increased bias dependence of the photocurrent (and therefore decreased fill factors) can be entirely explained by the higher charge-carrier densities causing bimolecular recombination to start competing with charge extraction and the bias dependence of this competition causing the bias dependence of the fill factor.[22] We therefore state that the primary limitation of the fill factor in the investigated PCDTBT:PCBM solar cells is the bias-dependent collection efficiency caused by the competition between nongeminate recombination and charge extraction rather than a field-dependent CT-state splitting as has often been suggested for related polymer:fullerene systems.[13,41] The reduction of the fill factor caused by this mechanism is more significant in the case of PCDTBT:PCBM than in P3HT:PCBM blends under standard operation conditions because the large energetic disorder of the PCDTBT creates a large population of low-energy polarons that have a limited mobility and therefore increase the carrier concentration in the device, possibly also leading to space-charge effects. This in turn leads to an increased rate of recombination that is more competitive with the rate of charge extraction. This view of the impact of energetic disorder on the recombination dynamics is qualitatively consistent with the recent suggestion of the impact of trap-assisted recombination (Shockley−Read−Hall (SRH) recombination) in PCDTBT:PCBM blends by Street and co-workers.[42] In a very recent work Cowan et al. have extended this concept and proposed that high charge carrier trap densities should lead to a decrease of the fill factor,[43] which our measurements experimentally corroborate in the model system herein reported. It appears that the recombination dynamics can be interpreted in the framework of the well-established Gaussian disorder model (GDM), which relies on

Journal of the American Chemical Society ARTICLE

energetic and positional disorder as the main parameters which influence the photophysics of conjugated materials. Within the framework of the GDM a charge carrier, which has been generated at a random site within the DOS, is expected to relax toward transport sites of lower energy, until it reaches its thermal equilibrium energy. From there it can be thermally excited toward transport sites of higher energy, which facilitate charge transport.[44−46] The relaxation is pronounced in systems, which exhibit a large energetic disorder, as is the case for the investigated PCDTBT:PCBM. A significant energetic disorder typically leads to lower charge carrier mobilities than observed for materials which have a lower energetic disorder.[46,47] The latter has been reported recently by us for the P3HT:PCBM reference system, which was shown to exhibit a comparably small energetic disorder of $\sigma = 40$ meV.[48] Thus, it is obvious from our experimental data that the present PCDTBT:PCBM system suffers from a rather broad density of states as indicated by the significant spectral shifts observed during exciton relaxation and charge carrier migration.

A straightforward consequence of the observed nanosecond geminate recombination, which we have previously shown for P3HT:PCBM and herein extend to PCDTBT:PCBM, is the breakdown of the Braun−Onsager model to explain the field-dependent photocurrents in these systems, which is in contradiction to models previously presented by Deibel and co-workers. In fact, much longer lifetimes of CT states than are directly monitored by optical spectroscopy, typically in the range of hundreds of nanoseconds or even microseconds, are required to satisfactorily reproduce the experimentally observed *IV*-curves, if a Braun−Onsager-type splitting of CT states is used to describe free carrier generation and the bias dependence of the photocurrent.[41,49−53] Therefore, we believe that ultrafast, sub-picosecond free carrier generation is a general feature of efficient polymer:fullerene photovoltaic systems that is strongly related to both energetic considerations and to the interfacial morphology of the blend. However, even if geminate recombination can be efficiently suppressed and the generation of free charge carriers approaches unity as found for the present case of PCDTBT:PCBM, other efficiency-limiting processes such as nongeminate recombination due to limited charge transport have to be overcome. We suggest that developing a further understanding of the pathways of nongeminate recombination is important to allow new material systems to reach the high fill factors achieved by P3HT:PCBM. For example the question of whether the high fill factor of P3HT:PCBM is simply a consequence of lower carrier densities in the device due to better transport, or whether the partition into more crystalline and amorphous regions allows higher carrier densities to be sustained without increasing the rate of nongeminate recombination has significant bearing on new material design and device engineering.

6. CONCLUSION

Using broadband pump−probe spectroscopy over the entire relevant time range of charge generation and recombination, we show that fast dissociation of the primary photoexcitations in as-cast PCDTBT:PCBM blends leads to the generation of free charge carriers and Coulombically bound interfacial charge-transfer states with a branching ratio of 89% free charge carriers to 11% CT states. The latter recombine monomolecularly to the ground state with a lifetime of about 2.5 ns and thus cannot contribute to the photocurrent. In fact, nanosecond time scale geminate recombination previously also demonstrated in P3HT:PCBM, appears to be a general phenomenon in polymer:fullerene blends as indicated by our present results, which calls into question the validity of models that describe the bias dependence of the photocurrent based on field-dependent Onsager−Braun-type separation of CT states that invoke CT state lifetimes longer than hundreds of nanoseconds. We note also that a field-dependent separation of the 11% of CT states could not make a large enough contribution to account for the field dependence of the experimentally observed photocurrent. We find that the large fraction of free charge carriers generated in an ultrafast process after photoexcitation recombines predominantly nongeminately on the time scale of nanoseconds to microseconds. In an operating PV device, these free charge carriers can be extracted almost quantitatively at short-circuit. However, at lower internal fields, i.e. in the typical operating range of the organic solar cell, the increased carrier density shifts the competition between carrier extraction and nongeminate recombination in favor of nongeminate recombination, which leads to a strong field dependence of the photocurrent that explains the poor fill factor of the device. This suggests that further optimization of this system should focus on increasing the rate of charge extraction, potentially by decreasing the energetic broadening of transport sites of the polymer in solid state. Also, determining the mechanism that reduces the EQE in spectral regions where the PCBM absorbs remains an open question with significant implications for the device performance.

■ ASSOCIATED CONTENT

Supporting Information. Further information about the dependence of the short circuit photocurrent on illumination intensity, spectral relaxation of the PL, the triplet decay dynamics of pristine PCDTBT, PIA measurements of pristine PCDTBT, short delay TAS measurements of PCDTBT:PCBM, and *IV*-curves together with the dark current of PCDTBT:PCBM solar cells. This material is available free of charge via the Internet at http://pubs.acs.org

■ AUTHOR INFORMATION

Corresponding Author
laquai@mpip-mainz.mpg.de; ian.howard@mpip-mainz.mpg.de; kslee@hnu.kr

■ ACKNOWLEDGMENT

This work is part of the International Research Training Group IRTG 1404 "Self-organized Materials for Optoelectronics" between Germany and Korea funded by the Deutsche Forschungsgemeinschaft (DFG). I.A.H. acknowledges a post-doctoral fellowship of the Alexander von Humboldt Foundation. R.M. and M.M. thank the Max Planck Graduate Center (MPGC) for financial support. F.L. acknowledges support from the Max Planck Society in the framework of the Max Planck Research Group funding scheme. K.S.L. also acknowledges funding of this work from Midcareer Researcher Program through NRF grant funded by the MEST (No. 2010-0000499) and the Asian Office of Aerospace and Development (AOARD 09-4045). We thank A. Becker for technical assistance. Enquiries about the PCDTBT polymer should be addressed to K.S.L., while enquiries about the photophysics should be addressed to F.L. and/or I.A.H.

REFERENCES

(1) Strobel, T.; Deibel, C.; Dyakonov, V. *Phys. Rev. Lett.* **2010**, *105*, 266602.
(2) Solarmer Energy, I. W. www.solarmer.com 2010.
(3) Chen, H.-Y.; Hou, J.; Zhang, S.; Liang, Y.; Yang, G.; Yang, Y.; Yu, L.; Wu, Y.; Li, G. *Nat. Photon* **2009**, *3*, 649–653.
(4) Howard, I. A.; Laquai, F. *Macromol. Chem. Phys.* **2010**, *211*, 2063–2070.
(5) van Bavel, S. S.; Barenklau, M.; de With, G.; Hoppe, H.; Loos, J. *Adv. Funct. Mater.* **2010**, *20*, 1458–1463.
(6) Chen, D.; Nakahara, A.; Wei, D.; Nordlund, D.; Russel, T. P. *Nano Lett.* **2010**, *11*, 7.
(7) Muller, C.; Ferenczi, T. A. M.; Campoy-Quiles, M.; Frost, J. M.; Bradley, D. D. C.; Smith, P.; Stingelin-Stutzmann, N.; Nelson, J. *Adv. Mater.* **2008**, *20*, 3510.
(8) Laquai, F.; Park, Y. S.; Kim, J. J.; Basche, T. *Macromol. Rapid Commun.* **2009**, *30*, 1203–1231.
(9) Pope, M.; Swenberg, C. E. *Electronic Processes in Organic Crystals and Polymers*; Oxford University Press: Oxford, 1999.
(10) Hertel, D.; Bässler, H. In *Organic Light Emitting Devices*; Müllen, K., Scherf, U., Eds.; Wiley-VCH: Weinheim, 2006.
(11) Howard, I. A.; Mauer, R.; Meister, M.; Laquai, F. *J. Am. Chem. Soc.* **2010**, *132*, 14866–14876.
(12) Guo, J.; Ohkita, H.; Benten, H.; Ito, S. *J. Am. Chem. Soc.* **2010**, *132*, 6154–6164.
(13) Deibel, C.; Strobel, T.; Dyakonov, V. *Adv. Mater.* **2010**, *22*, 4097–4111.
(14) Tvingstedt, K.; Vandewal, K.; Zhang, F.; Inganäs, O. *J. Phys. Chem. C* **2010**, *114*, 21824–21832.
(15) Veldman, D.; Meskers, S. C. J.; Janssen, R. A. J. *Adv. Funct. Mater.* **2009**, *19*, 1939–1948.
(16) Clarke, T. M.; Durrant, J. R. *Chem. Rev.* **2010**, *110*, 6736–6767.
(17) Braun, C. L. *J. Chem. Phys.* **1984**, *80*, 4157–4161.
(18) Onsager, L. *Phys. Rev.* **1938**, *54*, 554–557.
(19) Wojcik, M.; Tachiya, M. *J. Chem. Phys.* **2009**, *130*, 104107.
(20) Wojcik, M.; Michalak, P.; Tachiya, M. *Appl. Phys. Lett.* **2010**, *96*, 162102.
(21) Shuttle, C. G.; Hamilton, R.; O'Regan, B. C.; Nelson, J.; Durrant, J. R. *Proc. Natl. Acad. Sci. U.S.A.* **2010**, *107*, 16448–16452.
(22) Mauer, R.; Howard, I. A.; Laquai, F. d. r. *J. Phys. Chem. Lett.* **2010**, *1*, 3500–3505.
(23) Lee, J.; Vandewal, K.; Yost, S. R.; Bahlke, M. E.; Goris, L.; Baldo, M. A.; Manca, J. V.; Voorhis, T. V. *J. Am. Chem. Soc.* **2010**, *132*, 11878–11880.
(24) Park, S. H.; Roy, A.; Beaupre, S.; Cho, S.; Coates, N.; Moon, J. S.; Moses, D.; Leclerc, M.; Lee, K.; Heeger, A. J. *Nat. Photon* **2009**, *3*, 297.
(25) Sun, Y.; Seo, J. H.; Takacs, C. J.; Seifter, J.; Heeger, A. J. *Adv. Mater.* **2011**, *23*, 1679–1683.
(26) Blouin, N.; Michaud, A.; Leclerc, M. *Adv. Mater.* **2007**, *19*, 2295.
(27) Chu, T. Y.; Alem, S.; Verly, P. G.; Wakim, S.; Lu, J. P.; Tao, Y.; Beaupre, S.; Leclerc, M.; Belanger, F.; Desilets, D.; Rodman, S.; Waller, D.; Gaudiana, R. *Appl. Phys. Lett.* **2009**, *95*, 063304.
(28) Wakim, S.; Beaupre, S.; Blouin, N.; Aich, B. R.; Rodman, S.; Gaudiana, R.; Tao, Y.; Leclerc, M. *J. Mater. Chem.* **2009**, *19*, 5351–5358.
(29) Street, R. A.; Cowan, S.; Heeger, A. J. *Phys. Rev. B* **2010**, *82*, 121301.
(30) Tong, M.; Coates, N. E.; Moses, D.; Heeger, A. J.; Beaupre, S.; Leclerc, M. *Phys. Rev. B: Condens. Mater. Phys.* **2010**, *81*, 125210.
(31) Banerji, N.; Cowan, S.; Leclerc, M.; Vauthey, E.; Heeger, A. J. *J. Am. Chem. Soc.* **2010**, *132*, 17459–17470.
(32) Baek, N. S.; Hau, S. K.; Yip, H.-L.; Acton, O.; Chen, K.-S.; Jen, A. K. Y. *Chem. Mater.* **2008**, *20*, 5734–5736.
(33) Burkhard, G. F.; Hoke, E. T.; Scully, S. R.; McGehee, M. D. *Nano Lett.* **2009**, *9*, 4037–4041.
(34) Groves, C.; Blakesley, J. C.; Greenham, N. C. *Nano Lett.* **2010**, *10*, 1063–1069.
(35) Benson-Smith, J. J.; Ohkita, H.; Cook, S.; Durrant, J. R.; Bradley, D. D. C.; Nelson, J. *J. Chem. Soc., Dalton Trans.* **2009**, 10000–10005.
(36) Ohkita, H.; Cook, S.; Ford, T. A.; Greenham, N. C.; Durrant, J. R. *J. Photochem. Photobiol., A* **2006**, *182*, 225–230.
(37) Clarke, T. M.; Jamieson, F. C.; Durrant, J. R. *J. Phys. Chem. C* **2009**, *113*, 20934–20941.
(38) Guo, J.; Ohkita, H.; Benten, H.; Ito, S. *J. Am. Chem. Soc.* **2009**, *131*, 16869–16880.
(39) Hodgkiss, J. M.; Campbell, A. R.; Marsh, R. A.; Rao, A.; Albert-Seifried, S.; Friend, R. H. *Phys. Rev. Lett.* **2010**, *104*, 177701.
(40) Jamieson, F. C.; Agostinelli, T.; Azimi, H.; Nelson, J.; Durrant, J. R. *J. Phys. Chem. Lett.* **2010**, *1*, 3306–3310.
(41) Blom, P. W. M.; Mihailetchi, V. D.; Koster, L. J. A.; Markov, D. E. *Adv. Mater.* **2007**, *19*, 1551–1566.
(42) Street, R. A.; Schoendorf, M.; Roy, A.; Lee, J. H. *Phys. Rev. B* **2010**, *81*, 205307.
(43) Cowan, S. R.; Street, R. A.; Cho, S. N.; Heeger, A. J. *Phys. Rev. B* **2011**, *83*, 035205.
(44) Hertel, D.; Bassler, H. *ChemPhysChem* **2008**, *9*, 666–688.
(45) Arkhipov, V. I.; Fishchuk, I. I.; Kadashchuk, A.; Bässler, H. In *Photophysics of Molecular Materials*; Lanzani, G., Ed.; Wiley-VCH: Weinheim, 2006; pp 261−366.
(46) Laquai, F.; Wegner, G.; Bassler, H. *Philos. Trans. R. Soc. London, Ser. A* **2007**, *365*, 1473–1487.
(47) Laquai, F.; Wegner, G.; Im, C.; Bassler, H.; Heun, S. *J. Appl. Phys.* **2006**, 99.
(48) Mauer, R.; Kastler, M.; Laquai, F. *Adv. Funct. Mater.* **2010**, *20*, 2085–2092.
(49) Mihailetchi, V. D.; Koster, L. J. A.; Hummelen, J. C.; Blom, P. W. M. *Phys. Rev. Lett.* **2004**, *93*, 216601.
(50) Moet, D. J. D.; Lenes, M.; Morana, M.; Azimi, H.; Brabec, C. J.; Blom, P. W. M. *Appl. Phys. Lett.* **2010**, *96*, 213506.
(51) Moet, D. J. D.; Lenes, M.; Kotlarski, J. D.; Veenstra, S. C.; Sweelssen, J.; Koetse, M. M.; de Boer, B.; Blom, P. W. M. *Org. Electron.* **2009**, *10*, 1275–1281.
(52) Deibel, C.; Strobel, T.; Dyakonov, V. *Phys. Rev. Lett.* **2009**, *103*, 036402.
(53) Limpinsel, M.; Wagenpfahl, A.; Mingebach, M.; Deibel, C.; Dyakonov, V. *Phys. Rev. B* **2010**, *81*, 085203.

Supporting Information

Ultrafast Exciton Dissociation Followed by Nongeminate Charge Recombination in PCDTBT:PCBM Photovoltaic Blends

Fabian Etzold, Ian A. Howard, Ralf Mauer, Michael Meister, Tae-Dong Kim, Kwang-Sup Lee*, Nam Seob Baek, and Frédéric Laquai**

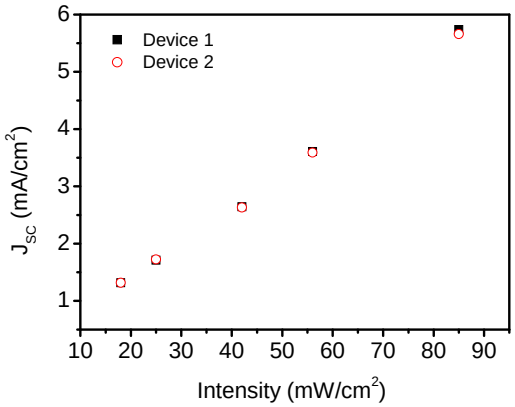

Figure S1. Dependence of the short circuit photocurrent density on the illumination intensity for two typical PCDTBT:PCBM (1:2) photovoltaic devices. Note the linear increase of the photocurrent with increasing illumination intensity.

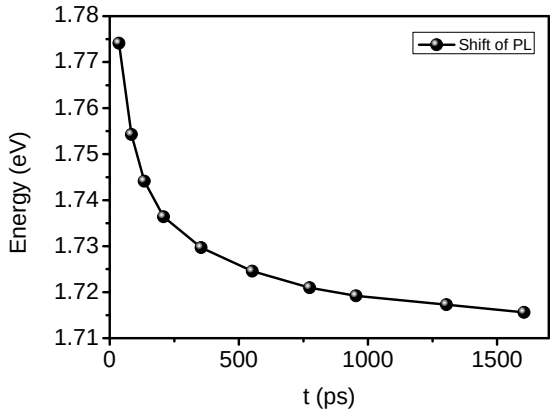

Figure S2. Spectral shift of the photoluminescence (PL) emission maximum obtained from streak camera measurements. The line follows the PL peak position at different delay times and is a guide to the eye.

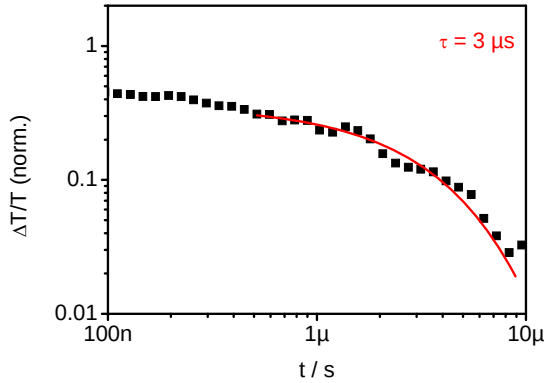

Figure S3. Long-delay transient absorption (TA) dynamics in pristine PCDTBT films integrated in the spectral region between 950 -960 nm. The solid line indicates a monoexponential fit to the data yielding a lifetime of 3 µs.

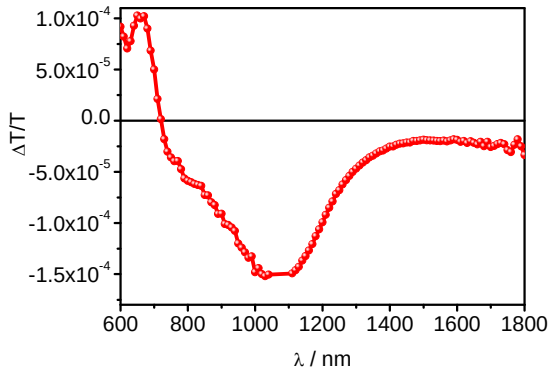

Figure S4. Photoinduced absorption spectrum of a PCDTBT:PCBM blend. The blend shows a ground state bleaching below 700 nm and a broad photoinduced absorption peaking around 1050 nm, which indicates the presence of charges in the blend. The maximum is truncated due to a filter change in this spectral region.

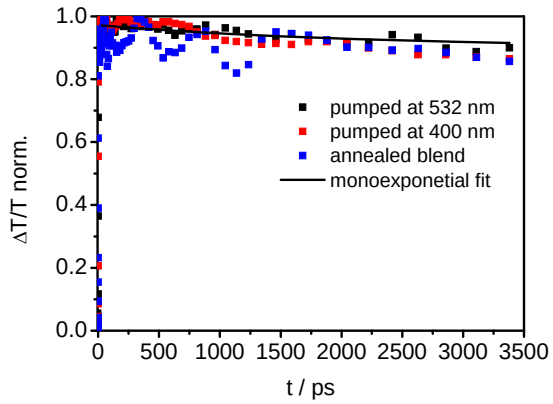

Figure S5. Short delay dynamics of the PA obtained from transient absorption spectroscopy on as-cast PCDTBT:PCBM blends and annealed blends (50 min @ 140°C) averaged between 865 – 1000 nm. The signal shows a decay of approximately 10 % in 3 ns. A monoexponential fit yields a lifetime of 2.2 ns.

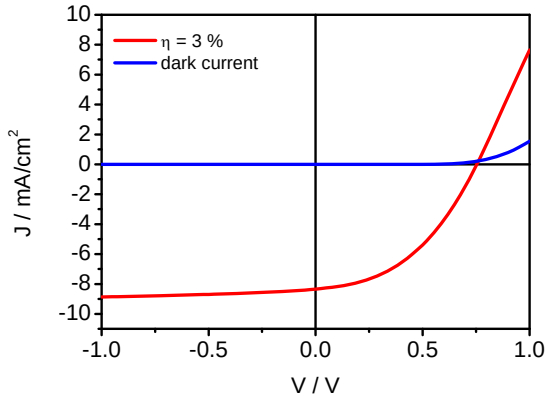

Figure S6. The current density – voltage (J-V) characteristics of PCDTBT:PCBM(1:2) solar cells under solar illumination conditions of 90 mW/cm^2 and the dark current of the same device.

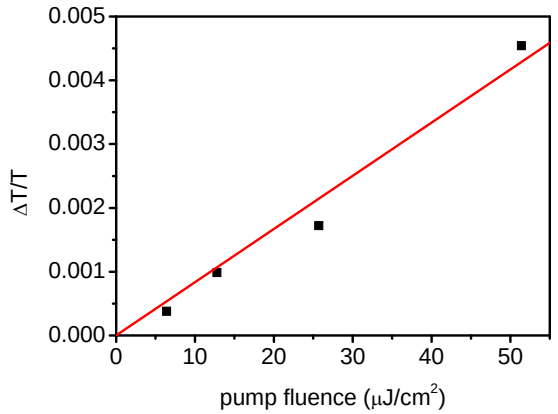

Figure S7. Excitation density dependence of the initial PA between 865 – 1000nm in PCDTBT:PCBM measured with the long-time transient absorption setup. The diagram shows that the TA measurements were carried out in the linear regime of the excitation density dependence with signal heights smaller than 0.005.

Calculation of the effective recombination coefficient

To calculate the effective Langevin recombination coefficient (λ=2) for charge carrier densities corresponding to an illumination with one sun ($n = 5 \times 10^{-15}$ 1/cm^3), we used the extracted fit values for γ and λ, so that

$$\gamma_{eff} n^2 - \gamma_{fit} n^{\lambda+1}$$

$$\gamma_{eff} = \gamma_{fit} n^{\lambda-1} = 1.7 \times 10^{-12} \frac{cm^3}{s}.$$

4.2 The Effect of Solvent Additives on Morphology and Excited-State Dynamics in PCPDTBT:PCBM Photovoltaic Blends

JACS
JOURNAL OF THE AMERICAN CHEMICAL SOCIETY
Article
pubs.acs.org/JACS

The Effect of Solvent Additives on Morphology and Excited-State Dynamics in PCPDTBT:PCBM Photovoltaic Blends

Fabian Etzold,[†] Ian A. Howard,[†] Nina Forler,[§] Don M. Cho,[‡] Michael Meister,[†] Hannah Mangold,[†] Jie Shu,[§] Michael Ryan Hansen,[§] Klaus Müllen,[‡] and Frédéric Laquai*,[†]

[†]Max Planck Research Group for Organic Optoelectronics, [§]Polymer Spectroscopy Group, and [‡]Synthetic Chemistry Group, Max Planck Institute for Polymer Research, Ackermannweg 10, 55128 Mainz, Germany

Supporting Information

ABSTRACT: The dependence of the thin film morphology and excited-state dynamics for the low-bandgap donor−acceptor copolymer poly[2,6-(4,4-bis-(2-ethylhexyl)-4*H*-cyclopenta[2,1-b;3,4-b′]-dithiophene)-*alt*-4,7-(2,1,3-benzothiadiazole)] (PCPDTBT) in pristine films and in blends (1:2) with [6,6]-phenyl-C_{61}-butyric acid methyl ester (PCBM) on the use of the solvent additive 1,8-octanedithiol (ODT) is studied by solid-state nuclear magnetic resonance (NMR) spectroscopy and broadband visible and near-infrared pump−probe transient absorption spectroscopy (TAS) covering a spectral range from 500−2000 nm. The latter allows monitoring of the dynamics of excitons, bound interfacial charge-transfer (CT) states, and free charge carriers over a time range from femto- to microseconds. The broadband pump−probe experiments reveal that excitons are not only generated in the polymer but also in PCBM-rich domains. Depending on the morphology controlled by the use of solvent additives, polymer excitons undergo mainly ultrafast dissociation (<100 fs) in blends prepared without ODT or diffusion-limited dissociation in samples prepared with ODT. Excitons generated in PCBM diffuse slowly to the interface in both samples and undergo dissociation on a time scale of several tens of picoseconds up to hundreds of picoseconds. In both samples a significant fraction of the excitons creates strongly bound interfacial CT states, which exhibit subnanosecond geminate recombination. The total internal quantum efficiency loss due to geminate recombination is estimated to be 50% in samples prepared without ODT and is found to be reduced to 30% with ODT, indicating that more free charges are generated in samples prepared with solvent additives. In samples prepared with ODT, the free charges exhibit clear intensity-dependent recombination dynamics, which can be modeled by Langevin-type recombination with a bimolecular recombination coefficient of 6.3×10^{-11} cm^3 s^{-1}. In samples prepared without ODT, an additional nanosecond recombination of polaron pairs is observed in conjunction with an increased intensity-independent trap-assisted nongeminate recombination of charges. Furthermore, a comparison of the triplet-induced absorption spectra of PCPDTBT with the charge-induced absorption in PCPDTBT:PCBM blends reveals that triplets have a very similar excited-state absorption spectrum compared to the free charge carriers, however, in contrast have a distinct intensity-independent lifetime. Overall, our results suggest that whether free charges or strongly bound CT states are created upon dissociation of excitons at the PCPDTBT:PCBM interface is determined instantaneously upon exciton dissociation and that once formed strongly bound CT states rapidly recombine and thus are unlikely to dissociate into free charges. The observation of a significantly larger bimolecular recombination coefficient than previously determined for poly(3-hexylthiophen-2,5-diyl):PCBM (P3HT:PCBM) and PCDTBT:PCBM samples indicates that nongeminate recombination of free charges considerably competes with charge extraction in PCPDTBT:PCBM photovoltaic devices.

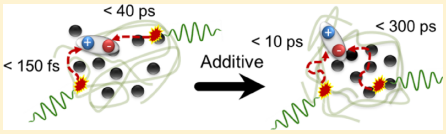

1. INTRODUCTION

Bulk heterojunction (BHJ) organic solar cells based on thin films of interpenetrating polymer:fullerene networks are an emerging technology that has the potential to provide a low-cost alternative to conventional silicon-based photovoltaic devices. Organic materials can easily be solution processed enabling large-area production of solar cells, for instance by roll-to-roll printing techniques.[1,2] Their efficiency, however, is still unsatisfactory for mass production leaving space for further improvements, if the efficiency-limiting processes can be understood and reliable structure−property relations can be developed.

In BHJ photovoltaic devices absorption of photons by one of the blend components leads to the formation of excitons, which undergo dissociation at the polymer:fullerene interface. The products of exciton dissociation are unbound (free) charge carriers and bound interfacial polaron pairs. In this context delocalization of the intermediate "hot" polaron pairs created during the exciton dissociation process at the interface has recently been shown to help overcome the exciton binding energy.[3] While the free charges can successively be extracted as photocurrent or undergo recombination according to a nongeminate (often also termed bimolecular) recombination pathway, the intermediate polaron pairs either can relax into strongly bound charge-transfer (CT) states that recombine to

Received: April 5, 2012
Published: May 21, 2012

the ground state by a monomolecular (geminate) recombination process or could potentially split by a field- or temperature-assisted process (often described by the Onsager−Braun model), yielding free charges that can additionally contribute to the total photocurrent. However, it is difficult, if not impossible, to judge from the shape of the device $J-V$ curve, whether nongeminate recombination in competition with charge extraction or a field-assisted charge liberation from polaron pairs or a combination of both governs the bias-dependence of the photocurrent and thus determines the device fill factor. We and others have recently shown for the reference system poly(3-hexylthiophen-2,5-diyl):[6,6]-phenyl-C_{61}-butyric acid methyl ester (P3HT:PCBM) that nongeminate recombination in competition with charge extraction determines the bias dependence of the photocurrent in these devices and that free charge generation is neither a temperature- nor a field-activated process in optimized devices.[4−6] However, it appears that P3HT:PCBM is rather an exception than a prototypic system due to the high crystallinity of the P3HT network facilitating free charge generation and fast extraction, while simultaneously suppressing nongeminate recombination.[6] In order to develop a broader picture, it is thus important to better understand these processes in other systems, which are less ordered than the exceptional and well-studied case of P3HT:PCBM. In particular low-bandgap alternating donor−acceptor (DA) copolymers have emerged as promising electron-donor materials and have already proven their potential in highly efficient bulk heterojunction organic solar cells in combination with fullerene derivatives as electron acceptors.[7−11] Their absorption extends further into the red to near-infrared (NIR) spectral region of the solar spectrum, and thus low-energy photons are more efficiently harvested than, for instance, in P3HT:PCBM, for which typically only moderate efficiencies of around 3−4% are obtained, and the maximum efficiency is limited to 4.4% due to the limited overlap with the solar illumination.[12] In the OPV community the low-bandgap polymer poly[2,6-(4,4-bis-(2-ethylhexyl)-4H-cyclopenta[2,1-b;3,4-b′]-dithiophene)-alt-4,7-(2,1,3-benzothiadiazole)] (PCPDTBT) has attracted particular interest, since its absorption spectrum extends beyond 800 nm, and efficiencies as high as 5.5% have been demonstrated under optimized conditions.[7,13,14] Nonetheless, PCPDTBT-based devices often suffer from a low fill factor and in general have a lower internal quantum efficiency in comparison to P3HT:PCBM devices, i.e., the efficiency gain due to enhanced photon harvesting in the red part of the solar illumination is in part offset by enhanced loss processes. Introducing solvent additives to control the blend intermixing and morphology during the spin-coating process has been shown to significantly increase the device performance, which makes PCPDTBT an appealing study subject, since the efficiency increase should be reflected in a significant change of the photophysical properties.[7] The impact of solvent additives on the morphology has already been intensively investigated by structural probes, such as GISAXS, etc.[15,16] From a morphological viewpoint the superior device efficiency obtained from blends processed with additives has been attributed to enhanced demixing. This reduces the interfaces for recombination of charges and leads to an increased structural order within the polymer-rich domains, facilitating fast charge transport and extraction. However, a conclusive picture of the entire cascade of the photophysical processes leading to photocurrent generation and the changes introduced by the film processing parameters, such as additives, is still lacking.

Blom and co-workers have recently assigned the increased efficiency of PCPDTBT:PCBM blends processed with additives to reduced geminate recombination losses by fitting the experimentally obtained $J-V$ curves of devices using a drift-diffusion model for free charges and an additional Onsager-Braun type CT-state dissociation mechanism.[17] From their model they estimated the lifetime of interfacial CT states to be from 500 ns to 3 μs. Recent work by us and others has shown that the inverse rate of CT-state recombination is rather in the range of nanoseconds, and therefore the CT-state recombination rates extracted from modeling $J-V$ curves should rather be considered a fitting parameter than a rate related to a photophysical process. Very recently, McNeill and co-workers demonstrated that charge-carrier trapping and, thus, the dwell time of free charge carriers are reduced in devices processed with additives by measuring the transient photovoltage characteristics of PCPDTBT:PCBM cells, which indicates that the efficiency of PCPDTBT:PCBM cells prepared without additives is hampered by trap-assisted nongeminate recombination in competition with charge extraction.[18] Cho et al. measured the charge-carrier mobility in bipolar field-effect transistors (BIFETs) and found a higher mobility in blends processed with additives.[19] In contrast, time-of-flight studies, which probe the bulk mobility and thus deliver a more meaningful estimate of the mobility in photovoltaic devices, did not show a significant increase of the bulk mobility upon using additives.[20] Neher and co-workers have very recently reported time-delayed collection field experiments on PCPDTBT:PCBM blends.[21] They demonstrated that the yield of free charges increases upon applying a prebias during excitation indicative of a field-dependent charge-generation process, which was found to be more pronounced in samples prepared without 1,8-octanedithiol (ODT). Furthermore, they observed a negative field dependence of the hole mobility, which was assigned to spatial disorder, and a large bimolecular recombination coefficient on the order of 10^{-11} cm^3 s^{-1}, indicating fast nongeminate recombination of free charges. The observation of a field-dependent charge generation is in stark contrast to earlier results reported by Durrant and co-workers. They used bias-dependent transient absorption spectroscopy to monitor the amplitude and dynamics of the charge-induced absorption from 100 ns onward and found both the amplitude and dynamics to be independent of an external electric field.[22] In samples prepared with an additive, the amplitude of the charge-induced absorption was found to be increased by a factor of 1.5, pointing toward a more efficient generation of free charges in samples prepared with additives. However, the pump fluences used were typically higher than 8 $\mu J/cm^2$, at which nongeminate recombination of free charges within the first 100 ns can be expected due to their high concentration. In an earlier study Durrant and co-workers probed the delayed recombination of free charges by means of single wavelength TA spectroscopy and came to the conclusion that the presence of solvent additives changes the ionization potential (IP) of the polymer and thereby also the free energy of the charge transfer process, resulting in an increased yield of free polarons upon processing with additives.[23] In general, optical probes, such as time-resolved spectroscopy and in particular pump−probe spectroscopy, are very powerful tools to study the dynamics of charge generation and recombination and to develop a general picture of the photophysical processes, if the entire relevant

spectral and dynamic range can be investigated. For example, Hwang et al. have used (ultrafast) transient absorption spectroscopy to elucidate the early time (up to 1500 ps) charge generation and recombination dynamics in PCPDTBT:PCBM. They reported ultrafast (<200 fs) electron transfer at the polymer:fullerene interface resulting in the formation of mobile carriers (free polarons) and interfacial CT states, the latter either recombining to the ground state (<600 ps) or dissociating into free charges in less than 20 ps. In a subsequent study by Heeger and co-workers the effect of solvent additives and blend composition was investigated, and the authors concluded that films processed with additives and those containing larger PCBM fractions showed enhanced splitting of the interfacial CT states.[20,24] A severe drawback of these studies is the very high fluences (up to 200 $\mu J/cm^2$) used in their experiments, necessary to achieve a reasonable signal-to-noise ratio. Furthermore, Grancini et al. have recently investigated the effect of the fraction of PCBM and of the solvent additive on the charge generation and recombination dynamics and concluded that charge generation is possible via direct hot exciton dissociation and an Onsager-like dissociation process. They covered the time range up to 400 ps only, so that a clear picture of the long time recombination dynamics is still missing.[25] Jarzab et al. have recently determined the (fluorescence) lifetime of the emissive interfacial CT states (referred to as CT excitons) to be 480 ps by NIR streak camera measurements in samples prepared without additives.[26,27] They concluded that the emissive CT states observed by photoluminescence spectroscopy are strongly bound and cannot be split by a field- or temperature-activated process into free charges and thus rather recombine to the ground state. However, their bias-dependent photoluminescence spectra showed a reduction of the amplitude of the CT-emission indicating a bias-induced variation of the initial population of the CT states not resolved by the time resolution of their experiment. Very recent work by Deschler et al. showed that the initial fraction of free charges created directly after photoexcitation can be increased in PCPDTBT:PCBM films by deliberate doping, implying that the fate of the primary photoexcitation, i.e., whether free charges or CT states are formed upon exciton dissociation, is determined on the ultrafast time scale.[28] The fluorescence lifetime of the CT excitons was determined to be 300 ps in line with the results by Jarzab et al. Janssen and co-workers have observed that the interfacial CT state can also undergo intersystem crossing to populate the polymer's triplet state and that the morphology obtained by processing in the presence of solvent additives can suppress this additional loss channel.[29]

In the present work we used solid-state NMR techniques to investigate the morphology of thin films of PCPDTBT:PCBM processed with and without the solvent additive ODT and broadband visible to NIR (vis-NIR) pump−probe spectroscopy to optically probe the charge generation and recombination dynamics. In contrast to earlier ultrafast pump−probe and microsecond transient absorption studies, we also report the very important time range between 2 and 100 ns and thus are able to monitor the full recombination dynamics and accurately determine the ratio between monomolecular and non-monomolecular recombination. Additionally, we present not only pump−probe spectra in the visible wavelength range from 500 to 1000 nm but also in the NIR (1000−2000 nm) spectral region, which we acquired with our newly developed NIR broadband probe and detection scheme. The unique combination of an extended temporal and spectral pump−probe range allowed us: (i) to differentiate between the temporal evolution of excitons, free charges, and CT states due to their individual absorption profiles in the NIR; (ii) to determine the lifetime of strongly bound interfacial CT states as well as the nongeminate recombination coefficient and recombination order of free charges; (iii) to study the effect of solvent additives on the above-mentioned processes and (iv) to elucidate the role triplet states play in the photophysics of PCPDTBT:PCBM blends. We relate our findings to the significant change of the photovoltaic efficiency observed upon processing of the blend with solvent additives.

2. RESULTS

In this section we first present a morphological study on PCPDTBT:PCBM blends prepared with and without ODT as cosolvent performed by solid-state NMR spectroscopy. Prior to presenting the early time (ps−ns) exciton and charge generation dynamics in PCPDTBT:PCBM blends as well as the delayed (ns−μs) charge recombination and triplet state dynamics and the effect of the cosolvent/additive on the dynamics, we will also briefly report the exciton dynamics of pristine PCPDTBT polymer films measured by vis-NIR pump−probe spectroscopy as these will be relevant for the interpretation of the pump−probe spectra of the blends. We further note that all pump−probe transient absorption experiments presented in the following paragraphs have been repeated on separately prepared polymer films and blends at least two times and that the experimental results were found to be similar within the typical experimental error.

2.1. Influence of ODT on Morphology Studied by Solid-State NMR. Solid-state NMR can provide insights into the local order and packing arrangement of functional organic materials. Recent examples include discotic liquid crystals,[30,31] polymers,[32−34] pharmaceuticals,[35,36] and very recently also organic solar cell materials based on the BHJ principle, like P3HT:PCBM and PCPDTBT:PCBM blends.[37−39] In 1D ^{13}C magic-angle spinning (MAS) NMR spectra the isotropic ^{13}C chemical shift (δ_{iso}) position reflects the different chemical environments in the sample, and the ^{13}C linewidth can be used as a measure for the distribution of local geometries. This makes ^{13}C a sensitive probe toward structural order or disorder, which is further enchanced by its broad chemical shift dispersion (200 ppm) and thus high chemical shift resolution.[40] Moreover, the linewidths are not affected by homonuclear dipolar coupling due to the low natural abundance of ^{13}C (1.1%). Higher spectral resolution can be obtained by employing 2D heteronuclear correlation techniques, such as $^{13}C\{^1H\}$ Frequency-Switched Lee−Goldburg HETeronuclear CORrelation (FSLG-HETCOR).[41] Here, structural information about spatial proximities between ^1H and ^{13}C can be derived based on the distance-dependent strength of the dipole−dipole coupling between the nuclei. Furthermore, the resolution for ^1H is improved due to the application of FSLG homonuclear $^1H-^1H$ decoupling.[42]

Figure 1 shows 1D $^{13}C\{^1H\}$ CP/MAS NMR spectra of pure PCPDTBT and PCBM as well as blends of PCPDTBT:PCBM (1:2) processed with and without ODT. All materials except PCBM were drop-cast from *o*-dichlorobenzene (*o*-DCB).

The ^{13}C resonances of the pure PCPDTBT polymer in general exhibit narrower linewidths than those of both PCPDTBT:PCBM blends, indicating a lower degree of local ordering in the blend materials. In particular, the splitting of the

Journal of the American Chemical Society Article

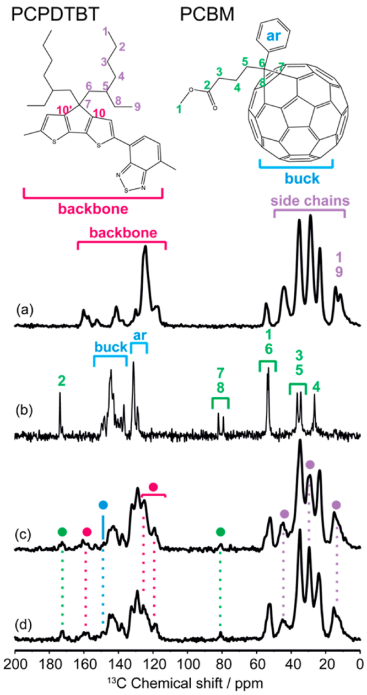

Figure 1. The top panel shows the chemical structures of PCPDTBT and PCBM. 1D $^{13}C\{^{1}H\}$ CP/MAS NMR spectra of (a) PCPDTBT, (b) PCBM, (c) PCPDTBT:PCBM (1:2), and (d) PCPDTBT:PCBM (1:2) processed with 2.4 vol % ODT. Apart from PCBM, which was used as a powder, all other materials were drop-cast from *o*-DCB. The assignment in (a–d) follows the color scheme given on the top. For the blends (c,d) the resonances that can be assigned unambiguously to PCPDTBT or PCBM are highlighted using the color scheme and marked with dashed lines.

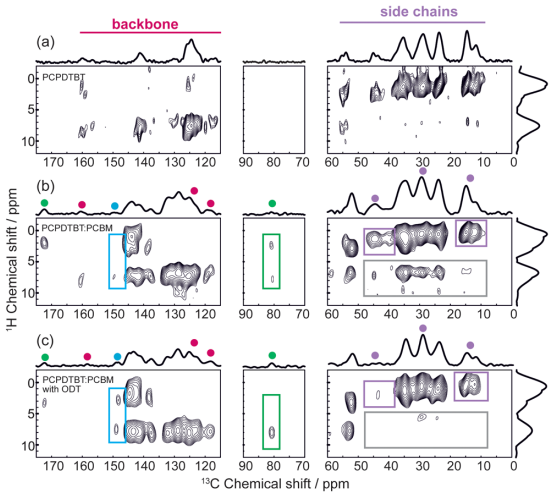

Figure 2. Selected regions of the 2D $^{13}C\{^{1}H\}$ FSLG-HETCOR NMR spectra for (a) PCPDTBT, (b) PCPDTBT:PCBM (1:2), and (c) PCPDTBT:PCBM (1:2) processed with 2.4 vol % ODT. All materials were drop-cast from *o*-DCB. The assignment is based on the color scheme given in Figure 1, and the main structural changes between (b) and (c) are marked with colored boxes. All spectra are plotted on the same intensity scale with contour lines from 10.1 to 90% of the maximum intensity.

signals from the methyl groups of PCPDTBT illustrates this behavior. For the pure PCPDTBT polymer, two well-resolved signals from the trans and gauche conformations (10–20 ppm) of the side-chain methyl groups arise, which in the case of the blends displays a broad overlap. This observation is in agreement with literature data where more amorphous environments in blends than in pure polymers have been reported.[43]

To gain a deeper insight into the local ordering and impact of ODT processing with respect to morphology, we have recorded 2D $^{13}C\{^{1}H\}$ FSLG-HETCOR NMR spectra of PCPDTBT and PCPDTBT:PCBM (1:2) blends as summarized in Figure 2.

In the 2D spectrum of the pure PCPDTBT polymer, all of the expected directly bound $^{1}H-^{13}C$ correlations are observed. However, no correlations between the hexyl–ethyl ($C_{6,2}$) side chains (0–60 ppm), attached at the bridging carbon of the fused dithiophene group, and the ^{1}H nuclei of the polymer backbone (>5 ppm) are observed. This suggests a well-defined packing arrangement of the PCPDTBT polymer with ordered regions for the $C_{6,2}$ side chains. In contrast, the PCPDTBT:PCBM (1:2) blend processed without ODT shows intense correlation peaks between aliphatic and aromatic moieties, see Figure 2b. The presence of these correlations suggests a homogeneous blend structure where the PCPDTBT polymer and PCBM acceptor of the BHJ are molecularly mixed, i.e., the alkyl side chains from PCPDTBT are in close proximity of the aromatic fragments of PCBM and vice versa. Interestingly, processing of PCPDTBT:PCBM (1:2) with ODT results in the disappearance of the correlation peaks between aliphatic and aromatic moieties as can be identified from Figure 2c. Furthermore, the processing with ODT leads to a signal reduction for the aliphatic groups related to the PCPDTBT polymer as marked in Figure 2c. This dramatic decrease in intensity can in principle result from the following evolutions of the PCPDTBT:PCBM blend morphology: First, the intermolecular interfaces can arrange in a more favorable manner, allowing the fullerene part of the PCBM to be in closer contact to the PCPDTBT polymer backbone. As a consequence, this leads to the elimination of alkyl–aromatic correlation peaks and to a more heterogeneous blend material. Second, the domain size in the blend material can grow due to the addition of ODT, which leads to a higher degree of demixing and a reduced number of intermolecular interfaces. Both of these changes in morphology do not exclude each other. AFM data (see Supporting Information, Figure S1) give evidence for increased domain sizes in the PCPDTBT:PCBM sample processed with ODT. In parallel, the 2D $^{13}C\{^{1}H\}$ FSLG-HETCOR spectrum of the blend processed with ODT (Figure 2c) exhibits correlation peaks that have narrower linewidths in both dimensions than the blend processed without ODT (Figure 2b). The latter observation points toward a higher degree of local ordering for both the PCPDTBT and PCBM domains upon addition of ODT. Thus, the addition of ODT results in a higher degree of demixing with increased domain sizes as well as in a higher degree of local order with better arranged intermolecular interfaces between donor and acceptor components of the BHJ. We note that similar conclusions about the increase in domain sizes upon processing with ODT (or other additives) have been

reported based on X-ray diffraction techniques for a number of different photovoltaic blends, including PCPDTBT:$PC_{70}BM$, PSBTBT:$PC_{60}BM$, and PTB-7:$PC_{70}BM$.[44−47]

2.2. Excited-State Dynamics in Pristine PCPDTBT. Due to the PCPDTBT polymer's long wavelength ground-state absorption extending up to 850 nm and the photoluminescence extending up to 950 nm, the excited-state photoinduced absorption (PA) features of the excitons are expected in the NIR probe range. Thus, we performed broadband NIR pump−probe spectroscopy covering the hitherto unobserved wavelength range from 1200−2000 nm in addition to pump−probe spectroscopy in the shorter wavelength region from 550−1050 nm, hereafter being referred to as visible wavelength region for reasons of simplicity.

Figure 3 displays examples of typical broadband visible and NIR pump−probe spectra from PCPDTBT thin films spin-cast

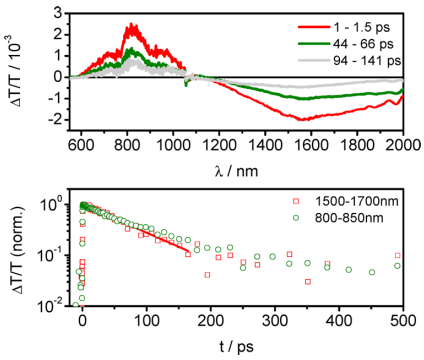

Figure 3. Early time transient absorption spectra of pristine PCPDTBT films spincast with ODT (top panel) excited with 5−6 $\mu J/cm^2$ at 550 nm. The bottom panel shows the dynamics of the stimulated emission and exciton-induced absorption on a semi-logarithmic scale including a single exponential fit to the NIR data with a lifetime of 78 ps.

with ODT monitored over a time range from one to several hundred ps using a low excitation fluence of 5−6 $\mu J/cm^2$ at 550 nm. The pump−probe spectrum of the polymer film shows distinct spectral features, namely a ground-state bleach (GSB) with an onset at 600 nm extending to 850 nm, where typically the ground-state absorption of the polymer is observed in steady-state absorption measurements, and a region of stimulated emission (SE) extending up to 1000 nm, which overlaps with the GSB in the shorter wavelength region. The wavelength region in which SE can be observed corresponds to the spectral region of fluorescence as both originate from the first excited singlet state. The dynamics of the SE signal, which tracks the population of singlet excitons, decays monoexponentially with a lifetime of 95 ps. The observed exciton lifetime is rather short, which must be a consequence of strong nonradiative deactivation processes competing with the emissive (fluorescent) decay of the exciton. This is in line with the low quantum yield of 6% recently reported for pristine PCPDTBT samples by Jarzab et al.[26] We note that the dynamics obtained by our pump−probe experiments are unaffected by higher order processes, such as exciton−exciton annihilation, since the pump fluence was kept well below the onset of these processes, which can be observed at higher fluences (see Supporting Information, Figure S2) and are typically indicated by accelerated exciton decay dynamics. The exciton lifetime we obtained from our pump−probe experiments is in excellent agreement with those recently reported by Jarzab et al., who determined the fluorescence lifetimes of PCPDTBT films by the streak camera technique.[26,27]

In the NIR spectral region of our pump−probe experiments we observe a photoinduced absorption covering the entire NIR wavelength range from 1200−2000 nm, which peaks at 1580 nm. In accordance with the visible pump−probe experiments, which showed stimulated emission indicating the presence of excited singlet states, we assign the PA to the presence of singlet excitons immediately generated after photoexcitation. The PA decay fits well to a single exponential with a lifetime of 78 ps, which is slightly shorter than observed for the visible pump−probe measurements, but within the experimental error of the experiment. We have also performed long-delay (ns−μs) pump−probe experiments on pristine PCPDTBT films and could observe a weak photoinduced absorption signal at 1300 nm with an approximate lifetime of 1 μs indicative of some triplet formation in the pristine polymer (see Supporting Information, Figure S3). In addition, low-temperature (80 K) steady-state photoinduced absorption measurements (PIA) on pristine PCPDTBT thin films also showed a double-peaked spectrum in the NIR typical of charge carriers in conjugated polymers, indicating that a fraction of excitons can undergo dissociation to charges even in the absence of an electron acceptor (see Supporting Information, Figure S4).

2.3. Photovoltaic Performance. In this section we report on the impact of the cosolvent on the device performance. For the PCPDTBT polymer used in the present study we obtained average power conversion efficiencies (PCE) of 1% (J_{SC} = 4 mA/cm^2, FF = 38%, V_{OC} = 0.56 V) from blends with $PC_{60}BM$ spin-cast from chlorobenzene solutions without ODT. The PCE was doubled to 2.1% (J_{SC} = 7 mA/cm^2, FF = 45%, V_{OC} = 0.6 V), when ODT was used as an additive during the spin-casting process, mainly due to an increased short circuit current and a minor improvement of the device fill factor, which is in line with previous studies on PCPDTBT:PCBM blends.[14,27] The $J-V$ curves of the devices are shown in Figure 4 alongside the steady-state absorption spectra of the thin films. EQE spectra can be found in the Supporting Information (Figure S5). While the qualitative effect of ODT is well reproduced in

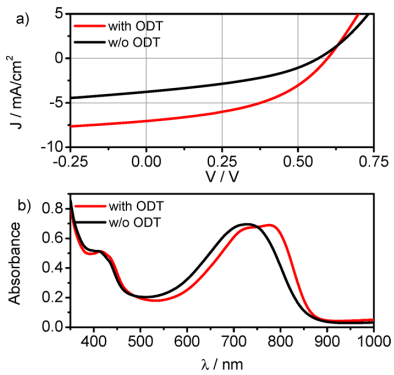

Figure 4. (a) $J-V$ curves of PCPDTBT:PCBM devices prepared with and without ODT. The PCE are 1% for the devices without ODT and 2% upon adding ODT. (b) Steady-state absorption of blend films prepared with and without ODT.

our present study, we found significantly lower average PCEs compared to the record efficiencies previously reported for this material system.[7] We would like to stress that several reasons can account for the lower average PCE compared to the record values, and we also note that the photovoltaic parameters are similar to those very recently reported by Scharber et al.[27] Among the most likely reasons: (i) a not fully optimized device structure; (ii) the use of $PC_{60}BM$ instead of $PC_{70}BM$, which inherently lowers the photon absorption of the blend; and (iii) the median molecular weight (M_n = 14.000 g/mol) of the polymer used for the present study. In particular the latter is known to have a pronounced effect on the PCE with higher molecular weights resulting in higher PCE values for reasons still not entirely understood. We note that we have used $PC_{60}BM$ for the present study to avoid a contribution of excited states on the fullerene to the pump–probe spectra of the blend, which can be neglected due to the comparably small excited-state cross sections of PCBM that would otherwise complicate the interpretation of the pump–probe spectra.[48] As has already been demonstrated by others, the ground-state absorption of the blend prepared with ODT is red-shifted compared to blends prepared without ODT and also exhibits a vibronic shoulder at the low-energy edge of the absorption spectrum (compare data in Figure 4b). This has previously been interpreted as increased order and enhanced component demixing in blends prepared with ODT and is well in line with the solid-state NMR results presented above. In comparison the blend film prepared without ODT shows a blue-shifted and less structured absorption spectrum indicative of a more amorphous film also implying smaller and less ordered polymer domains in line with our results obtained from solid-state NMR spectroscopy (see Section 2.1).

2.4. Early Time (ps–ns) Dynamics in PCPDTBT:PCBM Blends. In this section we present the early time (ps–ns) vis-NIR pump–probe spectra of PCPDTBT:PCBM (1:2) blends and the dynamics of charge formation and early time recombination studied by ultrafast transient absorption pump–probe spectroscopy.

2.4.1. Pump–Probe Spectra and Dynamics in the Visible. The early time (ps–ns) pump–probe spectra and dynamics of PCPDTBT:PCBM blends prepared without ODT can be found in Figure 5, while the spectra and dynamics for the films prepared with ODT are presented in Figure 6. Figures 5a and 6a display the pump–probe spectra of the respective sample, Figures 5b and 6b show the dynamics probed at the wavelength regions indicated, and Figures 5c and 6c show the intensity dependence of the dynamics monitored at the indicated spectral position. The early time visible pump–probe spectra of both samples exhibit two characteristic features, i.e., a positive signal in the shorter wavelength region from 600 to beyond 800 nm and a negative signal at longer wavelength extending further into the NIR beyond 1050 nm, which is typically the detection limit in visible pump–probe experiments, when silicon photodetectors are used. In line with the early time pump–probe spectra of the pristine film, the former can be assigned to the polymer's GSB. The latter is assigned to the onset of the charge-induced absorption.

The absence of any stimulated emission previously observed for wavelengths above 800 nm indicates rapid quenching and dissociation of the majority of the singlet excitons of the polymer at the PCPDTBT:PCBM interface. However, we will show later that some picosecond diffusion-limited dissociation of PCBM excitons occurs and that an additional diffusion-limited dissociation of polymer excitons can be observed in samples prepared with ODT. In both samples a small dynamic red-shift of the GSB over the entire nanosecond time scale is observed, indicating relaxation of the charges within the density of states. The red-shift is more pronounced in the sample prepared without ODT demonstrating that on the nanosecond time scale, charges relax into deeper tail states of the density of states, which is an indication of larger energetic disorder of the blend prepared without ODT. The sample prepared without ODT first exhibits a rise of the GSB followed by a decay of about 50% in the first 3 ns. In comparison, the blend prepared with ODT shows a decay of the bleach of only 30% after the signal rise, indicating a smaller fraction of geminate recombination and thus a larger fraction of free charge generation. To account for spectral relaxation of the bleach, the kinetics were extracted by tracking the maximum amplitude instead of using a single wavelength only. The reduced decay in the blend with ODT is in line with the results of Hwang et al., who deduced a reduction of the early time carrier loss (geminate recombination) in samples processed with ODT. However, they obtained a difference of 10% only, while here we observed a difference of 20%.[20] The dynamics of the GSB cannot be unambiguously assigned to a single photophysical process, since the recovery of the GSB represents the sum of the dynamics of all excited states present in the blend. In addition, the GSB can be superimposed by spectral relaxation phenomena and thermal effects, as has recently been suggested for P3HT:PCBM, and thus the absolute fractions of geminate recombination deduced from the ground-state recovery bear some uncertainty.[49]

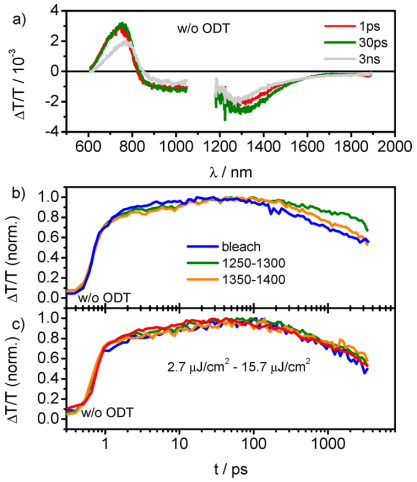

Figure 5. (a) Short delay (ps–ns) broadband transient absorption spectra of PCPDTBT:PCBM (1:2) blends prepared without ODT measured in the visible (600–1050 nm) and NIR (1100–1900 nm) spectral region at delay times of 1 ps (red), 30 ps (green), and 3 ns (gray). The pump fluence at 530 nm was 4.9 $\mu J/cm^2$ for the visible and 5.4 $\mu J/cm^2$ for the NIR measurements. (b) Short delay recombination dynamics of the photoinduced absorption probed at different wavelength regions in PCPDTBT:PCBM (1:2) blends prepared without ODT. (c) Intensity dependence of the early time dynamics tracked at 1350–1400 nm. Note that the dynamics are independent of pump fluence and the decay follows a single exponential with a mean lifetime of 1200 ps.

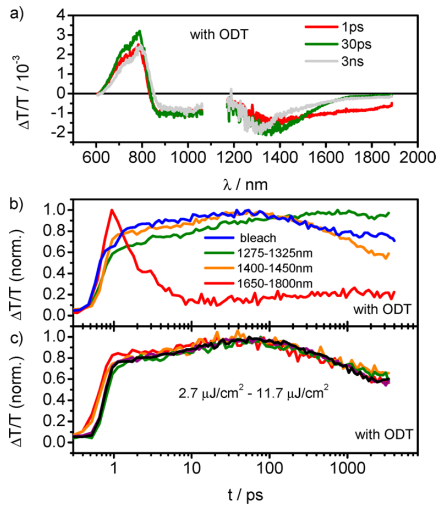

Figure 6. (a) Short delay (ps–ns) broadband transient absorption spectra of PCPDTBT:PCBM (1:2) blends prepared with ODT measured in the visible (600–1050 nm) and NIR (1100–1900 nm) spectral region at delay times of 1 ps (red), 30 ps (green), and 3 ns (gray). The pump fluence at 530 nm was 4.0 μJ/cm^2 for the visible and 3.9 μJ/cm^2 for the NIR measurements. (b) Early time dynamics of the exciton-induced absorption (1650–1800 nm) and the charge-induced absorption probed at different wavelength regions. Note the rapid decay of the signal in the region between 1650–1800 nm due to the diffusion-limited charge generation from polymer excitons. (c) Fluence dependence of the kinetics between 1400 and 1450 nm. The decay follows a single exponential with a mean lifetime of 700 ps.

As has already been mentioned above at longer wavelength, i.e., lower photon energy, the onset of the broad PA of charges can be observed in both blend films. The zero crossing between bleach and PA occurs at 825 nm for the blend prepared without ODT and at 835 nm for the blend prepared with ODT, respectively. Interestingly, the latter exhibits a more pronounced PA signal between 850–950 nm in contrast to the PA of the former. The appearance of a PA feature in this spectral region has previously been assigned to the presence of interfacial CT states, and its amplitude has qualitatively been correlated with the device performance by Hwang et al.[20,24] Here we observe a more pronounced PA from the blend prepared with ODT, which is inconsistent with the results of Hwang et al., who found that the PA in this spectral region vanishes if the sample is prepared with ODT and interpreted this to be due to more efficient splitting of CT states. In the present case we hypothesize that this feature may rather be related to the degree of order of the polymer-rich regions and the amount of demixing of the blend. We note that in the present study we have investigated PCPDTBT:PCBM blends with a ratio of 1:2. In fact, for this ratio Hwang et al. observed similar spectral features in line with our observations, which were reduced at higher PCBM concentrations of 1:3.6, suggesting a lower degree of order for the polymer domains at higher PCBM fractions.

On the basis of the above results we note that a clear assignment of the charge-induced PA signal seen in the visible pump–probe spectra appears difficult as only the tail can be observed up to 1050 nm, which, as we will show below, can reveal neither the conversion from excitons to interfacial CT states and free charges nor the individual recombination dynamics of free charges, trapped charges, and CT states. Quasi-steady-state photoinduced absorption (PIA) spectroscopy has previously demonstrated that the charge-induced absorption in PCPDTBT:PCBM peaks at around 1300 nm and extends even further into the NIR (see Supporting Information, Figure S6).[29] However, PIA probes a lifetime and concentration averaged sum of the ensemble of all excited states under quasi-equilibrium conditions, and for this reason only provides very limited or no information about the spectral profiles of individual states, especially if they are very short-lived as can be expected for CT states or singlet excitons. In addition a quantitative assessment of PIA data is difficult, as the cross sections of the species are typically not known. Hence, we have monitored the spectral profiles and dynamics of the entire charge-induced absorption in the NIR spectral region using a novel broadband NIR pump–probe setup and NIR detection scheme described in detail in the experimental part.

2.4.2. Pump–Probe Spectra and Dynamics in the NIR Region. Typical ps–ns NIR pump–probe spectra obtained for blends prepared without and with ODT are also presented in Figures 5 and 6, respectively, along with the visible pump–probe spectra discussed in the previous paragraph. In the following we will first concentrate on the results obtained for the sample prepared without ODT and then compare these results to those obtained for the sample prepared with ODT. The charge-induced PA of the sample prepared without ODT is rather broad spanning the entire NIR wavelength range from 1150–1900 nm. Figure 5b presents the dynamics of the PA signal probed at different wavelength regions. All dynamics exhibit an ultrafast rise due to the convolution of the pump and probe pulse lengths limiting the temporal resolution of our experiment to 100 fs. An additional slower but significant rise of the charge-induced PA signal within the first 50 ps is observed for the dynamics monitored between 1400–1450 nm. As can be seen from the spectra in Figure 5a, the amplitude of the bleach follows a similar rise over the same period of time, indicating that during the first 50 ps we observe a delayed generation of charges and CT states. Such a rise of the charge-induced absorption has previously been assigned in other polymer:fullerene systems to either a delayed transition from singlet excitons to charges or a liberation process of free charges from a precursor state, for instance, an intermediate polaron pair, that can either split into free charges or relax into strongly bound interfacial CT states.[50] We emphasize that in the latter case of a transition from intermediate polaron pairs to free charge carriers or CT states, a constant amplitude of the bleach during the conversion process is expected. This was not observed in our measurements. Furthermore, we rule out exciton diffusion in the polymer on the time scale of several tens of picoseconds as we observe neither stimulated emission nor the typical exciton-induced absorption, which, as we will show later, can be detected in samples prepared with ODT at wavelengths longer than 1600 nm in the first 10 ps. Hence, the most likely explanation is that we observe a prolonged diffusion of excitons in PCBM-rich domains, which are subsequently quenched at the interface, causing a signal rise of the polymer bleach due to the hole transfer to the polymer. To further support this interpretation, we repeated the measurements using a pump wavelength of 700 nm, where the fraction of polymer absorption was significantly larger compared to the absorption of PCBM, and thereby, a reduced amount of PCBM excitons is generated. Interestingly, upon excitation at 700 nm

the amplitude of the signal rise during the first 50 ps was reduced to less than 10% in contrast to the 20% amplitude increase observed after excitation at 532 nm. The dynamics after excitation at 700 nm can be found in the Supporting Information (Figures S7 and S8). Unfortunately, it is not possible to decompose the NIR spectrum into the individual photoinduced absorption spectra of free charges and bound polaron-pairs, since their absorption spectra are virtually similar, and thus the spectra and dynamics that we probe between 1250−1400 nm consist of contributions from both bound polaron-pairs and free charge carriers. We also note that Janssen et al. have recently reported that in samples prepared without ODT, the CT state can undergo intersystem crossing to a triplet state.[29] The latter could have a larger cross-section and could also cause a signal rise in the observed spectral region if CT states are converted into triplets, which is addressed later. After the initial clear signal rise caused by diffusion-limited exciton dissociation in the PCBM domains, we observe a large decay of the entire charge-induced PA band occurring within the time scale of the early time pump−probe experiment in line with the significant nanosecond decay of the GSB. The dynamics on this time scale can be fitted with a single exponential yielding a lifetime of 1200 ps, depending slightly on the signal offset used for fitting. Most importantly we found that neither the dynamics of the rise nor the early time decay between 1350−1400 nm are fluence dependent, i.e., they do not depend on the initial concentration of excited states as can be clearly seen in Figure 5c. In case of the signal rise, this indicates that prior to exciton dissociation we do not observe exciton annihilation at the pump fluences used, and in case of the decay, it proves that we observed a geminate recombination process of strongly bound and thus localized interfacial CT states that undergo nanosecond recombination to the ground state and cannot dissociate into free charges. Interestingly, the inverse recombination rate we obtained from the decay is in excellent agreement with the decay time recently reported for the CT state emission from PCPDTBT:PCBM blends by Jarzab et al., supporting our interpretation that here we indeed observe the recombination dynamics of relaxed (and thus luminescent) CT states.[26,27]

We now examine the NIR features observed for the blend prepared with ODT. Figure 6 shows the NIR pump−probe spectra and dynamics in different wavelength regions and the intensity dependence of the NIR PA signal dynamics. Before starting a detailed description, it is worth emphasizing that the NIR pump−probe spectra of the sample prepared with ODT contain significantly more spectral features than the NIR spectra obtained for the sample prepared without ODT. These features visible in the NIR contain significantly more information than those in the visible pump−probe spectra, allowing us to clearly recognize the dynamics of the individual species present in the blends. The following features can be identified in the blend prepared with ODT: (i) a rather short-lived PA between 1600 to 1900 nm that extends further into the IR region decaying within a few ps; (ii) a broad PA between 1400 and 1500 nm vanishing within several hundred ps; and (iii) a comparably narrow PA with a maximum at 1300 nm that continuously rises over the first 300 ps and then stays virtually constant on the investigated time scale. By comparing the NIR spectra of the blend to those of the pristine polymer shown in Figure 3, we conclude that the spectral region between 1600 to 1900 nm is dominated by polymer exciton-induced absorption and that the very short-lived feature seen in this spectral region is caused by polymer singlet excitons that must diffuse to an interface prior to their dissociation. The early time decay transients monitored from 1650−1800 nm, shown in Figure 6b, further reveal that the polymer excitons are entirely quenched after 10 ps in the blend with ODT. This is in contrast to the results obtained for the blend prepared without ODT where the polymer exciton-to-charge conversion happens on a time scale faster than the time resolution of our setup. The straightforward explanation for the difference is a change of the morphology toward enhanced demixing and polymer-enriched domains in the film prepared with ODT as a cosolvent, which is in line with our morphology studies by solid-state NMR techniques presented above.

The second feature that can be identified in the blend prepared with ODT is most prominent between 1400−1500 nm. Here, we again observed a rise of the signal similar to the sample prepared without ODT described above, followed by a decay extending to several nanoseconds. We extracted the dynamics for this spectral region and found the decay of the signal to follow a single exponential with a lifetime of about 700 ps (see Figure 6b). The lifetime was also found to be independent of the excitation intensity, and thus this decay can be assigned to CT states undergoing a monomolecular geminate recombination process. Interestingly, the lifetime of the geminate recombination is shorter compared to the recombination time observed for the CT excitons in the sample prepared without ODT. The decay observed in this spectral region is accompanied by a significant signal loss of the GSB observed in the visible pump−probe experiments, further supporting that these states return to the ground state on a subnanosecond time scale. The third feature, which is most prominent between 1275 and 1325 nm, remains after the decay of the signal between 1400 and 1500 nm is completed. In this spectral region we observe a clear signal rise up to several hundred picoseconds, after which the signal remains virtually constant in contrast to the measurements presented for the sample prepared without ODT. The observation of a first increasing and afterward constant signal at 1300 nm can be explained by diffusion-limited exciton dissociation in polymer and PCBM-rich domains. While the former appears to be completed after 10 ps, the latter process continues up to several hundred picoseconds in samples prepared with ODT, suggesting larger PCBM-rich domains in samples prepared with ODT. The significantly narrower charge-induced absorption peak that remains after 3.5 ns in the sample prepared with ODT compared to the broad PA observed in the sample prepared without ODT (compare also long delay spectra) also implies that the free charge carriers are mostly present in more ordered polymer-rich regions, while in the blend prepared without ODT, the charges remain in disordered and amorphous regions, in agreement with the morphology changes induced by ODT.

2.5. Delayed (ns−μs) Pump−Probe Spectra and Dynamics. *2.5.1. Pump−Probe Spectra in the Visible and NIR.* Having presented the early time charge generation and CT-state recombination dynamics in PCPDTBT:PCBM blend films as a function of the processing additive, we will now turn to the charge recombination occurring on a time scale from 1 ns to tens of μs, in which we probe the dynamics of long-lived charge carriers that can potentially contribute to the device photocurrent. Figure 7 compares the visible and NIR pump−probe spectra between 1 ns and 1 μs of both blends, i.e., the blend prepared with and without ODT in Figure 7a,b,

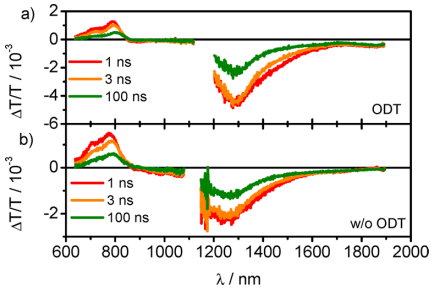

Figure 7. (a) Long delay (ns–μs) broadband transient absorption spectra of PCPDTBT:PCBM (1:2) blends prepared with ODT measured in the visible (600–1000 nm) and NIR (1100–1900 nm) spectral region at delay times of 1 ns (red), 3 ns (orange), and 100 ns (green). The samples were excited at 532 nm with a pump fluence of 8.7 μJ/cm^2 for the visible and 9.6 μJ/cm^2 for the NIR measurements. (b) Long delay (ns–μs) broadband transient absorption spectra of PCPDTBT:PCBM (1:2) blends prepared without ODT measured in the visible (600–1000 nm) and NIR (1100–1900 nm) spectral region at delay times of 1 ns (red), 3 ns (orange), and 100 ns (green). The samples were excited at 532 nm with a pump fluence of 6.1 μJ/cm^2 for the visible and 5.7 μJ/cm^2 for the NIR measurements.

respectively. As has already been evident from earlier experiments, the sample prepared with ODT exhibits stronger pronounced vibronic features of the GSB. From the shape of the GSB, it appears that those states surviving the first ns are mostly present in the more ordered regions of the polymer, while this is not the case for the sample prepared without ODT, which is in general less ordered. The dynamics of the GSB strongly depend on the spectral position probed, and it is therefore difficult to extract meaningful lifetimes and recombination dynamics as the recovery of the ground state mirrors the entire ensemble of excited states and their dynamics and is also subject to further spectral relaxation. The latter continues up to 100 ns in both samples, suggesting that charges slowly relax into tail states in the density of states. We note further that the charge PA in the visible spectral region is almost vanished for the sample prepared with ODT, while the onset can still be seen as a very weak signal in the sample prepared without ODT. The weak signal intensity of the charge-induced absorption in the visible spectral range complicates a meaningful extraction of the dynamics at times longer than several nanoseconds. However, the NIR spectral range still allows monitoring the charges, since the cross-section of charges in this spectral region is significantly larger than in the visible spectral region.

The samples prepared without ODT exhibit a peak of the charge-induced PA at 1240 nm, while the charge-induced absorption in the sample prepared with ODT peaks at 1285 nm. The first time slice measured for the sample prepared with ODT still shows a shoulder between 1400 and 1600 nm, which we have previously assigned to the presence of strongly bound interfacial CT states in the early time experiments. These CT decay dynamics are not resolved in the long delay experiment due to the limited time resolution (1 ns). Compared to the sample prepared without ODT, the peak is also narrower indicating that charges reside in more ordered domains in the blend prepared with ODT.

2.5.2. Spectra and Dynamics of Triplet States. A blue-shift of the NIR PIA band in samples prepared without ODT compared to samples prepared with ODT has very recently been reported by the Janssen group and was interpreted as evidence for enhanced triplet formation due to fast intersystem crossing from the CT state.[29] This process was found to be suppressed in samples prepared with ODT, which could in part explain the higher efficiency of these samples. However, triplet formation would require very fast intersystem crossing from the singlet CT state, which appears to be rather unlikely given the short subnanosecond CT recombination lifetime of strongly bound CT states observed in our early time experiments. On the other hand, some fraction of triplet formation cannot be entirely ruled out, as the position of the triplet-induced absorption is very similar to the absorption of charges, making them very difficult to distinguish from each other.[29] Therefore, to further elucidate the role of triplets, we studied thin films of PCPDTBT blended with a triplet sensitizer, namely platinum-octaethylporphyrin (PtOEP). PtOEP can be selectively excited into the Q-band at 532 nm, where the polymer absorption is weak. Upon excitation at 532 nm, the PtOEP singlet state is generated and rapidly converted into the triplet state. The triplet energy of PtOEP is around 1.9 eV and thereby significantly higher than the triplet of the polymer, allowing very efficient downhill Dexter-type triplet transfer from the sensitizer to the polymer. Some singlet energy transfer from the PtOEP to the polymer may also occur by Förster-type energy transfer, but due to the rapid ISC of PtOEP and short singlet state lifetime of PCPDTBT, the influence of singlet excitons on the PA spectrum can be neglected after 1 ns.

Figure 8 compares the NIR pump–probe spectra of the PCPDTBT:PtOEP blend with those obtained from a

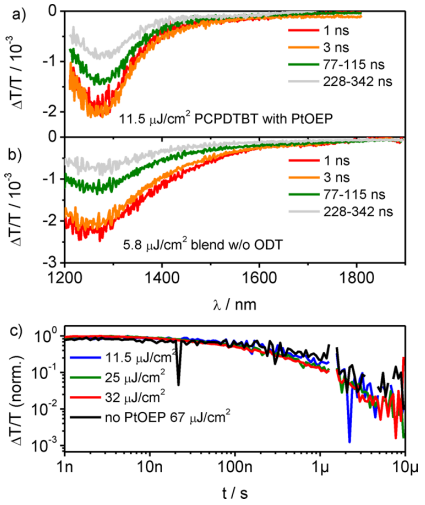

Figure 8. (a) NIR TA spectra of PCPDTBT blended with 40 wt % PtOEP and (b) NIR TA spectra of PCPDTBT:PCBM without ODT. (c) Fluence dependence of the triplet kinetics in the sample with PtOEP between 1250 and 1300 nm and for comparison the kinetics in the pristine polymer film (black line).

PCPDTBT:PCBM blend prepared without ODT and shows the intensity dependence of the triplet state decay dynamics. The peak position of the triplet-induced absorption is indeed very similar to the charge-induced absorption as reported by Janssen et al.[29] However, the triplet-induced absorption signal is much narrower than the charge-induced absorption seen in both blends. Furthermore, the decay dynamics we observed for

dx.doi.org/10.1021/ja303154g | J. Am. Chem. Soc. 2012, 134, 10569–10583

the triplet states are intensity-independent and very long-lived (1 μs) in contrast to the nongeminate charge recombination.

The unique long-lived, intensity-independent decay dynamics of the triplet excitons allows us to differentiate between triplet excitons and charges despite their similar spectral features. We will see that the absence of a 100 ns lifetime intensity-independent signal in the dynamics of the blends strongly suggests that no significant number of triplets is formed in the blends and that the differences in spectral features and kinetics in the blends can exclusively be explained in terms of differences in the charge populations.

2.5.3. Delayed (ns–μs) Recombination Dynamics of Charges. Figure 9 compares the dynamics of the charge-induced PA band for both PCPDTBT:PCBM blends monitored at the peak position. In the sample prepared without ODT, we observe an additional 10% signal loss during the first 10 ns even for the lowest excitation intensity. This is a significantly longer time scale than expected from the subnanosecond geminate recombination observed in the short-delay pump–probe experiments, which cannot be resolved here due to the poorer time resolution of our long-delay setup. The initial recombination exhibits a weak intensity dependence, and we therefore assign this process to recombination of loosely bound electron–hole pairs that cannot entirely escape their mutual coulomb attraction and thus have not managed to fully separate into free polarons. They undergo a slower nanosecond geminate recombination process, which is different from the fast geminate recombination of strongly bound interfacial CT states. After this initial recombination the dynamics clearly deviate from each other and become intensity dependent, indicating the recombination of separated charge carriers that undergo a nongeminate recombination process. The nongeminate recombination continues to about 10 μs, after which we could not obtain a meaningful residual signal anymore due to the limited signal-to-noise ratio. We have further analyzed the experimental data by fitting it to a previously introduced model that assumes a fraction of monomolecular polaron pair recombination and a separate fraction of nongeminate recombination of free charges without any interconversion between the two individual pools.[6] Using this model we could obtain an average decay time of the loosely bound polaron pairs in PCPDTBT:PCBM of 5 ns and a nongeminate recombination coefficient of 4×10^{-10} $(cm^3)^{\lambda}/s$ with a recombination order of $\lambda + 1 = 1.93$ in samples prepared without ODT as shown in Table 1. The order of recombination suggests a 3D Langevin-type of recombination with an effective (bimolecular) recombination rate of 3.2×10^{-11} cm^3/s at a charge-carrier density of 5×10^{15} $1/cm^3$.

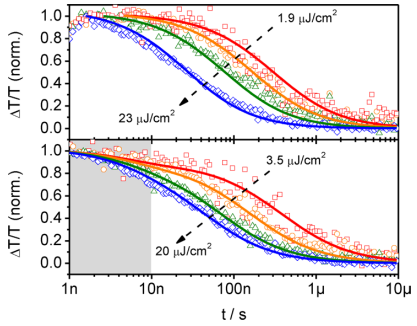

Figure 9. Intensity dependence of the long delay (ns–μs) decay dynamics of the charge-induced absorption in PCPDTBT:PCBM (1:2) blends prepared with ODT (top) and without ODT (bottom). The open symbols correspond to the experimental data, and the solid lines are fits obtained from a photophysical model as further described in the text. Note that in the bottom panel the additional intensity-independent decay phase has been highlighted by a light-gray box.

Table 1. Fit Parameters Extracted Form Long Delay TA Measurements[a]

parameter	with ODT	without ODT
$\lambda + 1$	1.86 ± 0.01	1.93 ± 0.01
$\gamma/(cm^3)^{\lambda}\ s^{-1}$	$(1.0 \pm 0.4) \times 10^{-8}$	$(4 \pm 2) \times 10^{-10}$
f	1	0.89 ± 0.01
k_{LBP}/s^{-1}	absent	$(1.9 \pm 0.5) \times 10^{8}$

[a] $\lambda + 1$ describes the order of the decay, γ is the nongeminate recombination coefficient, f equals the fraction of nongeminate recombination, and k_{LBP} is the geminate recombination rate of loosely bound polaron pairs.

In comparison to the blend prepared without ODT the dynamics of the charge-induced absorption probed at 1300 nm are significantly different in the sample prepared with ODT. Here we observe a very pronounced intensity dependence of the dynamics from the earliest delay times onward. In fact, the intensity-independent component observed in the sample prepared without ODT is entirely absent. At the lowest pump fluence (1.9 $\mu J/cm^2$) that we probed, the charge-induced absorption is virtually constant within the first 10 ns, indicating that nongeminate recombination does not affect the dynamics on this time scale if the pump fluence is kept sufficiently low. It is also apparent from the dynamics in the first 10 ns that with increasing pump fluence, i.e., higher charge-carrier density, nongeminate recombination is present even at very early times below 10 ns. We note that the onset of nongeminate recombination occurs at pump fluences much lower than used in previous transient absorption studies.[20,24] At the highest pump fluence measured in our experiment, free charge carriers undergo nongeminate recombination from the earliest times (1 ns) onward. This implies very fast recombination, and thus a large nongeminate recombination coefficient as will be deduced below. In order to gain further information about the nongeminate recombination dynamics, we fitted the experimental data to the same model used for the sample prepared without ODT, this time assuming exclusively Langevin-type recombination for the sample prepared with ODT, since any nanosecond geminate component due to loosely bound polaron pairs appears to be entirely absent. The results of the fitting procedure are again depicted in Figure 9 as solid lines overlaying the experimental data (open dots). For the sample prepared with ODT, the dynamics can be described with a recombination order of $\lambda + 1 = 1.86$ and a nongeminate recombination coefficient of 1×10^{-8} $(cm^3)^{\lambda}/s$. From this an effective (bimolecular) Langevin recombination rate of 6.3×10^{-11} cm^3/s at a charge-carrier density of 5×10^{15} $1/cm^3$ can be calculated. This is significantly larger compared to values that we have recently obtained by pump–probe spectroscopy on other polymer:fullerene blends, such as P3HT:PCBM and PCDTBT:PCBM,[6,51] and indicates that fast nongeminate recombination occurs even in PCPDTBT:PCBM blends prepared with ODT. The pronounced intensity dependence observed for the charge-induced absorption at 1300 nm, which

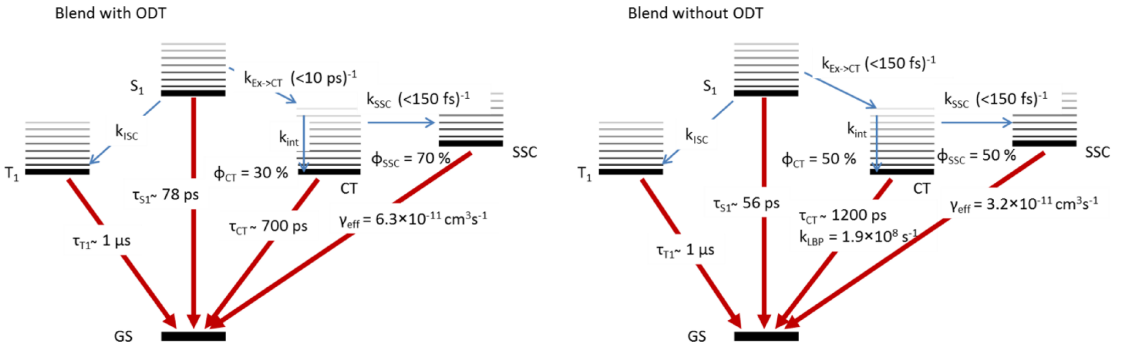

Figure 10. Scheme of the photophysical processes and their respective rates and lifetimes in PCPDTBT:PCBM blends processed with (left) and without (right) ODT. Upon excitation of the polymer, the excitons are quenched with a rate $k_{Ex\rightarrow CT}$, followed by the creation of spatially separated charge carriers (SSC) with the rate k_{SSC} or cooling of the CT state with the rate k_{int}. $\varphi_{SSC/CT}$ denotes the yield of the spatially separated charges and CT states, respectively. γ_{eff} is the effective bimolecular recombination coefficient of free charges, and τ_{CT} is the inverse geminate recombination rate of CT states to the ground state (GS). k_{ISC} is the intersystem crossing rate to the triplet level (T1), and $\tau_{T1/S1}$ is the lifetime of the singlet (S1) or triplet state in the pristine polymer, respectively. In the blend without ODT k_{LBP} describes the recombination rate of loosely bound polaron pairs.

is prominent even at early times, lets us conclude that around the PA peak position, we mainly probe the dynamics of the pool of free charge carriers. If we probe the dynamics at longer wavelength, for instance between 1450−1500 nm or even further in the NIR, the intensity dependence is much less pronounced, indicating that the charges that contribute to the PA in this wavelength region are much less mobile, i.e., present as trapped charges, and thus do not follow the same intensity dependent nongeminate Langevin-type recombination process. This effect is even more pronounced in case of the PCPDTBT:PCBM blend prepared without ODT. While we observed a pronounced intensity-dependent decay at a probe wavelength of 1260 nm (where the contribution of free charges is expected to be highest), the dynamics at longer wavelengths are virtually independent of the excitation intensity, indicating significant trapping and trap-assisted recombination of charges in samples prepared without ODT (see Supporting Information, Figure S10). Hence, it appears that ODT facilitates formation of mobile charge carriers, which recombine according to an intensity-dependent nongeminate recombination process and thus can escape trap-assisted recombination. In agreement with previous studies we also observe that if we take the early time (1 ns) amplitude at the peak position of the charge-induced absorption as a measure of the efficiency of free charge generation, a 1.5 times higher signal amplitude for samples prepared with ODT is observed compared to those without ODT independent of the fluence used. However, as has already been mentioned in the previous paragraph, one has to be very cautious when simply deducing charge-carrier yields by comparing signal amplitudes, since the absolute cross sections of the charges are not exactly known, and as we have shown above, the spectrum of free charges appears to be different from the spectrum of trapped charges and CT states in samples prepared with ODT.

3. SUMMARY AND IMPLICATIONS FOR PHOTOVOLTAIC PERFORMANCE

Exciton Dissociation. The efficiency-limiting photophysical processes occurring in bulk heterojunction organic solar cells can be categorized into: (i) exciton relaxation of those excitons, which fail to undergo dissociation at a nearby heterojunction; (ii) geminate recombination of interfacial CT states; (iii) nongeminate recombination of separated/free charge carriers prior to the extraction from the device; and (iv) trap-assisted nongeminate recombination of those charges which are immobile in the blend. Typically the polymer exciton dissociation yield in polymer:fullerene blends is close to unity, since excitons are very efficiently quenched in well-intermixed blends. This loss channel can only be relevant if the domain size is comparable to the exciton diffusion length. In fact, diffusion-limited exciton quenching on a time scale of several picoseconds has previously been shown in annealed RR-P3HT:PCBM blends, where PCBM is expelled from the P3HT crystalline domains upon annealing, and thus polymer-rich domains of high crystallinity are formed.[52] However, even for the exceptional case of RR-P3HT with its well-ordered solid-state structure, the total loss due to diffusion-limited exciton dissociation does amount to a few percent only. Diffusion-limited polymer exciton quenching is also observed in the present study on PCPDTBT:PCBM blends for samples prepared with ODT as cosolvent, while instantaneous quenching of polymer excitons was found in samples prepared without ODT. The straightforward explanation is that ODT increases the demixing leading to larger PCPDTBT-rich domains. Excitons created within these polymer domains have to reach the heterojunction to undergo charge transfer, which in the present system occurred on a time scale of 10 ps. Our early time pump−probe experiments also exhibited a rise of the bleach and charge-induced absorption on a time scale of several tens of picoseconds for samples prepared without ODT and even hundreds of picoseconds for samples prepared with ODT. In fact, the intensity-independent rise of the bleach in conjunction with the charge-induced absorption can only be explained by delayed exciton dissociation of excitons originally created in PCBM-rich domains. We note that in our previous experiments on P3HT:PCBM and PCDTBT:PCBM samples, we could never observe such a rise of the charge-induced PA on a time scale similar to the rise observed for PCPDTBT:PCBM in this study, which would otherwise have pointed to a delayed charge generation due to excitons created in PCBM. The most likely explanation is that the aforementioned polymers exhibit much stronger absorption at the excitation wavelength of 532 nm, and thus excitons are mostly created in the polymer. The observation of a pronounced diffusion-limited PCBM exciton

dissociation in PCPDTBT:PCBM films independent of the use of solvent additives implies a wavelength dependence of the photophysical processes in these blends and requires further investigation, since it could be a potential loss process, if, for instance, excitons in PCBM recombine before reaching the interface or undergo intersystem crossing to triplet states due to the rather slow exciton diffusion process. Figure 10 schematically summarizes all processes together with their corresponding time scales for PCPDTBT:PCBM blend films prepared with and without the processing additive ODT.

The role of Interfacial CT States. The second loss channel that needs to be considered is relaxation of intermediate polaron pairs into strongly bound interfacial CT states followed by geminate recombination in competition with the formation of free charges from those "hot" electron−hole pairs that provide sufficient excess energy for the charges to overcome their mutual attraction. In fact, it is evident that a large fraction of the intermediate polaron pairs created by exciton dissociation collapses into strongly bound CT states, as we observe a pronounced signal decay of the bleach and the charge-induced absorption following a single exponential decay with an inverse rate of 700 ps (ODT) and 1200 ps (without ODT) (compare data in Figure 10). It is not straightforward to determine the total fraction of the CT state recombination from the pump−probe experiments, since the exact cross sections and spectra of the free charges and strongly bound CT states are unknown, and their individual absorption spectra are strongly superimposed. Nonetheless, our pump−probe experiments have demonstrated that the main process occurring in the first few nanoseconds is a fast and intensity-independent geminate recombination process. Hence, in the absence of competing processes, such as nongeminate recombination, the ground-state recovery can be used as an approximate measure of the fraction of excited states that return to the ground state after exciton dissociation. Using this approximation we have determined a total loss due to geminate recombination of about 50% in samples prepared without ODT and 30% in samples prepared with ODT. Our findings are in line with the earlier findings by the Blom group,[17] which showed a reduced fraction of geminate recombination in samples prepared with solvent additives determined by photocurrent measurements. The difference observed in our study is larger compared to the results reported earlier by Hwang et al.,[20] who showed only a weak impact of solvent additives on the fraction of geminate recombination. It is also worth mentioning that the excess thermal energy that an electron gains during charge transfer from PCPDTBT to PCBM is significantly less than for instance in P3HT:PCBM. This lesser excess energy may reduce the yield of free charges compared to P3HT:PCBM blends. The local morphology at the interface, for instance, the donor−acceptor distance certainly plays an additional and important role in the charge separation efficiency as recently reported by Holcombe et al.[53] One may further argue that the interactions between the molecules directly located at the interface (those which participate in the charge separation) and the molecules in the bulk of the polymer or fullerene (those which transport charges away from the interface) play an important role for efficient charge separation, as has recently been suggested for polymer:-perylenediimide blends.[54]

In fact, in highly crystalline materials, such as P3HT, an additional thermodynamic driving force exists that supports charge transport from the disordered interface to the more ordered bulk material. In lesser ordered materials, as in the present case of PCPDTBT:PCBM, this driving force is expected to be reduced if not entirely absent.

Recombination of Loosely Bound Polaron Pairs and Free Charges. Let us now discuss the long time (>1 ns) recombination dynamics of charges in PCPDTBT:PCBM blends. After about 3 ns we consider the pool of strongly bound interfacial CT states to be emptied in both samples, and it is expected that nongeminate recombination processes of free charge carriers govern the dynamics on a ns−μs time scale. However, in the sample prepared without ODT the ns−μs decay of the charge-induced absorption probed at the peak position appears to be a superposition of an intensity-independent process on a longer time scale up to 10 ns and an intensity-dependent recombination process. The latter can clearly be seen after several tens of nanoseconds, while the former occurs on a significantly longer time scale than the fast geminate recombination of strongly bound CT states that we observed in the early time pump−probe experiments. In addition, the weak intensity-dependence points to a geminate-like recombination process different from the subnanosecond recombination observed in the early time experiments. Geminate recombination on time scales even up to 100 ns has previously been reported and assigned to the recombination of loosely bound charge pairs that have not entirely escaped their mutual attraction.[55] One may also argue that these are charge pairs that are spatially trapped in isolated domains, where they cannot escape into the charge percolation network. The nanosecond recombination of loosely bound pairs is prominent in samples prepared without ODT, where it clearly occurs in addition to the subnanosecond geminate recombination of strongly bound interfacial CT states (sometimes referred to as CT-excitons) that we have identified in the early time pump−probe experiments. Thus, the geminate recombination of loosely bound charge pairs contributes to the loss processes in samples prepared without ODT, implying an unfavorable morphology for fast free charge formation.

It is an interesting question to be addressed in future work, whether these loosely bound polaron pairs, that recombine on the time scale of several nanoseconds, can undergo a field-assisted separation and thus could potentially contribute to the photocurrent in real devices. On the other hand, the occurrence of an intensity-dependent recombination at times longer than 10 ns indicates that a significant fraction of free charges has also been generated in samples prepared without ODT, which can indeed be extracted as photocurrent from the device. This is reasonable since devices prepared without ODT still exhibit a short circuit current of 4 mA/cm^2. Samples prepared with ODT demonstrate a very pronounced intensity dependence even on a time scale of several nanoseconds, implying that loosely bound polaron pairs are entirely absent and that nongeminate recombination dominates the dynamics at 1300 nm from the very beginning. By fitting the intensity-dependent dynamics to a Langevin recombination model, we obtained a nongeminate recombination coefficient of 1×10^{-8} $(\mathrm{cm}^3)^{\lambda}/\mathrm{s}$ and a recombination order of $\lambda + 1 = 1.86$. From the recombination coefficient and order, the effective (i.e., bimolecular) recombination coefficient for 3D Langevin-type recombination was calculated to 6.3×10^{-11} cm^3/s for a charge-carrier density of 5×10^{15} 1/cm^3. We have recently reported the recombination dynamics of charges in P3HT:PCBM and PCDTBT:PCBM probed by ns−ms transient absorption experiments and fitted the experimentally observed dynamics by a photophysical model, assuming that exciton dissociation leads to the

Table 2. Comparison of Effective Langevin Recombination Coefficients Calculated for a Charge Carrier Density of 5×10^{15} 1/cm^3

system	with ODT	without ODT	PCDTBT	rr-P3HT (as cast)	rr-P3HT (annealed)
γ_{eff}/cm^{3}s^{-1}	6.3×10^{-11}	3.2×10^{-11}	1.6×10^{-12}	1.5×10^{-12}	2.2×10^{-13}

population of two pools, i.e., interfacial CT states and free charge carriers, not interacting with each other.[6]

Table 2 summarizes the effective Langevin recombination coefficients obtained for the previously reported polymer:fullerene blends[6,51] and compares these values to those obtained for the PCPDTBT:PCBM blends presented in this study. One significant difference is apparent from the comparison with previous results. The recombination coefficient of the PCPDTBT:PCBM blends is more than 2 orders of magnitude larger compared to annealed RR-P3HT:PCBM and also more than 1 order of magnitude larger than obtained for PCDTBT:PCBM blends. Hence, it appears that nongeminate recombination of free charge carriers is significantly faster in PCPDTBT:PCBM blends. The recombination coefficients we obtained by pump−probe spectroscopy are also in excellent agreement with those recently reported by Albrecht et al., which in general further supports the validity of our measurements and data analysis.[21] The significantly larger nongeminate recombination coefficient observed for PCPDTBT:PCBM blends compared to, for instance, P3HT:PCBM implies that free charges more frequently encounter each other at the interface, and/or each encounter has a larger recombination probability in PCPDTBT:PCBM. A simple reason for the former could be a very high charge-carrier mobility in PCPDTBT:PCBM compared to P3HT:PCBM, which is, however, experimentally not observed as we will discuss later. Another reason for more frequent encounters of free charges in PCPDTBT:PCBM compared to P3HT:PCBM could be of thermodynamic origin. We have already discussed that in the exceptional case of P3HT:PCBM, the high crystallinity of the polymer creates an additional thermodynamic driving force that supports the separation of charges and their transport from the interface toward the bulk. Vice versa the same argument may explain the small nongeminate recombination coefficient observed for P3HT:PCBM in comparison to PCPDTBT:PCBM. While in the former holes are more likely to reside in the bulk of the polymer and transport toward the interface is expected to require energy, the generally higher disorder in the latter may reduce the energetic difference between interface and bulk, and thus charges can more easily approach the interface, where they can nongeminately recombine, before they can be extracted as photocurrent from the device.

In general nongeminate recombination of free charges competes with charge-carrier extraction, as we have previously shown for RR-P3HT:PCBM devices.[4] By measuring the bias dependence of nongeminate recombination for the latter, we have determined that at short circuit conditions, the fraction of nongeminate recombination is only about 2%, i.e., most of the carriers can be extracted in RR-P3HT:PCBM.[56] However, the fraction of nongeminate recombination significantly increases toward open circuit conditions, since the extraction rate of charges decreases due to the weaker internal electric field. Hence, a larger nongeminate recombination coefficient in PCPDTBT:PCBM implies that these devices suffer substantially from nongeminate losses, which certainly contributes to the low device fill factor. We note that the increased nongeminate recombination coefficient can be compensated by faster charge extraction due to a higher charge-carrier mobility. For that, mobility would have to be 2 orders of magnitude higher than observed for RR-P3HT:PCBM blends to compensate the fast nongeminate recombination in PCPDTBT:PCBM. This is experimentally not observed, for instance, Albrecht et al. reported that PCPDTBT:PCBM blends prepared with additives have a mobility similar to annealed RR-P3HT:PCBM samples.[21] When we probe the recombination dynamics in the longer wavelength NIR region, at around 1500 nm or beyond, we observe a much weaker intensity dependence of the recombination dynamics, indicating that the charges we monitor in this spectral region are different from those absorbing at the peak position of the charge-induced absorption, which is around 1300 nm in the blend prepared with ODT. Thus, it appears that here we observe mostly trapped charges undergoing a trap assisted rather than a Langevin-type recombination. The observation of a significant fraction of trapped charges is also in good agreement with previously reported transient photocurrent results by McNeill et al.[18]

Impact on Photovoltaic Performance. Let us finally comment on the implications of the recombination processes for the PCPDTBT:PCBM device performance. The total short circuit current that can be expected from a PCPDTBT:PCBM device, assuming that all absorbed photons generate free charges that thereafter can be extracted as photocurrent is 19 mA/cm^2. Our early time pump−probe experiments have shown that geminate recombination contributes to the charge-carrier loss at open circuit voltage and amounts to approximately 30%. Hence, geminate recombination alone would reduce J_{SC} to 11 mA/cm^2 at the measured light intensity around 0.86 suns, assuming that the magnitude is similar at short circuit conditions, which is a simplification, since free charge generation was recently shown to be field dependent in PCPDTBT:PCBM.[21] However, given that we observed a short circuit current of 7 mA/cm^2 at 0.86 suns in devices made with ODT as cosolvent, it is reasonable to assume that the reduction of the short circuit current is not only caused by geminate recombination but also by fast recombination of free charge carriers, as implied by the large nongeminate recombination coefficient. We have also observed that excitons do not only dissociate instantaneously but also by a diffusion-limited process, which is even more pronounced, when excitons are generated in PCBM domains. In addition we have observed some loosely bound polaron pairs in samples prepared without ODT, which recombine within several nanoseconds. Again, one may speculate that these loosely bound pairs can fully separate into free charges, if excess energy is provided by an electric field. The electric field dependence should then be more pronounced in samples prepared without ODT supported by recent time-delayed collection field experiments of the Neher group.[21] Further work will address the temperature and field dependence of the charge-induced absorption of free charges and CT states in the NIR probe range.

4. CONCLUSION

Exciton dissociation in PCPDTBT:PCBM blends led to the formation of free charges and strongly bound CT states, where the latter undergo geminate recombination with an inverse rate of 700 ps in samples prepared with ODT and 1200 ps in samples prepared without ODT. The fast subnanosecond geminate recombination caused a total loss of excited states of about 50% within the first 3 ns after photoexcitation in samples prepared without ODT, which severely limited the performance of PCPDTBT:PCBM solar cells. The fraction of subnanosecond geminate recombination was lowered to 30% in samples prepared with ODT as a solvent additive, implying a higher yield of free charge carriers. In addition to ultrafast exciton dissociation, diffusion-limited dissociation of excitons created within polymer-rich domains was observed on a time scale of 10 ps in samples prepared with ODT. The occurrence of diffusion-limited exciton dissociation was attributed to larger polymer-rich domains in samples prepared with ODT, where the increased domain size was proven by 2D $^{13}C\{^{1}H\}$ HETCOR solid-state NMR spectroscopy. Independent of the use of solvent additives diffusion-limited dissociation of excitons generated in PCBM-rich domains occurred in both blends, leading to an additional delayed formation of free charges and CT states on a time scale up to 50 ps in samples prepared without ODT and 300 ps in samples prepared with ODT. After the early time diffusion-limited exciton dissociation and subnanosecond geminate recombination of strongly bound CT states, the free charges in samples prepared with additives exclusively undergo nongeminate recombination with an effective recombination coefficient of 6.3×10^{-11} cm^3 s^{-1}, i.e., two orders of magnitude faster than previously observed for the P3HT:PCBM reference system, indicating that in PCPDTBT:PCBM nongeminate recombination efficiently competes with charge extraction. An additional nanosecond recombination component is observed in samples prepared without ODT and assigned to loosely bound polaron pairs that have not entirely managed to escape their mutual attraction. Triplet state formation appears to be of minor importance in PCPDTBT:PCBM blends as geminate recombination of CT states is too fast to allow efficient intersystem crossing.

■ ASSOCIATED CONTENT

Supporting Information

Experimental section, AFM images of blends, further TA spectra and dynamics, and EQE measurements on devices. This material is available free of charge via the Internet at http://pubs.acs.org.

■ AUTHOR INFORMATION

Corresponding Author

laquai@mpip-mainz.mpg.de

Notes

The authors declare no competing financial interest.

■ ACKNOWLEDGMENTS

F.L. is very grateful to the Max Planck Society for funding a Max Planck Research Group and acknowledges support within the priority program 1355 of the Deutsche Forschungsgemeinschaft (DFG). F.E. and M.M. thank the Max Planck Graduate Center for funding. I.A.H. acknowledges a fellowship of the Alexander von Humboldt Foundation. F.L. and F.E. thank D. Neher and E. Riedle for helpful discussions. N.F., S.J., and M.R.H. acknowledge the continuing support of Prof. Hans Wolfgang Spiess. We acknowledge financial support by the International Research Training Group 1404 and the SFB 625.

■ REFERENCES

(1) Krebs, F. C. *Sol. Energy Mater. Sol. Cells* **2009**, *93*, 394−412.
(2) Galagan, Y.; de Vries, I. G.; Langen, A. P.; Andriessen, R.; Verhees, W. J. H.; Veenstra, S. C.; Kroon, J. M. *Chem. Eng. Process.* **2011**, *50*, 454−461.
(3) Bakulin, A. A.; Rao, A.; Pavelyev, V. G.; van Loosdrecht, P. H. M.; Pshenichnikov, M. S.; Niedzialek, D.; Cornil, J.; Beljonne, D.; Friend, R. H. *Science* **2012**, *335*, 1340−1344.
(4) Mauer, R.; Howard, I. A.; Laquai, F. *J. Phys. Chem. Lett.* **2010**, *1*, 3500−3505.
(5) Guo, J.; Ohkita, H.; Benten, H.; Ito, S. *J. Am. Chem. Soc.* **2010**, *132*, 6154−6164.
(6) Howard, I. A.; Mauer, R.; Meister, M.; Laquai, F. *J. Am. Chem. Soc.* **2010**, *132*, 14866−14876.
(7) Peet, J.; Kim, J. Y.; Coates, N. E.; Ma, W. L.; Moses, D.; Heeger, A. J.; Bazan, G. C. *Nat. Mater.* **2007**, *6*, 497−500.
(8) Chu, T.-Y.; Lu, J.; Beaupré, S.; Zhang, Y.; Pouliot, J.-R. m.; Wakim, S.; Zhou, J.; Leclerc, M.; Li, Z.; Ding, J.; Tao, Y. *J. Am. Chem. Soc.* **2011**, *133*, 4250−4253.
(9) Zhou, H.; Yang, L.; Stuart, A. C.; Price, S. C.; Liu, S.; You, W. *Angew. Chem., Int. Ed.* **2011**, *50*, 2995−2998.
(10) Amb, C. M.; Chen, S.; Graham, K. R.; Subbiah, J.; Small, C. E.; So, F.; Reynolds, J. R. *J. Am. Chem. Soc.* **2011**, *133*, 10062−10065.
(11) Hou, J.; Chen, H.-Y.; Zhang, S.; Li, G.; Yang, Y. *J. Am. Chem. Soc.* **2008**, *130*, 16144−16145.
(12) Dennler, G.; Scharber, M. C.; Brabec, C. J. *Adv. Mater.* **2009**, *21*, 1323−1338.
(13) Mühlbacher, D.; Scharber, M.; Morana, M.; Zhu, Z.; Waller, D.; Gaudiana, R.; Brabec, C. *Adv. Mater.* **2006**, *18*, 2884−2889.
(14) Albrecht, S.; Schäfer, S.; Lange, I.; Yilmaz, S.; Dumsch, I.; Allard, S.; Scherf, U.; Hertwig, A.; Neher, D. *Org. Electron.* **2012**, *13*, 615−622.
(15) Agostinelli, T.; Ferenczi, T. A. M.; Pires, E.; Foster, S.; Maurano, A.; Müller, C.; Ballantyne, A.; Hampton, M.; Lilliu, S.; Campoy-Quiles, M.; Azimi, H.; Morana, M.; Bradley, D. D. C.; Durrant, J.; Macdonald, J. E.; Stingelin, N.; Nelson, J. *J. Polym. Sci., Part B: Polym. Phys.* **2011**, *49*, 717−724.
(16) Morana, M.; Azimi, H.; Dennler, G.; Egelhaaf, H.-J.; Scharber, M.; Forberich, K.; Hauch, J.; Gaudiana, R.; Waller, D.; Zhu, Z.; Hingerl, K.; van Bavel, S. S.; Loos, J.; Brabec, C. J. *Adv. Funct. Mater.* **2010**, *20*, 1180−1188.
(17) Lenes, M.; Morana, M.; Brabec, C. J.; Blom, P. W. M. *Adv. Funct. Mater.* **2009**, *19*, 1106−1111.
(18) Li, Z.; McNeill, C. R. *J. Appl. Phys.* **2011**, *109*, 074513−074520.
(19) Cho, S.; Lee, J. K.; Moon, J. S.; Yuen, J.; Lee, K.; Heeger, A. J. *Org. Electron.* **2008**, *9*, 1107−1111.
(20) Hwang, I. W.; Cho, S.; Kim, J. Y.; Lee, K.; Coates, N. E.; Moses, D.; Heeger, A. J. *J. Appl. Phys.* **2008**, *104*, 33706−33714.
(21) Albrecht, S.; Schindler, W.; Kurpiers, J.; Kniepert, J.; Blakesley, J. C.; Dumsch, I.; Allard, S.; Fostiropoulos, K.; Scherf, U.; Neher, D. *J. Phys. Chem. Lett.* **2012**, 640−645.
(22) Jamieson, F. C.; Agostinelli, T.; Azimi, H.; Nelson, J.; Durrant, J. R. *J. Phys. Chem. Lett.* **2010**, *1*, 3306−3310.
(23) Clarke, T.; Ballantyne, A.; Jamieson, F.; Brabec, C.; Nelson, J.; Durrant, J. *Chem. Commun.* **2009**, 89−91.
(24) Hwang, I. W.; Soci, C.; Moses, D.; Zhu, Z.; Waller, D.; Gaudiana, R.; Brabec, C. J.; Heeger, A. J. *Adv. Mater.* **2007**, *19*, 2307−2312.
(25) Grancini, G.; Martino, N.; Antognazza, M. R.; Celebrano, M.; Egelhaaf, H.-J.; Lanzani, G. *J. Phys. Chem. C.* **2012**, *116*, 9838−9844.
(26) Jarzab, D.; Cordella, F.; Gao, J.; Scharber, M.; Egelhaaf, H.-J.; Loi, M. A. *Adv. Energy Mater.* **2011**, *1*, 604−609.

(27) Scharber, M. C.; Lungenschmied, C.; Egelhaaf, H.-J.; Matt, G.; Bednorz, M.; Fromherz, T.; Gao, J.; Jarzab, D.; Loi, M. A. *Energy Environ. Sci.* **2011**, 5077−5083.
(28) Deschler, F.; Da Como, E.; Limmer, T.; Tautz, R.; Godde, T.; Bayer, M.; von Hauff, E.; Yilmaz, S.; Allard, S.; Scherf, U.; Feldmann, J. *Phys. Rev. Lett.* **2011**, *107*, 127402−127405.
(29) Di Nuzzo, D.; Aguirre, A.; Shahid, M.; Gevaerts, V. S.; Meskers, S. C. J.; Janssen, R. A. J. *Adv. Mater.* **2010**, *22*, 4321−4324.
(30) Tasios, N.; Grigoriadis, C.; Hansen, M. R.; Wonneberger, H.; Li, C.; Spiess, H. W.; Müllen, K.; Floudas, G. *J. Am. Chem. Soc.* **2010**, *132*, 7478−7487.
(31) Hansen, M. R.; Feng, X.; Macho, V.; Müllen, K.; Spiess, H. W.; Floudas, G. *Phys. Rev. Lett.* **2011**, *107*, 257801−257805.
(32) Saalwächter, K. *Prog. Nucl. Magn. Reson. Spectrosc.* **2007**, *51*, 1−35.
(33) Bohle, A.; Brunklaus, G.; Hansen, M. R.; Schleuss, T. W.; Kilbinger, A. F. M.; Seltmann, J.; Spiess, H. W. *Macromolecules* **2010**, *43*, 4978−4985.
(34) Rapp, A.; Schnell, I.; Sebastiani, D.; Brown, S. P.; Percec, V.; Spiess, H. W. *J. Am. Chem. Soc.* **2003**, *125*, 13284−13297.
(35) Khan, M.; Enkelmann, V.; Brunklaus, G. *J. Am. Chem. Soc.* **2010**, *132*, 5254−5263.
(36) Mafra, L.; Santos, S. M.; Siegel, R.; Alves, I.; Almeida Paz, F. A.; Dudenko, D.; Spiess, H. W. *J. Am. Chem. Soc.* **2011**, *134*, 71−74.
(37) Yang, C.; Hu, J. G.; Heeger, A. J. *J. Am. Chem. Soc.* **2006**, *128*, 12007−12013.
(38) Nieuwendaal, R. C.; Ro, H. W.; Germack, D. S.; Kline, R. J.; Toney, M. F.; Chan, C. K.; Agrawal, A.; Gundlach, D.; VanderHart, D. L.; Delongchamp, D. M. *Adv. Funct. Mater.* **2012**, *22*, 1255−1266.
(39) Chambon, S.; Mens, R.; Vandewal, K.; Clodic, E.; Scharber, M.; Lutsen, L.; Gelan, J.; Manca, J.; Vanderzande, D.; Adriaensens, P. *Sol. Energy Mater. Sol. Cells* **2012**, *96*, 210−217.
(40) Schmidt-Rohr, K.; Spiess, H. W. *Multidimensional Solid-State NMR and Polymers*; Academic Press Limited: London, U.K., 1994.
(41) van Rossum, B. J.; Förster, H.; de Groot, H. J. M. *J. Magn. Reson.* **1997**, *124*, 516−519.
(42) Bielecki, A.; Kolbert, A. C.; Levitt, M. H. *Chem. Phys. Lett.* **1989**, *155*, 341−346.
(43) Vanlaeke, P.; Swinnen, A.; Haeldermans, I.; Vanhoyland, G.; Aernouts, T.; Cheyns, D.; Deibel, C.; D'Haen, J.; Heremans, P.; Poortmans, J.; Manca, J. V. *Sol. Energy Mater. Sol. Cells* **2006**, *90*, 2150−2158.
(44) Rogers, J. T.; Schmidt, K.; Toney, M. F.; Kramer, E. J.; Bazan, G. C. *Adv. Mater.* **2011**, *23*, 2284−2288.
(45) Rogers, J. T.; Schmidt, K.; Toney, M. F.; Bazan, G. C.; Kramer, E. J. *J. Am. Chem. Soc.* **2012**, *134*, 2884−2887.
(46) Lu, H.; Akgun, B.; Russell, T. P. *Adv. Energy Mater* **2011**, *1*, 870−878.
(47) Lou, S. J.; Szarko, J. M.; Xu, T.; Yu, L.; Marks, T. J.; Chen, L. X. *J. Am. Chem. Soc.* **2011**, *133*, 20661−20663.
(48) Dimitrov, S. D.; Nielsen, C. B.; Shoaee, S.; Shakya Tuladhar, P.; Du, J.; McCulloch, I.; Durrant, J. R. *J. Phys. Chem. Lett.* **2011**, *3*, 140−144.
(49) Albert-Seifried, S.; Friend, R. H. *Appl. Phys. Lett.* **2011**, *98*, 223304−223303.
(50) Zhang, F.; Jespersen, K. G.; Björström, C.; Svensson, M.; Andersson, M. R.; Sundström, V.; Magnusson, K.; Moons, E.; Yartsev, A.; Inganäs, O. *Adv. Funct. Mater.* **2006**, *16*, 667−674.
(51) Etzold, F.; Howard, I. A.; Mauer, R.; Meister, M.; Kim, T.-D.; Lee, K.-S.; Baek, N. S.; Laquai, F. *J. Am. Chem. Soc.* **2011**, *133*, 9469−9479.
(52) Agostinelli, T.; Lilliu, S.; Labram, J. G.; Campoy-Quiles, M.; Hampton, M.; Pires, E.; Rawle, J.; Bikondoa, O.; Bradley, D. D. C.; Anthopoulos, T. D.; Nelson, J.; Macdonald, J. E. *Adv. Funct. Mater.* **2011**, *21*, 1701−1708.
(53) Holcombe, T. W.; Norton, J. E.; Rivnay, J.; Woo, C. H.; Goris, L.; Piliego, C.; Griffini, G.; Sellinger, A.; Brédas, J.-L.; Salleo, A.; Fréchet, J. M. J. *J. Am. Chem. Soc.* **2011**, *133*, 12106−12114.
(54) Pensack, R. D.; Guo, C.; Vakhshouri, K.; Gomez, E. D.; Asbury, J. B. *J. Phys. Chem. C* **2012**, *116*, 4824−4831.
(55) Pal, S. K.; Kesti, T.; Maiti, M.; Zhang, F.; Inganäs, O.; Hellström, S.; Andersson, M. R.; Oswald, F.; Langa, F.; Österman, T.; Pascher, T.; Yartsev, A.; Sundström, V. *J. Am. Chem. Soc.* **2010**, *132*, 12440−12451.
(56) Mauer, R.; Howard, I. A.; Laquai, F. *J. Phys. Chem. Lett.* **2011**, *2*, 1736−1741.

Supporting Information

The Effect of Solvent Additives on Morphology and Excited State Dynamics in PCPDTBT:PCBM Photovoltaic Blends

Fabian Etzold, Ian A. Howard, Nina Forler, Don M. Cho, Michael Meister, Hannah Mangold, Jie Shu, Michael Ryan Hansen, Klaus Müllen and Frédéric Laquai*

1. Experimental Section

Polymer synthesis: The synthesis of PCPDTBT used in the present study has been described elsewhere.[1] The resulting polymer was purified using several techniques. It was first subject to multiple precipitations, dissolved first into dichlorobenzene and precipitated into rapidly stirring methanol (repeated 3 times). It was then subjected to a series of Soxhlet extractions, with hexanes, acetone, and ethyl acetate, respectively, as solvents, each washing the polymer for 24 hours. PCPDTBT was dissolved into dichlorobenzene and stirred at 50 ^{o}C with Basolite A100 for one hour. The solution was cooled to room temperature and passed through a column of celite, then precipitated into methanol and dried under vacuum.

Solid-state nuclear magnetic resonance spectroscopy: Solid-state magic-angle spinning (MAS) NMR experiments were carried out on a Bruker Avance III instrument (20.0 T, ν_L = 850.27 MHz for ^{1}H, ν_L = 213.82 MHz for ^{13}C) equipped with a commercial 2.5 mm double resonance probe (Bruker). 1D ^{13}C NMR spectra were obtained through ^{13}C{^{1}H} cross-polarization (CP) at a spinning frequency of 25.0 kHz using a repetition delay of 2 s and a total number of scans varying from 24576 to 49152, depending on the available amount of sample. 2D ^{13}C{^{1}H} Frequency Switched Lee-Goldburg (FSLG)[2] heteronuclear correlation (HETCOR)[3] spectra were recorded at a spinning frequency of 15.0 kHz using a repetition delay of 2s and a number of scans varying from 896 and 2176 for a total of 96 t_1 increments. The 2D experiments also employed LG-CP conditions. For both 1D and 2D NMR experiments, the specific CP conditions were preoptimized on L-alanine. The CP contact time was set to 1 ms for all spectra and two-pulse phase modulation (TPPM) high-power ^{1}H decoupling was applied during acquisition. All spectra were referenced to adamantane as a secondary standard (δ_{iso} = 1.85 ppm for ^{1}H, δ_{iso}= 38.484 for ^{13}C)[4]. Identical processing conditions were used for all 1D and 2D spectra. All 2D spectra are plotted on the same intensity scale with 13 contour lines from 10.1 to 90% of the maximum intensity using the DMFIT software.[5]

Sample preparation: For solar-cell preparation ITO-coated glass substrates (Präzisions Glas & Optik GmbH, Germany) were patterned by wet etching and successively cleaned in an ultrasonic bath with isopropanol and ethanol. Between the cleaning steps the samples were dried by blowing

with dry nitrogen gas. Prior to spin-coating of the organic films, the substrates were plasma etched for 15 min in argon plasma. After spincoating of a 20-nm layer of poly(3,4-ethylene-dioxythiopene):poly-(styrenesulfonate) (PEDOT:PSS) (Clevios P VP Al 4083, H.C. Stark), the samples were transferred into a nitrogen-filled glovebox and baked for 1 h at 120 °C. For preparation of the active layer PCPDTBT and PCBM were separately dissolved in chlorobenzene at 80 °C with concentrations of 20 mg/ml for PCPDTBT and 40 mg/ml for PCBM, stirred overnight and then mixed in a weight ratio of 1:2 so that a PCPDTBT concentration of 10 mg/ml is obtained. For devices prepared with the solvent additive additional 2.4 vol % 1,8-octanedithiol (ODT) were added to the solution. The hot solution was spin-cast at 80 °C at 1400 rpm for 40 s resulting in an active layer thickness of around 150 nm as measured by a Dektak profiler. Afterwards the thin films were kept overnight in high vacuum to remove the high boiling point ODT. Subsequently a 100 nm layer of aluminum was evaporated as top electrode.
The preparation of blend films for optical spectroscopy followed the same preparation procedure as for the devices with the only difference that quartz substrates were used instead of ITO substrates. For the preparation of pristine polymer films a polymer concentration of 15 mg/ml in chlorobenzene was used and for the PCPDTBT films with triplet sensitizer additional 40 wt.% of platinum-octaethyl-porphyrin (PtOEP) were added.

Solar cell characterization: Solar-cell device characterization was performed inside a nitrogen-filled glovebox employing a solar simulator (K.H. Steuernagel Lichttechnik GmbH, Germany) with a 575 W metal halide lamp combined with a filter system to create a spectrum according to AM1.5G conditions, however, with a reduced intensity of 86 mW/cm^2. The current-voltage curves were measured with a Keithley 236 Source-Measure-Unit.
For external quantum efficiency (EQE) measurements monochromatic light was created with a metal-helide lamp (Müller Elektronik-Optik XH100) and a monochromator (Model 1235 Digital Triple Grating Spectrograph, Princeton Applied Research) between 300 and 1000 nm. The light intensity was measured with a calibrated silicon diode. EQE measurements were performed in air at short circuit conditions with a Keithley 236 Source-Measure Unit.

Steady-State Spectroscopy: The absorption measurements were conducted with a Perkin-Elmer Lambda 25 spectrophotometer. For photoluminescence measurements the samples were excited by a 808 nm diode laser, and the photoluminescence was dispersed in a spectrograph (Shamrock SR-303i) and recorded by a CCD line array detector (Ames Photonics, Larry-2048).

Quasi steady-state Photoinduced Absorption Spectroscopy: Quasi steady-state photoinduced absorption spectroscopy (PIA) was performed with a pump-probe setup consisting of a 100 W tungsten-halogen lamp with a LOT Oriel Omni-λ 300 monochromator as the probe and a Newport LED (LED-527-HP) working at 524 nm with 100 $mWcm^{-2}$ used as a pump. As a further pump source a Helium-Neon-laser was used at 633 nm with $20mW/cm^2$. The samples were placed in a nitrogen-cooled optical cryostat (Oxford Instruments Optistat CF) at 80 K in helium atmosphere. The transmitted light was dispersed by a second identical monochromator and then detected by a photodetector. For measurements in the wavelength range from 500 to 1100 nm, an amplified silicon photodetector (Thorlabs PDA 100A) was employed, which was replaced by an amplified germanium detector (Thorlabs PDA 50B) for the wavelength range from 900 to 1800 nm. For the spectral range between 1750 to 4500 nm, a nitrogen cooled indium antimonide (InSb) detector from Teledyne Judson Technologies was used. The pump light was chopped at 317 Hz to induce changes in the transmission ΔT, which were measured by using a lock-in amplifier

(EG&G Princeton Applied Research model 5210). To calculate ΔT/T, the transmission was recorded prior to the PIA measurement and corrected for photoluminescence.

Transient Absorption Spectroscopy: Transient absorption (TA) measurements were performed with a home-built pump-probe setup. The output of a commercial titanium:sapphire amplifier (Coherent LIBRA HE, 3.5 mJ, 1 kHz, 100 fs) was split into two beams that independently pumped two optical parametric amplifiers (Coherent OPerA Solo). One optical parametric amplifier (OPA) was used to generate the excitation pulses in the visible, while the second OPA was used to generate the seed beam for white-light generation. For measurements in the spectral range between 550-1100 nm a 1300 nm seed was focused into a c-cut 3 mm thick sapphire window for white-light generation. The variable delay of up to 4 ns between pump and probe was introduced by a broadband retroreflector mounted on a mechanical delay stage. Only reflective elements were used to guide the probe beam to the sample to minimize chirp. The excitation pulse was chopped at 500 Hz, while the white-light pulses were dispersed onto a linear silicon photodiode array, which was read out at 1 kHz. Adjacent diode readings corresponding to the transmission of the sample after an excitation pulse and without an excitation pulse were used to calculate ΔT/T.
For measurements in the time range between 1 ns to 1 ms with a resolution of 600 ps, the excitation pulse was provided by an actively Q-switched Nd:YVO4 laser (AOT Ltd. MOPA) at 532 nm. The delay between pump and probe in this case was controlled by an electronic delay generator (Stanford Research Systems DG535). TA measurements were performed at room temperature under a dynamic vacuum of $<10^{-5}$ mbar.
For TA measurements in the NIR spectral range covering 1100 - 2000 nm a 2100 nm seed was used to generate white-light and a polished silicon substrate was added into the path of the white light to block the visible fraction of the supercontinuum. Furthermore, a dichroic mirror was used to separate the residual idler beam (2100 nm) from the white-light supercontinuum. The NIR white-light pulses were dispersed onto a Peltier-cooled 512 pixel long linear extended InGaAs array (Entwicklungsbüro Stresing) and read out as described above.

2. Additional Measurements

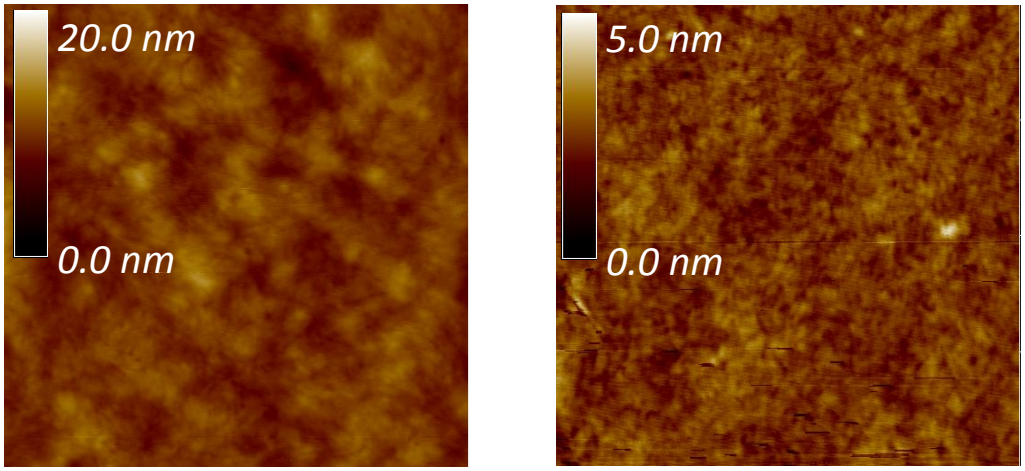

Figure S1. AFM height images of PCPDTBT:PCBM = 1:2 blend films processed with ODT (left) and without ODT (right). The size of the measured sample area is 1 × 1 µm^2.

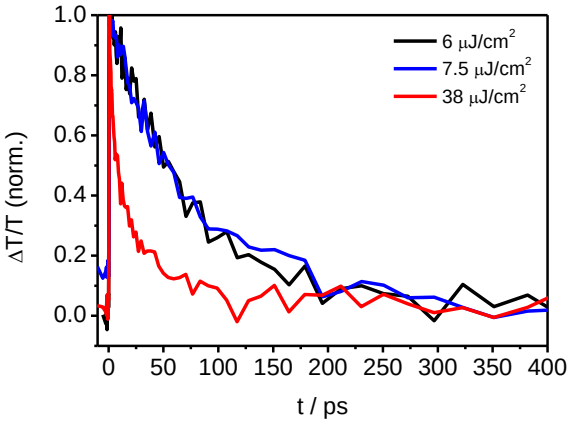

Figure S2. TA kinetics of pristine PCPDTBT films prepared with ODT averaged between 1500-1700 nm. The kinetics obtained at low fluences are virtually similar, whereas at a pump fluence of 38 µJ/cm^2 nonlinear effects such as singlet-singlet annihilation shorten the exciton lifetimes.

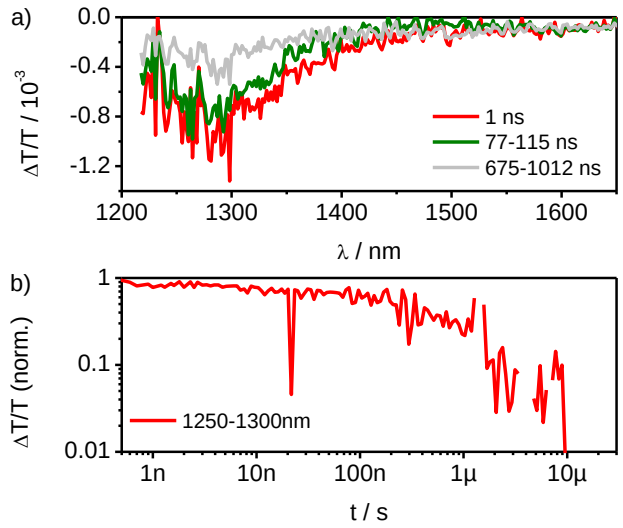

Figure S3. Long delay TA data of pristine PCPDTBT excited at 532 nm with a pump fluence of 67 µJ/cm^2. a) In the spectra of pristine PCPDTBT a very weak, long-lived transient signal between 1250-1350 nm can be observed indicating the existence of triplets. The spectrum is smoothed to reduce the noise at smaller wavelengths. b) The kinetics averaged between 1250-1300 nm show an average lifetime of 1 µs. However, they do not obey a mono-exponential decay.

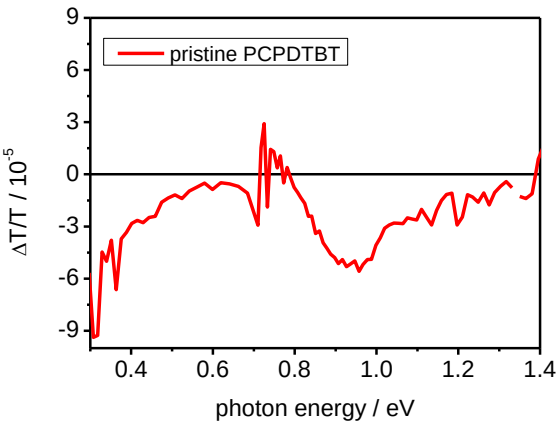

Figure S4. Quasi-steady-state photoinduced absorption spectrum of pristine PCPDTBT excited at 524 nm. The artifact at 0.7 eV is caused by a detector change during the wavelength scan. Interestingly the main peak at 0.9 eV is not only caused by long-lived triplets but also by charges, as a second photoinduced absorption around 0.4 eV can be observed.

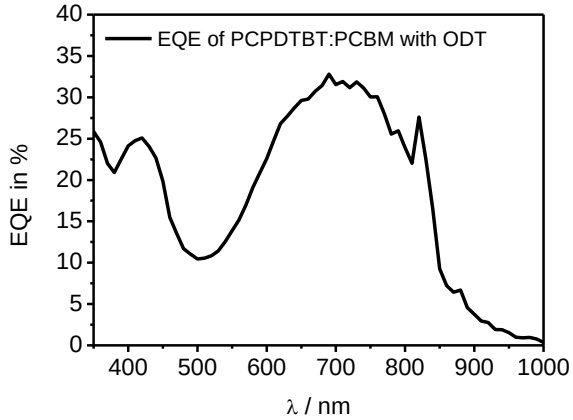

Figure S5. External quantum efficiency (EQE) for a PCPDTBT:PCBM = 1:2 device prepared with ODT. The low EQE of 30 % explains the poor performance of 2 % PCE.

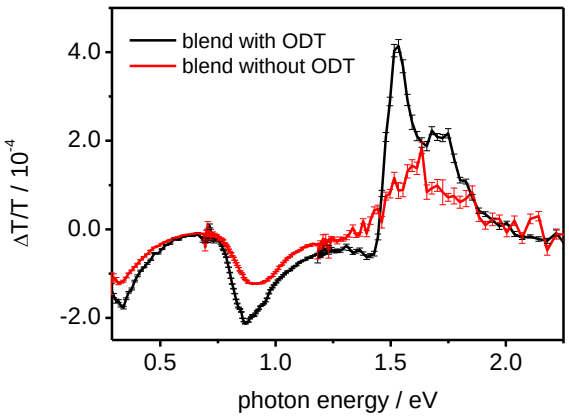

Figure S6. Quasi-steady-state photoinduced absorption spectrum of PCPDTBT:PCBM prepared with and without ODT. The samples were excited at 633 nm and ΔT/T is normalized to the fraction of absorbed photons for direct comparison of signal intensities. A typical charge-induced absorption spectrum can be seen in the NIR with one peak at 0.9 eV and second peak farther in the NIR at 0.4 eV.

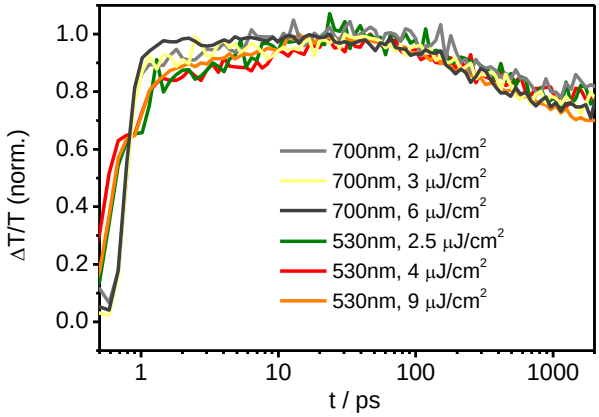

Figure S7. Short delay charge-induced absorption dynamics as obtained from TA measurements of PCPDTBT:PCBM films (1:2) processed with ODT and excited at at 530 nm and 700 nm, respectively. Upon excitation at 700 nm the initial rise during the first 50 ps is less than after excitation at 530 nm.

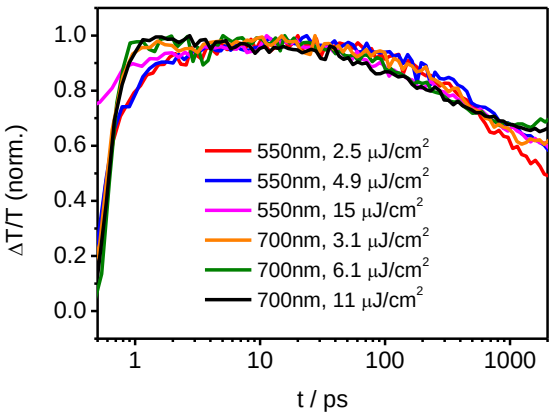

Figure S8. Short delay charge-induced absorption dynamics obtained from TA measurements on PCPDTBT:PCBM (1:2) films processed without ODT and excited at 530 nm and 700 nm, respectively. A clear difference in the amplitude of the rise can be observed.

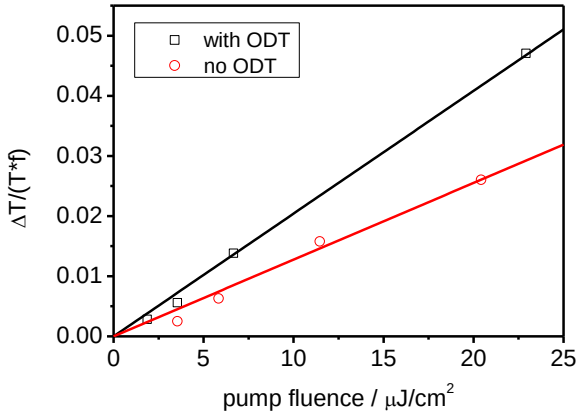

Figure S9. Maximum signal height at the peak position of charge-induced absorption taken from the long delay NIR-TA measurements for the blend prepared with and w/o ODT. The signal height is divided by the fraction of absorbed pump photons. Both signals follow a linear increase with pump fluence indicating the absence of higher order processes at the fluences used.

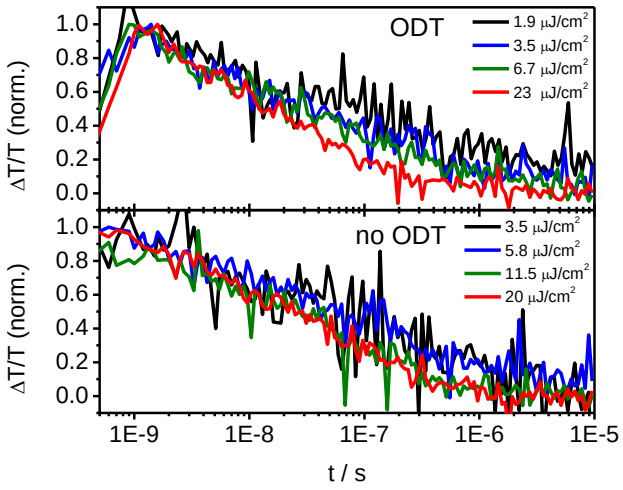

Figure S10. Dynamics of the charge-induced absorption of PCPDTBT:PCBM films prepared with or without ODT averaged over a wavelength range between 1450-1500 nm. The fluence dependence is strongly reduced compared to the dynamics obtained at the peak of the charge-induced absorption indicating that trapped charge carriers are probed in this spectral region.

(1) Zhang, M.; Tsao, H. N.; Pisula, W.; Yang, C.; Mishra, A. K.; Müllen, K. *J. Am. Chem. Soc.* **2007**, *129*, 3472.
(2) Bielecki, A.; Kolbert, A. C.; Levitt, M. H. *Chem. Phys. Lett.* **1989**, *155*, 341.
(3) van Rossum, B. J.; Förster, H.; de Groot, H. J. M. *J. Magn. Reson.* **1997**, *124*, 516.
(4) Morcombe, C. R.; Zilm, K. W. *J. Magn. Reson.* **2003**, *162*, 479.
(5) Massiot, D.; Fayon, F.; Capron, M.; King, I.; Le Calvé, S.; Alonso, B.; Durand, J.-O.; Bujoli, B.; Gan, Z.; Hoatson, G. *Magn. Reson. Chem.* **2002**, *40*, 70.

4.3 Sub-ns triplet generation in low-bandgap polymer fullerene blends

The third donor polymer investigated in this thesis is called poly[(4,4'-bis(2-ethylhexyl)dithieno[3,2-b:2',3'-d]silole)-2,6-diyl-alt-(2,1,3-benzothiadiazole)-4,7-diyl] (PSBTBT) and has strong similarities to PCPDTBT, discussed in the last section. The difference between the two polymers is the bridgehead atom, which is carbon in PCPDTBT and silicon in PSBTBT. The substitution is reported to have significant impact on the morphology and device performance in a blend with $PC_{70}BM$. Hou et al. published the synthesis of PSBTBT first and reported a three times larger organic field effect transistor (OFET) hole mobility compared to PCPDTBT, which led to a PCE of 5.1 % in a solar cell with $PC_{70}BM$.[114]. According to Chen et al. the increase in hole mobility can be explained by improved π-π stacking caused by a larger bond length of C-Si in PSBTBT compared to the C-C bond in PCPDTBT. The greater bond length reduces steric hindrance from the bulky alkyl chains and transforms the amorphous PCPDTBT morphology into a more crystalline structure for PSBTBT.[115] Similar conclusions were drawn by Morana et al., who used XRD to confirm the improved π-π-stacking.[116] They further reported a higher charge photogeneration yield for PSBTBT and correlated that to a reduction of CT state recombination. To reach high efficiencies exceeding 5 % a reduced amount of PCBM is needed as balanced charge transport is only possible at lower acceptor concentrations. Compared to PCPDTBT, PSBTBT exhibits a larger phase segregation, which is similar to that of PCPDTBT processed upon addition of a high boiling point cosolvent.[116] The importance of balanced charge transport was further investigated by Choudhury et al., who used current-voltage measurements to demonstrate the build-up of space charge, limiting the device performance in a system with unbalanced charge transport.[117] A further explanation for the higher performance of the silicon-substituted polymer was put forward by Distler et al. With cw-PIA measurements they demonstrated that recombination into the polymer triplet state could limit the device performance in PCPDTBT, whereas this loss channel seemed to be reduced in PSBTBT.[118] Rao et al. recently proposed a similar loss channel for PCPDTBT:PCBM solar cells which they further investigated by employing TAS.[119].

The photogeneration of a singlet exciton in OPV blends is directly followed by a charge transfer reaction in which hot CT states with spin singlet character are generated. The cooling of the CT state is then in kinetic competition with the dissociation of the CT state into free charge carriers. Previous investigations revealed that relaxed CT states undergo geminate recombination and thus contribute a loss channel to the solar cell performance.[11, 75, 78, 112] A second pathway to populate CT states results from bimolecular recombination of free charge carriers which either dissociate again or recombine to the ground state. As recently discussed by Chow et al., the population of CT states with spin triplet character via a bimolecular recombination reaction has been neglected in the OPV community so far, as the CT state was usually considered to be the lowest accessible state in the system.[120] However, if the triplet state of the donor or acceptor is energetically lower, the CT triplet state can transfer into this state, and this process competes with the redissociation of the CT triplet state into free charge carriers. Rao et al. and Chow et al. observed these processes on a ns timescale for two low-bandgap systems.[119, 120] By employing high sensitivity broadband NIR transient absorption spectroscopy in combination with global analysis, we present further proof for the role of triplet states as a loss channel in PSBTBT:$PC_{70}BM$. We observe carrier concentration dependent triplet generation in this material system, even on a sub-ns timescale and discuss possible generation pathways. Finally, the results are compared to those previously obtained for PCPDTBT, where investigation with the NIR-extended TAS setup (see 3.3.2) and the novel soft modeling data analysis method led us to revisit the previous conclusions.

4.3.1 Device performance and steady-state spectroscopy

The solar cells using PSBTBT:$PC_{70}BM$ as an active layer were fabricated in a 1:1.5 donor acceptor ratio from solution, with a donor concentration of 14 mg/ml. o-DCB was used as a solvent. Figure 4.1a displays the J-V curves for PSBTBT:$PC_{70}BM$ devices compared to the performance of PCPDTBT. Clearly, PSBTBT:$PC_{70}BM$ is the best performing material system with efficiencies exceeding 4.5 % (see table 4.1) and the highest fill-factor of 64 %. It is worth mentioning that these efficiencies were obtained without additional cosolvents like ODT or DIO, which clearly increased the performance when the carbon bridged donor polymer was used.

Additionally, thermal annealing did not increase the performance for PSBTBT-based devices although literature results are controversial in this respect.[35, 121] Figure 4.1b shows the corresponding absorption spectra for the different blend systems, from which a comparable optical bandgap for PCPDTBT and PSBTBT can be deduced. A broader absorption can therefore be ruled out as the reason for the higher performance of PSBTBT-based devices. Interestingly, the absorption spectrum of the PSBTBT blend exhibits stronger vibronic structures, which is in good agreement with improved packing and higher order of this material system reported by Chen et al.[115]

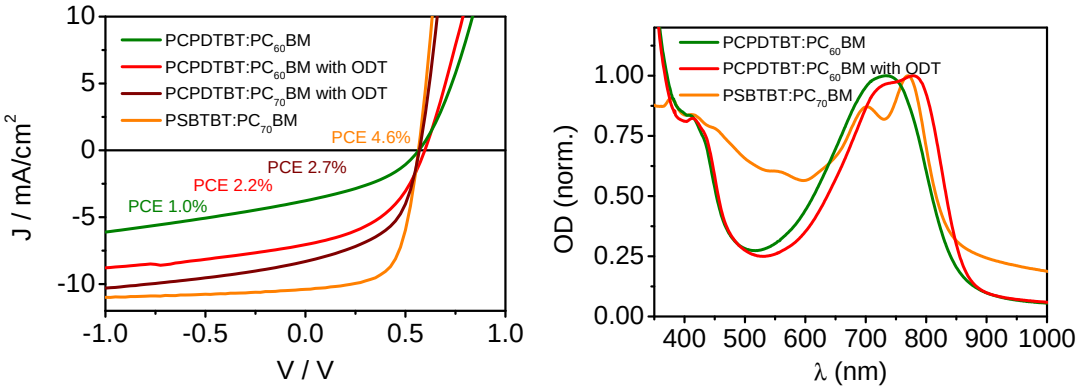

Figure 4.1: Device performance and steady-state absorption spectra of PCPDTBT:$PC_{60}BM$, PCPDTBT:$PC_{60}BM$ with ODT, PCPDTBT:$PC_{70}BM$ with ODT, and PSBTBT:$PC_{70}BM$.

System	PCE	FF	J_{SC} / mA/cm^2	V_{OC} / V
PCPDTBT:PC_{60}BM	1.0	0.38	3.8	0.57
PCPDTBT:PC_{60}BM ODT	2.2	0.45	7.0	0.60
PCPDTBT:PC_{70}BM ODT	2.7	0.51	8.3	0.57
PSBTBT:PC_{70}BM	4.6	0.64	10.4	0.57

Table 4.1: PCE, fill-factor, short-circuit current, and open-circuit voltage of the devices.

4.3.2 Investigation of ns-μs excited state dynamics

In this section we want to focus on the long time excited state kinetics in PSBTBT:PC_{70}BM. The NIR TA data surface for an excitation of 2.9 μJ/cm^2

at 532 nm is displayed in figure 4.2a, showing a prominent peak that slightly shifts to the red at longer times. The blend produces decent OPV performance and therefore charge carrier absorption definitely contributes to the NIR TA spectrum. This is in agreement with a previous assignment from cw-PIA by Distler et al.[118] However, the situation is more complicated than that, as an evolving factor analysis (see 3.3.4) of the long time data reveals that two species are present almost throughout the entire time range of the experiment. Figure 4.2b shows the EFA of the data in figure 4.2a. The black lines indicate the forward EFA in which the rise of each black line represents the time point at which the species represented by the line contributes to the signal. The red lines are obtained from the backward EFA and the rise of this line starting from the right side can be used to approximately determine how long the represented species is present. Two components in the figure clearly rise above the background level, meaning that those two components carry the information describing the data surface, whereas the other components ideally only contain experimental noise. To identify the second long-lived species besides the charge carriers, MCR-ALS

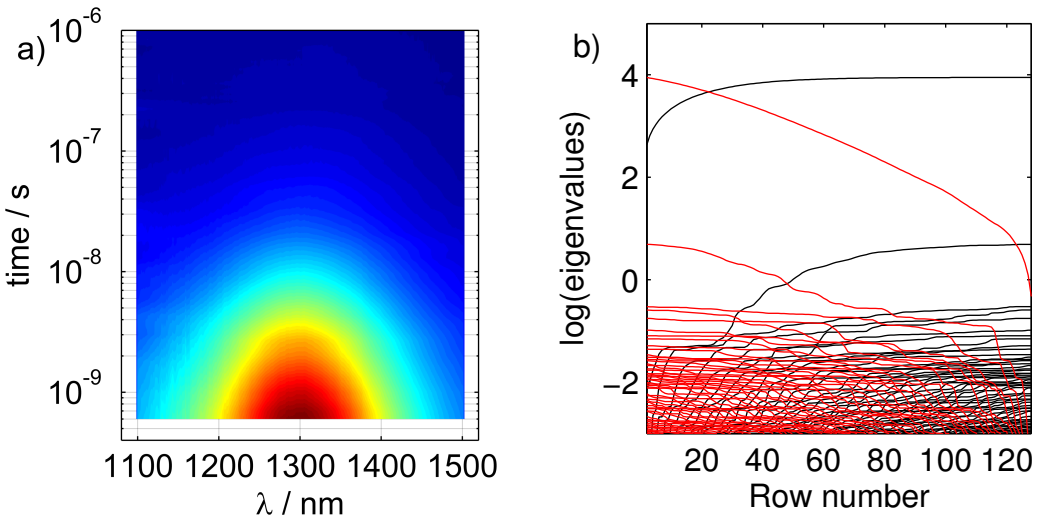

Figure 4.2: a) Normalized data surface of the long time TA experiments for PSBTBT:$PC_{70}BM$ excited at 532 nm with 2.9 $\mu J/cm^2$. b) Corresponding evolving factor analysis. The black lines represent the forward EFA, the red lines are the backward EFA. The first two components rise above the majority of the residual components, indicating that two long-lived species are present in this blend system.

analysis was performed on six different excitation densities at the same time. Figure 4.3a shows the initial results of the deconvolution as open squares for species one. The absorption of triplet states on the polymer is shown for comparison as a solid black line, and it represents an almost perfect match of the spectrum of species one obtained from MCR-ALS. This implies that the second long-lived species present in the blend are polymer triplet states. The triplet spectrum was measured on a blend film consisting of PSBTBT and the triplet sensitizer PtOEP. The sensitizer was chosen to increase the polymer triplet population via Dexter energy transfer from the porphyrin, as the ISC rate is small in the pristine polymer. Additional measurements on the pristine material revealed a similar triplet spectrum (but with very small signal height) confirming that the energy transfer from PtOEP to PSBTBT works. From this experiment, we know the spectrum of one species and thus can use it as an input for the MCR-ALS analysis. The results of the convolution for species two are shown in figure 4.3a as a thick black dashed line together with the corresponding kinetics of the species in figure 4.3b for an excitation density of $4\,\mu\mathrm{J/cm^2}$.

The deconvolution of the data matrix with MCR-ALS produces two spectra and concentration profiles which well describe the measured data in terms of a least-squares deviation. Unfortunately, this decomposition is not unique as can be seen from the following transformation.[106] The measured data matrix D can be written as the product of the matrix C containing the concentration profiles and the matrix S, which are the cross-sections of the species. However, any invertible matrix T can be introduced to change C and S creating a new set of concentrations and species that equally well describe the initial matrix. Mathematically this can be written as

$$D = CS = (CT)(T^{-1}S) = C_{new}S_{new}. \tag{4.1}$$

The matrix T can be represented by a mixing matrix M and a scaling matrix F, so that in the case of two species the new concentration profiles and spectra are given by [106]

$$\boldsymbol{C_{1,new}} = \boldsymbol{C_1} + c\boldsymbol{C_2} \tag{4.2}$$

$$\boldsymbol{C_{2,new}} = b\boldsymbol{C_1} + \boldsymbol{C_2} \tag{4.3}$$

$$\boldsymbol{S_{1,new}} = (\boldsymbol{S_1} - b\boldsymbol{S_2})\frac{1}{1-bc} \tag{4.4}$$

$$\boldsymbol{S_{2,new}} = (-c\boldsymbol{S_1} + \boldsymbol{S_2})\frac{1}{1-bc}, \tag{4.5}$$

with

$$T = MF = \begin{pmatrix} 1 & b \\ c & 1 \end{pmatrix} \begin{pmatrix} a & 0 \\ 0 & d \end{pmatrix} \tag{4.6}$$

$$CS = (\boldsymbol{C_1}, \boldsymbol{C_2}) \begin{pmatrix} \boldsymbol{S_1} \\ \boldsymbol{S_2} \end{pmatrix}. \tag{4.7}$$

In our case, we know the spectrum of the triplet, and therefore further restrictions for the subset of possible solutions can be imposed. If $\boldsymbol{S_1}$ represents the triplets then it directly follows that the parameter $b = 0$, and only c can be further varied.[106] The colored lines in figures 4.3a and 4.3b show how the second spectrum and the corresponding kinetics vary with the rotation parameter c. The values for c are already chosen in a way that neither spectra nor kinetics show negative values because negative concentrations are not physically meaningful and negative spectra would indicate a bleaching or emission which is also unlikely in this blend at this spectral position. The initial solution is already the most sequential solution possible without creating negative values in the spectra or concentration profiles, restricting the allowed values for the rotation parameter c to positive values. Figure 4.3a shows the changes of species two for an increasing c parameter. The larger c gets, the more spectrally separated the two species become, causing a more parallel solution. However, between the values of $c = 0.5$ and $c = 0.7$ the spectrum of species 2 starts to mirror the peak position of species 1 to artificially enable even more parallel solutions. This is rather unlikely and shows that the true solution approximately lies in the parameter space of $c = 0$ to $c = 0.5$. With this analysis we were able to decrease the subset of possible solutions, but a look at the corresponding kinetics in figure 4.3b clearly demonstrates that the uncertainty is still too large to draw meaningful conclusions. The uncertainty in the deconvolution is especially challenging in this material system as the spectra of the two species are so strongly overlapping.

For further analysis more information about the charge-induced absorption spectrum needs to be obtained. For this reason we carried out chemical oxidation

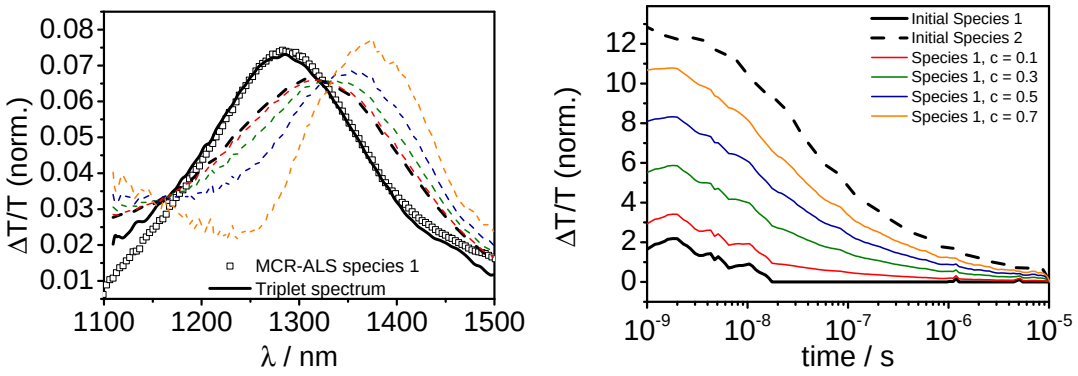

Figure 4.3: Deconvolution obtained from MCR-ALS analysis together with the rotational ambiguity shown for the excitation density of 4 $\mu J/cm^2$. For the analysis an augmented matrix containing 6 fluences is used, which is normalized and constrained to positive values for spectra and concentration profiles. a) shows the spectrum of the first species initially generated by MCR-ALS as open squares and the triplet spectrum as thick black solid line measured on a PSBTBT:PtOEP blend and on a pristine PSBTBT film at long times (40 ns). The thick black dashed line represents species 2 obtained by using the triplet spectrum for species 1 in the MCR-ALS analysis. By fixing the spectrum of the first species, rotation of the solution leads to the colored dashed lines. In b) the corresponding concentration profiles are displayed. Note that the solutions of species 2 are not shown because they are only scaled by the rotation.

experiments on the pristine polymer as well as the polymer:fullerene blend to rule out additional effects of the PCBM. Figure 4.4a shows the steady-state absorption of the PSBTBT:$PC_{70}BM$ film dipped into a $FeCl_3$ acetonitrile solution for different exposure times with different $FeCl_3$ concentrations. For comparison the blend was oxidized in iodine vapor and measured repeatedly after exposure as the oxidation seemed to be reversible with iodine. For both oxidizers the peak position of the charge absorption shifts to the red with a decreasing degree of oxidation. For oxidation with iodine the position seems to be slightly red-shifted compared to $FeCl_3$, but for low concentrations the spectra are equal. The decrease in absorption between 600-800 nm further indicates that it is indeed the polymer that is oxidized as this explains the observed bleaching of the ground state.

To evaluate to what extent this charge absorption spectrum is comparable to the transient absorption data, figure 4.4b shows the spectrum obtained at the

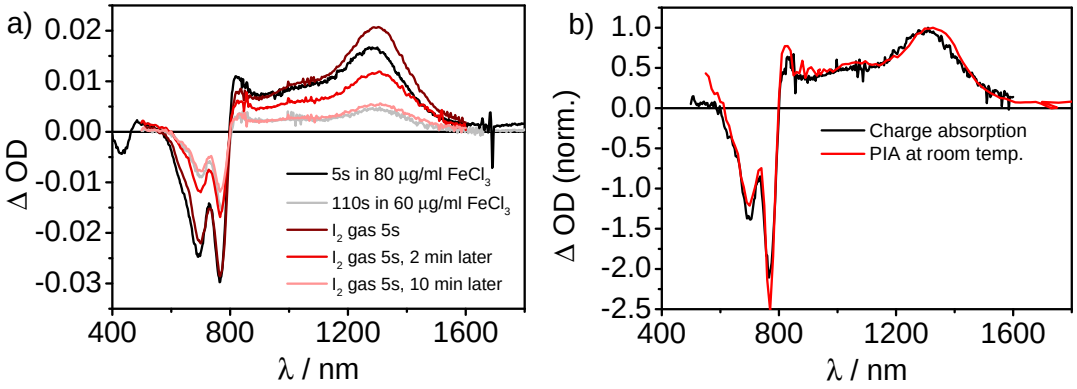

Figure 4.4: a) Change of absorption of a PSBTBT:$PC_{70}BM$ film upon mild oxidation. The black and gray spectra are obtained from dipping the film into a $FeCl_3$ solution followed by rinsing with acetonitrile. For the red spectra the film was exposed to iodine vapor for 5 seconds and repeatedly measured as the oxidation with I_2 seems to be reversible. With an increasing degree of oxidation the main charge peak shifts to the blue. b) Comparison of the charge absorption in the mildest oxidized film with the quasi-steady state PIA spectrum measured at room temperature on a PSBTBT:$PC_{70}BM$ film.

weakest oxidation level in comparison to a cw-PIA measurement of the blend. The spectrum obtained from oxidation reproduces all features of the cw-PIA spectrum with the difference that the charge absorption of the oxidized film exhibits a minor blue shift. We know from the sensitizer experiments that the triplet spectrum is the bluest component, and as the evolving factor analysis revealed that only two species are present, the reason for the bluer charge absorption in the oxidized film has to result from the degree of oxidation. Milder oxidation was unfortunately not possible due to the limited signal-to-noise ratio of the absorption spectrometer, but from figure 4.4b we can conclude that the shape of the charge absorption obtained by oxidation is correct, however, slightly shifted.

Taking this into account, an optimization routine was implemented that compares the shape of the charge absorption measured on the oxidized sample to the spectrum of species 2 by shifting the peak position of absorption to the peak position of species 2. Figure 4.5 shows a scheme of the routine. This is done for all possible solutions of species 2 obtained from rotation in the above restricted parameter space, and the solution of species 2 which exhibits the smallest deviation from the shape of the charge absorption is taken as the spectrum of species

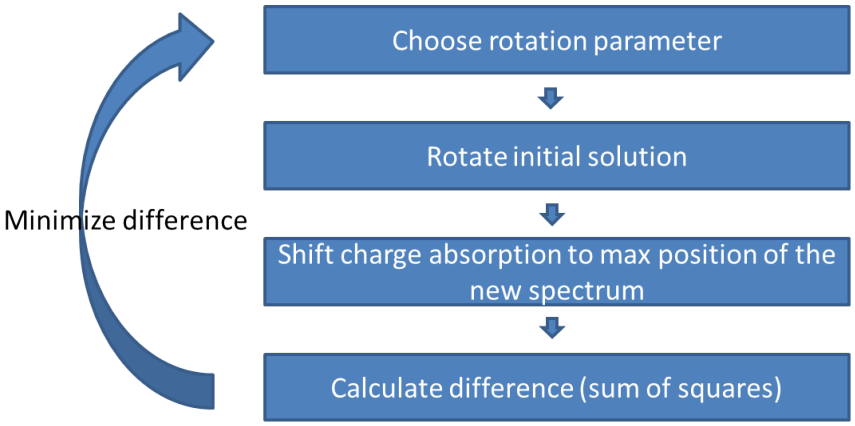

Figure 4.5: Charge shape optimization procedure. The charge spectrum from the oxidation experiments is taken and moved in position so that the difference between the charge spectrum from the rotation of the MCR-ALS solution and the shifted oxidation spectrum is minimized.

2 in the deconvolution of the TA data. The obtained spectra are shown in figure 4.6a and compared to the measured TA spectra. The changes between the two different population pools explain the observed spectral shifts. Note that the charge and triplet spectrum are normalized in figure 4.6a and do not represent the absolute cross-sections. In figure 4.6b the results of the deconvolution are displayed without the experimental data, and with these the concentration profiles of the triplets (figure 4.6c) and the charges (figure 4.6d) can be directly calculated. They are shown for six different excitation densities demonstrating that for the triplets as well as for the charges a strong concentration dependent decay is present. For the triplets this points to a rapid quenching by a bimolecular process as a normal triplet decay would not exhibit a concentration dependence and also a longer lifetime. The triplets could either undergo triplet-triplet annihilation, or decay by triplet-charge annihilation, in which the triplet transfers its energy to the charge carrier and thereby returns to the ground state. Note that the charge carrier does not decay in this process. Due to the high performance of the working solar cell, it is reasonable to assume a high free charge carrier density in this material system, which supports the assumption of the second triplet decay mechanism.

So far the data surface has been deconvoluted with the knowledge of the spectra of both species, and we obtained the corresponding kinetics. However, due

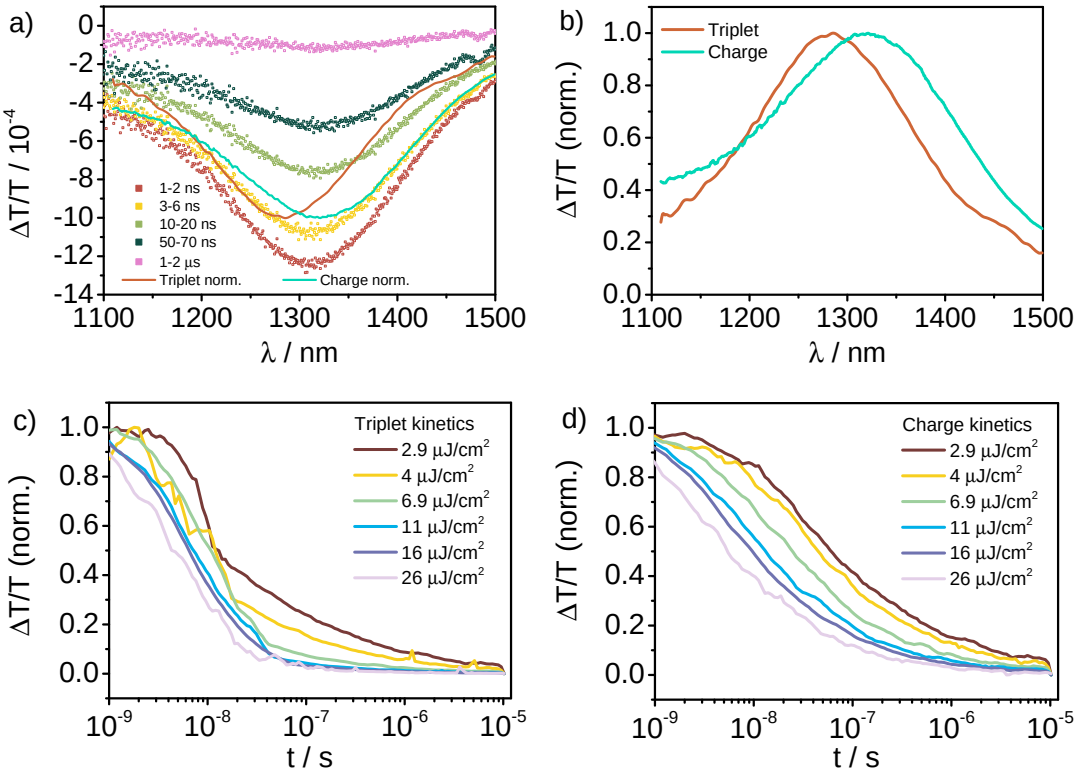

Figure 4.6: Deconvolution of the ns to µs TA data of PSBTBT:$PC_{70}BM$ obtained from analyzing an augmented matrix with six fluences excited at 532 nm. a) TA spectra of the blend between 1 ns and 1 µs for the lowest fluence (squares) compared to the spectra obtained from the deconvolution after optimizing the charge shape (lines). Note that the deconvoluted spectra are normalized and do not represent the absolute cross-sections. b) Normalized charge and triplet spectra after optimizing the charge shape. The triplet spectrum is taken from a PSBTBT:PtOEP TA experiment. c) and d) Corresponding triplet and charge concentration profiles for the six different excitation densities. With increasing excitation density charge and triplet populations decay faster due to increased non-geminate charge recombination, triplet-charge annihilation, or triplet-triplet annihilation.

to the scaling matrix in (4.6) the absolute charge and triplet contributions are not uniquely determined. For that the absolute cross-sections of the species are needed. Following the approach in [120], we assume that after 20-30 ps all excitons in the polymer:fullerene blend are quenched and have generated charge carriers, and we can therefore use this data to calculate the cross-section of the charge carriers σ_c according to

$$\sigma_c = \frac{(\frac{\Delta T}{T})_{30ps}}{Nd}, \tag{4.8}$$

in which $(\frac{\Delta T}{T})_{30ps}$ is the signal height at 30 ps, N is the number of absorbed photons, and d the sample thickness. This leads to a charge carrier cross-section of $\sigma_c = 3.5 \times 10^{-16}\,1/\mathrm{cm}^2$. The determination of the triplet cross-section is more challenging. Although we demonstrated that by excitation of the triplet sensitizer PtOEP in a blend with the polymer triplets can be generated on the polymer, the quantitative analysis of this process is not possible as it is difficult to estimate how many of the initial porphyrin excitations are transferred to the polymer. Chow et al. proposed a method for PCPDTBT in which they measured TA on a very diluted polymer solution, so that the excitation is confined on one polymer chain. They further assumed that the singlet excitation causes the same ground state bleach as the triplet exciton, and by measuring the GSB in the visible and PIA in the NIR, they calculated the cross-section of the triplets to be a factor of 2 larger than that of the charges.[120] Assuming a similar cross-section ratio in PSBTBT, we can now calculate the absolute contributions of charge carriers and triplets leading to the kinetics shown in figure 4.7a. With the above determined cross-sections of charges and triplets, the population densities of the species can be calculated for low fluences at 1 ns delay time. For high fluences the assumption that all absorbed photons create charge carriers is no longer valid. Figure 4.7b displays the contribution of the individual species in relation to the number of initially absorbed photons for the lowest excitation density of $2.9\,\mu\mathrm{J/cm}^2$. At 1 ns the triplets make up 11 % of the initial photoexcitations, whereas the remaining 89 % are charges.

The question that remains is how the triplets are created in the blend system. As we know from measurements on a pristine polymer film, the ISC is too slow in the polymer to explain the amount of triplets generated because in the blend the singlets are completely quenched at the interface within 10-15 ps. A further

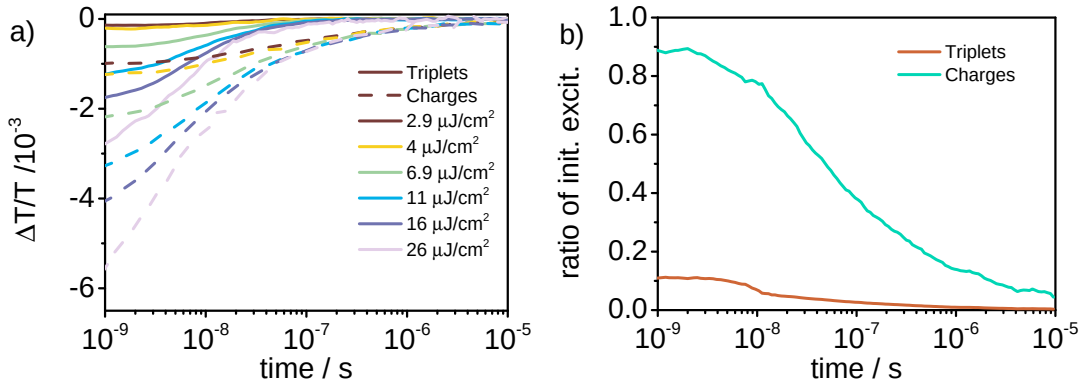

Figure 4.7: a) Signal contribution of triplets and charges in ns-µs PSBTBT:$PC_{70}BM$ measurements with a cross-section ratio of $\sigma_t = 2\sigma_c$. The solid lines represent the triplets, the dashed lines the charges. With increasing fluence, the fraction of the triplet contribution increases. b) With $\sigma_c = 3.5 \times 10^{-16}$ 1/cm², the ratio of charges and triplets from the initial number of absorbed photons is calculated.

indication contradicting direct ISC can be decuded from the fluence dependence. By calculating the ratio of the triplet and charge signal contribution at 1 ns shown in table 4.2, it gets clear that the triplet generation is a concentration dependent process, proposing that the triplets are generated by bimolecular recombination of free charges already on a sub-ns timescale. Hence, we also performed fs to ns transient absorption measurements for further investigation of the triplet formation mechanism.

	2.9 µJ/cm²	4 µJ/cm²	6.9 µJ/cm²	11 µJ/cm²	16 µJ/cm²	26 µJ/cm²
f	0.14	0.17	0.28	0.38	0.43	0.50

Table 4.2: Ratio of the triplet and charge signal contribution at 1 ns in PSBTBT:$PC_{70}BM$.

4.3.3 Sub-ns triplet generation in PSBTBT:$PC_{70}BM$

The nanosecond to microsecond transient absorption measurements revealed that the generation of triplets occurs already on a sub-ns timescale, because after the system response (approx. 1.5 ns) the triplets already contribute to the total TA signal (see figure 4.7a). Using a second setup with approximately 150 fs time

resolution, we therefore explored the fs to ns kinetics in the visible and NIR spectral region. For consistency with the long time data, we excited the samples at 530 nm, but also at 800 nm, as this avoids fullerene excitation. By monitoring the GSB of the polymer, the total signal build-up of excited states on the polymer can be measured, as shown in figure 4.8a for excitation at 530 nm where mainly the fullerene absorbs, and at 800 nm (4.8b) where mainly the polymer absorbs. The dynamics is clearly wavelength dependent, shown by the excitation intensity dependent long rise time after fullerene excitation, whereas after polymer excitation the signal rise time is response-limited. In agreement with previous measurements, it appears that the charge generation process following fullerene excitation is largely diffusion-limited, with the prolonged signal rise pointing to delayed hole transfer from the fullerene to the polymer.[49] The fluence dependence of the rise time can be explained by fullerene exciton-exciton-annihilation that is facilitated by the prolonged fullerene exciton lifetime. The annihilation process further explains the necessity to use low excitation densities, especially on the long time scale, because at a higher excitation fluence the calculation of the cross-sections otherwise fails due to the breakdown of the assumption that all absorbed photons generate charge carriers. However, after excitation of the polymer no fluence dependence of the charge generation process is observed pointing to mainly ultrafast charge generation as further investigated below. The delayed charge generation process following 530 nm excitation complicates the interpretation of the data, especially when trying to deconvolute the data. We therefore focused on the short time data generated following polymer excitation as in this case fullerene absorption and excited state generation play only a minor role and can be safely neglected.

In figure 4.9 the NIR data surface of the blend excited at 800 nm with 1.4 μJ/cm^2 is displayed. The large PIA signal reaching up to 1500 nm that vanishes after approximately 10 ps can be assigned to polymer singlet excitons in accordance with measurements on a pristine polymer sample. The singlet excitons are quenched and a smaller PIA peaking between 1300 - 1350 nm remains that undergoes a progressive blue shift up to 1 ns. The surface already demonstrates that at least two species contribute to the entire data surface of which we have already identified the polymer excitons. To further analyze the number of species generated in this blend, we performed a rank analysis of the data as previously shown for

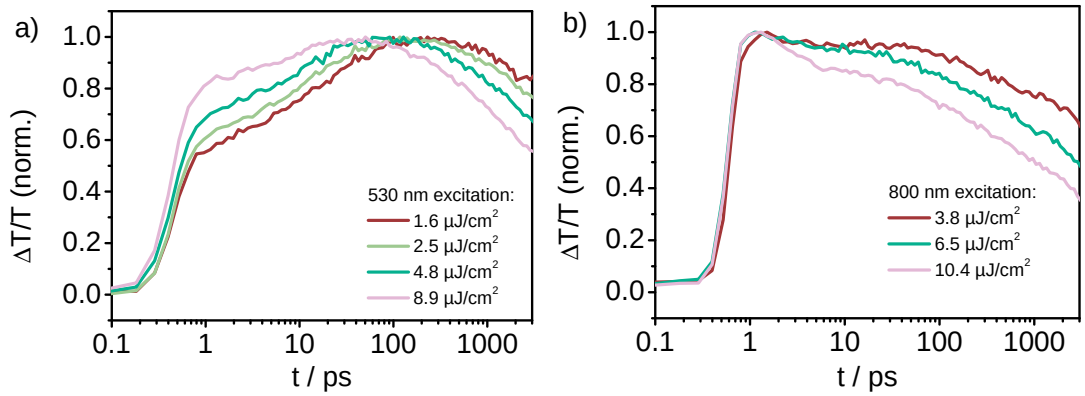

Figure 4.8: GSB kinetics (760-780 nm) in PSBTBT:$PC_{70}BM$ after excitation at 530 nm (a) and 800 nm (b).

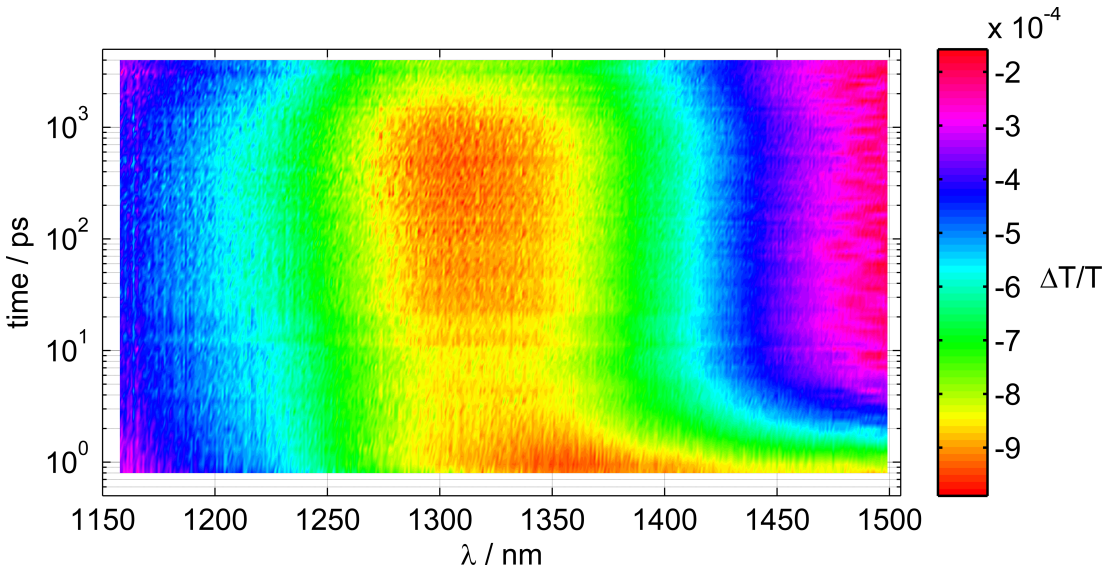

Figure 4.9: NIR data surface of the PSBTBT:$PC_{70}BM$ short time experiments excited at 800 nm with 1.4 $\mu J/cm^2$.

the long time measurements. The presence of the excitons is already known, and since the absorption of charges and triplets is weak around 1500 nm, we can determine the exciton lifetime to be smaller than 10 ps by monitoring the temporal evolution of the signal at this wavelength. Therefore, we started the EFA at 10 ps. Figures 4.10a-4.10e show the results for increasing excitation densities. The black lines represent the forward EFA and the red lines the backward EFA. Clearly one species is present the whole time, whereas with increasing fluence the onset of the generation of a second species shifts to earlier times, and this species becomes more dominant. The observation of a fluence dependent rise time of one species implies a concentration dependent generation mechanism. Together with the blue shift observed on the first 1 ns and taking into account the long time data, namely that the triplets exhibit an absorption at slightly higher energy than the charges, we conclude that the first species generated are charges, which successively undergo bimolecular recombination to form triplet states.

For the deconvolution of the whole short time data set, we need, in addition to the charge and triplet spectrum, the shape of the exciton-induced absorption and the corresponding value of the cross-section. From measurements conducted on a pristine polymer film we know the exciton spectrum, and with the assumption that at short delay times (5 ps) only singlet excitons are present, a cross-section of $\sigma_s = 9.9 \times 10^{-16}\, 1/cm^2$ at 1500 nm can be calculated by using equation (4.8). The charge-induced absorption spectrum obtained from the charge shape optimization of the long time experiments is virtually similar to the spectrum at short delay times after exciton quenching, supporting the aforementioned assumption of the calculation of the charge cross-section. Knowing the spectra of all three species enables us to calculate the corresponding concentration profiles from the original data matrix by matrix right division. Figure 4.11a displays the normalized spectra of the individual species compared to the measured TA data, and in figure 4.11b the normalized spectra are shown without experimental data for a better overview. In figure 4.11c the deconvoluted concentration profiles are shown for three excitation densities. For all excitation densities a certain amount of charges is immediately formed following photoexcitation, which then further increases correlated to the singlet exciton quenching dynamics up to 10-20 ps. The decay of excitons is concentration independent indicating that at the fluences shown the quenching is faster than any exciton annihilation process. After the

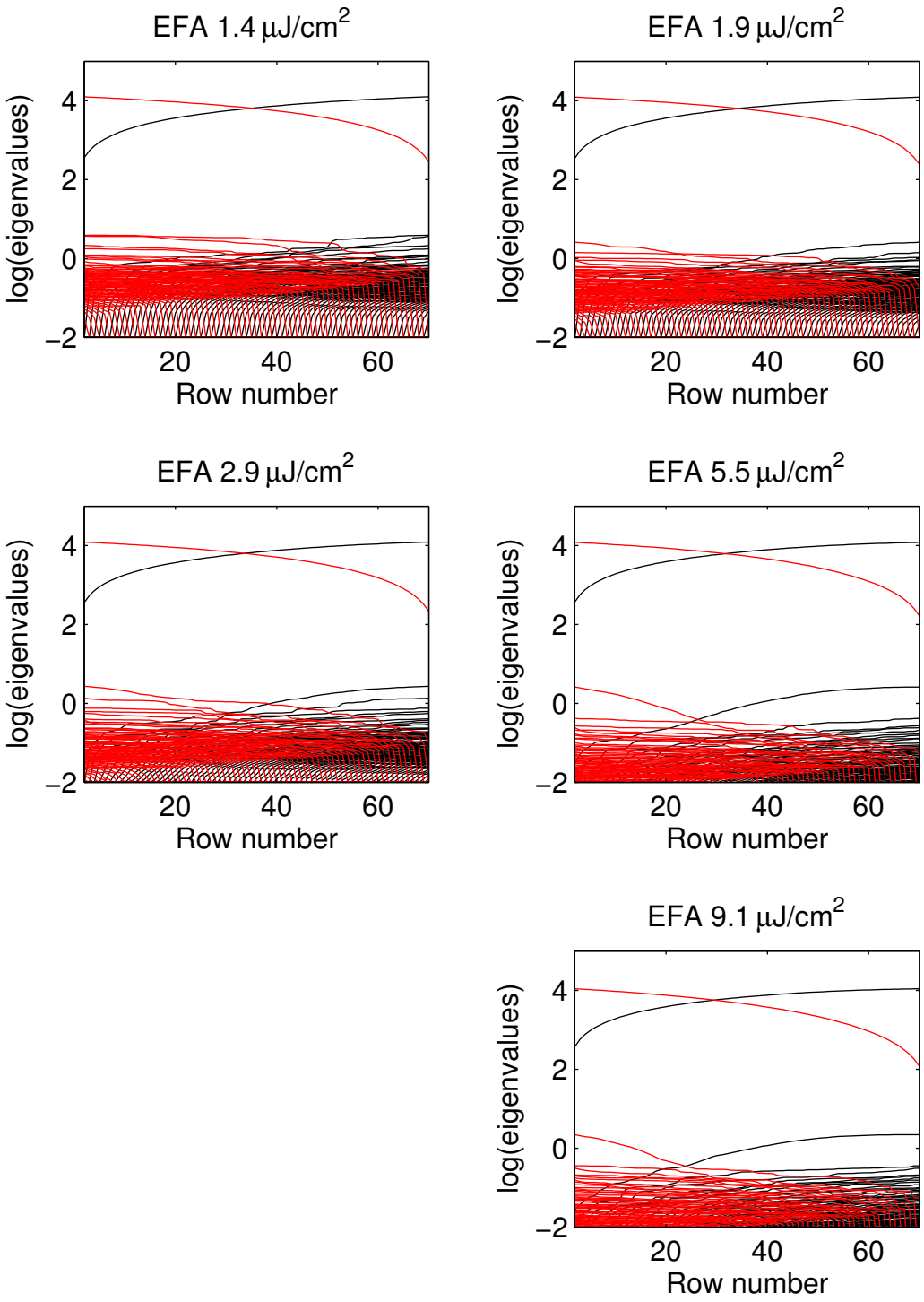

Figure 4.10: EFA of the short time PSBTBT:$PC_{70}BM$ data excited at 800 nm. The first 10 ps are left out of the analysis to suppress the singlet contribution for clarity. With increasing excitation energy, the second component of the forward EFA (black lines) rises at earlier times.

charge generation an intensity dependent decay decreases the charge population (see normalized charge kinetics in figure 4.11d) in correlation with an increase of the triplet population. The observed kinetics confirm the results obtained from the EFA analysis and indicate that the triplet generation process starts already at approximately 100 ps by fast non-geminate recombination of free charges.

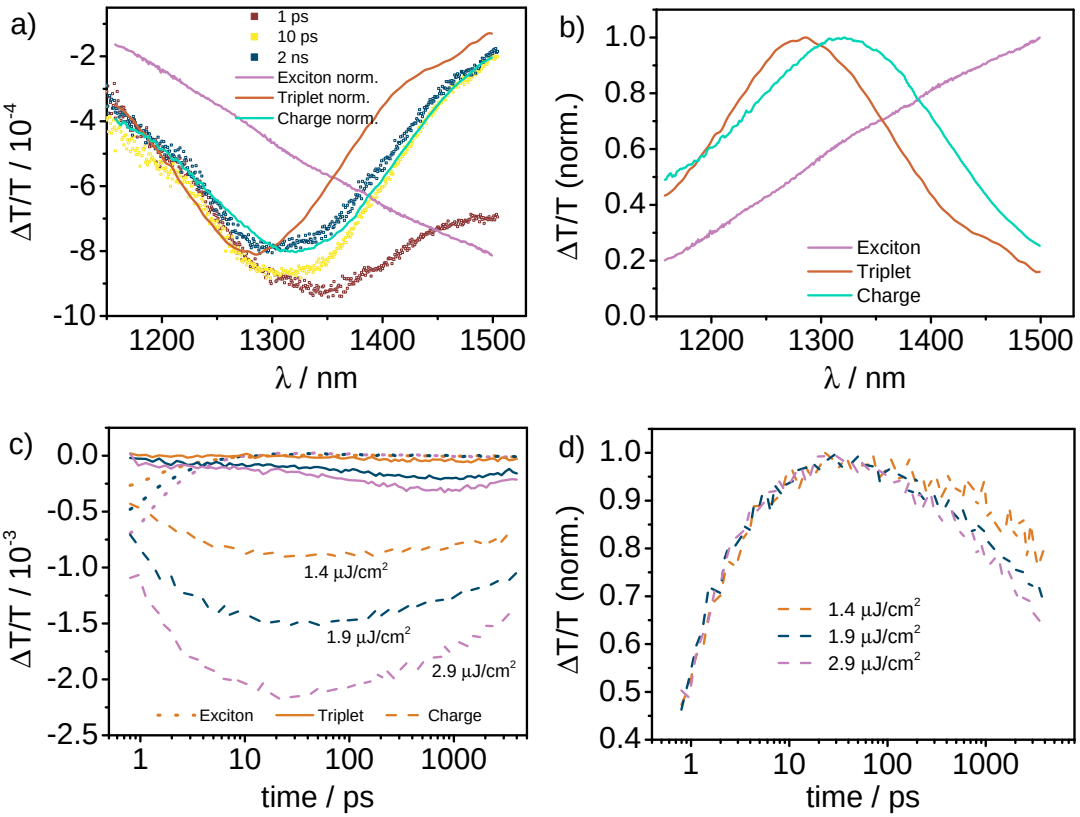

Figure 4.11: Deconvolution of the short time PSBTBT:$PC_{70}BM$ data after excitation at 800 nm. a) Spectra used for the deconvolution (lines) compared to the measured TA spectra at the lowest fluence (squares). The charge and triplet spectra are taken from the long time data deconvolution, and the exciton spectrum is obtained from measurements on a pristine polymer film. b) Normalized spectra of the different species shown without experimental data for a better overview. c) Exciton (dotted line), triplet (solid line), and charge (dashed line) kinetics obtained from the deconvolution. To calculate the absolute signal contribution the cross-section of the singlet excitons was determined in measurements on a pristine film. d) Normalized charge kinetics.

4.3.4 Revisiting of the results on PCPDTBT:$PC_{60}BM$

The above findings for the blend containing the PSBTBT donor polymer led us to revisit the interpretation of the results obtained on of the carbon bridged polymer PCPDTBT to further investigate the role of triplet generation as a loss channel after charge generation. In fact, the data previously measured and published in [49] exhibited too much noise in the high energy region of the NIR, where triplet absorption is expected to occur, to successfully apply the MCR deconvolution analysis. We therefore took the NIR data again using the improved transient absorption setup. As reported in [49, 122, 123] the addition of a high boiling point co-solvent had a significant impact on the photophysics and morphology, and therefore both blends are compared in this section. In the following blend with or without ODT means that the sample was processed with or without ODT.

Figures 4.12a and 4.12b show the short time transient data surfaces with and without the solvent additive ODT for the lowest pump fluences measured of $0.5\,\mu J/cm^2$ and $0.4\,\mu J/cm^2$, respectively, excited at 800 nm, so that mainly excitations on the polymer are generated. To compare the data to our previously measured datasets, we again used $PC_{60}BM$ as an electron acceptor. In agreement with the results from [49], the sample processed with ODT exhibits clear polymer singlet exciton signatures up to 10 ps, whereas in the blend without ODT excitons are quenched on a timescale faster than the system response time. Additionally, the blend with ODT exhibits a broader photoinduced absorption which clearly shifts to the blue at later times. To analyze the number of species contributing to the signal and their generation characteristics, we performed an EFA on the data of both blends. We started in both cases after the polymer singlet excitons were quenched. In the blend without ODT as well as in the blend with ODT one species dominates the signal at early times but a second component is created over time. Similar to PSBTBT, the generation process is fluence dependent, which can be seen from the earlier rise of the second EFA component at higher fluence indicating that also in the PCPDTBT samples non-geminate recombination can lead to the generation of triplet states. The data is shown in the supporting information in figure 4.17 for the sample without ODT and figure 4.18 for the sample with ODT.

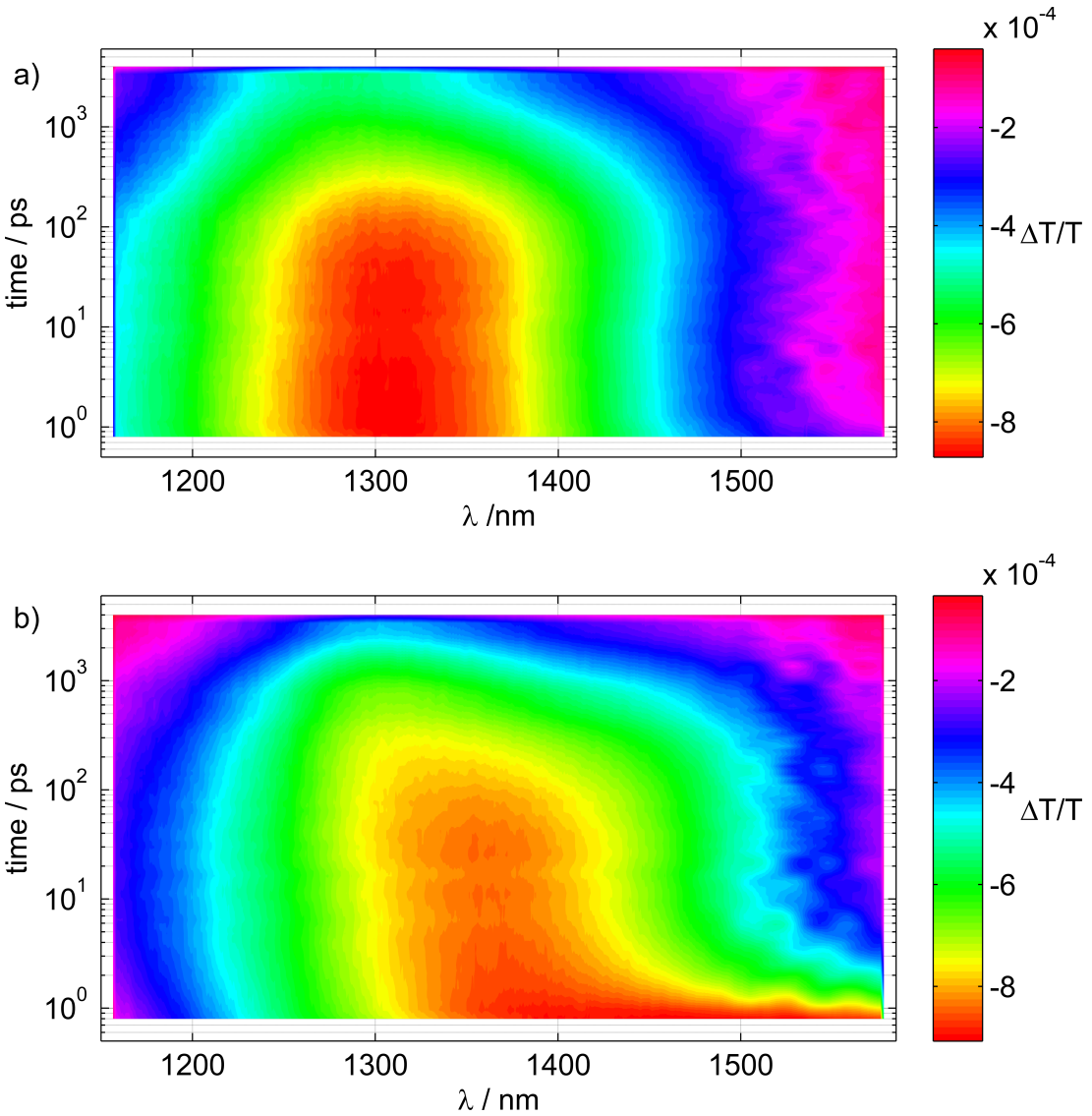

Figure 4.12: Short delay TA data surfaces of PCPDTBT:$PC_{60}BM$ without ODT (a) and with ODT (b) excited at 800 nm with 0.5 $\mu J/cm^2$ and 0.4 $\mu J/cm^2$, respectively.

For the deconvolution of the transient absorption data, we applied MCR-ALS analysis, and the obtained spectra are shown in figure 4.13a for the blend without ODT. The first component of the analysis very well matches the absorption of the polymer triplet state (dashed line), measured in a pristine polymer sample after 4 ns delay time and in a polymer:PtOEP triplet sensitizer blend, indicating that triplets indeed play a role. The second component of the deconvolution is almost coincident with the 20 ps transient absorption spectrum of the blend, and is therefore assigned to charge carrier absorption.

However, as already demonstrated for PSBTBT, the deconvolution of a data surface with two overlapping spectra bears a high degree of rotational ambiguity. Of course the good match of the triplet-induced absorption indicates that the assignment of species 1 is correct, but the charges could very well absorb further in the red implying that triplets are already present at 20 ps in the blend film. For PSBTBT oxidation experiments were carried out to decrease the ambiguity. For PCPDTBT a different strategy is presented. Here, we combined all fluences measured for the short time and long time of the regular blend together with long time data of a blend composition that contained a reduced amount of PCBM, namely 5 wt.%, to create one large augmented matrix. By performing MCR-ALS analysis on this matrix we obtained the above discussed spectra, and by rotating the solution with a fixed triplet spectrum, we could evaluate the rotational ambiguity for this sample. This is shown in the SI in figure 4.19. It can be seen that shifting the spectra towards larger overlap (rotation parameter: -0.1) directly creates negative concentration profiles and is therefore not physically meaningful. A rotation in the other direction does not create negative concentrations, but the spectrum of species 2 starts to exhibit a dent at the peak position of species one, which is neither physically meaningful nor very likely. This shows that the rotational ambiguity is small in the blend without ODT ($c = 0 - 0.05$), and the fact that the spectrum of species 2 matches that of the blend after 20 ps further supports this solution. The deviation of the deconvolution from the measured data surface is shown in figure 4.23.

Figure 4.13b displays the spectra of the blend with ODT obtained by MCR-ALS. The triplet spectrum is slightly shifted to the red compared to the blend without ODT as is also the charge-induced spectrum. These results contain a

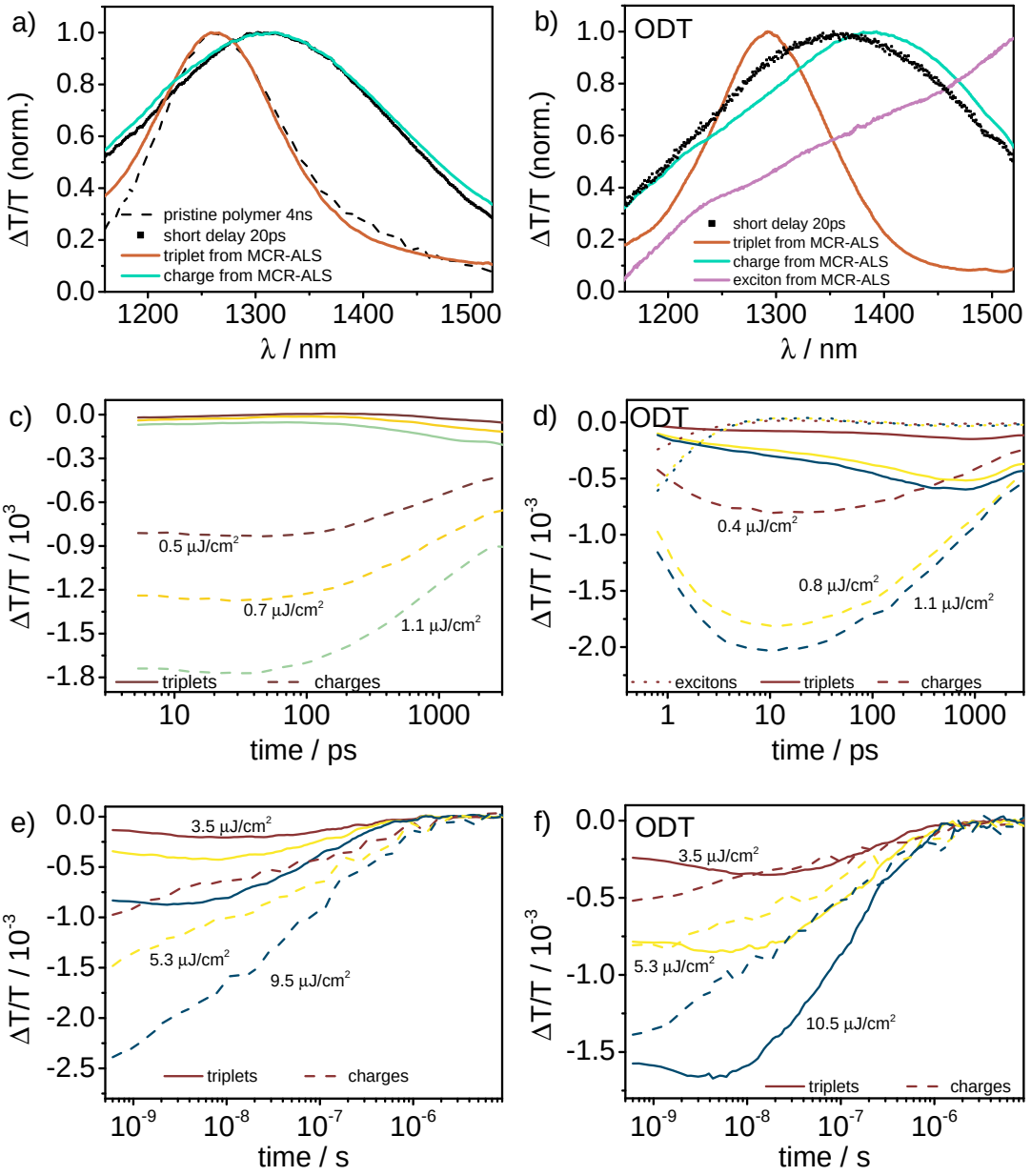

Figure 4.13: Deconvolution of PCPDTBT:$PC_{60}BM$. The left column displays the results for the blend without ODT, and the right column shows the data for the blend with ODT. See main text for further explanation.

high degree of rational ambiguity, but as we know neither the triplet-induced absorption spectrum nor charge-induced absorption spectrum in the blend with ODT, the determination of the ambiguity is difficult. However, Chow et al. recently investigated the same donor polymer with a genetic algorithm technique to deconvolute the data surface and produced almost exactly the same spectra for the blend with ODT as we obtained from the MCR-ALS analysis, which supports the validity of our solution. For comparison the 20 ps TA spectrum of the blend is also shown in figure 4.13b (squares). The spectrum was recorded for the lowest measured fluence, and the fact that the charge-induced absorption spectrum from MCR-ALS is red-shifted compared to the 20 ps spectrum indicates that already on this short time scale triplets are present in the blend. Interestingly, in the blend without ODT the lowest fluence did not show any triplet contribution at this early time, but the results are reasonable when comparing how the 20 ps spectra of both blends shift with increasing pump fluence. In figures 4.14a and 4.14b the TA spectra of both blends are shown after 20 ps delay for different pump fluences. Clearly, for both samples the spectra shift to the blue with increasing fluence, but the effect is much stronger for the sample with ODT. Additionally, the first two fluences of the blend without ODT are almost identical, demonstrating that at the lowest fluence used the fraction of triplets generated after 20 ps is negligible. In the blend with ODT a shift can already be seen between the first two fluences indicating that triplets might already be present even after excitation at the lowest fluence. The MCR-ALS analysis started at 10 ps so that the influence of the polymer singlet exciton could be neglected. After optimization of the charge- and triplet-induced absorption spectra, the exciton-induced absorption spectrum was added and the concentration profiles were obtained by matrix right division. The exciton-induced absorption spectrum was measured in the TA experiment of the pristine polymer sample. Figure 4.25 in the SI displays the deviation of the simulated data matrix from the experiment.

The direct deconvolution of the long time TA data with the spectra obtained from the deconvolution of the short time data produced large systematic deviations for the sample with ODT, and also the analysis of long and short time data in one augmented matrix as demonstrated for the blend without ODT failed. Therefore, the analysis was repeated separately for the long time data, and the corresponding spectra are shown in the SI in figure 4.20. The charge- and triplet-

induced absorption spectra obtained from the long time data are slightly shifted compared to the short time data. This can easily occur by a small error in the wavelength calibration as the short and long time data were recorded in different setups.

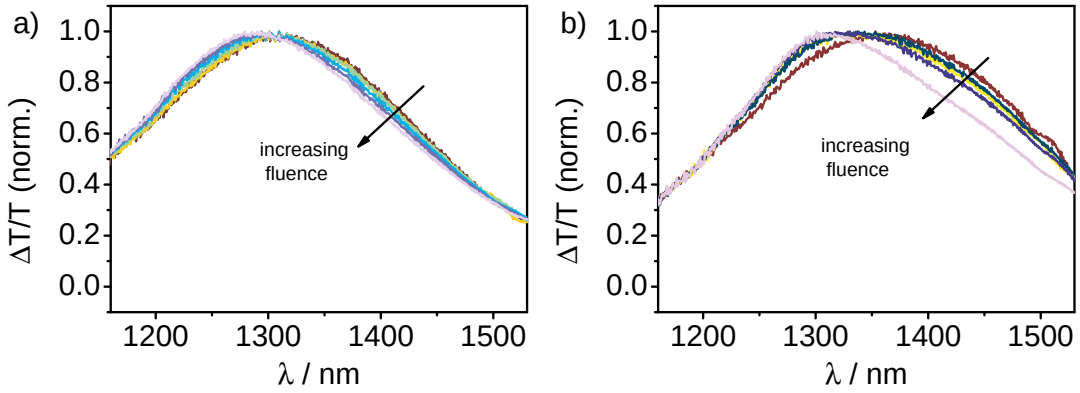

Figure 4.14: Fluence dependence of the early time blue shift in PCPDTBT:$PC_{60}BM$ without ODT (a) and with ODT (b). For the blend without ODT excitation energies between 0.5 - 4 $\mu J/cm^2$ were used, and for the blend with ODT the excitation energies varied between 0.4 - 3 $\mu J/cm^2$.

The corresponding concentration profiles of the deconvolution on the short time scale can be seen in figure 4.13c for the blend without ODT and in figure 4.13d for the blend with ODT. A crossection ratio of $\sigma_t = 2\sigma_c$ and $\sigma_{ex} = 2.83\sigma_c$ was used for triplets, charges, and excitons in the deconvolution (see 4.3.2). Whereas the triplet generation is slow in the blend without additive, the sample containing the solvent additive exhibits faster triplet generation, which is in part already present at very short delay times (< 20 ps). The higher triplet contribution is also visible on the long time scale in figures 4.13e and 4.13f showing that charges as well as triplets are long-lived species. The presence of the two species can also be seen in the EFA of the two samples shown in the SI (see figures 4.21a and figures 4.21b). The normalized concentration profiles for the blend without ODT exhibit only a weak fluence dependence for the charges on the long time scale and a stronger one for the triplet population including a fluence dependent rise at early times (see SI figure 4.22a). In the blend with ODT (SI figure 4.22b) the fluence dependence of the decay is stronger for the charges compared to the blend without ODT indicating that more free charge carriers are present in this blend,

which is line with literature results. The higher charge carrier density further explains the faster triplet generation upon addition of ODT, because the fluence dependent generation mechanism of the triplets, which can be directly seen from the EFA, suggests that the triplets are formed from non-geminate recombination of free charge carriers.

4.3.5 Supporting Information

The PSBTBT:$PC_{70}BM$ samples for spectroscopy were spin-cast from a dichlorobenzene solution with a total concentration of 35 mg/ml in a polymer:fullerene ratio of 1:1.5 at 1400 rpm for 40 s. The PCPDTBT:$PC_{60}BM$ samples were spin-cast from a chlorobenzene solution with a total concentration of 30 mg/ml in a polymer fullerene ratio of 1:2. The samples prepared with the solvent additive contained 2.4 vol% ODT. The samples were spin-cast at 1400 rpm for 40 s.

The errors of the convolution are displayed as contour plots obtained from taking the difference between the simulated data matrix and the measured matrix. Note that each error matrix consists of several individual measurements for different fluences, which are each normalized to their maximum.

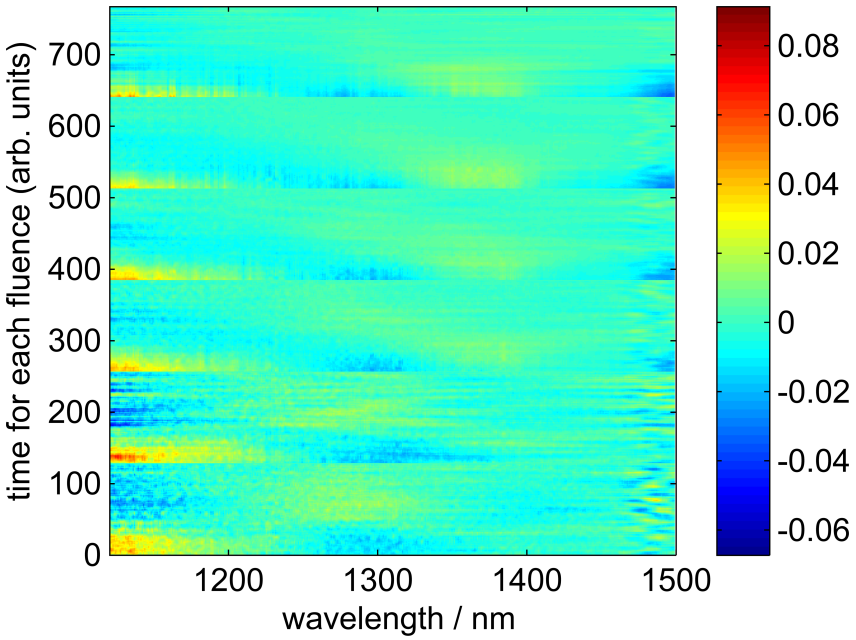

Figure 4.15: Error of the long time deconvolution of PSBTBT:$PC_{70}BM$

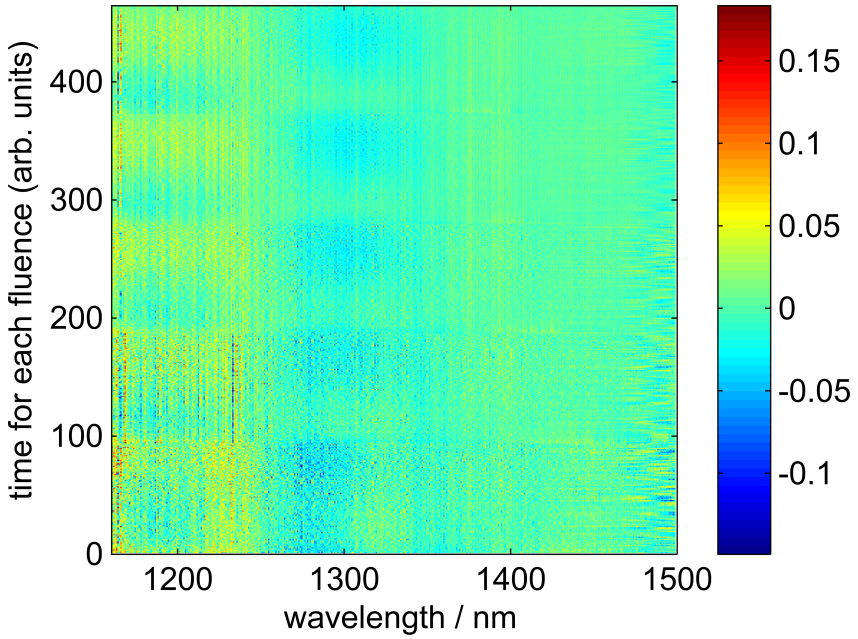

Figure 4.16: Error of the short time deconvolution of PSBTBT:$PC_{70}BM$

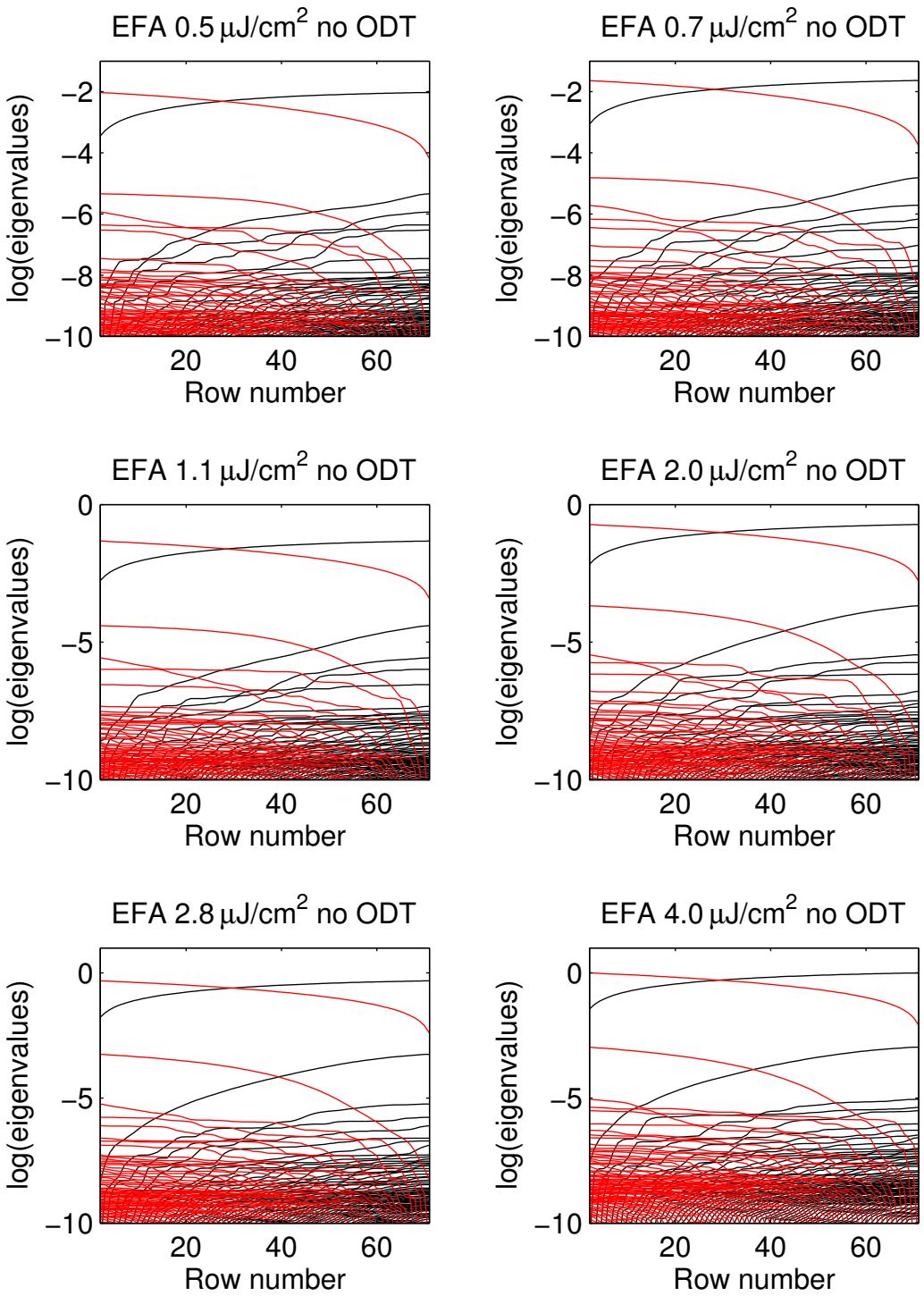

Figure 4.17: EFA of short time PCPDTBT:$PC_{60}BM$ without ODT data excited at 800 nm. The first 10 ps are left out of the analysis to suppress the singlet contribution for clarity. With increasing excitation energy the second component of the forward EFA (black lines) rises at earlier times.

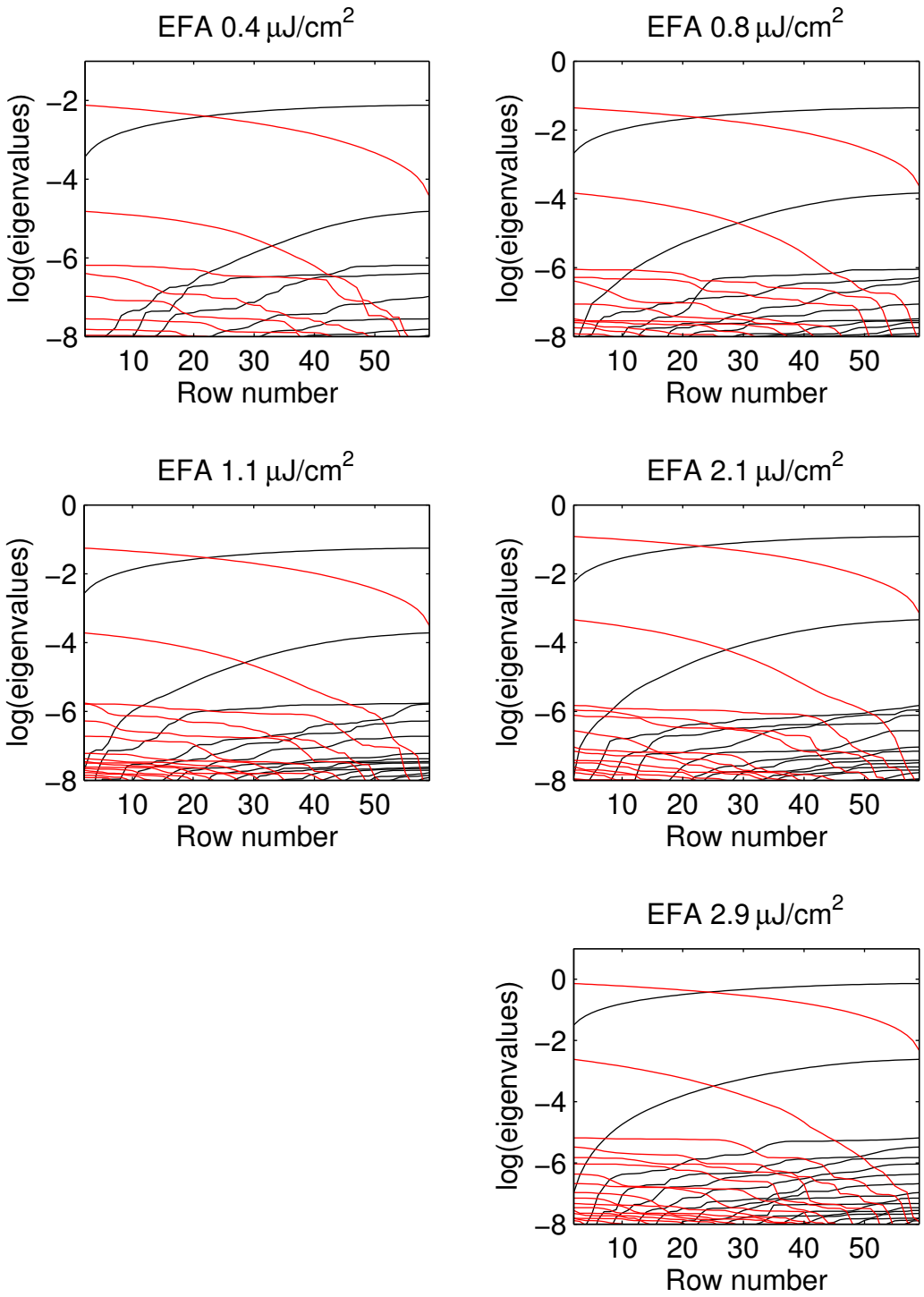

Figure 4.18: EFA of short time PCPDTBT:$PC_{60}BM$ with ODT data excited at 800 nm. The first 10 ps are left out of the analysis to suppress the singlet contribution for clarity. With increasing excitation energy the second component of the forward EFA (black lines) rises at earlier times.

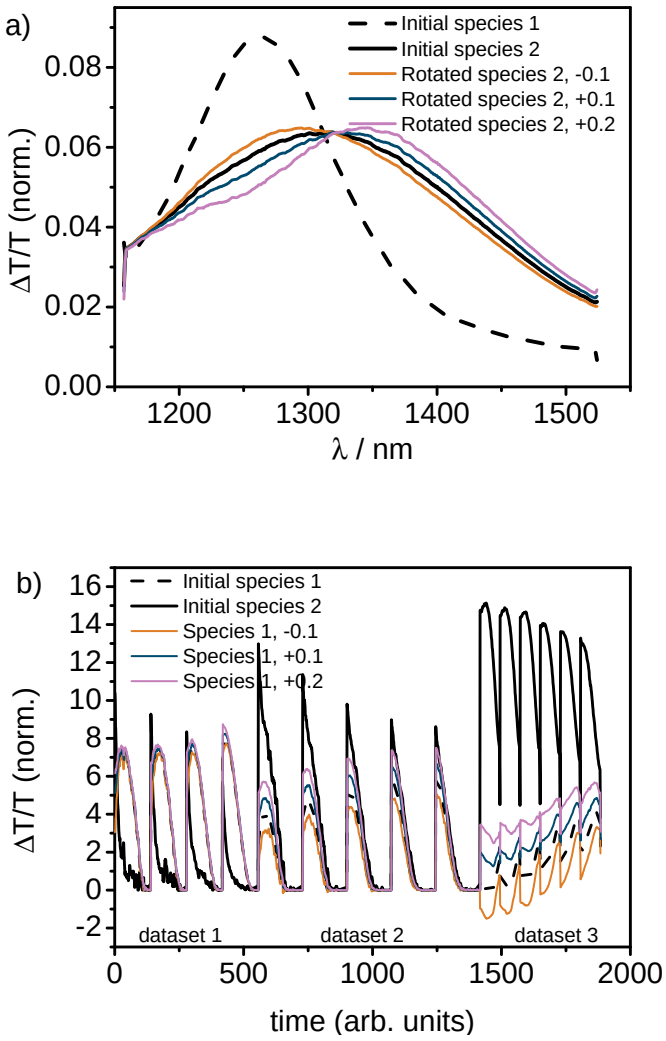

Figure 4.19: Rotational ambiguity of PCPDTBT:$PC_{60}BM$ without ODT. The spectrum of species 1 is fixed and the augmented matrix consists of long time measurements performed on PCPDTBT:5wt.%PCBM (dataset1), and long time (dataset 2) and short time (dataset 3) measurements performed on the normal blend. a) Initial and rotated spectra. b) Concentration profiles of the initial solutions and the rotations. For the rotations only the solutions for species 1 are shown, as the concentration profiles of species 2 are only scaled when spectrum 1 is fixed.

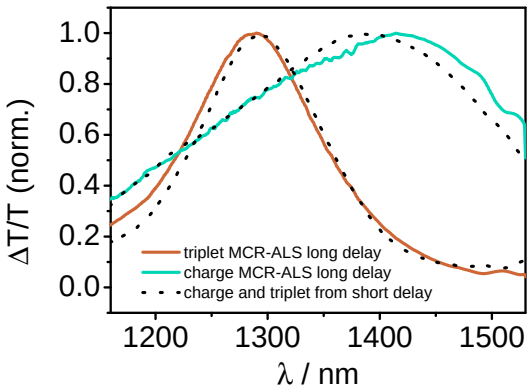

Figure 4.20: Deconvolution of the PCPDTBT:$PC_{60}BM$ with ODT long time data compared to the spectra obtained from the short time analysis.

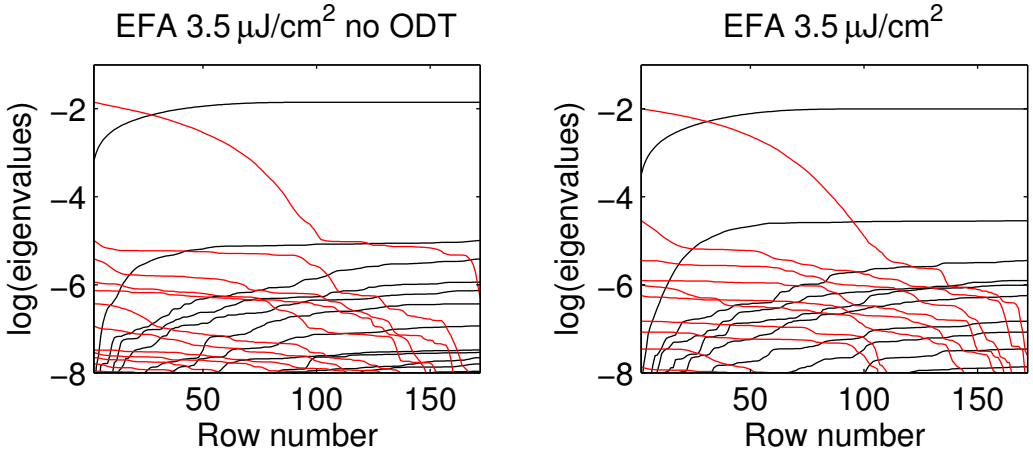

Figure 4.21: EFA of long time PCPDTBT:$PC_{60}BM$ data excited at 532 nm with 3.5 $\mu J/cm^2$ for both blends. Left: PCPDTBT:$PC_{60}BM$ without ODT. Right: PCPDTBT:$PC_{60}BM$ with ODT.

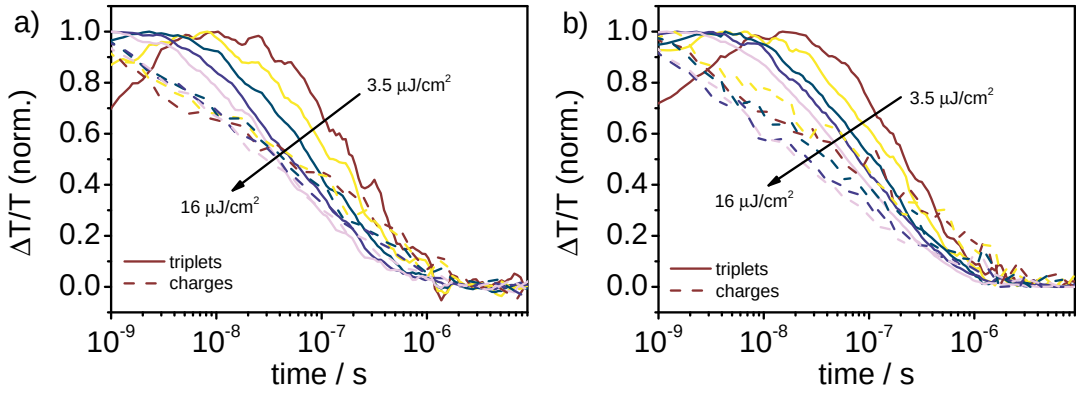

Figure 4.22: Normalized concentration profiles of PCPDTBT:$PC_{60}BM$ long time data for the blend without ODT (a) and with ODT (b).

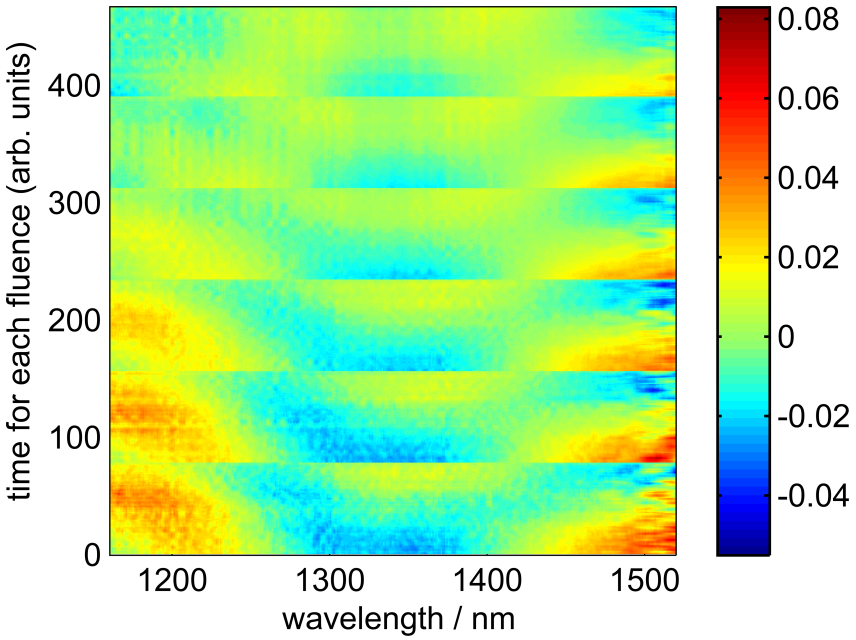

Figure 4.23: Error of the short time deconvolution of PCPDTBT:$PC_{60}BM$ without ODT

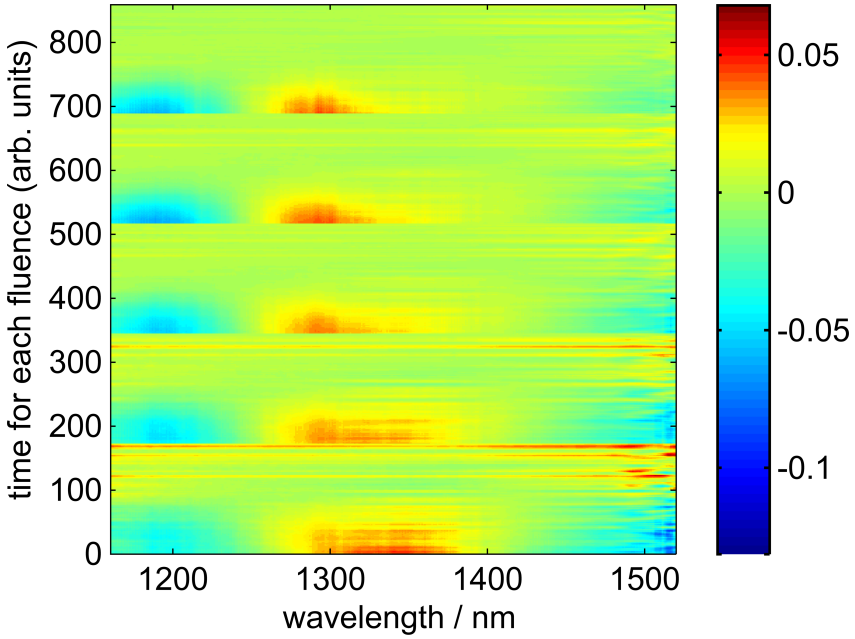

Figure 4.24: Error of the long time deconvolution of PCPDTBT:$PC_{60}BM$ without ODT

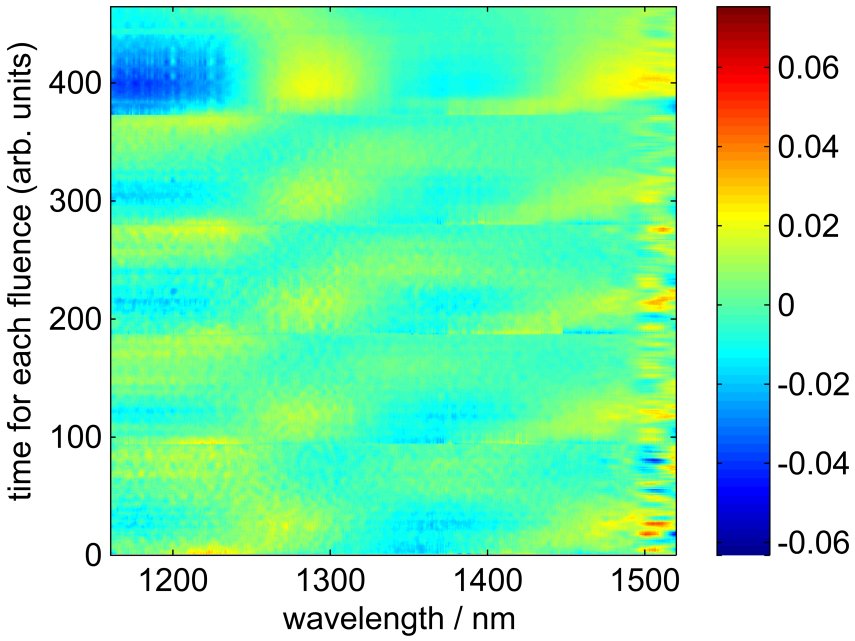

Figure 4.25: Error of the short time deconvolution of PCPDTBT:$PC_{60}BM$ with ODT

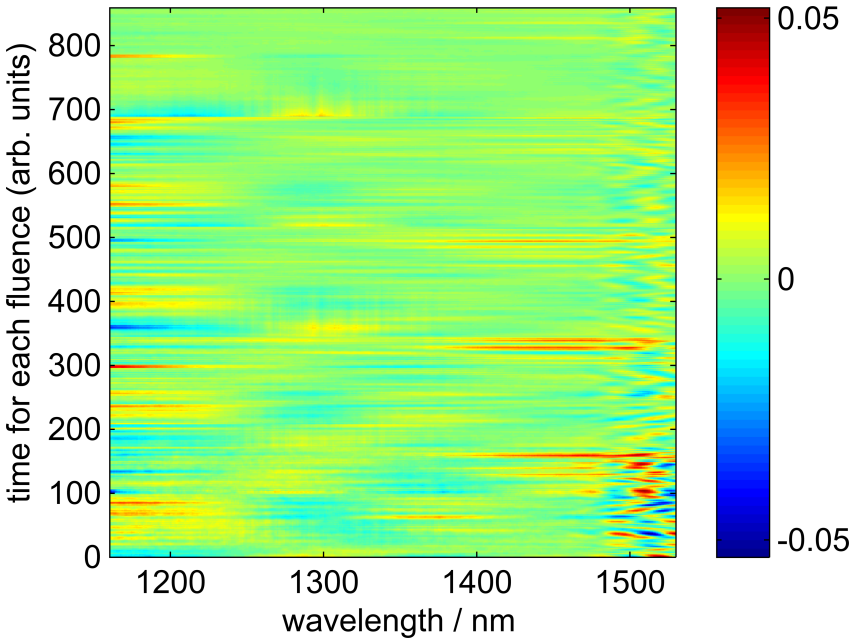

Figure 4.26: Error of the long time deconvolution of PCPDTBT:$PC_{60}BM$ with ODT

4.4 Discussion

The generation of triplets states in the three investigated low-bandgap polymer/fullerene blends caused a blue-shift of the observed transient absorption spectra in the NIR spectral region at early times. Depending on the number of triplets generated and their decay dynamics, this blue-shift was partially reversed at longer delay times. In order to disentangle the contributions of both triplets and charges, MCR-ALS analysis was performed on the data obtained for all material systems, and strategies to decrease the rotational ambiguity of the MCR-ALS solutions were presented. In this section we compare the triplet generation in the three material systems and discuss their generation mechanisms.

4.4.1 Mechanisms of triplet generation

4.4.1.1 Triplet generation by bimolecular recombination of free charge carriers

An overview over the possible triplet generation mechanisms is presented in figure 4.27. For all mechanisms displayed the precursor of the polymer triplet states (T_1) is a ^{3}CT state, as direct ISC from the polymer singlet state is very unlikely due to the fast singlet exciton quenching in the blend. If the T_1-state is energetically lower than the ^{3}CT state, the redissociation of the ^{3}CT state into free charges is in kinetic competition to a transfer to the T_1-state, so that depending on the relative rate between the two processes polymer triplets can be generated.[119] The ^{3}CT states are either populated by ISC from a singlet geminate pair ^1CT,[10] or by bimolecular recombination of free charge carriers.[119] The lifetime of ^{1}CT states was measured by Jarzab et al. to be approximately 500 ps, which is too short for efficient ISC to occur and therefore can be neglected for the investigated material systems. From a purely statistical perspective charge-transfer states with spin singlet character (^{1}CT) and spin triplet character (^{3}CT) are formed in a ratio of 1:3 by bimolecular recombination of free charge carriers of uncorrelated spin. For all investigated material systems the EFA analysis revealed that bimolecular recombination indeed plays a role in triplet generation as the triplet generation kinetics were found to be fluence dependent (figures 4.10, 4.17, 4.18). We want to stress that this result is independent of the uncertainty in the TA surface deconvolution because the EFA is a model-free analysis. The triplet generation

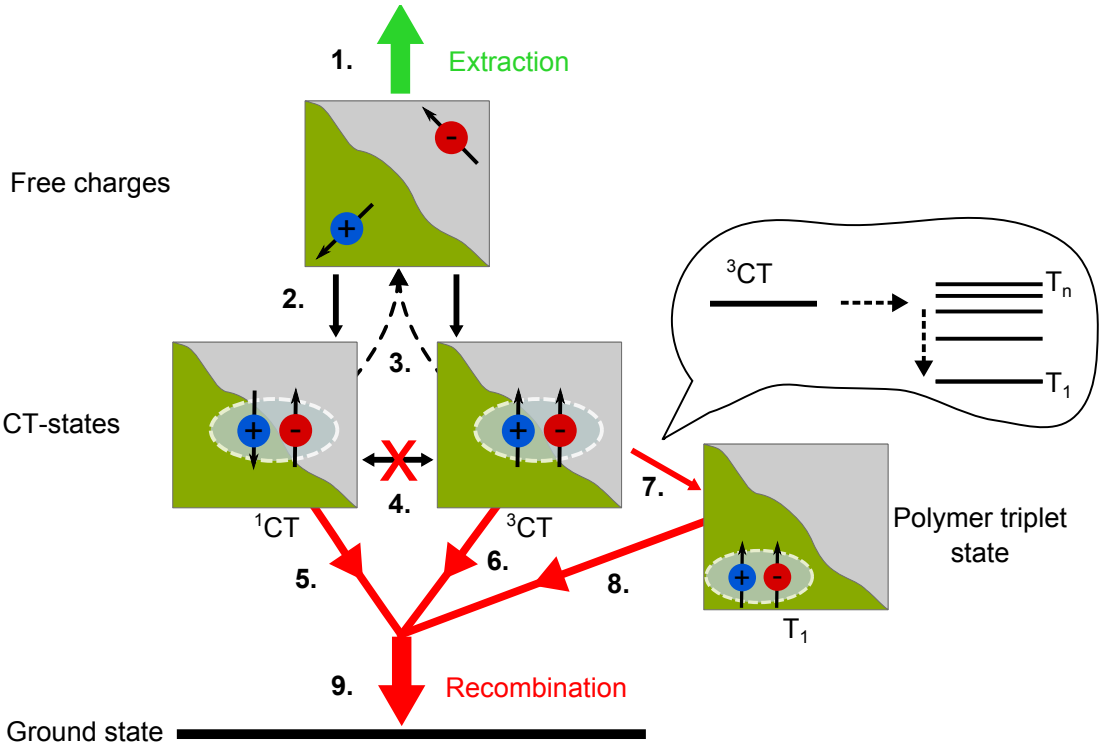

Figure 4.27: Triplet generation by bimolecular recombination of free charge carriers. The extraction of free charge carriers (green) (1.) is in kinetic competition with their recombination (red) (9.). When free charge carriers of uncorrelated spin recombine (2.), CT states with spin singlet and spin triplet character are formed in a statistical ratio of 1:3. If they do not redissociate again (3.), the ^{1}CT states relax to from a tightly bound CT state (not shown) and recombine geminately to the ground state (5.). It is also possible for the ^{1}CT states to turn into ^{3}CT states by spin dephasing, but in the observed materials the lifetime of the ^{1}CT states is too short (4.). The geminate recombination of the ^{3}CT states is much slower than that of the ^{1}CT states (6.), so that the dominating processes are the redissociation (3.) and the competing transfer to the polymer triplet state (7.). The polymer triplets undergo mainly charge-triplet annihilation to the ground state (8.).

process started as early as 50-100 ps for the lowest fluences in PSBTBT and in PCPDTBT without ODT, and continued as long as free charge carriers were present. For PCPDTBT with ODT the onset of triplet generation was found even earlier.

To avoid confusion, the nature of the CT states involved in this process is briefly discussed, as the term CT state is often ambiguously used in literature. In our previously published two-pool model of charge generation and recombination two

separate pools of species are formed upon exciton dissociation, i.e. free charge carriers and bound CT states, which recombine non-geminately and geminately, respectively.[11, 112] These CT states are a terminal loss channel which distinguishes them from the CT states described above in the triplet generation mechanism, as in the latter redissociation is explicitly allowed. This is not a contradiction but it rather implies that the properties of the states involved are different. It is likely that the CT states, that can redissociate again, are more loosely bound compared to the tightly-bound relaxed CT states that undergo geminate recombination, and hence are more similar to an intermediate encounter complex $\{D^+ \cdots A^-\}$ described by Ferguson et al. as a state that consists of two charges that are loosely bound across the interface when they meet each other.[124] These intermediate encounter complexes can relax into a strongly bound CT state or redissociate again. For simplicity, figure 4.27 only shows CT states that can redissociate and leaves out tightly-bound, i.e. relaxed CT states. In the following, the term CT states represents charge-transfer states that can redissociate again.

The kinetic competition between the redissociation of the ^{3}CT states and the population of T_1-states, which determines how fast triplets are generated, is reported to critically depend on the energetics and morphology at the interface. Rao et al. showed that the redissociation can be thermally activated leading to the suppression of triplet generation at room temperature, whereas at low temperatures the population of the T_1 state dominates.[119] They further demonstrated that the amount of fullerene plays a critical role, as larger amounts of fullerene led to enhanced crystallization of the fullerene phase driving charge dissociation. If we compare the signal contribution of the polymer triplet states and the timescale on which they are formed in our measurements, we see that the PCPDTBT:PC_{60}BM blend processed with ODT forms a larger fraction of triplets on a shorter timescale compared to PCPDTBT:PC_{60}BM without ODT and PSBTBT:PC_{70}BM. Considering only the amount of free charge carriers generated in the blend, the PSBTBT system should show the largest triplet contribution and the fastest generation followed by PCPDTBT with ODT and the blend without ODT. The reduced triplet generation in PSBTBT compared to PCPDTBT with ODT therefore has to result from differences of the charge-transfer state at the interface, more specifically the arrangement of the ^{3}CT energy level with respect to the T_n levels and the delocalization of the CT states.

The PSBTBT blend contained less PCBM than the PCPDTBT blends, but still the triplet contribution after 1 ns was smaller in the former. We do not know how the energy levels of the ^{3}CT states and the T_n-states are arranged in the different blends and therefore cannot rule out its influence on the kinetic competition, but it is likely that the differences in the morphology of the blends are also of importance. The PSBTBT polymer shows enhanced crystallinity, which was already mentioned in section 4.3. It seems reasonable that due to the higher crystallinity in PSBTBT compared to PCPDTBT the delocalization of the CT states is higher, causing a reduction of the energetic barrier for redissociation, which in turn increases the associated rate and reduces the triplet transfer to the polymer. This process effectively reduces the rate of non-geminate recombination to the ground state and explains why the free charge carriers in the PSBTBT blend have a longer lifetime than in the other blends. The redissociation of the charge pairs is also a reason for the observed reduced recombination rate in organic photovoltaic blends compared to Langevin recombination (see 2.5.2). The PCPDTBT blend with ODT also shows a high yield of free charge carriers, but the redissociation of the CT state seems to be less efficient as the recombination of the free charge carriers leads to fast triplet formation, which in turn significantly reduces the charge carrier lifetime. The morphology of the blend prepared without ODT is the most intermixed one of the three samples and should accordingly provide the worst conditions for charge-pair dissociation. This manifests itself in the low free charge carrier yield that explains the slower and smaller triplet contribution. The shorter lifetime of the free charge carriers compared to PSBTBT indicates that non-geminate recombination to the ground state is fast. Hence, the redissociation rate of the CT states is also small.

In all blends the decay of triplets is fluence dependent and much faster than a typical triplet lifetime. This indicates that the triplet population is quenched by triplet-triplet annihilation or by charge-triplet annihilation, from which the latter is more probable due to the high charge carrier densities present in these photovoltaic blends.

4.4.1.2 Additional mechanisms of fast triplet generation

The generation of polymer triplet states from bimolecular recombination of free charge carriers provides a reasonable explanation for the observed polymer triplet

generation at low fluences. However, figures 4.14a and 4.14b suggest that at high fluences triplets are generated even faster on a sub-10 ps timescale. The fluence dependent shift of the 10 ps TA-spectra further indicates that this fast generation process is fluence dependent, ruling out any mechanism which would lead to the direct transition of a polymer singlet exciton into a ^{3}CT state at the interface by charge-transfer. Free charge carriers are generated in all of the blends on a timescale faster than 150 fs, so that bimolecular recombination of free charge carriers is a possible mechanism. Bimolecular recombination on a ps timescale, however, would require a high carrier mobility, so that the outcome of an encounter of two charges with high mobility is likely to be their redissociation. A further investigation is therefore necessary to fully understand the triplet generation mechanisms in OPV blends at early times.

4.4.1.3 Comparison to literature

The role of triplet states in the three material systems was also investigated by Di Nuzzo et al. and Distler et al. who performed cw-PIA measurements on the three material systems.[118, 122] Di Nuzzo et al. observed an increase in the free charge carrier generation upon addition of ODT to the PCPDTBT:PCBM blend and explained this by an energetically higher-lying T_1-state in the blend prepared with ODT, which suppresses the transfer from the ^{3}CT state. Without ODT, they argued, that a high amount of triplets is formed due to the lower lying T_1-state. As a pathway for the generation of ^{3}CT states they propose spin dephasing of ^{1}CT states, which is however rather unlikely as discussed above.[81] Chow et al. and Rao et al. observed in TA measurements on the same material systems a higher triplet population in the blend with ODT in agreement with our results and argued that due to the faster generation and quenching of the triplets in the blend with ODT, the PIA signal shows a smaller triplet contribution, as the PIA signal is always a live-time averaged signal.[119, 120] Distler et al. extended the cw-PIA experiments to PSBTBT:PCBM. Same as Di Nuzzo et al. they assigned the PIA around 1 eV to charge- as well as triplet-induced absorption and compared that to the relative signal height at 0.4 eV, where exclusively charge carriers absorb.[118] They performed measurements at room temperature and at 80 K, and compared the difference between the two normalized spectra to the cw-PIA of a pristine polymer film to see if triplets were formed. For PCPDTBT, the

difference spectrum clearly resembled the triplet-induced absorption spectrum indicating that with decreasing temperature the amount of triplets, living long enough to be detected, increases. For PSBTBT they came to the conclusion that almost no triplets were formed. These results are in line with our results as they in general support the presence of triplets states in low-bandgap systems. Conclusions about the relative contributions of two species with different lifetimes from cw-PIA experiments are, however, not completely reliable due to the fact that lifetime as well as population density affect the cw-PIA signal.

4.4.2 Revisiting our previous PCPDTBT:$PC_{60}BM$ results

On the basis of this analysis some of our results previously published in [49] on PCPDTBT:PCBM need to be revisited. The model used to fit the long time recombination dynamics assumed only two pools of excited states, namely free charge carriers and relaxed CT states. The appearance of a third species, namely the triplet population, changes the meaning of the extracted fit parameters to be more of a general parametrization, characterizing the total signal decay. Nevertheless, the conclusion from the modeling of the long time data that fast non-geminate recombination limits the device performance in PCPDTBT:PCBM solar cells is still valid, and the analysis in this chapter further delivers an explanation why non-geminate recombination is fast in these low-bandgap material systems. The presence of the energetically low polymer triplet state opens up an additional decay channel for CT-excitons with spin triplet character, which is in direct competition to the redissociation of these states. The fast generation of triplets further shows that the transfer to the polymer triplet state is fast and therefore significantly reduces the probability of ^{3}CT-excitons to dissociate into free charge carriers again. With an energetically higher lying T_1-state non-geminate recombination might be slower, as the ^{3}CT states formed via bimolecular recombination effectively reduce the recombination rate, if they have enough time and a favorable interface to redissociate.

We further estimated the amount of geminate recombination from the decay of the ground state bleach on the first few ns. For the blend without ODT, in which only few triplets are generated on the short time scale at low fluence, this might

still be a valid assumption, however for the blend with ODT the situation is more complex. We clearly observed significant sub-ns triplet generation in this blend indicating that fast non-geminate recombination is present in the first ns. Neglecting the recombination to the ground state on the first ns and assuming that almost all charges that recombine form triplet states, we still have to assume that the cross-section of the GSB of triplet states is the same as for the charges in order to extract information about the fraction of geminate recombination in the blend. As the cross-section of the GSB is difficult to measure and overlaid by differing PIAs of the excited states, quantization of the geminate losses in PCPDTBT:PCBM as well as in PSBTBT:PCBM is not possible without further assumptions. Nonetheless, by estimating the IQEs of the material systems an approximation of the total loss is given in the next section.

4.4.3 Implications for photovoltaic performance

In an operating device the extraction of free charge carriers is in kinetic competition to non-geminate recombination. The above discussed analysis revealed that by increasing the rate of transfer from the ^3CT-state to the T_1-state or by decreasing the redissociation rate of the ^{3}CT states, the rate of the non-geminate recombination of charge carriers to the ground state is increased. This causes a reduction of the free charge carrier lifetime, which directly influences the charge extraction.

The quantification of the processes and their influence on device performance is difficult because the triplet population is rapidly quenched by the charges and created by bimolecular recombination throughout the whole time scale, meaning that the number of triplets generated cannot simply be read from their concentration profile. The bimolecular recombination also critically depends on the charge carrier density present in the device. Chow et al. performed TA measurements at slightly lower excited state densities, i.e. between 10^{16}-10^{17} 1/cm^3 and observed slightly slower triplet generation. This is reasonable as our lowest excitation density is approximately $2-3\times10^{17}$ 1/cm^3. Credington et al. measured the charge carrier density in a device at open-circuit voltage by charge extraction to be between 10^{16}-10^{17} 1/cm^3,[125] indicating that the results from our lowest excitation densities are close to working conditions of organic solar cells.

The fill-factor of the PSBTBT:$PC_{70}BM$ devices is with 64 % the highest of the investigated material systems, compared to 45 % for PCPDTBT:$PC_{60}BM$ with ODT and 38 % for the blend without ODT. Non-geminate recombination decreases the fill-factor due to the bias dependence of extraction, explaining the smaller fill-factor of PCPDTBT with ODT compared to PSBTBT. The fill-factor of PCPDTBT without ODT is even worse, although we demonstrated that the non-geminate recombination in the blend with ODT is faster due to the faster triplet generation. However, by comparing the field-dependence of charge generation in all three blends (figure 4.28a) measured by Albrecht et al by TDCF experiments,[84] the strongest bias dependence of charge generation can be observed in PCPDTBT without additive, which further reduces the fill-factor.

Assuming that all absorbed photons create charge carriers that contribute to the photocurrent, i.e. an internal quantum efficiency of 100 %, the maximum obtainable short-circuit current for the different systems can be calculated using

$$J_{sc} = \frac{e}{hc} \int \lambda \cdot EQE(\lambda) \cdot P_{AM1.5G}(\lambda) d\lambda, \tag{4.9}$$

in which $EQE(\lambda)$ is exchanged by the fraction of absorbed photons. The results are shown in table 4.3 compared to the short-circuit currents obtained from the EQE. For the low-bandgap material systems the short-circuit current obtained from the EQE is always higher than that from the JV-curves (4.1a). This can be explained by the large mismatch factor of our solar simulator for low-bandgap systems and the reduced power of only approx. 0.8 suns of the solar simulator. For PSBTBT the short-circuit current calculated from the EQE is in good agreement with the values measured with different solar simulators for exactly the same material system.[126] By comparing the values from the EQE with

System	J_{SC} from EQE	J_{SC} from absorption
PCDTBT:$PC_{60}BM$	8.38	11.2
PCPDTBT:$PC_{60}BM$(ODT)	7.8	15
PCPDTBT:$PC_{60}BM$	4.2	15
PSBTBT:$PC_{70}BM$	14.5	20

Table 4.3: Comparison of the short-circuit current in mA/cm^2 obtained from equation (4.9) *with the measured EQE (J_{SC} from EQE) and the theoretical limit if a all absorbed photons contribute to the photocurrent generation (J_{SC} from absorption).*

the one obtained for an IQE of 100 %, the IQE in the PSBTBT system can be estimated to be approximately 73 %, which is in good agreement with the results from Albrecht et al. who obtained a value of 70 %.[126] The 30 % loss are therefore distributed between geminate recombination and non-geminate recombination. The high fill-factor in the PSBTBT system suggests that most of the losses are geminate. It could, however, also be possible that field-independent fast non-geminate losses caused by the population of triplet states are present. We performed time-delayed double pump measurements on the system (see [91] for experimental details) and observed that only at high negative bias, starting around -4 V, the recombination could be suppressed in favor of extraction as shown in figure 4.28b, which is larger than usual OPV operation conditions. We cannot quantify the different loss channels, but the analysis indicates that fast non-geminate recombination due to triplet generation may cause a reduction of the OPV performance although the fill-factor is high.

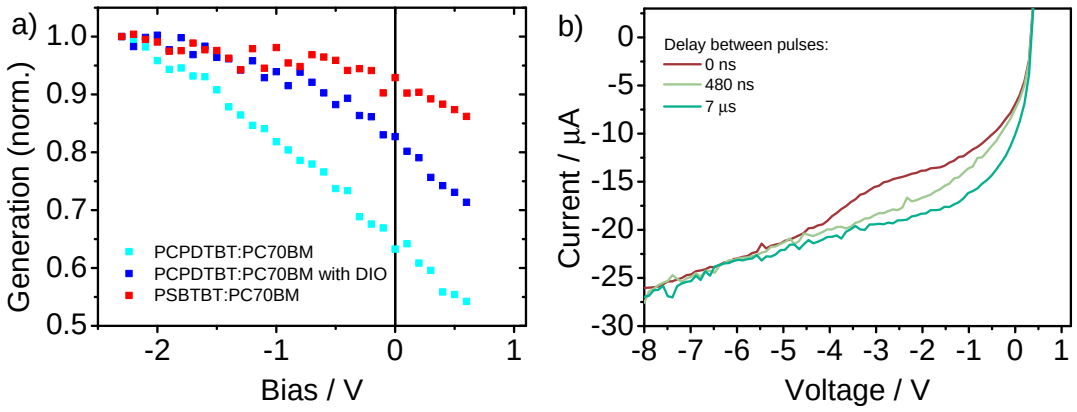

Figure 4.28: a) Field-dependent charge generation in the low-bandgap polymer systems. PSBTBT:$PC_{70}BM$ (red), PCPDTBT/$PC_{70}BM$ with additive (dark blue), PCPDTBT/$PC_{70}BM$ without additive (light blue). Data measured by Albrecht et al.[84] b) Time-delayed double pump experiments on PSBTBT:$PC_{70}BM$. The different colors represent the delay time between the two pulses.

For the PCPDTBT systems the estimated IQE is 52 % with ODT and only 28 % without ODT. For both devices the effect of non-geminate recombination is clearly visible in the strong field dependence of the JV-curve (4.1a) indicating that fast non-geminate recombination is a major loss channel. The small intensity dependence of the charge carrier dynamics in PCPDTBT:PCBM without ODT

together with the low free charge carrier yield reported elsewhere,[122] demonstrates that the decay in the first few ns is dominated by geminate recombination, which therefore makes up a second large loss channel and further decreases the device efficiency. For the lowest fluence the maximum of the GSB decayed approximately to 50 % on the first 2 ns in this system,[49] which is accordingly the upper limit of geminate recombination. Chow et al. obtained a value of $(43 \pm 5)\%$ for the system with $PC_{70}BM$, which is in good agreement with our results.[120] For the blend with ODT the influence of geminate recombination is even more difficult to determine, as non-geminate recombination strongly overlays the decay on the first few ns. This is obvious from the fast rise of the triplet population. Due to the changed morphology caused by the addition of ODT, the free charge carrier yield is higher, hence, geminate recombination should be suppressed and fast non-geminate recombination appears to be the major loss channel in this system.

4.4.4 Comparison of low- and mid-bandgap materials

The first donor material investigated in this work, PCDTBT, is a mid-bandgap donor polymer, still ranging among the best performing materials with efficiencies approaching 7 % in blends with $PC_{70}BM$.[127] The other two donor materials, PCPDTBT and PSBTBT, are low-bandgap polymers, guaranteeing largely broadened absorption spectra, which push the limit of photocurrent generation above 800 nm. But despite the broad absorption, the desired increase in OPV performance is not achieved. Figure 4.29 shows the EQE spectra of the the three donor materials blended with $PC_{60}BM$ and $PC_{70}BM$, respectively, in which the advantage of low-bandgap materials regarding broad photon harvesting becomes clearly visible. However, if by calculating the IQE for the PCDTBT system from the short-circuit current comparison as above, a value of 85 % is obtained, which is much larger than those of the low-bandgap systems. For a fully optimized device consisting of PCDTBT and $PC_{70}BM$ even higher IQEs approaching 100 % were reported,[32] indicating that loss mechanisms are completely suppressed in this blend. This is in line with our results obtained from TAS, in which we found that only 11 % of the initial photoexcitations form strongly bound CT states that recombine on a ns timescale. The deviations from the 100 % IQE reported in lit-

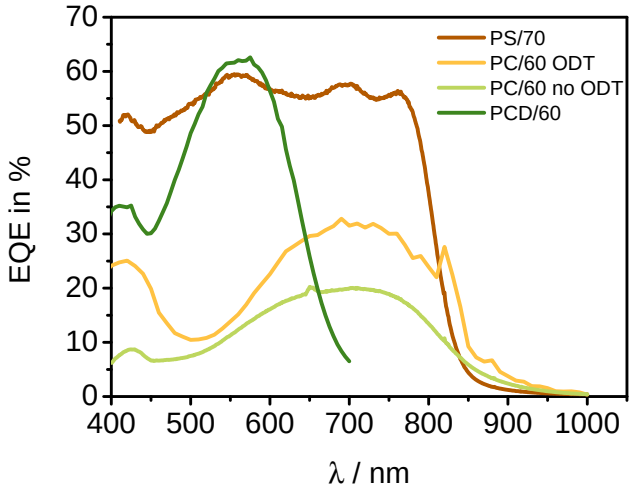

Figure 4.29: External quantum efficiencies of PSBTBT:$PC_{70}BM$ (PS/70), PCPDTBT:$PC_{60}BM$ with ODT (PC/60 ODT), PCPDTBT:$PC_{60}BM$ without ODT (PC/60 no ODT), and PCDTBT:$PC_{60}BM$ (PCD/60).

erature are probably due to the different molecular weight of the donor material used in our experiments.

The benchmark system P3HT:PCBM, for comparison, has an onset of absorption similar to that of PCDTBT:PCBM and also a high IQE, but lower device performances are obtained. Comparing the donor HOMO energy levels of P3HT (-4.9 eV)[128] and PCDTBT (-5.5 eV)[30] it is obvious that PCDTBT has the lower HOMO level that causes, according to (2.5), a higher open-circuit voltage. From our experiments open-circuit voltages as high 0.75 V were measured, which already exceeds that of P3HT by 0.15 V. In literature even higher values of up to 0.88 V were reported, and higher currents were obtained by introducing an optical spacer to optimize the light management in the device.[32] The drawback of the PCDTBT system is the necessity of a rather thin active layer, as the material is limited by strong carrier trapping. The low film thickness in turn limits the total amount of photons that can be absorbed by the photoactive layer.[129]

The investigated low-bandgap polymer systems generate only moderate open-circuit voltages which is a second reason besides the lower IQE for the lower device performance compared to PCDTBT. However, it was shown before that high-open circuit voltage devices can suffer from geminate recombination into the

polymer triplet state, before free charge carriers are generated, which effectively reduces the device performance.[10] It was further empirically found that the CT state energy level is approximately 0.45-0.47 eV higher than the open-circuit voltage.[122] This means that by increasing V_{OC} the probability to shift the CT state level above the polymer triplet level increases, which may also increase loss mechanisms involving triplet state generation. In this work, we demonstrated that for the investigated low-bandgap materials fast non-geminate recombination due to the generation of triplet states reduces the device efficiency, indicating that although the open-circuit voltages are only moderate, the triplet level is already accessible. Higher open-circuit voltages in these devices could facilitate the polymer triplet generation to a point where it competes even stronger with charge carrier extraction. In PCDTBT:PCBM we did not observe any triplet generation, which may in part explain the high IQE of the system. This does not mean that the triplet level is necessarily higher in energy than the CT state as a rough approximation demonstrates. The onset of absorption in PCDTBT is around 1.85 eV, and assuming that this is the S_1 energy level, the T_1 energy level should be around 1.15 eV due to the exchange energy which was found to be approximately 0.7 eV in conjugated polymers.[130] With a measured V_{OC} of 0.75 V the CT state should be around 1.2 eV.[122] These values are only rough approximations, but they indicate that also for the high performing systems the triplet level could be energetically accessible, however, without consequences for device performance. It is therefore necessary, especially for systems with a low donor triplet energy level, to provide a morphology which guarantees efficient and fast CT state splitting or redissociation and strong suppression of non-geminate recombination. Rao et al. suggested that the delocalization of the interfacial states plays a critical role as further delocalization might increase the dissociation of these states and thereby effectively decrease the amount of geminate recombination as well as slow down non-geminate recombination.[119] It still remains an open question how far these processes are influenced by the large disorder present in the efficient PCDTBT system. In conclusion, we found that in addition to geminate recombination all investigated low-bandgap systems suffer from fast non-geminate recombination caused by polymer triplet state generation, whereas in the high open-circuit mid-bandgap material this loss channel did

not play a significant role. This may explain the much higher IQE observed in the mid-bandgap material.

Chapter 5

Conclusions and Outlook

5.1 Charge generation and recombination in polymer:fullerene blends

The TAS performed on the mid-bandgap polymer:fullerene blend PCDTBT:PCBM revealed that after photoexcitation singlet excitons are rapidly quenched on a time scale faster than our system response (approx. 150 fs). In this process two pools of charged species are formed, i.e. tightly-bound, relaxed CT states and free charge carriers. Due to the system response time, we cannot observe potential intermediate states during free charge generation, but recent literature results indicate that quenching of the singlet excitons creates hot CT states which either directly dissociate into free charge carriers or relax into tightly-bound CT states faster than 1 ps.[75] To model the decay of the TA signal on the long time scale, we therefore assumed a pool of relaxed CT states that recombines geminately plus a pool of separated free charge carriers that undergo non-geminate recombination. This is different from the Onsager-Braun mechanism of charge separation which explicitly includes a kinetic competition between recombination and dissociation of the intermediate CT states. The successful description of the data by our two-pool model demonstrates that the Onsager-Braun model is not required to describe the recombination of relaxed CT states and free charge carriers.

We further analyzed the different pathways of charge generation by selectively exciting the polymer and the fullerene, which is possible due to the spectrally sep-

arated absorptions of the low-bandgap polymers and the fullerene. We found that in contrast to the ultrafast charge generation observed for the quenching of polymer singlet excitons, excitation of the fullerene led to a diffusion-limited exciton quenching process, indicating exciton diffusion in the fullerene domains is much slower, thereby resulting in delayed charge generation up to several 100 ps. The prolonged diffusion of fullerene excitons also led to the observation of fullerene singlet-singlet annihilation and/or exction-charge annihilation.

5.2 Effect of disorder on charge generation and recombination

We have demonstrated that PCDTBT:PCBM blends exhibit a large degree of energetic disorder. This manifested itself in a pronounced red-shift of the time-resolved fluorescence of a pristine polymer film, as well as a red-shift of the ground state bleach in transient absorption measurements on a polymer:fullerene blend. The relaxation of the ground state bleach started after approx. 100 ps and continued to 100 ns resulting in a total shift of 200 meV. It was assigned to the relaxation of the hole polaron within the density of states. Morphological investigations of PCDTBT:PCBM blends revealed poor short-range order,[129] but nonetheless internal quantum efficiencies approaching unity have been reported.[32] The large energetic disorder may play an important role for charge separation in this system, as a charge injected into sites of high energy within the density of states should have a high mobility, which facilitates effective charge separation and may explain the low fraction of geminate recombination observed in this system. The drawback of the large disorder is, however, a charge carrier mobility limited by traps, which in turn limits the useful thickness of the active layer in a device. Hence, not all of the photons can be absorbed.[129]

5.3 The effect of solvent additives on the photophysics of PCPDTBT:PCBM blends

The addition of a high boiling point co-solvent during the processing of the low-bandgap polymer PCPDTBT:PCBM blend has been reported to largely increase

the performance of the photovoltaic device.[123] In a photophysical study on this system by means of TAS, we observed diffusion-limited exciton quenching of polymer excitons up to approx. 10 ps in the sample prepared with ODT, in contrast to the sample prepared without ODT, in which the initially generated polymer excitons could not be detected. ODT, therefore, causes a demixing of the blend's components so that larger domains are formed, which in turn increases the average diffusion length of the excitons. Solid state NMR measurements provided further evidence for the change in morphology. Agostinelli et al. reported an increase in the photocurrent upon addition of ODT measured by transient photovoltage experiments and explained this with a higher order of the blend prepared with ODT,[131] which is in good agreement with our results. The effect of the co-solvent is, therefore, very similar to the effect of thermal annealing of regio-regular P3HT:PCBM blends, which has also been reported to change the charge generation from exclusively ultrafast exciton quenching on a sub-100 fs time scale to partially diffusion-limited polymer exciton quenching.[11] This indicates that the ideal morphology for efficient charge generation and separation is a trade-off between the maximum interface of an intimately-mixed blend and a blend with larger and purer domains driving charge separation. The larger domains on the one hand reduce the amount of interface so that a small fraction of excitons might be lost before quenching, but on the other hand enable enhanced wavefunction delocalization of the interfacial states created directly after charge transfer, thereby facilitating their separation. Furthermore, larger and purer domains enhance the percolation of the system so that charge transport to the electrodes is facilitated. In PCPDTBT:PCBM and P3HT:PCBM the latter processes outweigh the exciton losses and accordingly improve the device performance.

5.4 The role of triplet states in OPV blends

The analysis of the TA data of the low-bandgap materials PCPDTBT:PCBM and PSBTBT:PCBM by model-free multi-variate curve resolution revealed that after photoexcitation all blends show a long-lived species in addition to the free charge carriers, whose generation is a fluence dependent process. This species was identified as the polymer triplet, which showed lifetimes of several 100 ns.

By deconvoluting the transient data surfaces, we showed that the polymer triplet states are generated by non-geminate recombination of free charge carriers. In fact, the polymer triplet energy level was reported to be lower or close to that of the CT state, making this transition energetically possible.[122]

When fully separated charge carriers meet at the interface, they form loosely-bound CT states of which, from an entirely statistical point of view, 25 % have spin singlet character (^{1}CT) and 75 % have spin triplet character (^{3}CT). These states either redissociate into free charge carriers or recombine. We found that the direct precursor of the observed polymer triplet states are ^{3}CT states generated by non-geminate recombination of free charge carriers. Theoretically, the ^{3}CT states could also be generated by spin-dephasing of ^{1}CT states,[10] but the short sub-ns CT-lifetime reported for these systems prevents this mechanism.[81] The transfer from the ^{3}CT state to the polymer triplet state therefore opens up a new decay channel for the ^{3}CT states, which is in kinetic competition to their redissociation. The generation of polymer triplet states increases the rate of non-geminate recombination so that the competition between extraction and non-geminate recombination of free charge carriers is shifted towards the latter and thus reduces the device efficiency.

Of the three investigated low-bandgap systems, i.e. PCPDTBT:$PC_{60}BM$ prepared without and with ODT, and PSBTBT:$PC_{70}BM$, the PCPDTBT system prepared with ODT showed the fastest rise of the triplet contribution in agreement with recent literature results.[120] With respect to PCPDTBT prepared without ODT this is interesting as the device performance of the blend with ODT is twice as high as of the system prepared without ODT. This can be explained by the lower yield of free charge carriers in the system without ODT,[131] indicating that geminate losses are strong (up to 50 %). Due to the morphology of the blend prepared with ODT, the yield of free charge carriers is higher, which in turn indicates that geminate losses are smaller, and therefore non-geminate recombination has to be the dominating loss channel. The poor fill-factor of the devices is in good agreement with the conclusion that fast triplet generation makes non-geminate recombination a serious loss channel in the blend prepared with ODT. The PSBTBT devices showed the best power conversion efficiency with an average IQE of 70 %. Due to the higher fraction of free charge carriers, a higher

triplet yield could be expected, but this decay channel seemed to be suppressed compared to PCPDTBT prepared with ODT, causing the free charge carriers in the PSBTBT blend to exhibit the longest lifetime at open-circuit conditions, i.e. in a film without electrodes (no carrier extraction). Still, time-delayed double pump experiments revealed that fast, field-independent non-geminate recombination reduced the amount of extractable current, indicating that the 30 % loss in the PSBTBT system are distributed between geminate and non-geminate recombination. The rate of polymer triplet generation depends on the energy level alignment of the ^{3}CT states with respect to the polymer triplets, but also thermal activation and the influence of morphology were recently presented to play a critical role.[119] This is in agreement with our results, showing that the sample with the highest crystallinity, which is PSBTBT:PCBM, exhibited the slowest triplet generation rate. Our analysis revealed that a broad absorption alone does not guarantee efficient OPV devices. We found that especially if the polymer triplet state is energetically accessible, fast redissociation of encountering oppositely charged carriers is necessary to reduce the non-geminate recombination losses. Rao et al. proposed that delocalization of the CT states might help,[119] which is in good agreement to our results, as the better order of PSBTBT might enhance these processes.

5.5 Outlook

5.5.1 Strategies to improve organic photovoltaic performance

For the improvement of organic solar cells and the development of novel OPV materials a detailed understanding of the underlying processes of charge generation and recombination is necessary. Although the knowledge of the photophysics of OPV blends has been increased over the last years, several aspects still remain unclear. In this thesis we observed large energetic disorder in a material system reported to yield efficiencies exceeding 6 % in a solar cell,[32] which indicates that disorder might also have positive effects on device performance. As this in contrast to the long-time benchmark system P3HT:PCBM, in which the enhanced crystallinity after thermal annealing is responsible for efficient operation,

a systematic investigation of the effect of energetic disorder in OPV materials could help to develop new materials. Especially in the light of the herein reported mechanism of polymer triplet state generation more insight into how disorder suppresses or enhances this loss channel is valuable. The high stability of PCDTBT:PCBM devices of up to 7 years makes carbazole-based materials very promising as a starting point for novel material development.[132]

Due to the limited absorption in devices containing PCDTBT as a donor polymer (bandgap approx. 1.8 eV), PCDTBT is a suitable candidate for tandem solar cells. Recently, Li et al. published efficiencies approaching 9 % in a system containing PCDTBT:$PC_{70}BM$ as a front cell and the low-bandgap small molecule blend PMDPP3T:$PC_{60}BM$ as a back cell shown in figure 5.1.[133] The drawback of tandem cells with different active layers is usually the required current matching, meaning that the total current of a tandem cell is limited to that of the sub-cell with the lower current. By splitting the back cell into two identical sub-cells, they further increased the PCE from 8.9 % to 9.6 % due to the reduced current loss in the back cell. You et al. approached this problem by developing a donor material yielding high photoresponse between 300-950 nm in a solar cell. By stacking two sub-cells with identical donor polymers on top of each other, they reported efficiencies exceeding 10 %.[6] This indicates that tandem cells might be a possible way to push the efficiency of organic solar cells above the barrier for commercialization, however, we have to keep in mind that with every additional layer the production gets more complicated and more expensive, especially for solution processing. For organic solar cells fabricated by the co-evaporation of small molecule donors and acceptors, multi-layer systems are easier to produce and with reported efficiencies of 12 % this technology is very promising.[43]

The investigated low-bandgap systems all exhibited only moderate open-circuit voltages. A next step would therefore be to develop methods to increase the open-circuit voltage that these materials yield in a OPV blend. An interesting approach has been presented by Albrecht et al., who showed that the fluorination of PCPDTBT lowered the HOMO energy level of the polymer resulting in an increased open-circuit voltage of 0.74 V.[134] They further reported a reduction of geminate and non-geminate recombination caused by the fluorination, stressing the importance of this approach.

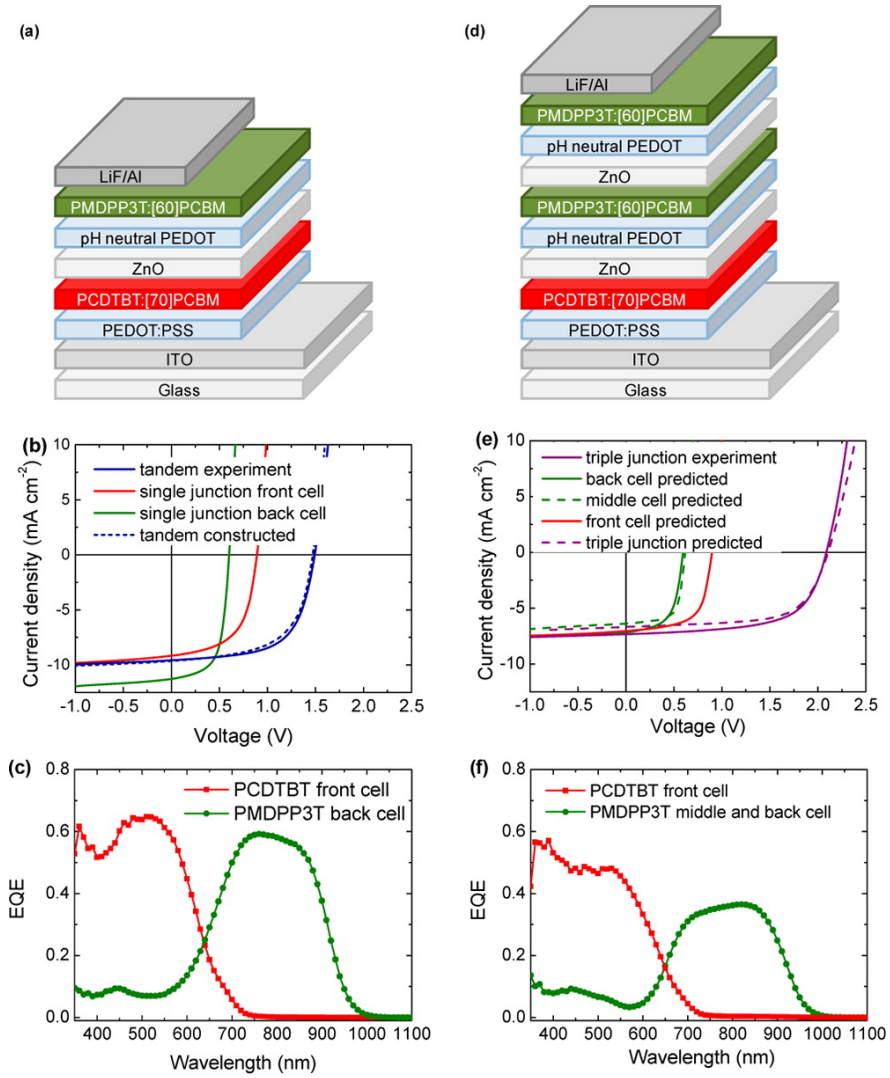

Figure 5.1: Tandem and triple-junction solar cells made from PCDTBT:$PC_{70}BM$ and PMDPP3T:$PC_{60}BM$. a) and d) display the layer stacks of the devices, b) and e) the JV-curves, and c) and f) the external quantum efficiencies. Reprinted with permission from [133]. Copyright (2013) American Chemical Society.

So far only progress on novel donor polymers has been discussed. However, alternative acceptor materials could also help to improve organic solar cells. Currently, fullerene derivates are the most used electron acceptors in organic photovoltaics because of their high electron affinity, high electron mobility, isotropic meaning three dimensional charge transport, and their favorable nanoscale morphology in blends with a polymeric donor.[135] Liu et al. further proposed that the existence of low-lying excited states of the fullerene anion increases the charge separation without increasing recombination.[135] Fullerenes are, however, expensive and have low absorption. One of the most promising alternatives to fullerenes are perylene diimide molecules (PDIs) which exhibit strong and tunable absorption throughout the visible spectral range and good charge transport properties (see [136] for an overview). Figure 5.2 shows the absorption spectra of an unsubstituted PDI (N,N'-bis(α-ethylpropyl)-3,4:9,10-tetra-carbonic acid diimide) film and a PSBTBT film together with the solar photon flux, indicating that the strong absorption of PDI around 500 nm ideally matches the complementary absorption of a low-bandgap polymer. The reported efficiencies with P3HT as a

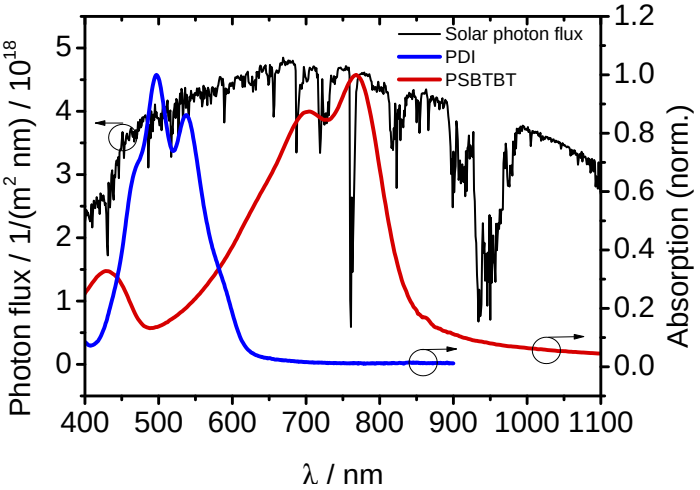

Figure 5.2: Absorption spectra of unsubstituted PDI and PSBTBT together with the solar photon flux.

donor are, however, only around 1 %,[137, 138], but by employing non-planar PDIs with the low-bandgap polymer PBDTTT-C-T as a donor, efficiencies of 2.77 % have been achieved.[40] Instead of using small molecule acceptors, polymeric acceptors also offer an alternative to fullerenes. Especially naphthalene

diimide copolymers (NDIs) have been investigated due to their high electron mobility (0.012 $cm^2V^{-1}s^{-1}$ in n-channel transistors), high electron affinity, and good stability.[139–141] The highest reported efficiencies so far exceed 3 %,[140] and Polyera recently reported an even better 6.4 % all-polymer solar cell, however, without revealing the used materials.[142] This clearly indicates that non-fullerene acceptors are on a good, promising way to compete with fullerene based organic solar cells.

5.5.2 Improvement of experimental techniques

The investigation of the non-geminate recombination of free charge carriers in OPV blends by transient absorption spectroscopy is always a trade-off between the signal-to-noise ratio and the excited state density caused by the pump laser fluence. For the materials investigated in this work, we measured at excited state densities of around $2 \times 10^{17}\,1/cm^3$. Especially for the deconvolution techniques described in this work a good signal quality is necessary so that small spectral shifts can be distinguished from noise. The carrier density in working devices under 1 sun conditions is however still lower, so that improvements of the signal-to-noise ratio are valuable. A possible strategy could be the implementation of a digital filter, rejecting probe pulses that show strong deviations due to temporal strong oscillations of the probe pulse stability. A further possibility might be alternations in the whitelight generation, e.g. using a 3.1 μm seed laser to drive whitelight generation in a YAG crystal as reported by Silva et al.[143] They observed supercontinuum generation with a spectral range of 450-4500 nm.

Low-bandgap materials exhibit polaron- and tripet-induced absorptions between 1000-2000 nm, meaning that it is not possible to record GSB and PIA with a silicon detector at the same time. Furthermore, grating spectrometers, as the ones used in our setup, are limited to a certain spectral range because higher diffraction orders of visible signals are superimposed onto the NIR signal contributions when both are measured at the same time. Therefore, the use of suitable filters is necessary. An alternative approach is to use a prism instead of a grating to disperse the signal laser pulse, in which higher order diffraction is absent.[144] This would enable recording the GSB and PIA at the same time, whereas at the moment two separate experiments are necessary.

The deconvolution of transient data surfaces was shown to contain a high degree of rotational ambiguity. In subsection 4.3.2 we saw that in the case of two species the spectrum of species 1 is directly correlated to the concentration profile of species 2 and vice versa. This means by measuring the concentration profile of one species, we obtain the spectrum of the other. In the case of charges and triplets in low-bandgap polymers this is difficult, because we have overlapping contributions throughout the whole spectral range detected. However, several publications demonstrated that charge carriers in low-bandgap materials exhibit a second absorption peak around 0.3 eV.[75, 122] By using difference frequency generation (see subsection 2.6.3.1), we can access this spectral region and could conduct single wavelengths experiments with, e.g. an InSb detector, to exclusively measure charge carrier dynamics. This approach would help to reduce the rotational ambiguity of the data analysis. If triplets were one of the species in the experiment, the quantitative observation of their spectra and cross-sections would also facilitate the analysis. We carried out experiments with the triplet sensitizer PtOEP, but the energy levels involved in the experiments were not optimal, so that it was not possible to estimate how many of the initial excitations resulted in polymer triplet states. The development of novel, red-absorbing triplet sensitizers could enable a more quantitative analysis of the triplet cross-section, helping to quantify loss channels in organic solar cells.

Bibliography

[1] Bundgaard, E. and Krebs, F. C. *Solar Energy Materials and Solar Cells* **91**(11), 954–985 (2007).

[2] *Deutscher Wetterdienst* (2012).

[3] *Statistisches Bundesamt* (2012).

[4] Krebs, F. C. *Solar Energy Materials and Solar Cells* **93**(4), 394–412 (2009).

[5] He, Z., Zhong, C., Su, S., Xu, M., Wu, H., and Cao, Y. *Nature Photonics* **6**(9), 591–595 (2012).

[6] You, J., Chen, C. C., Hong, Z., Yoshimura, K., Ohya, K., Xu, R., Ye, S., Gao, J., Li, G., and Yang, Y. *Adv Mater* **25**(29), 3973–8 (2013).

[7] *NREL: National Center for Photovoltaics* (2013).

[8] Peierls, R. *Quantum theory of solids*. Clarendon Press: Oxford, (1955).

[9] M. Schwoerer, H. W. *Organic Molecular Solids*. WILEY-VCH Verlag GmBH u. Co. KGaA, (2005).

[10] Westenhoff, S., Howard, I. A., Hodgkiss, J. M., Kirov, K. R., Bronstein, H. A., Williams, C. K., Greenham, N. C., and Friend, R. H. *Journal of the American Chemical Society* **130**(41), 13653–13658 (2008).

[11] Howard, I. A., Mauer, R., Meister, M., and Laquai, F. *Journal of the American Chemical Society* **132**(42), 14866–14876 (2010).

[12] Lee, J., Vandewal, K., Yost, S. R., Bahlke, M. E., Goris, L., Baldo, M. A., Manca, J. V., and Voorhis, T. V. *Journal of the American Chemical Society* **132**(34), 11878–11880 (2010).

[13] Kamm, V. *Substituierte Perylendimide als Elektronenakzeptoren in organischen Solarzellen.* PhD thesis, (2013).

[14] Kasha, M. *Discussions of the Faraday Society* **9**(0), 14–19 (1950).

[15] Gregg, B. A. *The Journal of Physical Chemistry B* **107**(20), 4688–4698 (2003).

[16] Thompson, B. C. and Fréchet, J. M. J. *Angewandte Chemie International Edition* **47**(1), 58–77 (2008).

[17] Brédas, J.-L., Cornil, J., and Heeger, A. J. *Advanced Materials* **8**(5), 447–452 (1996).

[18] Kearns, D. and Calvin, M. *The Journal of Chemical Physics* **29**(4), 950–951 (1958).

[19] Weinberger, B. R., Akhtar, M., and Gau, S. C. *Synthetic Metals* **4**(3), 187–197 (1982).

[20] Glenis, S., Tourillon, G., and Garnier, F. *Thin Solid Films* **139**(3), 221–231 (1986).

[21] Tang, C. W. *Applied Physics Letters* **48**(2), 183–185 (1986).

[22] Sariciftci, N. S., Braun, D., Zhang, C., Srdanov, V. I., Heeger, A. J., Stucky, G., and Wudl, F. *Applied Physics Letters* **62**(6), 585–587 (1993).

[23] Yu, G., Gao, J., Hummelen, J. C., Wudl, F., and Heeger, A. J. *Science* **270**(5243), 1789–1791 (1995).

[24] Halls, J. J. M., Walsh, C. A., Greenham, N. C., Marseglia, E. A., Friend, R. H., Moratti, S. C., and Holmes, A. B. *Nature* **376**(6540), 498–500 (1995).

[25] Asadi, K., Kronemeijer, A. J., Cramer, T., Koster, L. J., Blom, P. W., and de Leeuw, D. M. *Nature Communications* **4**, 1710 (2013).

[26] Wetzelaer, G.-J. A. H., Van der Kaap, N. J., Koster, L. J. A., and Blom, P. W. M. *Advanced Energy Materials* **3**(9), 1130–1134 (2013).

[27] Dennler, G., Scharber, M. C., and Brabec, C. J. *Advanced Materials* **21**(13), 1323–1338 (2009).

[28] Brabec, C. J., Gowrisanker, S., Halls, J. J. M., Laird, D., Jia, S., and Williams, S. P. *Advanced Materials* **22**(34), 3839–3856 (2010).

[29] Irwin, M. D., Buchholz, D. B., Hains, A. W., Chang, R. P. H., and Marks, T. J. *Proceedings of the National Academy of Sciences* **105**(8), 2783–2787 (2008).

[30] Blouin, N., Michaud, A., Gendron, D., Wakim, S., Blair, E., Neagu-Plesu, R., Belletête, M., Durocher, G., Tao, Y., and Leclerc, M. *Journal of the American Chemical Society* **130**(2), 732–742 (2007).

[31] Blouin, N., Michaud, A., and Leclerc, M. *Advanced Materials* **19**(17) (2007).

[32] Park, S. H., Roy, A., Beaupre, S., Cho, S., Coates, N., Moon, J. S., Moses, D., Leclerc, M., Lee, K., and Heeger, A. J. *Nature Photonics* **3**(5), 297–U5 (2009).

[33] Shrotriya, V., Ouyang, J., Tseng, R. J., Li, G., and Yang, Y. *Chemical Physics Letters* **411**(1–3), 138–143 (2005).

[34] Mühlbacher, D., Scharber, M., Morana, M., Zhu, Z., Waller, D., Gaudiana, R., and Brabec, C. *Advanced Materials* **18**(21), 2884–2889 (2006).

[35] Lu, H., Akgun, B., and Russell, T. P. *Advanced Energy Materials* **1**(5), 870–878 (2011).

[36] Albrecht, S., Schäfer, S., Lange, I., Yilmaz, S., Dumsch, I., Allard, S., Scherf, U., Hertwig, A., and Neher, D. *Organic Electronics* **13**(4), 615–622 (2012).

[37] Liang, Y., Xu, Z., Xia, J., Tsai, S.-T., Wu, Y., Li, G., Ray, C., and Yu, L. *Advanced Materials* **22**(20), E135–E138 (2010).

[38] Jayakannan, M., van Hal, P. A., and Janssen, R. A. J. *Journal of Polymer Science Part A: Polymer Chemistry* **40**(2), 251–261 (2002).

[39] Scharber, M. C., Muehlbacher, D., Koppe, M., Denk, P., Waldauf, C., Heeger, A. J., and Brabec, C. J. *Advanced Materials* **18**(6), 789–794 (2006).

[40] Rajaram, S., Shivanna, R., Kandappa, S. K., and Narayan, K. S. *The Journal of Physical Chemistry Letters* **3**(17), 2405–2408 (2012).

[41] Sun, Y., Welch, G. C., Leong, W. L., Takacs, C. J., Bazan, G. C., and Heeger, A. J. *Nat Mater* **11**(1), 44–48 (2012).

[42] Wang, D. H., Kyaw, A. K. K., Gupta, V., Bazan, G. C., and Heeger, A. J. *Advanced Energy Materials* **3**(9), 1161–1165 (2013).

[43] *Heliatek press release* (2013).

[44] Hoppe, H. and Sariciftci, N. S. *Journal of Materials Research* **19**(07), 1924–1945 (2004).

[45] Clarke, T. M. and Durrant, J. R. *Chemical Reviews* **110**(11), 6736–6767 (2010).

[46] Carsten, D. and Vladimir, D. *Reports on Progress in Physics* **73**(9), 096401 (2010).

[47] Banerji, N. *Journal of Materials Chemistry C* **1**(18), 3052–3066 (2013).

[48] Herrmann, D., Niesar, S., Scharsich, C., Köhler, A., Stutzmann, M., and Riedle, E. *Journal of the American Chemical Society* **133**(45), 18220–18233 (2011).

[49] Etzold, F., Howard, I. A., Forler, N., Cho, D. M., Meister, M., Mangold, H., Shu, J., Hansen, M. R., Mullen, K., and Laquai, F. *Journal of the American Chemical Society* (2012).

[50] Shaw, P. E., Ruseckas, A., and Samuel, I. D. W. *Advanced Materials* **20**(18), 3516–3520 (2008).

[51] Ward, A. J., Ruseckas, A., and Samuel, I. D. W. *The Journal of Physical Chemistry C* **116**(45), 23931–23937 (2012).

[52] Jamieson, F. C., Domingo, E. B., McCarthy-Ward, T., Heeney, M., Stingelin, N., and Durrant, J. R. *Chemical Science* **3**(2), 485–492 (2012).

[53] Banerji, N., Cowan, S., Leclerc, M., Vauthey, E., and Heeger, A. J. *Journal of the American Chemical Society* **132**(49), 17459–17470 (2010).

[54] Banerji, N., Cowan, S., Vauthey, E., and Heeger, A. J. *The Journal of Physical Chemistry C* **115**(19), 9726–9739 (2011).

[55] Cowan, S. R., Banerji, N., Leong, W. L., and Heeger, A. J. *Advanced Functional Materials* **22**(6), 1116–1128 (2012).

[56] Collini, E. and Scholes, G. D. *Science* **323**(5912), 369–373 (2009).

[57] Collini, E. and Scholes, G. D. *The Journal of Physical Chemistry A* **113**(16), 4223–4241 (2009).

[58] Caruso, D. and Troisi, A. *Proceedings of the National Academy of Sciences* **109**(34), 13498–13502 (2012).

[59] Marcus, R. A. *The Journal of Chemical Physics* **24**(5), 966–978 (1956).

[60] Jortner, J. *The Journal of Chemical Physics* **64**(12), 4860–4867 (1976).

[61] Onsager, L. *Physical Review* **54**(8), 554–557 (1938).

[62] Braun, C. L. *The Journal of Chemical Physics* **80**(9), 4157–4161 (1984).

[63] Tachiya, M. *The Journal of Chemical Physics* **89**(11), 6929–6935 (1988).

[64] Wojcik, M. and Tachiya, M. *Radiation Physics and Chemistry* **74**(3–4), 132–138 (2005).

[65] Nayak, P. K., Narasimhan, K. L., and Cahen, D. *The Journal of Physical Chemistry Letters* **4**(10), 1707–1717 (2013).

[66] Blom, P. W. M., Mihailetchi, V. D., Koster, L. J. A., and Markov, D. E. *Advanced Materials* **19**(12), 1551–1566 (2007).

[67] Mihailetchi, V. D., Koster, L. J. A., Hummelen, J. C., and Blom, P. W. M. *Physical Review Letters* **93**(21), 216601 (2004).

[68] Lenes, M., Morana, M., Brabec, C. J., and Blom, P. W. M. *Advanced Functional Materials* **19**(7), 1106–1111 (2009).

[69] van der Hofstad, T. G. J., Di Nuzzo, D., van den Berg, M., Janssen, R. A. J., and Meskers, S. C. J. *Advanced Energy Materials* **2**(9), 1095–1099 (2012).

[70] Morteani, A. C., Sreearunothai, P., Herz, L. M., Friend, R. H., and Silva, C. *Physical Review Letters* **92**(24), 247402 (2004).

[71] Ohkita, H., Cook, S., Astuti, Y., Duffy, W., Tierney, S., Zhang, W., Heeney, M., McCulloch, I., Nelson, J., Bradley, D. D. C., and Durrant, J. R. *Journal of the American Chemical Society* **130**(10), 3030–3042 (2008).

[72] Clarke, T. M., Ballantyne, A. M., Tierney, S., Heeney, M., Duffy, W., McCulloch, I., Nelson, J., and Durrant, J. R. *The Journal of Physical Chemistry C* **114**(17), 8068–8075 (2010).

[73] Shoaee, S., Clarke, T. M., Eng, M. P., Huang, C., Barlow, S., Espíldora, E., Luis Delgado, J., Campo, B., Marder, S. R., Heeney, M., McCulloch, I., Martín, N., Vanderzande, D., and Durrant, J. R. *Journal of Photonics for Energy* **2**(1), 021001–1 (2012).

[74] Clarke, T., Ballantyne, A., Jamieson, F., Brabec, C., Nelson, J., and Durrant, J. *Chemical Communications* (1), 89–91 (2009).

[75] Bakulin, A. A., Rao, A., Pavelyev, V. G., van Loosdrecht, P. H. M., Pshenichnikov, M. S., Niedzialek, D., Cornil, J., Beljonne, D., and Friend, R. H. *Science* **335**(6074), 1340–1344 (2012).

[76] Dimitrov, S. D., Bakulin, A. A., Nielsen, C. B., Schroeder, B. C., Du, J., Bronstein, H., McCulloch, I., Friend, R. H., and Durrant, J. R. *Journal of the American Chemical Society* **134**(44), 18189–18192 (2012).

[77] Jailaubekov, A. E., Willard, A. P., Tritsch, J. R., Chan, W.-L., Sai, N., Gearba, R., Kaake, L. G., Williams, K. J., Leung, K., Rossky, P. J., and Zhu, X. Y. *Nature Materials* **12**(1), 66–73 (2013).

[78] Grancini, G., Maiuri, M., Fazzi, D., Petrozza, A., Egelhaaf, H. J., Brida, D., Cerullo, G., and Lanzani, G. *Nature Materials* **12**(1), 29–33 (2013).

[79] Veldman, D., Ipek, O., Meskers, S. C. J., Sweelssen, J., Koetse, M. M., Veenstra, S. C., Kroon, J. M., Bavel, S. S. v., Loos, J., and Janssen, R. A. J. *Journal of the American Chemical Society* **130**(24), 7721–7735 (2008).

[80] Marsh, R. A., Hodgkiss, J. M., and Friend, R. H. *Advanced Materials* **22**(33), 3672–6 (2010).

[81] Jarzab, D., Cordella, F., Gao, J., Scharber, M., Egelhaaf, H.-J., and Loi, M. A. *Advanced Energy Materials* **1**(4), 604–609 (2011).

[82] Jamieson, F. C., Agostinelli, T., Azimi, H., Nelson, J., and Durrant, J. R. *The Journal of Physical Chemistry Letters* **1**(23), 3306–3310 (2010).

[83] Hwang, I. W., Cho, S., Kim, J. Y., Lee, K., Coates, N. E., Moses, D., and Heeger, A. J. *Journal of Applied Physics* **104**(3) (2008).

[84] Albrecht, S., Schindler, W., Kurpiers, J., Kniepert, J., Blakesley, J. C., Dumsch, I., Allard, S., Fostiropoulos, K., Scherf, U., and Neher, D. *The Journal of Physical Chemistry Letters* , 640–645 (2012).

[85] Kniepert, J., Schubert, M., Blakesley, J. C., and Neher, D. *The Journal of Physical Chemistry Letters* **2**(7), 700–705 (2011).

[86] Mauer, R., Howard, I. A., and Laquai, F. *The Journal of Physical Chemistry Letters* **1**(24), 3500–3505 (2010).

[87] Chirvase, D., Parisi, J., Hummelen, J. C., and Dyakonov, V. *Nanotechnology* **15**(9), 1317 (2004).

[88] Reid, O. G., Malik, J. A. N., Latini, G., Dayal, S., Kopidakis, N., Silva, C., Stingelin, N., and Rumbles, G. *Journal of Polymer Science Part B: Polymer Physics* **50**(1), 27–37 (2012).

[89] M. Pope, C. S. *Electronic Processes in Organic Crystals and Polymers*. Oxford University Press, (1999).

[90] Deibel, C., Baumann, A., and Dyakonov, V. *Applied Physics Letters* **93**(16), 163303 (2008).

[91] Mauer, R., Howard, I. A., and Laquai, F. *The Journal of Physical Chemistry Letters* **2**(14), 1736–1741 (2011).

[92] Koster, L. J. A., Kemerink, M., Wienk, M. M., Maturová, K., and Janssen, R. A. J. *Advanced Materials* **23**(14), 1670–1674 (2011).

[93] Juška, G., Arlauskas, K., Stuchlik, J., and Österbacka, R. *Journal of Non-Crystalline Solids* **352**(9–20), 1167–1171 (2006).

[94] Juska, G., GeneviCius, K., Nekrasas, N., Sliauzys, G., and Osterbacka, R. *Applied Physics Letters* **95**(1), 013303 (2009).

[95] Keller, U. *Nature* **424**(6950), 831–838 (2003).

[96] Saleh, B. E. A. and Teich, M. C. *Fundamentals of Photonics*. John Wiley and Sons, Inc., (2007).

[97] Couairon, A. and Mysyrowicz, A. *Physics Reports* **441**(2-4), 47–189 (2007).

[98] Bergé, L. and et al. *Reports on Progress in Physics* **70**(10), 1633 (2007).

[99] Gaeta, A. *Spatial and Temporal Dynamics of Collapsing Ultrashort Laser Pulses*, volume 114 of *Topics in Applied Physics*, chapter 16, 399–411. Springer New York (2009).

[100] Dudley, J. M., Genty, G., and Coen, S. *Reviews of Modern Physics* **78**(4), 1135–1184 (2006).

[101] Alfano, R. R. and Shapiro, S. L. *Physical Review Letters* **24**(11), 592 (1970).

[102] Gaeta, A. L. *Physical Review Letters* **84**(16), 3582–3585 (2000).

[103] Rothenberg, J. E. *Opt. Lett.* **17**(19), 1340–1342 (1992).

[104] Bradler, M., Baum, P., and Riedle, E. *Applied Physics B: Lasers and Optics* **97**(3), 561–574 (2009).

[105] Brodeur, A. and Chin, S. L. *Journal of the Optical Society of America B-Optical Physics* **16**(4), 637–650 (1999).

[106] Howard, I. A., Mangold, H., Etzold, F., Gehrig, D., and Laquai, F. *Transient absorption data analysis by soft-modeling*. Series in Optics and Photonics: Volume 8. World scientific (2013).

[107] van Wilderen, L. J. G. W., Lincoln, C. N., and van Thor, J. J. *PLoS ONE* **6**(3), e17373 (2011).

[108] de Juan, A., Maeder, M., Martínez, M., and Tauler, R. *Chemometrics and Intelligent Laboratory Systems* **54**(2), 123–141 (2000).

[109] de Juan, A. and Tauler, R. *Analytica Chimica Acta* **500**(1–2), 195–210 (2003).

[110] Jaumot, J., Gargallo, R., de Juan, A., and Tauler, R. *Chemometrics and Intelligent Laboratory Systems* **76**(1), 101–110 (2005).

[111] de Juan, A. and Tauler, R. *Critical Reviews in Analytical Chemistry* **36**(3-4), 163–176 (2006).

[112] Etzold, F., Howard, I. A., Mauer, R., Meister, M., Kim, T.-D., Lee, K.-S., Baek, N. S., and Laquai, F. *Journal of the American Chemical Society* **133**(24), 9469–9479 (2011).

[113] Zhang, M., Tsao, H. N., Pisula, W., Yang, C., Mishra, A. K., and Müllen, K. *Journal of the American Chemical Society* **129**(12), 3472–3473 (2007).

[114] Hou, J., Chen, H.-Y., Zhang, S., Li, G., and Yang, Y. *Journal of the American Chemical Society* **130**(48), 16144–16145 (2008).

[115] Chen, H.-Y., Hou, J., Hayden, A. E., Yang, H., Houk, K. N., and Yang, Y. *Advanced Materials* **22**(3), 371–375 (2010).

[116] Morana, M., Azimi, H., Dennler, G., Egelhaaf, H.-J., Scharber, M., Forberich, K., Hauch, J., Gaudiana, R., Waller, D., Zhu, Z., Hingerl, K., van Bavel, S. S., Loos, J., and Brabec, C. J. *Advanced Functional Materials* **20**(7), 1180–1188 (2010).

[117] Choudhury, K. R., Subbiah, J., Chen, S., Beaujuge, P. M., Amb, C. M., Reynolds, J. R., and So, F. *Solar Energy Materials and Solar Cells* **95**(8), 2502–2510 (2011).

[118] Distler, A., Kutka, P., Sauermann, T., Egelhaaf, H. J., Guldi, D. M., Di Nuzzo, D., Meskers, S. C. J., and Janssen, R. A. J. *Chemistry of Materials* **24**(22), 4397–4405 (2012).

[119] Rao, A., Chow, P. C., Gelinas, S., Schlenker, C. W., Li, C. Z., Yip, H. L., Jen, A. K., Ginger, D. S., and Friend, R. H. *Nature* **500**(7463), 435–9 (2013).

[120] Chow, P. C., Gelinas, S., Rao, A., and Friend, R. H. *submitted* (2013).

[121] Colsmann, A., Puetz, A., Bauer, A., Hanisch, J., Ahlswede, E., and Lemmer, U. *Advanced Energy Materials* **1**(4), 599–603 (2011).

[122] Di Nuzzo, D., Aguirre, A., Shahid, M., Gevaerts, V. S., Meskers, S. C. J., and Janssen, R. A. J. *Advanced Materials* **22**(38), 4321–4324 (2010).

[123] Peet, J., Kim, J. Y., Coates, N. E., Ma, W. L., Moses, D., Heeger, A. J., and Bazan, G. C. *Nature Materials* **6**(7), 497–500 (2007).

[124] Ferguson, A. J., Kopidakis, N., Shaheen, S. E., and Rumbles, G. *The Journal of Physical Chemistry C* **115**(46), 23134–23148 (2011).

[125] Credgington, D., Hamilton, R., Atienzar, P., Nelson, J., and Durrant, J. R. *Advanced Functional Materials* **21**(14), 2744–2753 (2011).

[126] Albrecht, S. *unpublished data* .

[127] Sun, Y., Takacs, C. J., Cowan, S. R., Seo, J. H., Gong, X., Roy, A., and Heeger, A. J. *Advanced Materials* **23**(19), 2226–2230 (2011).

[128] Shrotriya, V., Li, G., Yao, Y., Chu, C. W., and Yang, Y. *Applied Physics Letters* **88**(7) (2006).

[129] Beiley, Z. M., Hoke, E. T., Noriega, R., Dacuña, J., Burkhard, G. F., Bartelt, J. A., Salleo, A., Toney, M. F., and McGehee, M. D. *Advanced Energy Materials* **1**(5), 954–962 (2011).

[130] Köhler, A. and Beljonne, D. *Advanced Functional Materials* **14**(1), 11–18 (2004).

[131] Agostinelli, T., Ferenczi, T. A. M., Pires, E., Foster, S., Maurano, A., Mueller, C., Ballantyne, A., Hampton, M., Lilliu, S., Campoy-Quiles, M., Azimi, H., Morana, M., Bradley, D. D. C., Durrant, J., Macdonald, J. E., Stingelin, N., and Nelson, J. *Journal of Polymer Science Part B: Polymer Physics* **49**(10), 717–724 (2011).

[132] Beaupre, S. and Leclerc, M. *Journal of Materials Chemistry A* **1**(37), 11097–11105 (2013).

[133] Li, W., Furlan, A., Hendriks, K. H., Wienk, M. M., and Janssen, R. A. J. *Journal of the American Chemical Society* **135**(15), 5529–5532 (2013).

[134] Albrecht, S., Janietz, S., Schindler, W., Frisch, J., Kurpiers, J., Kniepert, J., Inal, S., Pingel, P., Fostiropoulos, K., Koch, N., and Neher, D. *Journal of the American Chemical Society* **134**(36), 14932–14944 (2012).

[135] Liu, T. and Troisi, A. *Advanced Materials* **25**(7), 1038–1041 (2013).

[136] Huang, C., Barlow, S., and Marder, S. R. *The Journal of Organic Chemistry* **76**(8), 2386–2407 (2011).

[137] Kozma, E., Kotowski, D., Luzzati, S., Catellani, M., Bertini, F., Famulari, A., and Raos, G. *RSC Advances* **3**(24), 9185–9188 (2013).

[138] Kamm, V., Battagliarin, G., Howard, I. A., Pisula, W., Mavrinskiy, A., Li, C., Müllen, K., and Laquai, F. *Advanced Energy Materials* **1**(2), 297–302 (2011).

[139] Yuan, M., Durban, M. M., Kazarinoff, P. D., Zeigler, D. F., Rice, A. H., Segawa, Y., and Luscombe, C. K. *Journal of Polymer Science Part A: Polymer Chemistry* **51**(19), 4061–4069 (2013).

[140] Earmme, T., Hwang, Y.-J., Murari, N. M., Subramaniyan, S., and Jenekhe, S. A. *Journal of the American Chemical Society* **135**(40), 14960–14963 (2013).

[141] Schubert, M., Dolfen, D., Frisch, J., Roland, S., Steyrleuthner, R., Stiller, B., Chen, Z., Scherf, U., Koch, N., Facchetti, A., and Neher, D. *Advanced Energy Materials* **2**(3), 369–380 (2012).

[142] Polyera. *Polyera press release* (2012).

[143] Silva, F., Austin, D. R., Thai, A., Baudisch, M., Hemmer, M., Faccio, D., Couairon, A., and Biegert, J. *Nat Commun* **3**, 807 (2012).

[144] Megerle, U., Pugliesi, I., Schriever, C., Sailer, C., and Riedle, E. *Applied Physics B: Lasers and Optics* **96**(2), 215–231 (2009).

List of Acronyms

A	Acceptor
AM1.5G	Air Mass 1.5 Global Solar Spectrum Norm
BHJ	Bulk Heterojunction
CCD	Charge-coupled Device Camera Sensor
CELIV	Charge Extraction By Linear Increasing Voltage
CT	Charge Transfer
cw-PIA	Quasi-steady-state PIA
D	Donor
DFG	Difference Frequency Generation
EFA	Evolving Factor Analysis
EQE	External Quantum Efficiency
FF	Fill-factor
GSB	Ground State Bleach
GVD	Group Velocity Dispersion
HOD	Higher Order Dispersion
HOMO	Highest Occupied Molecular Orbital

ISC	Intersystem Crossing
IQE	Internal Quantum Efficiency
ITO	Indium Tin Oxide
J_{SC}	Short-circuit Current
KLM	Kerr Lens Modelocking
LED	Light Emitting Diode
LUMO	Lowest Unoccupied Molecular Orbital
MCR	Multi-variate Curve Resolution
M_w	Weight average of the Molecular weight
MPP	Maximum Power Point
Nd:YAG	Neobdym doped Yttrium Aluminum Garnet
NIR	Near Infrared
OD	Optical density
OFC	Optical Frequency Conversion
OFET	Organic Field Effect Transistor
OPA	Optical Parametric Amplifier
OPO	Optical Parametric Oscillator
OPV	Organic Photovoltaics
OR	Optical Rectification
OSC	Organic Solar Cell
P3HT	Poly(3-hexylthiophene)
PCBM	[6,6]-phenyl-C61-butyric acid methyl ester

PCDTBT	poly[N-11”-henicosanyl-2,7-carbazole-alt-5,5-(4’,7’-di-2-thienyl-2’,1’,3’-benzothiadiazole)]
PCE	Power Conversion Efficiency
PCPDTBT	poly[2,6-(4,4-bis-(2-ethylhexyl)-4H-cyclopenta[2,1-b;3,4-b’]-dithiophene)-alt-4,7-(2,1,3-benzothiadiazole)
PEDOT:PSS	Poly(ethylenedioxythiophene):polystyrenesulphonic acid
PIA	Photoinduced Absorption
PL	Photoluminescence
PSBTBT	poly[(4,4’-bis(2-ethylhexyl)dithieno[3,2-b:2’,3’-d]silole)-2,6-diyl-alt-(2,1,3-benzothiadiazole)-4,7-diyl]
SC	Supercontinuum
SE	Stimulated Emission
SFG	Sum Frequency Generation
SHG	Second Harmonic Generation
SMU	Source Measure Unit
SPDC	Spontaneous Parametric Downconversion
SPM	Self-phase Modulation
SVEA	Slowly Varying Envelope Approximation
TAS	Transient Absorption Spectroscopy
TDCF	Time-delayed Collection Field
TR-2PPE	Time-resolved two-photon photoemission

UV	Ultraviolet
Vis	Visible spectral range
XRD	X-ray Diffraction
YAG	Yttrium aluminium garnet ($Y_3AL_5O_12$)
YVO_4	Yttrium orthovanadate

List of Scientific Contributions

Publications in Peer-Reviewed Journals

- **F. Etzold, I. A. Howard, R. Mauer, M. Meister, T.-D. Kim, K.-S. Lee, N. S. Baek and F. Laquai**, "Ultrafast Exciton Dissociation Followed by Nongeminate Charge Recombination in PCDTBT:PCBM Photovoltaic Blends", J. Am. Chem. Soc. **2011**, 133 (24), 9469-9479.

- **F. Etzold, I. A. Howard, N. Forler, D. M. Cho, M. Meister, H. Mangold, J. Shu, M. R. Hansen, K. Mullen and F. Laquai**, "The Effect of Solvent Additives on Morphology and Excited State Dynamics in PCPDTBT:PCBM Photovoltaic Blends", J. Am. Chem. Soc. **2012**, 134 (25), 10569-10583

- **D. Gehrig, I. A. Howard, V. Kamm, C. Dyer-Smith, F. Etzold and F. Laquai**, "Charge generation in polymer:perylene diimide blends probed by Vis-NIR broadband transient absorption pump-probe spectroscopy", Proc. SPIE 8811 **2013**, Physical Chemistry of Interfaces and Nanomaterials XII, 88111F

- **I. A. Howard, F. Etzold, F. Laquai, and M. Kemerink**, "Nonequilibrium Charge Dynamics in Organic Solar Cells", submitted

- **F. Etzold, I. A. Howard, F. Laquai**, "Sub-ns triplet generation in low-bandgap polymer:fullerene solar cells", *manuscript in preparation*

Chapters in Edited Books

- **I. A. Howard, H. Mangold, F. Etzold, D. Gehrig and F. Laquai**, "Transient absorption data analysis by soft-modeling", Ultrafast Dynamics in Molecules, Nanostructures and Interfaces (World scientific, **2013**).

Conference Contributions

- **F. Etzold**, I. A. Howard, R. Mauer, M. Meister, T.D. Kim, K.S. Lee, N. S. Baek, F. Laquai "Charge Generation and Recombination in PCDTBT:PCBM Photovoltaic Blends", Korea-Germany IRTG Meeting, Seoul, South Korea, 2011

- **F. Etzold**, I. A. Howard, R. Mauer, M. Meister, T.D. Kim, K.S. Lee, N. S. Baek, F. Laquai "Charge Generation and Recombination in PCDTBT:PCBM Photovoltaic Blends", DPG Spring Meeting, Dresden, Germany, 2011

- **F. Etzold**, I. A. Howard, R. Mauer, M. Meister, T.D. Kim, K.S. Lee, N. S. Baek, F. Laquai, "Ultrafast Exciton Dissociation Followed by Nongeminate Charge Recombination in PCDTBT:PCBM Photovoltaic Blends", Korea-Germany IRTG Meeting, Mainz, Germany, 2011

- **F. Etzold**, I. A. Howard, R. Mauer, M. Meister, T.D. Kim, K.S. Lee, N. S. Baek, F. Laquai "Charge Generation and Recombination in PCDTBT:PCBM Photovoltaic Blends", 12^{th} Pacific Polymer Conference, Jeju, South Korea, 2011

- **F. Etzold**, I. A. Howard, D. Cho, M. Meister, K. Muellen, F. Laquai "Exciton and Charge Dynamics in PCPDTBT:PCBM Blends Probed by Broadband VIS-NIR Transient Absorption Spectroscopy", DPG Spring Meeting, Berlin, Germany, 2012

- **F. Etzold**, I. A. Howard, N. Forler, D. Cho, M. Meister, H. Mangold, J. Shu, M. R. Hansen, K. Muellen, F. Laquai "The Effect of Solvent Additives on Morphology and Excited State Dynamics in PCPDTBT:PCBM Photovoltaic Blends", SPP1355 workshop, Wuerzburg, Germany, 2012

- **F. Etzold**, I. A. Howard, N. Forler, D. Cho, M. Meister, H. Mangold, J. Shu, M. R. Hansen, K. Muellen, F. Laquai "The Effect of Solvent Additives on Morphology and Excited State Dynamics in PCPDTBT:PCBM Photovoltaic Blends", MRS Fall Meeting, Boston, USA, 2012
- **F. Etzold**, I. A. Howard, F. Laquai "Charge generation and recombination in PCPDTBT:PCBM and PSBTBT:PCBM bulk heterojunction photovoltaic blends", DPG Spring Meeting, Regensburg, Germany, 2013